

# Flow and Entropy Characteristics around Airfoils in Subsonic and Supersonic Flows

by

Enrique G. Martínez Martí

A thesis submitted in partial fulfillment of the requirements for the degree of

MASTER OF SCIENCE  
in  
MECHANICAL ENGINEERING

UNIVERSITY OF PUERTO RICO  
MAYAGÜEZ CAMPUS  
2006

Approved by:

---

R. Vikram Raj Pandya, PhD  
President, Graduate Committee

---

Date

---

Nellore Venkataraman, PhD  
Member, Graduate Committee

---

Date

---

Gustavo Gutierrez, PhD  
Member, Graduate Committee

---

Date

---

Paul Castillo, PhD  
Representative of Graduate Studies

---

Date

---

Paul Sundaram, PhD  
Chairperson of the Department

---

Date

## ABSTRACT

The presented research work analyzes numerically the flow characteristics such as density, pressure, and temperature at subsonic and supersonic speeds for flows past airfoils and explain their difference. Also, it analyzed the usage of the Entropy Generation Rate as a viable and effective way to design and model aerospace airfoils under different atmospheric environments. The goal of this research is to study the flow characteristics and the steady entropy production due to friction and heat transfer. To accomplish these goals, a wedge, a diamond wedge, and three different supercritical airfoils, the NACA 64215, the Grumman K2, and the Whitcomb Supercritical Integral Airfoil were studied. To verify the accuracy of the numerical program, an inviscid supersonic flow past a wedge at Mach 2.6 was analyzed to verify the accuracy of the Computation Fluid Dynamics (CFD) program. Two of the airfoils were analyzed at five different Mach numbers, while the third one was analyzed at four different Mach numbers. The flow characteristics and the entropy generation for the NACA 64215 and the K2 were investigated at five different speeds. Four of the speeds, Mach 0.3, 0.6, 2.0, and 3.0, were similar for all the airfoils at standard atmospheric conditions while the last speed varied depending on the experimental data taken from wind tunnels. These Mach number were selected in order to have two subsonic cases and two supersonic cases. The viscous diamond wedge airfoil was analyzed only at Mach 0.6 and Mach 2.0 and at an angle of attack ( $\alpha$ ) of one degree to compare its entropy generation rate with the entropy generation from the three airfoils.

The entropy generation rate was determined by using the results obtained from the NASA CFL3D CFD program and input those results into a Fortran program that was done for this thesis. CFL3D is a structured grid CFD solver program that analyzes the time dependent conservation form of the Reynolds-Averaged thin-layer Navier-Stokes equations. It uses a semi-discrete finite-volume approach in order to spatially discretized the formulas with upwind-biasing for the convective and pressure terms and central differencing for the shear stress and heat transfer terms. An implicit method is used in order to advance in time and solving for either steady or unsteady flows. Experimental data is used to validate the results of the program.

## RESUMEN

La presente investigación analiza numéricamente las características del flujo como densidad, presión, y temperatura a velocidades subsónicas y supersónicas alrededor de alas y explica las diferencias. También se analiza la Razón de Generación de Entropía como herramientas viables para el diseño de alas aeroespaciales bajo ambientes atmosféricos diferentes. La meta de esta investigación es de estudiar las características del flujo y la producción de entropía estable debido a la fricción y la transferencia de calor. Para alcanzar estos objetivos, una cuña, una cuña en forma de diamante y tres distintos tipos de alas, la NACA 64215, la Grumman K2, y la Whitcomb Supercritical Integral fueron estudiadas. Para verificar la precisión del programa numérico, se estudio el flujo supersónico sin fricción alrededor de una cuña teniendo un número de Mach de 2.6 para verificar la precisión del programa de Dinámica de Fluidos Computacionales (CFD, en inglés). Dos de las alas fueron analizadas en cinco distintos tipos de números de Mach, mientras que la tercera ala fue analizada en cuatro distintos números de Mach. A las alas NACA 64215 y K2 se les investigó las características del flujo y la generación de entropía a cinco distintas velocidades. Cuatro de las velocidades, Mach 0.3, Mach 0.6, Mach 2.0 y Mach 3.0 eran similares en todas las alas bajo condiciones atmosféricas estándar y la última velocidad depende para igualar la velocidad en la data obtenida en túneles de viento. Estas velocidades fueron escogidas para tener dos velocidades subsónicas y dos velocidades supersónicas. La cuña en forma de diamante fue analizada a un número de Mach de 0.6 y Mach 2.0 solamente para comparar la razón de la generación de entropía creada con la generación de entropía de las otras tres alas.

La razón de generación de entropía es determinado utilizando los resultados obtenidos por el programa de Dinámicas de Flujo Computacional CFL3D de la NASA. Estos resultados son entrados en un programa hecho en el lenguaje de Fortran específicamente para esta tesis. El programa CFL3D es un programa de CFD que soluciona mallas estructuradas para la forma conservadora dependiente en tiempo de las ecuaciones de Reynolds-Averaged thin-layer Navier-Stokes. El enfoque del programa es de volumen-finito semi-discreto para discretizar en espacio utilizando un upwind-biasing para las partes de presión y de convección y una diferencia-central para las partes de esfuerzo cortante y de transferencia de calor. Un método implícito es utilizado para avanzar en tiempo para ambos casos estables y casos inestables. Data experimental fue utilizada para validar los resultados del programa.

## DEDICATION

To my family, David, Carmen, Melisa, and Luis for always encouraging me to discover the limits of my capabilities, for their unconditional support, inspiration and love. I have been fortunate in this life, not for only having met the best role models anybody can strive to become, but for also having both of them as parents. I hope some day I can gain the stature of these two people.

To all the actions of love and support of my grandparents Arturo and Fela during all my life. For some things, not even Alzheimer is strong enough to make you forget. You have reached farther than so many people with so little and I will never forget. Also, for all the love of two great aunts, Rosa and Raquel. Rosa, with your loss I gain your spirit, and Raquel who has always been there with love and attention.

Last, but not least, to my future wife Erika for all of her love and support. Behind all great men, there are great women.

“Life and all we do in life generates entropy. Time could not go by without generating entropy. The question is how much entropy are we willing to generate to reach our goals.”

Enrique G. Martinez Marti

## ACKNOWLEDGEMENTS

During the development of my graduate studies in the University of Puerto Rico several persons collaborated directly and indirectly with my research. Without their support it would be impossible for me to finish my work. That is why I wish to dedicate this section to recognize their support.

I want to start expressing a sincere acknowledgement to my advisor, Dr. R. Vikram Pandya for all his time, help, and patience during all this time. Especially for believing in and providing me his guidance during all this time. I will like to thank the members of committee Dr. Nellore Venkataraman and Dr. Gustavo Gutierrez for helping me with this thesis and with all my classes. I want to thank Mrs. Zoraida Santiago for helping me so much with the administrative part of my degree. It will be hard to ever see the Mechanical Engineering Department without the hands of such a secretary as Mrs. Santiago.

Also I would like to thank Dr. James Keenan for all his time and help during the process of learning new CFD programs and methods.

# Table of Contents

ABSTRACT.....	II
RESUMEN .....	IV
DEDICATION .....	VI
ACKNOWLEDGEMENTS.....	VII
TABLE OF CONTENTS .....	VIII
TABLE LIST.....	X
FIGURE LIST .....	XI
<b>1 INTRODUCTION.....</b>	<b>2</b>
1.1 LITERATURE REVIEW .....	7
1.2 SUMMARY OF FOLLOWING CHAPTERS.....	35
<b>2 THEORETICAL BACKGROUND.....</b>	<b>36</b>
2.1 NAVIER STOKES EQUATIONS .....	36
2.1.1 Continuity and Momentum Equations .....	36
2.1.2 Conservation of Energy.....	37
2.2 CROCCO’S THEOREM.....	38
2.3 ENTROPY GENERATION.....	40
2.4 CFD PROGRAM.....	42
2.4.1 CFL3D Equations.....	42
2.4.2 Turbulence Model.....	48
2.5 GRID GENERATION .....	50
2.5.1 Generating a C-Type Grid.....	50
2.5.2 Viscous Grid and MultiGrid.....	54
<b>3 FLOW CHARACTERTISTICS .....</b>	<b>57</b>
3.1 TEST CASES .....	58
3.2 NACA 64215 AIRFOIL.....	68
3.2.1 Mach 0.3 .....	69
3.2.2 Mach 0.6.....	76
3.2.3 Mach 0.65 .....	83
3.2.4 Mach 2.0 .....	90
3.2.5 Mach 3.0.....	97
3.2.6 Entropy Generation Rate Comparison .....	104
3.3 K2 AIRFOIL.....	106
3.3.1 Mach 0.3 .....	106
3.3.2 Mach 0.6.....	113

3.3.3	<i>Mach 0.6</i> .....	121
3.3.4	<i>Mach 2.0</i> .....	128
3.3.5	<i>Mach 3.0</i> .....	135
3.3.6	<i>Entropy Generation Rate Comparison</i> .....	142
<b>3.4</b>	<b>WHITCOMB INTEGRAL SUPERCRITICAL AIRFOIL</b> .....	<b>144</b>
3.4.1	<i>Mach 0.3</i> .....	144
3.4.2	<i>Mach 0.6</i> .....	152
3.4.3	<i>Mach 2.0</i> .....	159
3.4.4	<i>Mach 3.0</i> .....	166
3.4.5	<i>Entropy Generation Rate Comparison</i> .....	173
<b>3.5</b>	<b>DIAMOND WEDGE</b> .....	<b>175</b>
3.5.1	<i>Mach 0.6</i> .....	175
3.5.2	<i>Mach 2.0</i> .....	178
3.5.3	<i>Entropy Generation Rate Comparison</i> .....	181
<b>4</b>	<b>CONCLUSIONS AND FUTURE WORK</b> .....	<b>182</b>
	<b>APPENDIX A. RANKINE-HUGONIOT RELATIONS</b> .....	<b>188</b>
	<b>APPENDIX B. ENTROPY GENERATION RATE</b> .....	<b>189</b>
	<b>APPENDIX B1 NACA 642A215 AIRFOIL</b> .....	<b>189</b>
	<b>APPENDIX B.2 K-2 AIRFOIL</b> .....	<b>194</b>
	<b>APPENDIX B.3 WHITCOMB INTEGRAL SUPERCRITICAL AIRFOIL</b> .....	<b>199</b>
	<b>APPENDIX C. EXPERIMENTAL DATA</b> .....	<b>203</b>
	<b>APPENDIX C.1 K-2 AIRFOIL</b> .....	<b>203</b>
	<b>APPENDIX C.2 WHITCOMB INTEGRAL SUPERCRITICAL AIRFOIL</b> .....	<b>205</b>
	<b>APPENDIX D. ENTROPY GENERATION RATE PROGRAM</b> .....	<b>206</b>
	<b>APPENDIX E. FANNO CURVE</b> .....	<b>210</b>

## Table List

<b>Table</b>	<b>Page</b>
<b>Table 4.1. Flow and Entropy Characteristics.....</b>	<b>183</b>

# Figure List

Figures	Page
Figure 2.1 C-Type Two Dimensional Grid.....	50
Figure 2.2 Airfoil Point Database .....	51
Figure 2.3 Connectors for the database.....	52
Figure 2.4 Structured Grid with Point Clustering.....	53
Figure 2.5 Close-up on Structured Grid.....	54
Figure 3.1 Wedge Grid with 30-degree step.....	59
Figure 3.2 Residual and Coefficient of Drag for Wedge .....	61
Figure 3.3 Mach 2.6 Contour for Wedge .....	62
Figure 3.4 Mach 2.6 Contour Closeup.....	62
Figure 3.5 Pressure Ratio Contour for Wedge.....	64
Figure 3.6 Temperature Ratio for Wedge .....	64
Figure 3.7 Mach Number change along a vertical distance at x = 24.5 on the wedge .....	65
Figure 3.8 Pressure and Temperature Ratio along a vertical distance at x = 24.5.....	66
Figure 3.9 Entropy Generation Rate ( $\frac{W}{m^3 K}$ ) around Wedge Step .....	67
Figure 3.10 Residual for NACA 64 <sub>2</sub> A215 airfoil from CFL3D .....	69
Figure 3.11 Mach 0.3 Contour around NACA 64 <sub>2</sub> A215 airfoil .....	70
Figure 3.12 Pressure Ratio Contour around NACA 64 <sub>2</sub> A215 airfoil .....	71
Figure 3.13 Temperature Ratio Contour around NACA 64 <sub>2</sub> A215 airfoil .....	72
Figure 3.14 Density Ratio Contour around NACA 64 <sub>2</sub> A215 airfoil .....	73
Figure 3.15 Coefficient of Pressure around NACA 64 <sub>2</sub> A215 airfoil.....	74
Figure 3.16 Coefficient of Lift and Drag Convergence for NACA 64 <sub>2</sub> A215 airfoil.....	75
Figure 3.17 Residual for NACA 64 <sub>2</sub> A215 airfoil from CFL3D .....	76
Figure 3.18 Mach 0.6 Contour around NACA 64 <sub>2</sub> A215 airfoil .....	77
Figure 3.19 Pressure Ratio Contour around NACA 64 <sub>2</sub> A215 airfoil .....	78
Figure 3.20 Temperature Ratio Contour around NACA 64 <sub>2</sub> A215 airfoil .....	79
Figure 3.21 Density Ratio Contour around NACA 64 <sub>2</sub> A215 airfoil .....	80
Figure 3.22 Coefficient of Pressure around NACA 64 <sub>2</sub> A215 airfoil.....	81
Figure 3.23 Coefficient of Lift and Drag Convergence on NACA 64 <sub>2</sub> A215 airfoil.....	82
Figure 3.24 Residual for NACA 64 <sub>2</sub> A215 airfoil from CFL3D .....	83
Figure 3.25 Mach 0.65 Contour around NACA 64 <sub>2</sub> A215 airfoil .....	84
Figure 3.26 Pressure Ratio Contour around NACA 64 <sub>2</sub> A215 airfoil .....	85
Figure 3.27 Temperature Ratio Contour around NACA 64 <sub>2</sub> A215 airfoil .....	86
Figure 3.28 Density Ratio Contour around NACA 64 <sub>2</sub> A215 airfoil .....	87
Figure 3.29 Coefficient of Pressure around NACA 64 <sub>2</sub> A215 airfoil.....	88
Figure 3.30 Coefficient of Lift and Drag Convergence for NACA 64 <sub>2</sub> A215 airfoil.....	89

Figure 3.31 Residual for NACA 64 <sub>2</sub> A215 airfoil from CFL3D .....	90
Figure 3.32 Mach 2.0 Contour around NACA 64 <sub>2</sub> A215 airfoil .....	91
Figure 3.33 Pressure Ratio Contour around NACA 64 <sub>2</sub> A215 airfoil .....	92
Figure 3.34 Temperature Ratio Contour around NACA 64 <sub>2</sub> A215 airfoil .....	93
Figure 3.35 Density Ratio Contour around NACA 64 <sub>2</sub> A215 airfoil .....	94
Figure 3.36 Coefficient of Pressure around NACA 64 <sub>2</sub> A215 airfoil.....	95
Figure 3.37 Coefficient of Lift and Drag Convergence on NACA 64 <sub>2</sub> A215 airfoil.....	96
Figure 3.38 Residual for NACA 64 <sub>2</sub> A215 airfoil from CFL3D .....	97
Figure 3.39 Mach 3.0 Contour around NACA 64 <sub>2</sub> A215 airfoil .....	98
Figure 3.40 Pressure Ratio Contour around NACA 64 <sub>2</sub> A215 airfoil .....	99
Figure 3.41 Temperature Ratio Contour around NACA 64 <sub>2</sub> A215 airfoil .....	100
Figure 3.42 Density Ratio Contour around NACA 64 <sub>2</sub> A215 airfoil .....	101
Figure 3.43 Coefficient of Pressure around NACA 64 <sub>2</sub> A215 airfoil.....	102
Figure 3.44 Coefficient of Lift and Drag Convergence for NACA 64 <sub>2</sub> A215 airfoil.....	103
Figure 3.45 Entropy Generation Rate ( $\frac{W}{m^3 K}$ ) around NACA 64 <sub>2</sub> A215 airfoil .....	104
Figure 3.46 Residual for K2 airfoil from CFL3D.....	106
Figure 3.47 Mach 0.3 Contour around K2 airfoil .....	107
Figure 3.48 Pressure Ratio Contour around K2 airfoil .....	108
Figure 3.49 Temperature Ratio Contour around K2 airfoil .....	109
Figure 3.50 Density Ratio Contour around K2 airfoil .....	110
Figure 3.51 Coefficient of Pressure around K2 airfoil .....	111
Figure 3.52 Coefficient of Lift and Drag Convergence for K2 airfoil.....	112
Figure 3.53 Residual for K2 airfoil from CFL3D.....	113
Figure 3.54 Mach 0.6 Contour around K2 airfoil .....	114
Figure 3.55 Pressure Ratio Contour around K2 airfoil .....	116
Figure 3.56 Temperature Ratio Contour around K2 airfoil .....	117
Figure 3.57 Density Ratio Contour around K2 airfoil .....	118
Figure 3.58 Coefficient of Pressure around K2 airfoil .....	119
Figure 3.59 Coefficient of Lift and Drag Convergence for K2 airfoil.....	120
Figure 3.60 Residual for K2 airfoil from CFL3D.....	121
Figure 3.61 Mach 0.6 Contour around K2 airfoil .....	122
Figure 3.62 Pressure Ratio Contour around K2 airfoil .....	123
Figure 3.63 Temperature Ratio Contour around K2 airfoil .....	124
Figure 3.64 Density Ratio Contour around K2 airfoil .....	125
Figure 3.65 Coefficient of Pressure around K2 airfoil .....	126
Figure 3.66 Coefficient of Lift and Drag Convergence for K2 airfoil.....	127
Figure 3.67 Residual for K2 airfoil from CFL3D.....	128
Figure 3.68 Mach 2.0 Contour around K2 airfoil .....	129
Figure 3.69 Pressure Ratio Contour around K2 airfoil .....	130
Figure 3.70 Temperature Ratio Contour around K2 airfoil .....	131
Figure 3.71 Density Ratio Contour around K2 airfoil .....	132
Figure 3.72 Coefficient of Pressure around K2 airfoil .....	133

Figure 3.73 Coefficient of Lift and Drag Convergence for K2 airfoil.....	134
Figure 3.74 Residual for K2 airfoil from CFL3D.....	135
Figure 3.75 Mach 3.0 Contour around K2 airfoil .....	136
Figure 3.76 Pressure Ratio Contour around K2 airfoil .....	138
Figure 3.77 Temperature Ratio Contour around K2 airfoil .....	138
Figure 3.78 Density Ratio Contour around K2 airfoil .....	139
Figure 3.79 Coefficient of Pressure around K2 airfoil .....	140
Figure 3.80 Coefficient of Lift and Drag Convergence for K2 airfoil.....	141
Figure 3.81 Entropy Generation Rate ( $\frac{W}{m^3 K}$ ) around K2 airfoil .....	142
Figure 3.82 Residual for Whitcomb airfoil from CFL3D.....	144
Figure 3.83 Mach 0.3 Contour around Whitcomb airfoil .....	145
Figure 3.84 Pressure Ratio Contour around Whitcomb airfoil .....	147
Figure 3.85 Temperature Ratio Contour around Whitcomb airfoil .....	148
Figure 3.86 Density Ratio Contour around Whitcomb airfoil .....	149
Figure 3.87 Coefficient of Pressure around Whitcomb airfoil .....	150
Figure 3.88 Coefficient of Lift and Drag Convergence around Whitcomb airfoil .....	151
Figure 3.89 Residual for Whitcomb airfoil from CFL3D.....	152
Figure 3.90 Mach 0.6 Contour around Whitcomb airfoil .....	153
Figure 3.91 Pressure Ratio Contour around Whitcomb airfoil .....	154
Figure 3.92 Temperature Ratio Contour around Whitcomb airfoil .....	155
Figure 3.93 Density Ratio Contour around Whitcomb airfoil .....	156
Figure 3.94 Coefficient of Pressure around Whitcomb airfoil .....	157
Figure 3.95 Coefficient of Lift and Drag Convergence for Whitcomb airfoil.....	158
Figure 3.96 Residual for Whitcomb airfoil from CFL3D.....	159
Figure 3.97 Mach 2.0 Contour around Whitcomb airfoil .....	160
Figure 3.98 Pressure Ratio Contour around Whitcomb airfoil .....	161
Figure 3.99 Temperature Ratio Contour around Whitcomb airfoil .....	162
Figure 3.100 Density Ratio Contour around Whitcomb airfoil .....	163
Figure 3.101 Coefficient of Pressure around Whitcomb airfoil .....	164
Figure 3.102 Coefficient of Lift and Drag Convergence for Whitcomb airfoil.....	165
Figure 3.103 Residual for Whitcomb airfoil from CFL3D.....	166
Figure 3.104 Mach 3.0 Contour around Whitcomb airfoil .....	167
Figure 3.105 Pressure Ratio Contour around Whitcomb airfoil .....	168
Figure 3.106 Temperature Ratio Contour around Whitcomb airfoil .....	169
Figure 3.107 Density Ratio Contour around Whitcomb airfoil .....	170
Figure 3.108 Coefficient of Pressure around Whitcomb airfoil .....	171
Figure 3.109 Coefficient of Lift and Drag Convergence for Whitcomb airfoil.....	172
Figure 3.110 Entropy Generation Rate ( $\frac{W}{m^3 K}$ ) around Whitcomb airfoil .....	173
Figure 3.111 Residual for Diamond airfoil from CFL3D.....	175
Figure 3.112 Mach 0.6 Contour around Diamond Airfoil.....	176
Figure 3.113 Pressure Contour around Diamond Airfoil.....	176

Figure 3.114 Temperature Contour around Diamond Airfoil.....	176
Figure 3.115 Density Contour around Diamond Airfoil.....	176
Figure 3.116 Coefficient of Lift and Drag Convergence for Diamond Airfoil .....	177
Figure 3.117 Residual for Diamond airfoil from CFL3D.....	178
Figure 3.118 Mach 2.0 Contour around Diamond airfoil... ..	179
Figure 3.119 Pressure Ratio Contour around Diamond airfoil .....	179
Figure 3.120 Temperature Ratio Contour around Diamond Airfoil .....	179
Figure 3.121 Density Ratio Contour around Diamond Airfoil .....	179
Figure 3.122 Coefficient of Lift and Drag Convergence for Diamond Airfoil .....	180
Figure 3.123 Entropy Generation Rate ( $\frac{W}{m^3 K}$ ) around Diamond Airfoil .....	181

# 1 INTRODUCTION

Although great improvements and new research in the area of aerodynamics has led to great inventions such as jet airplanes, there are still a large number of unanswered questions. Fluid flow dynamics can be divided and studied depending on the speed at which the flow is traveling. It can be divided into three areas of interest, subsonic, transonic, and supersonic. A flow is said to be traveling at a subsonic speed when its speed is less than the speed of sound. On the other hand, a flow is considered to be supersonic when it is traveling faster than the speed of sound. Flow characteristics such as temperature, density and pressure at those two different regimes are different and at the same time keep varying as the speed keeps increasing within each regime.

One term that is commonly used to describe the speed of the flow is the Mach number, in honor of the Austrian physicist Ernst Mach. It is defined as the ratio of the speed of the flow to the speed of sound. When the Mach number is one, the flow is said to be at sonic. The flow is subsonic when the Mach number is less than one and supersonic when the Mach number is more than one. One important thing that makes these two flows regimes different is the ability of a gas to change its path direction as it goes around a body such as an airfoil. If the flow is subsonic, the gas will change its path in order to go around the body. For a supersonic flow, the gas does not have enough time to divert around the body. When this happens in supersonic flow, a compression shock wave is formed in the location where the gas strikes the body.

In order to study these two ranges of flow speeds, both the first and the second law of thermodynamics are used. Two of the pillars on which physics is founded are the first and second law of thermodynamics. The first law provides a relation between work and all the different forms of energy. It is an application of the conservation of energy which states that energy cannot be created or destroyed but that instead it changes from one form to another. Although several scientists worked with the concept of energy, it was Rudolf Clausius who in 1850 first stated that “There is a state function  $E$ , called ‘energy’, whose differential equals the work exchanged with the surroundings during an adiabatic process.” Mathematically, for a closed system where mass is not entering or leaving, the first law of thermodynamics can be written as:

$$dE = \delta Q - \delta W$$

where  $dE$  is a infinitesimal change in internal energy,  $\delta Q$  is an infinitesimal change in heat, and  $\delta W$  infinitesimal change in work. During the 1820s, Sadi Carnot started to investigate the possibility of the maximum amount of mechanical work that can be developed from heat. This search led him to develop what we now know as the Carnot type engine. The Carnot type engine represented the ideal reversible engine which can be describe as one where the process can be reversed while obtaining the same initial values. In other words, a cycle where there are no dissipative effects such as friction or heat transfer at finite temperature difference.

In a paper in 1850, Rudolf Clausius was the first one to express the second law of thermodynamics by stating that “Heat cannot pass spontaneously from a region of lower temperature to a region of higher temperature.” Then in 1865, Clausius extended on work

done by others like Carnot and stated in a paper the First and Second Law of Thermodynamics by expressing that:

The energy of the universe is constant.

The entropy of the universe tends to a maximum.

He developed what is now known as Clausius inequality:

$$\oint \frac{\delta Q}{T} \leq 0$$

and defined for the first time the change in entropy as:

$$dS = \frac{\delta Q}{T} \quad (\text{internally reversible and adiabatic})$$

where  $T$  is the temperature. An adiabatic process which is internally reversible, is called isentropic. Kelvin and Planck defined the Second Law of Thermodynamics in what it is now known as the Kelvin-Planck Statement which states that it is not possible to make a heat engine which produces no other effects than the extraction of heat from a single source and the generation of an equal amount of work. If such an engine could exist, it will be called a perpetual motion machine. Later on, in 1877 Ludwig Boltzmann modified the definition of entropy to represent a statistical measurement of disorder, which J. Willard Gibbs later refined and brought about the theory of statistical mechanics.

One of the important aspects and main usages of the second law of thermodynamics and the concept of entropy is that it provides a mean to quantify the efficiency of a process. Given that the maximum amount of work that can be output from a process can be quantified by assuming a Carnot-type engine, then it is possible to calculate the efficiency of a process and quantify the different losses.

Until 1937 most of the work done with the second law of thermodynamics was related to reversible or irreversible thermodynamic transformations in engines and to determine efficiencies. In 1937, Luigi Crocco developed Crocco's theorem by combining the first and second law of thermodynamics. It related both the translational and rotational movements of a fluid element through a flowfield to the second law of thermodynamics. It was the first mathematical relation between the gradient of entropy, the flow vorticity and total enthalpy gradient. One of the important outcomes of Crocco's theorem is that it proves that all flows behind a curved shock wave are rotational even in inviscid flow. This outcome is important in aerospace engineering in order to study and define flows at supersonic speeds around airplanes.

Although the concept of entropy and the second law of thermodynamics have been used in aerodynamics, most of its usage has been for flows at high supersonic speeds and only then by oversimplifying the problems. With the technological advancement of computers, the new area of Computation Fluid Dynamics (CFD) has allowed engineers and scientist the opportunity to program the common equations used to study flows around airplanes. Given the complexity of these equations and the speed of new computers, now it is possible to obtain results by programming the complex partial differential equations that before would have taken too long to solve without a computer. This new area of CFD has also allowed engineers and scientist to start analyzing the efficiency of aerospace parts in more detail. Only until recently, scientist and engineers such as Adrian Bejan[1] has started to use the concept of entropy to start talking about the entropy generation rate of different things. This concept of the entropy generation rate allows the study of the efficiency of different things in

time. Therefore, it is now possible to study the entropy generation rate of an airfoil which is mainly caused by friction and heat dissipative effects. In doing so, it is possible to study the efficiency of an airfoil and do comparative tests. For this thesis, the study and comparison of the flow characteristics and entropy generation rate will be the main goal.

## Motivation

The work of Luigi Crocco in 1937 has allowed aerospace engineers and scientist to use the second law of thermodynamics and entropy in a different way. For the most part, his work has been used to analyze compressible flows phenomena like shock waves and to help characterize them. In recent years, different researches have studied the concept of minimization of entropy to analyze and quantify in more detail the losses in mechanical systems and ways in which their efficiency can be improved. Some of these losses that are taken into consideration and that cause a process to become irreversible are friction and heat dissipation.

In the area of aerospace engineering, one of the major concerns in all airplane designs is the selection of the best suited airfoil shape. Although iterative methods exist for the selection of an airfoil shape, it is still an area of discussion and not so much research has been done. Lately, several papers have been published that attempt to analyze different airfoils in terms of the entropy that each one produces. Given that the main purpose of a wing is to hold the weight of an airplane by producing lift, it is the intent of this thesis to determine the flow characteristics at subsonic and supersonic speeds and also to calculate the entropy generation rate that is generated at close proximity to an airfoil for a specific amount of lift. In doing so,

the entropy generated together with the lift-to-drag ratio will help to determine the level of efficiency of the airfoil. For this study, the NACA 64<sub>2</sub>A215 airfoil, the K-2 Grumman airfoil, and Whitcomb Supercritical Integral airfoil will be analyzed. These three airfoils are all consider supercritical airfoils due to their ability to achieve high subsonic speeds while delaying the drag rise that is caused by the formation of a compression shock at free stream speeds close to sonic speed. These supercritical airfoils were chosen due to their good aerodynamic qualities such as low drag and because of available experimental data that will be used to compare with the numerical results from the CFL3D program. Unless specified, all the airfoil tests were run in CFL3D assuming standard atmospheric conditions with a pressure of 101.325 KPa and a temperature of 288.15K. This study will also present the way in which entropy is generated around an airfoil. The results from CFL3D were input into a Fortran program in order to analyze the entropy generation rate of each airfoil at each different Mach number.

All the cases were analyzed using a Pentium Celeron D 2.8GHz processor with the Intel Fortran Compiler and MPICH 1.2.7.

## **1.1 Literature Review**

M. Kostic [1] analyzed the philosophical and practical aspects of energy and entropy having as a goal to establish the concept of reversible heat transfer. Several conclusions were found. First, energy is indivisible from matter and space, associated with all processes and thus indivisible from time. For a given state, the addition of energy will randomly distribute over the space the system occupies called internal thermal energy, increase its potential energy

(temperature) and energy displacement (entropy). Energy and mass are conserved within the interacting systems and the energy will transfer from a higher to a lower potential which will result in energy displacement or entropy. Entropy could be transferred by reversible paths from one system to another and also generated due to irreversibility because of heat and work transfer.

Bejan (1995) [3] described the entropy generation minimization as a new analysis for the thermodynamics of finite-size devices and finite time processes. The entropy generation minimization (EGM) is a method for modeling and optimizing devices that are affected by thermodynamic irreversibilities as heat transfer, mass transfer, and fluid flow irreversibilities. In this paper he outlined the way in which the entropy generation minimization method is used to analyze and optimize different components of a system. The EGM has been used in the study of cryogenics, heat transfer, education, storage systems, nuclear and fossil power plants, solar power plants, and refrigerators. Also, the use of the EGM might vary from one application. In the case of heat exchangers, the purpose might be to minimize the entropy generation while in the case of power plants the goal is to maximize the power output. The EGM consists of taking into account the first and second law. In his paper, he starts by deriving the Gouy-Stodola theorem. In pure thermodynamics the Gouy-Stodola theorem is used which states that the destroyed power is proportional to the total rate of entropy generation. The difference between the Gouy-Stodola theorem (exergy analysis) and the EGM method is that the goal of the EGM method is to minimize the calculated entropy generation rate. In order to minimize the entropy generation rate it is necessary to use the relations between temperature difference, heat transfer, pressure differences, and mass flow

rates. In this sense, there is no need to make use of the exergy concept to calculate the entropy generation rate and minimize it. The EGM method also makes use of the entropy generation number which is a ratio between the entropy generation rate and the minimized entropy generation rate. For the case of heat transfer an equation is given for the entropy generation rate per unit tube length which takes into account the wall-stream heat transfer coefficient and the frictional pressure drop along the tube. One interesting characteristic is that in all heat transfer devices with fluid flow the entropy generation rate caused by heat transfer competes with entropy generation rate caused by fluid friction. They have opposite signs as the diameter of the tube changes and because of this, there is an optimum tube diameter that minimizes the total entropy generation rate. Other heat transfer devices rely on external convection in order to accomplish the necessary heat transfer. In order to analyze the entropy generation rate of this system it can be model as the heat transfer between a fluid and a body immersed in the fluid. He gives the entropy generation rate of such a system which is composed of a contribution from the heat transfer and another contribution from the drag on the immersed body. As the first heat transfer case, there are two entropy generation rates which will compete one against the other. This points to a minimum total entropy generation rate for the optimal body size. The necessary parameters and a chart is provided to view the optimal sizes of a plate, a cylinder, and a sphere. Some emphasis is put into a group that use EGM to explain and predict damping in homogeneous and inhomogeneous elastic systems in a theory that they called elastothermodynamic damping. In this case, it is shown that the damping effect is caused by the entropy generated by conduction throughout the material.

Denton, J. D. [4] analyzed and described the origins and effect of the losses in turbomachines. The sources of entropy that he described are in general viscous effects in boundary layers, viscous effects in mixing processes, shock waves, heat transfer across temperature differences. He started by explaining how efficiency was categorized in the past and the models that engineers and scientist used to use. These earlier models divided the sources of loss in turbomachines in different categories such as profile loss, secondary loss, and tip leakage loss and attempted to predict the effect of each individual loss separately. Still, these models depended greatly on correlations of experimental data obtained from tests or performance of the machines. Due to this dependence, little development was achieved to comprehend the nature of these losses and people had to adjust all their models to the empirical data obtained. The development in 1970 and 1980 of improved instruments as the laser anemometer and the ensemble-average hot-wire data helped identify and characterized how the flow behaved in turbomachines.

He then described the effect of each individual category, starting with profile loss. Profile loss is described as the loss created in the blade boundary layers away from the end walls. The loss that is generated from the trailing edge is also included as a profile loss. Endwall loss, which is also classify as secondary loss, is created due to the annulus boundary layers pass through a blade row, but he points out the difficulty in trying to distinguish between profile loss and secondary loss since sometimes the losses occur due to a combination of both. The third category of loss, tip leakage, arises from the loss of useful flow from the tips of blades and hub clearances of stator blades. The importance of each individual category dependences on each system plus other factors such as blade aspect ration and tip clearance.

He described that in general, loss refers to anything that reduces the efficiency of a turbomachine, but this does not include factors that change the cycle efficiency as opposed to turbine or compressor efficiency.

A loss coefficient is defined that which is different from the ones that are currently in use. The most common loss coefficient is the stagnation pressure loss coefficient because of its ease to calculate it from test data, but not necessarily the most useful for design purposes. A better coefficient for design purposes will be the use of energy or enthalpy loss coefficient. Isentropic efficiency in a machine is a comparison between the actual work and the isentropic work of a machine. Since in most cases the flow is adiabatic, the losses come from entropy creation due to irreversibilities. For this reason it is more useful from a design point of view to use entropy increase instead of stagnation pressure or kinetic energy loss. At the same time, the use of entropy does not change if it is viewed from a rotating or stationary blade row. There are different definitions of entropy loss coefficients, but at low speeds, all definitions approach the same value. Denton explains the relation between the efficiency of a system and the entropy change. From the definition of efficiency in a compressor, it can be seen that the loss of efficiency is proportional to the increase in specific entropy and to the exit temperature. On the other hand, when entropy is generated as a fluid dynamic process, it is inversely proportional to the local temperature. Therefore, a flow at a high temperature creates less entropy than the same process at a lower temperature given that it has fixed values for loss coefficient and flow velocity and this is the origin of the “reheat effect” which affects the polytropic efficiency to be different from the isentropic efficiency.

Denton then describes and characterizes the entropy generation from the different sources. He starts by describing the entropy generated from the boundary layers and describes how the viscous shear work at the boundary layer causes entropy generation by being converted to heat at a specific temperature. It is noted that in the boundary layer that since the velocity gradient is higher near the surface, then most of the entropy generation is concentrated in the inner part of the layer. In turbulent boundary layers most of the entropy generated occurs within the laminar sublayer and logarithmic region which are called the “universal velocity profile”. One important fact is that in turbulent boundary layers the dissipation coefficient described, is less dependent on the condition of the boundary layer, like the shape factor, than is the skin friction coefficient. Also, the entropy generated by a laminar boundary layer is less, by a factor between 2 and 5, than that for a turbulent. An equation was written that aids in determining the total entropy generation in the boundary layer.

Entropy is also generated in a mixing process. He explains that even in an irrotational flow, the fluid is being sheared and this shearing gives rise to an entropy generation. In wakes, due to the high rates of shearing, entropy generation is considerably higher due to a higher effective viscosity, over 100 times larger, than in laminar flow. Sometimes, high entropy generation due to turbulent flow is desired, like in the case of a heat exchanger which could lead to a smaller exchange area. Several approaches are analyzed. One of these approaches is using a control volume to the mixing, which has the advantage of being able to compute the losses without knowing the details that caused the losses.

In shock waves, entropy is generated due to heat conduction and high viscous normal stresses that are present within only a few molecular free path of thickness. As a comparison a

normal shock wave will always generate more entropy than an oblique shock wave with the same Mach number. An increase in entropy generation is also caused by the interaction between shock waves and boundary layers. In boundary layers, it is shown that suction surfaces of a blade produce more entropy. An expression is also put describing a way to find an optimum relation for pitch-to-chord ratio for turbines given a specified combination of inlet and outlet flow angles. Using the same pitch-to-chord ratio method, the predictions for compressors are not realistic and that is probably because the method does not take into account the boundary layer separation.

The effect of Mach number in entropy generation is explained. As the upstream flow approaches sonic speed, the local speed in the suction surface approaches sonic speed at a faster rate and usually ends in a normal shock which will greatly increase the entropy generated. Also, there will possibly be a significant contribution of entropy creation due to boundary layer separation. Some of the ways used to delay local sonic speed at the suction surface is to design thin blades and blades with low or reverse suction surface camber in order to maintain the local Mach number as close to the inlet Mach number. In this design, lift is achieved by a low speed at the pressure surface instead of high lift at the suction surface and also helps to minimize the boundary layer loss.

Emphasis is put in the difficulty of understanding and calculating accurately a priori the losses of a two dimensional cascade and the dependence in empirical data. For some problems such as tip leakage loss and loss due to separation there is an understanding of the mechanisms for these losses but cannot quantify the improvements in a design before an actual test. At the other hand, there are losses which are yet not fully understood such as

endwall losses, transonic trailing edge losses, and mixing losses. Accurate predictions of these losses depend greatly on the use of empirical correlations which may not necessarily provide an accurate representation of the physics involved.

H. Li & G. Ben-Dor [5 & 6] applied the principle of minimum entropy production to the case of shock wave reflections. They started by defining the governing equations of a steady, two-dimensional flow for a perfect inviscid gas. These equations were applied for the case of transonic and supersonic flows. Theoretically, there exists the possibility of two solutions with straight and attached shock waves. They examined the transition from regular to Mach reflection and viceversa using the principle of minimum entropy and found the regular reflection wave configurations to be stable within the dual-solution domain.

Ed Walsh, Mark Davies, and Roy Myose [7] studied a technique to minimize the entropy generation rate in the boundary layers of turbomachinery blades. One of the possible outcomes of minimizing entropy generation in blades is to increase their efficiency of the whole system for a given power output, which will lead to less fuel consumption. They focused their work first on analyzing the entropy generated in the laminar region of the boundary layer in the suction surface of non-film cooled turbine blades and then modified the boundary layer in order to find ways in which the entropy generated is minimized. They used an analytical polynomial representation of the boundary layer edge velocity distribution in the laminar region put forward by Pohlhausen and others in order to minimize the entropy creation. Specifically, they varied the undefined variables of a fifth order polynomial representation of the boundary layer following some constraints as the work output and boundary conditions as keeping low the rate of diffusion in the decelerating regions in order

to avoid separation. As a result they developed a method to determine the optimum boundary layer velocity distribution in order to minimize entropy and an increase in stage efficiency of approximately 0.06%.

Ed J. Walsh, Mark R. D. Davies, and Donal M. McEligot [8] considered the use of entropy to predict boundary layer stability. They suggest a new hypothesis that attempts to put together different parameters that affect the location of the transition of the boundary layer from a laminar to a turbulent flow. They claim that the driving force of the boundary layer transition onset is the entropy generation rate alone. Even though the goal is to lower the entropy generation they cautioned that minimizing entropy is not always a good thing. As an example, even though laminar flow has lower entropy generation rates than turbulent flow, turbulent flow induces high rates of heat transfer which might be desirable in some systems or some sections. A relation is established between different parameters known to affect the transition of boundary layer and the entropy generation rate.

Ed Walsh, Mard R.D. Davies, Philip C. Griffin, and Francis K. O'Donnell [9] studied the effect of Reynolds number, compressibility, and free stream turbulence on the profile entropy generation rate. For their study, they assumed an adiabatic and quasi-isothermal flow. For the case of subsonic flow, they assumed an adiabatic and two-dimensional, therefore the only source of entropy for that case is the one arising from fluid friction. Some of their observations include a thicker turbulent boundary layer, and higher shear strain rates in the laminar boundary layer than those seen at 0.8% turbulence intensity caused by an earlier transition. Also, they noticed the presence of fluctuating components of velocity in the laminar boundary layer which lead to the notion of a hybrid boundary layer. This hybrid

layer consisted of both laminar and turbulent characteristics in the case where there is free stream turbulence. They use the boundary layer velocity profile to obtain the entropy generation rate per unit volume. For the case of entropy generation due to compressibility at a Reynolds number of 163,000 and an exit Mach number of 0.37 they did not observe any appreciable generation, even though quantitative measurements were limited because of the thin nature of the boundary layer. For the case of free stream turbulence it affected in different ways the entropy generated. First, the free stream turbulence increase the entropy generation due to the increase in viscous shear in the laminar layer, but on the other hand, they did not observe a significant effect in the turbulent region compared to when the free stream is laminar.

Philip A. Thompson, Thomas W. Strock, and David S. Lim [10] studied a way to estimate the thickness of a shock wave based on the entropy production. They estimated the thick of the shock wave at supersonic speeds in an ideal gas by relating the internal entropy production to the increase in entropy found from Rankine-Hugoniot equations. Under the assumptions of continuum flow and local thermodynamic equilibrium, they relate the entropy jump across the shock to the entropy production within the shock. The entropy production was found by adding the detailed entropy balance over the shock while the entropy jump is found from the Rankine-Hugoniot equations assuming a one-dimensional flow with constant heat capacity. They found good agreement with experiments for the shock thickness using argon.

Salas (1991), [11] studied the shock wave interaction with an abrupt area change. The interaction of the shock wave with a sudden area change was analyzed in terms of the

incident shock wave Mach number and the area-jump ratio. In this analysis the entropy production for the wave system was used as well as the principle of minimum entropy production in order to resolve a nonuniqueness problem. The problem been analyzed depends on two parameters; the strength of the incident shock measured by the wave Mach number and the area ratio across the discontinuity. In this study, the area ratio is defined as well as the Rankine-Hugoniot relations that were used. Also, the pressure and density were nondimensionalized by their initial values and all the velocities were nondimensionalized by the speed of sound in a specific region. For this study, the case of area divergence and area convergence were analyzed. In the case of area divergence, it was shown that if the initial Mach number is less than 2.068, then a weak rarefaction is reflected which would accelerate the flow before it enters the area of divergence. As the shock strength continues to increase, the shock moves to where the area jumps, but as it keeps increasing, a shock moves to the entrance of the divergence area and then the exit area. One result for the case of area contraction is that if the initial shock is greater than 2.068, the reflected wave is a shock and then the subsonic flow behind this shock is accelerated to sonic conditions due to the area convergence. Then the flow is further accelerated due to the rarefaction wave running downstream. In this case, in general the transmitted shock is stronger and the incident shock. The author used the minimum entropy production principle to correct some results obtained by other investigations. Using the entropy production in an interval of time and integration over the whole area, it was demonstrated how is that the case of a standing shock solution can link two different cases for an area ratio larger than the one for the standing shock solution and the case for a smaller area ratio. One of the conclusions is that for an area

contraction and an incident Mach number greater than 2.068 a region was found where three wave patterns satisfied all the governing equations. At least, it was known that one of the patterns, which consisted of the standing shock solution, is an unstable configuration. It was also shown how to prove the exact solutions using the entropy generation rate and the principle of minimum entropy production.

Gino Moretti and Maurizio Pandolfi [12] analyzed the entropy layer on a blunt-nosed cone and a predictor-corrector integration scheme is used. For a given free stream Mach number, a numerical method is given that describes at different distances from the nose, what fraction of the shock layer is made up of the entropy layer. Several versions of their predictor-corrector scheme were analyzed in order to minimize the amount of computational time. First, the numerical scheme is analyzed using equally spaced nodes. An accumulation of truncation errors was seen which produced oscillations in the entropy distribution and also the Mach number became erratic due to its dependence to the entropy. The second method that they used was to stretch the coordinates by using a stretching function. This method caused high truncation errors in regions where the entropy change was very high. The last method that they used was to have two computational regions. This means that they analyzed all regions where a function undergoes rapid changes as a discontinuity. In other words, any parameter like entropy which has a strong gradient in a small area, is going to be analyzed as a jump instead of a gradual but steep change. Other methods were analyzed but the conclusion was that even though some methods can give better results than others, the choice of which method to use depends greatly on the problem that is being analyzed.

Abu-Hijleh and Heilen [13] examined the entropy generation due to laminar natural convection over a heated rotating cylinder. The study consisted of numerically analyzing the entropy generation due to laminar mixed convection on an isothermal rotating cylinder over a wide range of Reynolds number and buoyancy parameter. The buoyancy parameter is based on a ratio between the Grashof number and the Reynolds number. First, the necessary equations for a steady state two-dimensional laminar mixed convection for a horizontal rotating cylinder are presented. These equations are given in cylindrical coordinates. Then, the equations were put in non-dimensional form using the stream-vorticity function formulation and also the boundary conditions. The local entropy generation, as well, was put in non-dimensional form in two-dimensional cylindrical coordinates. Using the local entropy generation, the total entropy generation was calculated by integrating the local entropy generation over the entire domain. In the case study, the entropy equation consisted of two parts. One part that contributed to the entropy generation comes from heat by conduction while the second part is due to the viscous dissipation. Numerically, the entropy generation was calculated after the velocity and temperature profiles in the program had converged. Higher values of Reynolds number and/or buoyancy parameter caused smaller viscous and thermal boundary layers. On the other hand, this result means a higher velocity and temperature gradients, thus higher rates of entropy generation. The steepest increase in the rate of entropy generation was found at low values of the buoyancy parameter. It was found that high values of buoyancy increased the heat transfer but at the expense of higher entropy generation but very high values of buoyancy resulted in a minimal increase in entropy generation. Therefore, higher heat transfer rates could be obtained without the consequence

of lower efficiency. Another result is that an increase in the cylinder radius caused a decrease in total entropy generation. The explanation for this is that increasing the radius of the cylinder will result in a smaller velocity and temperature gradients for a given Reynolds number and buoyancy parameter and thus a decrease in the entropy generation rate.

Creager [14] investigated the effect of leading edge thickness on the flow over a flat plate at a mach number of 5.7. There was a need for agreement between the measured surface pressures and those obtained from a linear combination of blast wave and weak viscous interaction parameters. It was found that the boundary layer for the thickest plate was in the high entropy layer. One of their results is that the impact pressure increases less above the boundary layer than the under and it reaches a peak value at the shock wave. Another result, is that the boundary layer's decay depends primarily on the distance from the leading edge while the shape of the shock wave depends on both the distance from the leading edge and also on the leading edge thickness. The data obtained suggested the appearance of the boundary layer out of the high entropy layer. In the case of blunt plates, the boundary layer developed in the high entropy layer. In the case of thin leading edge plates, the boundary layer growth varied linearly with the distance from the leading edge.

Camberos and Heng Chen [15] worked on a continuum breakdown parameter that is based on entropy generation rates. As part of their research, they review different parameters and suggested a continuum breakdown parameter based on local entropy production rates that could be use as a way to quantify the extend to which the continuum assumption in fluid flow dynamics is acceptable. One area of much research involve rarefied gas dynamics where the length of the molecular mean free path is equivalent to a defined macroscopic reference

dimension of the flow field. Some cases that involve the rarefied gas effect include areas of strong velocity, pressure, and/or temperature gradients such as high speed flight at high altitudes. One problem when analyzing these types of cases is the ambiguity in the choice of an appropriate length scale. One of the parameter that is currently being used to know when the continuum hypothesis breaks down is the Knudsen Number. They suggested that instead of using the Navier-Stokes equations up to a Knudsen number of 0.1, use a local Knudsen number that has the characteristic length been defined as gradients. Such gradients may come from temperature, density, or pressure variations. In their study they start by deriving some of the equations use for entropy and entropy generation rates and incorporating entropy into a proposed continuum breakdown parameter. They tested their result for the case of incompressible boundary layer in a flat plate heat transfer with constant wall temperature, for a flat plate laminar boundary layer entropy production, and for the one dimensional plane shock wave. Their parameter had good agreement for the case of one-dimensional shock wave.

Naterer and Camberos [16] described the use of entropy and the second law of thermodynamics to analyze various computational thermo-fluid dynamics. Entropy and the second law is used in computational fluid dynamics (CFD) for things like to determine the numerical error, convergence criteria, or time step limitations in a computer program. They give a description of the evolution of entropy and different ways in which it can be expressed for cases like incompressible and compressible fluid flow. In order to be able to fully express the second law, two important mathematical properties are described. The first mathematical property, concavity, is use to bound entropy from above while it is in the

process of achieving a maximum value at an equilibrium condition. The second mathematical property, compatibility, is a condition that gives a consistency condition between the fluxes of entropy and the conserved variables. Some of the applications in which entropy has been used are for compressible flows, incompressible flows, phase change heat transfer, and turbulence.

Salas and Iollo [17] investigated the entropy jump across an inviscid shock wave. They showed how to derive the shock jump conditions for the Euler equations in their primitive form. One of the things that they make emphasis is that the inviscid entropy profile has a local maximum within the shock layer. They start by first writing the one-dimensional conservation laws for an inviscid flow of perfect gas. In this paper they derived in a mathematical form the shock jump conditions for the Euler equations starting from their primitive form using generalized functions. They also showed how is that the variables have different shock profiles and that the entropy can not be represented by a single Heaviside function, but that instead, it needs two Heaviside functions for a proper representation.

Walsh, Myose, and Davies [18] studied a prediction method for the local entropy generation rate in a transitional boundary layer with a free stream pressure gradient. They presented a method that could be used to predict the entropy generation rate in steady, two-dimensional, incompressible, adiabatic boundary layer flows. It is based upon five relations in order to determine, the entropy generated in the laminar region, the entropy generated in the turbulent region, the location of transition, the length of transition, and the entropy generated in the transition region. In order to use this method, knowledge of the boundary layer edge velocity distribution and the turbulence intensity is necessary. They claimed that one of the benefits

of this method is that it does not rely upon dissipative CFD predictions which can be slow and not sufficiently trustworthy. In order to determine the entropy generated in the boundary layers, they suggested to first curve fit a given boundary layer edge velocity profile. Then, use Thwaites separation criteria, which can be expressed in terms of the boundary layer edge velocity, in order to determine the location of transition. Third, determine the length of the transition. Lastly, after the transition region has been defined, determine the entropy generation rate in the laminar, transition, and turbulent regions.

Stack [19] studied the design of different types of airfoils that could delay the compressibility bubble. The type of airfoil that he investigated was designated the NACA 16 series and have increased critical Mach number. Apparently, in order to attain the highest critical speed, an airfoil needs to have a flat pressure distribution curve instead of having a high negative pressure in the nose, which gradually changes into the air stream conditions at or after the trailing edge of an airfoil. A derivation of two airfoil parameters was given. First, the derivation of the camber line was given in terms of the circulation around an airfoil which might correspond to a certain distribution of vorticity along the airfoil surface. Then, a derivation for the thickness form of an airfoil is given. Induced velocities were assumed to be negligibly small as compared to stream velocity which for thin airfoils at low lifts, this is valid, but not with increase in lift or thickness. In both derivations, use of thin airfoil theory is assumed. For this NACA 16 series, low drag comes from having a longer region of laminar flow in the boundary layer which results in a rearward position of the point of maximum negative pressure. From the different airfoils studied, the NACA 16-106 had the

lowest drag coefficient which is contrary to the expectation that a symmetrical NACA 16-009 airfoil would normally have the lowest minimum drag coefficient.

Oswatitsch [20] wrote about the recent advances and some of the challenges that are still been worked in transonic flows. Attention is put into the relation of potential flow, drag, and entropy flux. Although potential flow usually assumes isentropic flow, in the case of transonic flow over a thin body, the first order entropy disturbance can not be disregard when calculating drag although by the momentum theorem it does not occur in the first or second order vorticity equation. Several equations are written that describe the relation between the x-component of the velocity and the entropy disturbance across a weak shock wave. For the case of a weak shock wave, the entropy increase is proportional to the third power of the x-component of the velocity across the shock. The irrotationality of the transonic flow field is also verified using Crocco's Vortex Law. An equation for the drag coefficient is derived which consist of two parts; one part arrives from the effect of the pressure coefficient and the other part comes from the effect of the thickness distribution of the airfoil. For the case of a slightly supersonic flow the integration of the first order drag coefficient is done up to the bow shock. A distinction is made about the dominance of either the kinetic terms or the entropy term in the Trefftz plane at different distances from the trailing edge. At a small distance from the trailing edge in the Trefftz plane, the kinetic terms dominate while farther downstream the entropy term becomes important and can not be neglected.

Stewart, Whitney, and Wong [21] studied the boundary layer characteristics of turbomachine blade rows and the relation to over all blade loss. The study of the boundary layer is of importance in turbomachine blade rows because that is where the viscous losses are

generated in the blade surface and at the end walls. Proof was also presented for a relation between over all blade loss and the momentum boundary layer thickness. At the same time, the momentum boundary layer thickness is related to the Reynolds number and the total blade surface diffusion. The parameters that they used in their study were the displacement thickness, the momentum thickness, a form factor, and an energy factor. The form factor used is a ratio of the total displacement thickness to the total thickness. The energy factor is a ratio of the total energy thickness to the total momentum thickness. These factors were derived as functions of Mach number and a power velocity profile exponent which is usually assumed for turbulent boundary layer. For their study of boundary layer characteristics related to blade row losses, they determine the losses by means of a momentum loss and a kinetic-energy loss. For the kinetic-energy loss they found that it consisted of the two-dimensional cascade loss, the end wall loss, and the mixing loss downstream of the blade trailing edge. Good agreement was found using a specific exponent which is also used in turbulent boundary-layer and also found that all the losses could be evaluated by means of a momentum thickness ratio. They also investigated the relation between the momentum thickness with diffusion and reaction. For this, they used the Zweifel's method and defined a total diffusion parameter taken as the sum of the suction and pressure surface diffusion parameters. It was shown that the over all efficiency can be determined in an unknown region of Reynolds number from the relation of boundary layer momentum thickness with Reynolds number and the relation of blade loss with momentum boundary layer thickness.

Charles B. Johnson and Lillian R. Boney [22] analyzed an integral method for computing the behavior of turbulent boundary layer with variable entropy effects on a blunt axisymmetric

body. In order to obtain the heat transfer they made use the Reynolds analogy factor together with the local Stanton number. The value of the Reynolds analogy factor will depend on which local turbulent skin-friction theory is used, either the Spalding-Chi skin-friction or the Van Driest II skin-friction. Their results were compared to experimental data for heat transfer on a flat plate, on a blunt-cone, and the difference in other parameters such as skin friction and density. For the case of the flat plate, in general, the heat transfer prediction was close to the data whenever the Van Driest II function was derived for a linear Crocco relationship. For the case of the blunt-cone, when there is a peak heating for fully turbulent flow, the use of the Spalding-Chi skin-friction theory overestimate the experimental data and the Van Driest II underestimate slightly from the experimental data. In order to calculate other parameters they used different techniques. In order to calculate the different boundary layer velocity profiles an N power-law correlation was used and in order to calculate the density profiles a modified Crocco relationship.

James L. Amick [23] derived a method to select the thickness, hollowness, and size which will give the least drag and acceptable bending strength for a supersonic wing at specified flight conditions. The chord of the wing was chosen in order to provide the maximum lift-drag ratio at the design conditions. The weight of the wing was neglected. The wing is considered to be satisfactorily strong if the maximum bending stress at the root area given by the beam formula is at all times less or equal to the maximum allowable stress. The design procedure that they used was to first determine the flight characteristics such as Mach number and altitude. Then, determine the weight of the airplane, the wing plan form, the profile shape, material, and maximum permissible bending stress. As the second step,

assume a value for the wing chord and then calculate the ratio of the weight of a solid wing for a specific thickness to the weight of the airplane without the wing. Also, calculate the ratio of the thickness drag to the drag caused by the lift of a solid wing weight for a given chord. Then, several other parameters like hollowness ratio, lift and drag coefficients, and wing drag are obtain from different equations. The results that they obtained were that the flight characteristics to a large extend determines the shape of the wing to use. As an example, at low altitudes, steel wings appeared to have less drag than aluminum wings while at high altitudes the reverse appears to be true.

J. M. Délery [24] surveyed and reviewed the physical aspects of several problems encounter by designers when analyzing shock wave phenomena at high speeds. He described the shock wave equations, the flow properties that give rise to shock waves, and the major consequences of shock wave phenomena in aerospace applications. Problems such as shock-shock interference of different types, shock-boundary-layer interaction with different interaction control techniques were discussed. At the end, several suggestions were made. First, more work is needed to correctly and accurately capture shock waves by numerical codes in order to model transfer processes like the development of transitional shears layers. Secondly, a full understanding and prediction of structures associated with shock intersection or reflection. More work is also needed to study the thermochemical processes initiated by strong shocks in hypersonic flows. Finally, more study is needed for the modeling of turbulence in shock-separated flows. This last item is crucial in order to predict the physics of flows involving strong shockwave-boundary-layer interaction. In this sense, the model

use today, transport equation model, is unable to accurately predict the physics as soon as a separated region forms.

Eric B. Ratts and Atul G. Raut [25] studied the entropy generation minimization of fully developed internal convective flows with constant heat flux. They analyzed the optimal Reynolds number by using the Entropy Generation Minimization method for laminar and turbulent flow and the thermodynamic optimum of a single-phase convective heat transfer for fully developed flow with uniform and constant heat flux. In order to minimize the entropy generated, the generations due to viscous dissipation and heat transfer dissipation in the flow passage was summed and then minimized modifying the Reynolds number based on hydraulic diameter. For the case of laminar flow, the optimal Reynolds number was determined for different cross sections such as square, equilateral triangle, and rectangular. In their conclusion they found the optimal configuration for laminar and turbulent flow in a tube with an uniform heat flux boundary for a specific necessary total heat transfer rate and mass flow rate. They reached several conclusions based on the results. First, the entropy generation is smaller for heat dissipation than for viscous dissipation given the same deviation from optimal Reynolds number for both laminar and turbulent flow although for laminar flow is more noticeable. The minimum Reynolds number scaled proportional to the tube length for laminar flow. For optimum Reynolds number, the circular tube had the longest length while the rectangular tube had the shortest length but high aspect ratio. In the case of the circular cross-section with laminar flow, they found a 5:1 ratio of heat dissipation to viscous dissipation while a 29:9 ratio for turbulent flow. For the cross sections considered in laminar flow, the rectangular cross section with an aspect ratio of 8 and 2, had the lowest

entropy generation. The high aspect rectangular cross section was 50% of the minimum entropy generation of the circular cross section while the low aspect ratio rectangular cross section had 90% of the minimum entropy generation of the circular cross section.

Li and Figliola [26] studied an exergy based design methodology for airfoil shape optimization. The purpose of this investigation was to use an exergy based method to apply it to a two dimensional airfoil shape. The problem studied was for a viscous, incompressible flow represented by the Reynolds-average (RANS) form. The necessary equations were provided and each term was explained. As it is explained, the entropy generation is not computed directly, but instead is calculated based on other properties. The local entropy generation rate equation for a three-dimensional flow field is composed of two terms. The first terms comes from the thermal convective exchange that there is between the body and the environment either directly or indirectly by internal and aerodynamics heating. The second term results as a consequence from the velocity field around a moving body. In the case of laminar flow, the velocity profile can be easily obtained but for the case of turbulent flow, attention was put to replace the laminar viscosity with the effective viscosity which is a sum from the laminar and the turbulence viscosity. Computer simulations were made using the Fluent computational fluid dynamic code (CFD) and all the cases were compared by using the NACA 0012 airfoil as the benchmark airfoil. The optimization was performed for a fixed chord length, Reynolds number and angle of attack but varied the lift-to-drag ratio in order to minimize entropy generation. In order to have a representation of the coordinates of the airfoils as the parameters are changes, the airfoil was optimized using the NURBS curve. It was found that entropy generation increases as the lift-to-drag ratio was increased but that

did not mean that the lift-to-drag ratio increases as the entropy generation increased. Also, it was found that both the lift-to-drag ratio and the entropy generation increased as the airfoil became flatter.

Kock and Herwig [27] studied the local entropy production in turbulent shear flows using a high Reynolds number model with wall functions. They investigated the entropy production in incompressible turbulent shear flows of Newtonian fluids. This study is based on the assumption that the only way to achieve higher efficiency in designing modern thermal systems is through a comprehensive understanding of the available work and the amount of entropy production which can be analyzed using the second law of thermodynamics. The study starts by providing the transport equation of entropy and providing the time averaging of this equation which yields the Reynolds average Navier Stokes equations (RANS). In this equation they take into account four different terms that affect entropy. The terms that are involved are the convective terms, the entropy production by dissipation, and the entropy production by heat transfer. The four groups of entropy production terms in turbulent flows are the entropy production rate by direct dissipation, the entropy production rate by indirect dissipation, the entropy production rate by heat conduction with mean temperature gradients, and entropy production rate by heat transfer with fluctuating temperature gradients. Of the four entropy sources, the two that they modeled were the entropy production rate by indirect dissipation and the entropy production rate by heat transfer. In order to model the entropy production by indirect dissipation terms one of the steps they took was the use of the two-equation  $\kappa$ - $\epsilon$  turbulence model. They also modified the entropy production caused by the fluctuating temperature by assuming a local equilibrium, a Boussinesque approach, and a

constant turbulent Prandlt number. All their equations were compared with Direct Numerical Simulations (DNS) and at the same time modified by the DNS results in order to be able to predict the minimum entropy production. They found that the peak values of the entropy production occurred close to the wall.

Morduchow [28] investigated the analysis and calculation by integral methods of laminar compressible boundary layer with heat transfer and with and without pressure gradient. The proposed a simple method to be used to calculate several properties of the laminar compressible boundary layer in an axial pressure gradient with heat transfer at the wall. Also, a method is presented to aid in determining the separation point in a compressible flow with an adverse pressure gradient over a surface with a uniform wall temperature. Several integral methods for the laminar boundary layer analysis are presented and compared for their benefits. The first integral method discussed is the Karman-Pohlhausen method, which is the most widely applied. Some of the advantages of this method is that for certain assumed velocity profiles then an ordinary differential equation is obtained and basically leaves the boundary layer thickness as the unknown. There are, however, two disadvantages in using this method for practical cases. One of the disadvantages is in its inability to predict accurately the separation point in an adverse pressure gradient and also it fails to provide accurate results for the derivatives of the profiles to be use in the laminar boundary layer calculations. Another integral method that has been developed consists in using integral equations in addition to the Karman momentum integral. Another refinement of the Karman-Pohlhausen method is to use the Karman integral together with profiles of higher degree other than the fourth. This last method was the one that they used but with a sixth-degree

profile due to its accurateness and ease to use. Some of their assumptions were having an ideal gas, a coefficient of viscosity proportional to the absolute temperature in order to satisfy Sutherland's relation, for the case of a flow with pressure gradient the wall temperature is uniform, use a unity Prandtl number, and constant specific heats as well Prandtl number. From the proposed method the boundary layer characteristics can be found for either a flow with and without a pressure gradient. For the case of a flow without a pressure gradient the characteristics can be found as long as the Prandtl number is constant. In the case of a flow with a pressure gradient the characteristics can only be found for the case of a unity Prandtl number and uniform wall temperature. In terms of wall cooling, they found that it tends to diminish the effect of a pressure gradient like delaying the separation in an adverse pressure gradient, while heating tends to enhance it. It is also shown that while cooling of the wall tended to stabilize the laminar boundary layer, at moderate supersonic speeds, the cooling may completely stabilize the boundary layer. Finally, a now common conclusion is that a favorable pressure gradient tended to stabilize the laminar boundary layer while an adverse pressure gradient had a destabilizing effect.

Whitcomb and Clark [29] proposed a method of an airfoil shape for efficient flight at supercritical mach numbers. At supercritical Mach numbers, there is a local region of supersonic flow that extends vertically from an airfoil and usually terminates in a shock wave. This shock wave causes an energy loss and an increase in drag. Also, it produces a positive pressure gradient at the surface of the airfoil that can cause boundary layer separation and another source of drag increase associated with it. The studied had as a goal to find a way to delay the drag rise that is associated with the development of local supersonic flow on the

upper surface of a wing. Some of the approaches that had been used until that point were based on using thinner airfoils, sweepback, area ruling, and antishock bodies. Other approaches tried to eliminate the shock-induced separation by special camber distribution, vortex generators, and injection of high energy air into the boundary layer near the shock wave. The airfoil shape that was suggested in this study included a slot between the upper and lower surfaces near the trailing edge in order to delay the shock-induced separation on both surfaces. In order to reduce the shock losses, the airfoil incorporates negative camber in front of the slot combined with significant positive camber rearward of the slot. The proposed airfoil shape had a drag rise at a Mach number of 0.79 compared to a drag rise at a Mach number of 0.67 for the NACA 64A-series airfoil which is the one that was used as a comparison. The purpose of having the slot is to eliminate the shock-induced separation by introducing stream energy air under the upper surface boundary layer at a specific point. Another goal is to reduce the vertical extent of the supersonic region that ends in a shock wave and reduces the supersonic Mach number ahead of the wave. To accomplish this goal, the proposed airfoil incorporates a reduction in camber that diminishes the curvature of the upper surface. The airfoil shape has a roughly uniform surface curvature and near zero mean slope from the rearward of the leading edge to the probable position of the shock. This reduction in camber also causes a reduction of lift. In order to counteract this reduction in lift, the wing shape has an increase of the incidence of the fore region in front of the slot that is achieved by a significant positive camber on the lower surface. Several results were achieved using the proposed supercritical airfoil shape. First, for a normal (lift) force coefficient of 0.65, the drag rise occurred at a Mach number of 0.79 instead of a Mach

number of 0.67 for the NACA 64A-series airfoil. Most of the drag for a Mach number less than the 0.78 optimum was due almost entirely to skin friction losses. For the less than optimum Mach number, the drag value is approximately 10 percent greater than that for the NACA 64A-series. Second, there is a more negative pitching moment coefficient for the supercritical airfoil than for conventional airfoils. There is an increase in stall normal force coefficients at high subsonic Mach numbers and it provides delays in drag rise at off-design lift coefficients. The operation of the supercritical airfoil appears to be most critical at normal force coefficients below the design value.

In conclusion, only one paper has been found that relates entropy generation and external flow characteristics to airfoil shape, although the study only investigated incompressible flows. All other papers help to have some understanding of the magnitude for the effect of friction and heat transfer and the areas where these two dissipation forms are usually present. Although this thesis investigates compressible subsonic and supersonic flows, most of the entropy generation created by friction is expected to happen inside the boundary layer as the researched papers suggest. Also, it is expected that the entropy generation by heat transfer becomes more important at the supersonic speeds.

## **1.2 Summary of Following Chapters**

In this thesis Chapter 1 shows the necessary previous work that has been done about this topic. Chapter 2 deals with the model theory, including all the formulas, and the description of the computer program and grid generator that was used in the experiments. The third chapter presents all the experiments that were done. Conclusions are presented in Chapter 4.

## 2 THEORETICAL BACKGROUND

### 2.1 Navier Stokes Equations

Although a set of equations for inviscid fluid were developed by Leonhard Euler, the Navier-Stokes Equations describe the motion of a viscous, Newtonian fluid such as air and water. The equations developed by Claude-Louis Navier and George Gabriel Stokes, relates the change in momentum of the fluid to the change in pressure and dissipative viscous forces.

#### 2.1.1 Continuity and Momentum Equations

The Navier-Stokes Equations represents Newton's Second Law applied to the case of fluids and for that reason they are sometimes classified under Newtonian Mechanics. As part of Newtonian Mechanics and one of physics' conservation laws, the continuity equation represents a mathematical expression of the Conservation of Mass. It states that mass can neither be created nor destroyed and can be written as:

$$\frac{D\rho}{Dt} + \rho \nabla \cdot V = 0 \quad 2.1$$

where  $\rho$  is density,  $V$  is the velocity field vector, and  $\frac{D}{Dt}$  is the substantial derivative

$$\frac{D}{Dt} = \frac{\partial}{\partial t} + u \frac{\partial}{\partial x} + v \frac{\partial}{\partial y}.$$

The Navier-Stokes Equations, which are sometimes refer to as the Momentum Equations, can be written for a 2-D case as:

$$\begin{aligned}\rho \frac{Du}{Dt} &= -\frac{\partial p}{\partial x} + \frac{\partial}{\partial x} \left[ \frac{2}{3} \mu \left( 2 \frac{\partial u}{\partial x} - \frac{\partial v}{\partial y} \right) \right] + \frac{\partial}{\partial y} \left[ \mu \left( \frac{\partial u}{\partial y} + \frac{\partial v}{\partial x} \right) \right] \\ \rho \frac{Dv}{Dt} &= -\frac{\partial p}{\partial y} + \frac{\partial}{\partial y} \left[ \frac{2}{3} \mu \left( 2 \frac{\partial v}{\partial y} - \frac{\partial u}{\partial x} \right) \right] + \frac{\partial}{\partial x} \left[ \mu \left( \frac{\partial u}{\partial y} + \frac{\partial v}{\partial x} \right) \right]\end{aligned}\tag{2.2}$$

where  $u$  and  $v$  are the components of the velocity field in the x-direction and y-direction respectively,  $p$  is the pressure field,  $\mu$  is the molecular viscosity coefficient.

### 2.1.2 Conservation of Energy

The Conservation of Energy, also one of the conservation laws in physics, states that energy can not be neither created nor destroyed but instead that it changes from one form to another. It is a representation of the first law of thermodynamics and can be mathematically represented as:

$$\rho \frac{De}{Dt} = \nabla \cdot (k \nabla T) - p \nabla \cdot V + \Phi\tag{2.3}$$

where  $e$  is the specific internal energy,  $k$  is the thermal conductivity, and  $\Phi$  is the viscous dissipation function in 2-dimensions:

$$\Phi = -\frac{2}{3} \mu (\nabla \cdot V)^2 + 2\mu \left[ \left( \frac{\partial u}{\partial x} \right)^2 + \left( \frac{\partial v}{\partial y} \right)^2 \right]\tag{2.4}$$

## 2.2 Crocco's Theorem

The first law and the second law of thermodynamics can be combined in such a way for the case of fluid flows, to end with Crocco's theorem. If it is assumed that the specific heat transfer is reversible,  $\partial q_{rev} = Tds$ , and substituting it into the first law:

$$Tds = de + pdv \quad 2.5$$

Then, using the definition of enthalpy,  $h = e + pv$ , it can be substituted into equation 2.5 to get,

$$Tds = dh - vdp = dh - \frac{dp}{\rho} \quad 2.6$$

where  $v$  is the specific volume  $v = 1/\rho$ . Equation 2.6 can be written as

$$T\nabla s = \nabla h - \frac{\nabla p}{\rho} \quad 2.7$$

given that at any instant in time, a particle can change its state to that of the neighboring particle. If the viscous terms are eliminated from the Navier Stokes Equation, the resulting equations are called the Euler equations:

$$\rho \frac{\partial V}{\partial t} + \rho(V \cdot \nabla)V = -\nabla p \quad 2.8$$

The gradient of pressure in the equation 2.7 can be substituted into equation 2.8 to get:

$$T\nabla s = \nabla h + \frac{\partial V}{\partial t} + (V \cdot \nabla)V \quad 2.9$$

Equation 2.9 can be modified to incorporate the total enthalpy of a system or flow. If the total enthalpy is defined as

$$h \equiv h_o - \frac{V^2}{2} \quad 2.10$$

and then get its gradient,

$$\nabla h = \nabla h_o - \nabla \left( \frac{V^2}{2} \right) \quad 2.11$$

then, equation 2.11 can be substituted into the resulting entropy equation 2.9 to get

$$T\nabla s = \nabla h_o - \nabla \left( \frac{V^2}{2} \right) + \frac{\partial V}{\partial t} + (V \cdot \nabla)V \quad 2.12$$

Now, using the vector identity

$$\nabla \left( \frac{V^2}{2} \right) - (V \cdot \nabla)V = V \times (\nabla \times V)$$

in equation 2.12, allows it to be changed to get

$$T\nabla s = \nabla h_o - V \times (\nabla \times V) + \frac{\partial V}{\partial t} \quad 2.13$$

This equation is called Crocco's theorem. For a steady case,  $\frac{\partial V}{\partial t}$  will be zero and the equation will reduce to

$$T\nabla s = \nabla h_o - V \times (\nabla \times V) \quad 2.14$$

It is based on the assumption of an inviscid flow and for a steady flow it provides a relation between the gradient of entropy, the total enthalpy gradient,  $\nabla h_o$ , and the flow vorticity or curl,  $\nabla \times V$ . This equation provides the starting point to show that the entropy that is going

to be calculated numerically for a viscous case includes two parts, the vorticity and the change in enthalpy.

## 2.3 Entropy Generation

Although compressible flow and sound waves can be describe by assuming an isentropic flow, a shock wave is a highly irreversible phenomena. The calculation of the entropy generation might help to provide a mean to be certain that airfoil that is chosen is the best airfoil shape for the flight regime that to which it will be exposed. In order to calculate the entropy generation close to the surface of an airfoil, the derivation done by Bejan [2] for external flows will be used for the calculations. Assuming that the fluid is in local thermodynamic equilibrium, an account of all the mass fluxes, energy transfers, and entropy transfers interactions can be express as:

$$\dot{S}_{gen}''' = \frac{1}{T} \nabla \cdot \tilde{q} - \frac{1}{T^2} \tilde{q} \cdot \nabla T + \rho \frac{Ds}{Dt} \quad 2.15$$

where  $\dot{S}_{gen}'''$  is the volumetric entropy generation rate having units of  $\left(\frac{W}{m^3 K}\right)$ , and  $\tilde{q}$  is the

heat transfer rate vector. Now, the first law of thermodynamics can be written as[2]:

$$\rho \frac{D\tilde{e}}{Dt} = -\nabla \cdot \tilde{q} - p(\nabla \cdot \nu) + \mu\Phi \quad 2.16$$

where  $\tilde{e}$  is the specific internal energy per unit volume.

If the entropy relation  $d\tilde{e} = Tds - Pd\left(\frac{1}{\rho}\right)$  is used and the substantial derivative is taken on both sides of the equation then:

$$\rho \frac{Ds}{Dt} = \frac{\rho}{T} \frac{D\tilde{e}}{Dt} - \frac{p}{\rho T} \frac{D\rho}{Dt} \quad . \quad 2.17$$

If this entropy equation, equation 2.17, is combined with equation 2.16 and 2.15 one gets:

$$\dot{S}_{gen}''' = -\frac{1}{T^2} \tilde{q} \cdot \nabla T + \frac{\mu}{T} \Phi \quad 2.18$$

Using now Fourier law of heat conduction  $\tilde{q} = -k\nabla T$  and substituting it in equation 2.18, then

$$\dot{S}_{gen}''' = \frac{k}{T^2} (\nabla T)^2 + \frac{\mu}{T} \Phi \quad 2.19$$

which in two-dimensional Cartesian coordinates, can be expressed as:

$$\dot{S}_{gen}''' = \frac{k}{T^2} \left[ \left( \frac{\partial T}{\partial x} \right)^2 + \left( \frac{\partial T}{\partial y} \right)^2 \right] + \frac{\mu}{T} \left\{ 2 \left[ \left( \frac{\partial u}{\partial x} \right)^2 + \left( \frac{\partial v}{\partial y} \right)^2 \right] + \left( \frac{\partial u}{\partial y} + \frac{\partial v}{\partial x} \right)^2 \right\} \quad 2.20$$

The first term on the right hand side is the entropy generation due to heat transfer diffusion while the second term on the right hand side is the entropy generation due to viscous dissipation. This is the equation that will later be discretized in order to calculate the volumetric entropy generation close to an airfoil. In order to obtain the data for the heat transfer and the viscous dissipation, a CFD approach was used. The program and the model will be explained in the next section.

## 2.4 CFD Program

### 2.4.1 CFL3D Equations

In order to acquire data to input into the entropy generation equation, a Computational Fluid Dynamics (CFD) program called CFL3D was used for the experiments. Several different surfaces and airfoil shapes were tested in order to verify the usability of the program. First, it is important to explain in some detail how the program works and how the program interprets the Navier Stokes equations and interpret the inputs given. Depending on the case of study, CFL3D works with either the Navier Stokes equations or Euler equations. Excluding body forces and external heat sources, the full three dimensional compressible Navier Stokes equations are expressed as:

$$\frac{\partial Q}{\partial t} + \frac{\partial f}{\partial x} + \frac{\partial g}{\partial y} + \frac{\partial h}{\partial z} = 0 \quad 2.21$$

where

$$Q = \begin{bmatrix} \rho \\ \rho u \\ \rho v \\ \rho w \\ \tilde{E} \end{bmatrix} \quad 2.22$$

$$f = \begin{bmatrix} \rho u \\ \rho u^2 + p - \tau_{xx} \\ \rho uv - \tau_{xy} \\ \rho uw - \tau_{xz} \\ (\tilde{E} + p)u - u\tau_{xx} - v\tau_{xy} - w\tau_{xz} + q_x \end{bmatrix} \quad 2.23$$

$$g = \begin{bmatrix} \rho v \\ \rho uv - \tau_{xy} \\ \rho v^2 + p - \tau_{yy} \\ \rho vw - \tau_{yz} \\ (\tilde{E} + p)v - u\tau_{xy} - v\tau_{yy} - w\tau_{yz} + q_y \end{bmatrix} \quad 2.24$$

$$h = \begin{bmatrix} \rho w \\ \rho uw - \tau_{xz} \\ \rho vw - \tau_{yz} \\ \rho w^2 + p - \tau_{zz} \\ (\tilde{E} + p)w - u\tau_{xz} - v\tau_{yz} - w\tau_{zz} + q_z \end{bmatrix} \quad 2.25$$

where  $\tilde{E}$  is the total energy per unit volume. In these equations the stresses are defined as:

$$\tau_{xx} = \frac{2}{3}\mu \left( 2\frac{\partial u}{\partial x} - \frac{\partial v}{\partial y} - \frac{\partial w}{\partial z} \right) \quad 2.26$$

$$\tau_{yy} = \frac{2}{3}\mu \left( 2\frac{\partial v}{\partial y} - \frac{\partial u}{\partial x} - \frac{\partial w}{\partial z} \right) \quad 2.27$$

$$\tau_{zz} = \frac{2}{3}\mu \left( 2\frac{\partial w}{\partial z} - \frac{\partial u}{\partial x} - \frac{\partial v}{\partial y} \right) \quad 2.28$$

$$\tau_{xy} = \mu \left( \frac{\partial u}{\partial y} - \frac{\partial v}{\partial x} \right) = \tau_{yx} \quad 2.29$$

$$\tau_{xz} = \mu \left( \frac{\partial w}{\partial x} - \frac{\partial u}{\partial z} \right) = \tau_{zx} \quad 2.30$$

$$\tau_{yz} = \mu \left( \frac{\partial v}{\partial z} - \frac{\partial w}{\partial y} \right) = \tau_{zy} \quad 2.31$$

and using the ideal gas assumption, the pressure can be defined from the perfect gas law as:

$$p = (\gamma - 1) \left[ \tilde{E} - \frac{\rho}{2} (u^2 + v^2 + w^2) \right] \quad 2.32$$

Although CFL3D solves the conservative form of the Navier Stokes equations, the primitive variables are some of the results that can be obtained. The primitive variables are obtained by a transformation matrix of the form:

$$M = \frac{\partial Q}{\partial q} \quad 2.33$$

where,

$$Q = \begin{bmatrix} \rho \\ \rho u \\ \rho v \\ \rho w \\ \tilde{E} \end{bmatrix} \quad \text{and} \quad q = \begin{bmatrix} \rho \\ u \\ v \\ w \\ p \end{bmatrix} \quad 2.34$$

The energy variable is obtained from a transformation of the ideal gas relation,

$$\tilde{E} = \frac{p}{\gamma - 1} + \frac{\rho}{2} (u^2 + v^2 + w^2) \quad 2.35$$

and

$$M = \begin{bmatrix} 1 & 0 & 0 & 0 & 0 \\ u & \rho & 0 & 0 & 0 \\ v & 0 & \rho & 0 & 0 \\ w & 0 & 0 & \rho & 0 \\ \frac{u^2 + v^2 + w^2}{2} & \rho u & \rho v & \rho w & \frac{1}{\gamma - 1} \end{bmatrix} \quad 2.36$$

In CFL3D, all of these equations are transformed to a generalized coordinate system in order to evaluate them. These transformation are accomplish by using a generalized coordinate transformation:

$$\begin{aligned} \xi &= \xi(x, y, z, t) \\ \eta &= \eta(x, y, z, t) \\ \zeta &= \zeta(x, y, z, t) \end{aligned} \quad 2.37$$

and using the chain rule for multiple variables:

$$\begin{aligned} d\xi &= \xi_x dx + \xi_y dy + \xi_z dz + \xi_t dt \\ d\eta &= \eta_x dx + \eta_y dy + \eta_z dz + \eta_t dt \\ d\zeta &= \zeta_x dx + \zeta_y dy + \zeta_z dz + \zeta_t dt \\ dt &= t_x dx + t_y dy + t_z dz + t_t dt \end{aligned} \quad 2.38$$

Since  $t_x = t_y = t_z = 0$  and  $t_t = 1$ , then the set of equations can be put in matrix form as:

$$\begin{bmatrix} d\xi \\ d\eta \\ d\zeta \\ dt \end{bmatrix} = \begin{bmatrix} \xi_x & \xi_y & \xi_z & \xi_t \\ \eta_x & \eta_y & \eta_z & \eta_t \\ \zeta_x & \zeta_y & \zeta_z & \zeta_t \\ 0 & 0 & 0 & 1 \end{bmatrix} \begin{bmatrix} dx \\ dy \\ dz \\ dt \end{bmatrix} \quad 2.39$$

and the Cartesian coordinates with

$$\begin{bmatrix} dx \\ dy \\ dz \\ dt \end{bmatrix} = \begin{bmatrix} x_\xi & x_\eta & x_\zeta & x_t \\ y_\xi & y_\eta & y_\zeta & y_t \\ z_\xi & z_\eta & z_\zeta & z_t \\ 0 & 0 & 0 & 1 \end{bmatrix} \begin{bmatrix} d\xi \\ d\eta \\ d\zeta \\ dt \end{bmatrix} \quad 2.40$$

Using these last two equations, it is possible to determine the Jacobian and its inverse:

$$J = \frac{\partial(\xi, \eta, \zeta, t)}{\partial(x, y, z, t)} = \begin{vmatrix} \xi_x & \xi_y & \xi_z & \xi_t \\ \eta_x & \eta_y & \eta_z & \eta_t \\ \zeta_x & \zeta_y & \zeta_z & \zeta_t \\ 0 & 0 & 0 & 1 \end{vmatrix} \quad 2.41$$

in order to convert the initial three dimensional Cartesian coordinate compressible Navier Stokes equations into a generalized Navier Stokes equations:

$$\frac{\partial \tilde{Q}}{\partial t} + \frac{\partial(\hat{F} - \hat{F}_v)}{\partial \xi} + \frac{\partial(\hat{G} - \hat{G}_v)}{\partial \eta} + \frac{\partial(\hat{H} - \hat{H}_v)}{\partial \zeta} = 0 \quad 2.42$$

This conservative generalized Navier-Stokes equation can be easily modified to analyze an inviscid case by simply eliminating the viscous terms. The conserved density, momentum and total energy per unit volume are written as:

$$\hat{Q} = \frac{Q}{J} = \frac{1}{J} \begin{bmatrix} \rho \\ \rho u \\ \rho v \\ \rho w \\ \tilde{E} \end{bmatrix} \quad 2.43$$

where the inviscid flux terms are expressed as

$$\hat{F} = \frac{F}{J} = \frac{1}{J} \begin{bmatrix} \rho U \\ \rho U u + \xi_x p \\ \rho U v + \xi_y p \\ \rho U w + \xi_z p \\ (\tilde{E} + p)U - \xi_i p \end{bmatrix} \quad 2.44$$

$U$  represents the contravariant velocity in the  $\xi$  generalized coordinate defined as

$$U = \xi_x u + \xi_y v + \xi_z w + \xi_t \quad 2.45$$

Similar contravariant velocities  $V$  and  $W$  are defined for the  $\eta$  and the  $\zeta$  generalized coordinates. The viscous flux terms are defined by

$$\hat{F}_v = \frac{F_v}{J} = \frac{1}{J} \begin{bmatrix} 0 \\ \xi_x \tau_{xx} + \xi_y \tau_{xy} + \xi_z \tau_{xz} \\ \xi_x \tau_{xy} + \xi_y \tau_{yy} + \xi_z \tau_{yz} \\ \xi_x \tau_{xz} + \xi_y \tau_{yz} + \xi_z \tau_{zz} \\ \xi_x b_x + \xi_y b_y + \xi_z b_z \end{bmatrix} \quad 2.46$$

and similarly for  $\hat{G}_v$  and  $\hat{H}_v$ . For the cases of where an inviscid solution is desirable, all viscous terms like  $\hat{F}_v$  are omitted. The resulting inviscid equations will be Euler equations. The shear stress and heat flux terms are nondimensionalized by using the free stream density,  $\tilde{\rho}_\infty$  free stream speed of sound,  $\tilde{a}_\infty$ , and the free stream molecular viscosity,  $\tilde{\mu}_\infty$  in the tensor form as:

$$\tau_{x_i x_j} = \frac{M_\infty}{\text{Re}_{\tilde{L}_R}} \left[ \mu \left( \frac{\partial u_i}{\partial x_j} + \frac{\partial u_j}{\partial x_i} \right) + \lambda \frac{\partial u_k}{\partial x_k} \delta_{ij} \right] \quad 2.47$$

$$b_{x_i} = u_j \tau_{x_i x_j} - \dot{q}_{x_i} \quad 2.48$$

$$\dot{q}_{x_i} = - \left[ \frac{M_\infty \mu}{\text{Re}_{\tilde{L}_R} \text{Pr}(\gamma - 1)} \right] \frac{\partial a^2}{\partial x_i} \quad 2.49$$

Finally, in order to close the Navier Stokes equations in generalized form, the Stokes hypothesis for viscosity  $\left( \lambda + \frac{2\mu}{3} = 0 \right)$  and the Sutherland's interpolation formula

$$\frac{\mu}{\mu_0} = \left( \frac{T}{T_0} \right)^{3/2} \frac{T_0 + S_1}{T + S_1} \quad 2.50$$

are use where  $\mu_0$  is the reference viscosity at a reference temperature  $T_0$  of 110.4K.

### 2.4.2 Turbulence Model

CFL3D offers the possibility of several turbulence models. For the cases that were analyzed in this thesis, two turbulence models were used. The one-equation Spalart-Allmaras Model for turbulence is one that was used more frequently, although the two-equation Menter's  $k - \omega$  Shear Stress Transport Model was used in some cases to verify the results of both models. The Spalart-Allmaras solves the one-equation model for a variable  $\hat{\nu}$  related to the eddy viscosity  $\mu_T = \rho \hat{\nu} f_{\nu_i}$ , see Reference [32].

In order to calculate the entropy generation rate by using equation 2.18, a Fortran program was developed (Appendix D). For equation 2.18, the viscosity and the thermal conductivity were modified to account for turbulence.

Using the Prandtl number definition:

$$\text{Pr} = \frac{c_p \mu}{k} \quad 2.51$$

the thermal conductivity were obtained. A constant Prandtl number for air having a value of 0.72 was used to obtain the thermal conductivity when the viscosity used in equation 2.49 was the molecular viscosity ( $\mu$ ). A constant Prandtl for air of 0.9 was used to calculate the turbulent thermal conductivity when the eddy viscosity ( $\mu_T$ ) is used. Therefore, in order to use equation 2.18, the viscosity used was the sum of the molecular and the eddy viscosity. At the same time, the thermal conductivity used in equation 2.18 was the sum of the viscous thermal conductivity and the turbulent thermal conductivity. The assumed constant Prandtl numbers were taken based on numbers that have been used before and that closely match experimental results.

The two-equation Menter's  $k - \omega$  Shear Stress Transport (SST) Model solves for both variables  $k$  and  $\omega$ . It also provides a different eddy viscosity relation

$$\mu_T = \min \left[ \frac{\rho k}{\omega}, \frac{a_1 \rho k}{\Omega F_2} \left( \frac{\text{Re}}{M} \right) \right], \text{ see Reference 32.}$$

## 2.5 Grid Generation

### 2.5.1 Generating a C-Type Grid

In order to have CFL3D interpret the different cases, a computer aided design needed to be created first and then the grid. All designs and grids were created using the computer program GRIDGEN. A C-type structured grid was designed for all airfoil shapes similar to the one below.

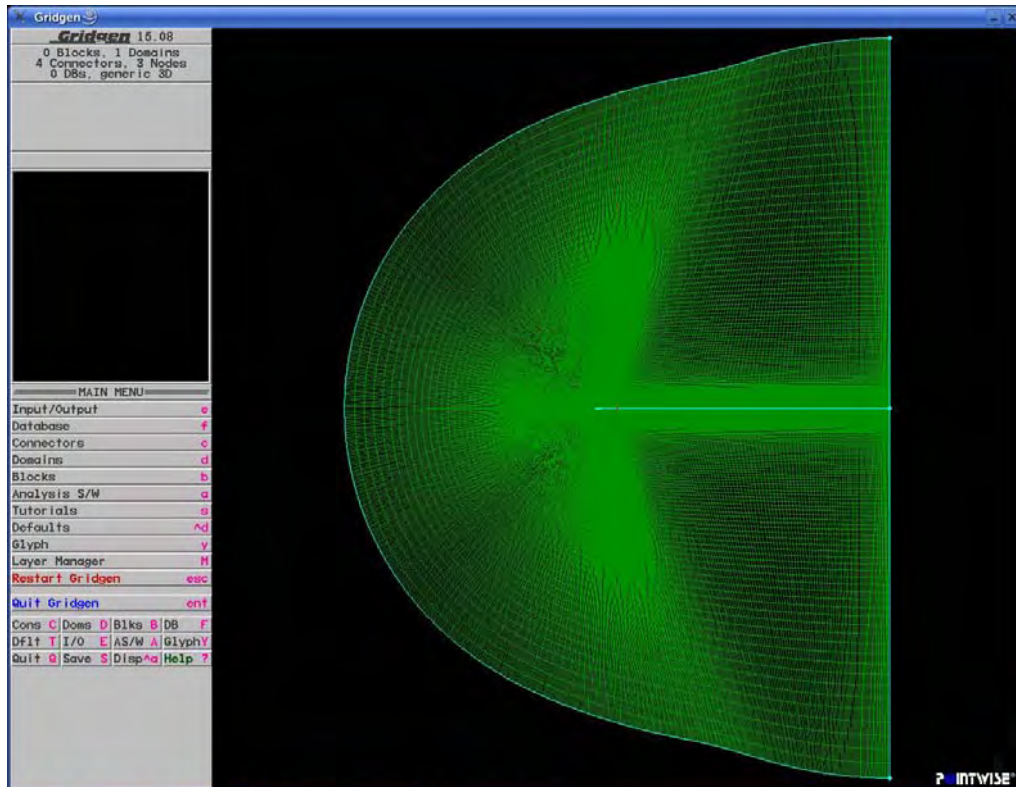
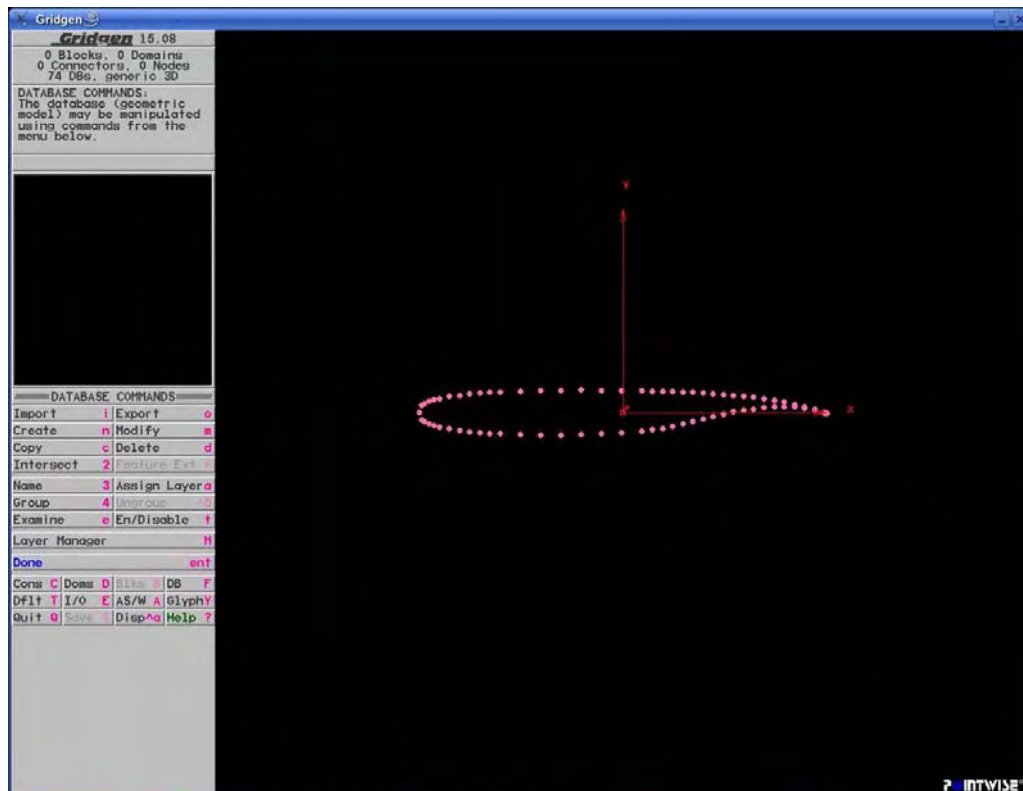


Figure 2.1 C-Type Two Dimensional Grid

In a typical case, the first part is to create data points that will simulate the shape of the model



**Figure 2.2 Airfoil Point Database**

The second step, is to create connectors around all the points and also to create a connector away from the shape that will be the path and distance that the grid will follow.

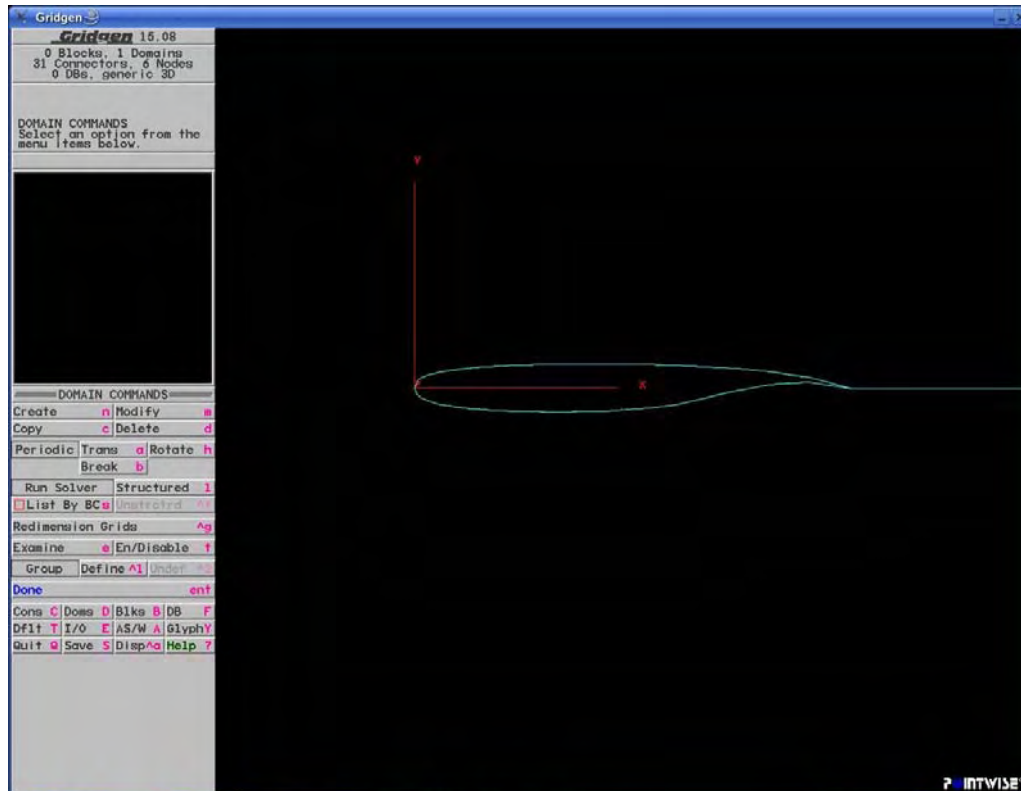


**Figure 2.3 Connectors for the database.**

In order to study the entropy generation rate due to viscous effects on an airfoil shape it is necessary to create a grid that could provide a reasonable level of resolution. For that reason, all the airfoil shapes that were studied needed a viscous grid having the initial grid spacing from the surface to be defined by a dimensionless  $y^+$ , which will be explained later. The third step in order to create the grid is to create the domain. Although this part is more of a trial-and-error method, some of the features that were used are a C-type structured volume grid, a hyperbolic tangent growth from the body to the outside, a 1.05 marching step distance, and thirty body lengths of distance for the outer boundary.

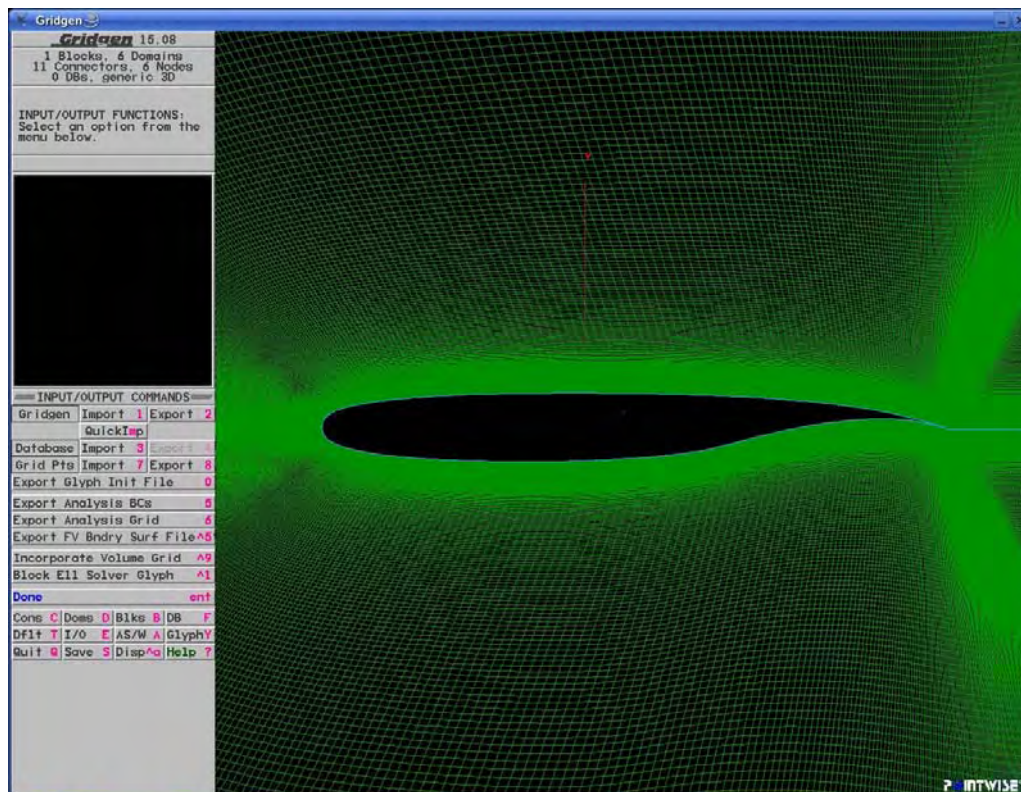


**Figure 2.4 Structured Grid with Point Clustering**

A microscopic zoom to the leading edge of the airfoil shows how each next step increases by approximately 1.05 from the last grid point, and it also shows the growth following a hyperbolic tangent formula.

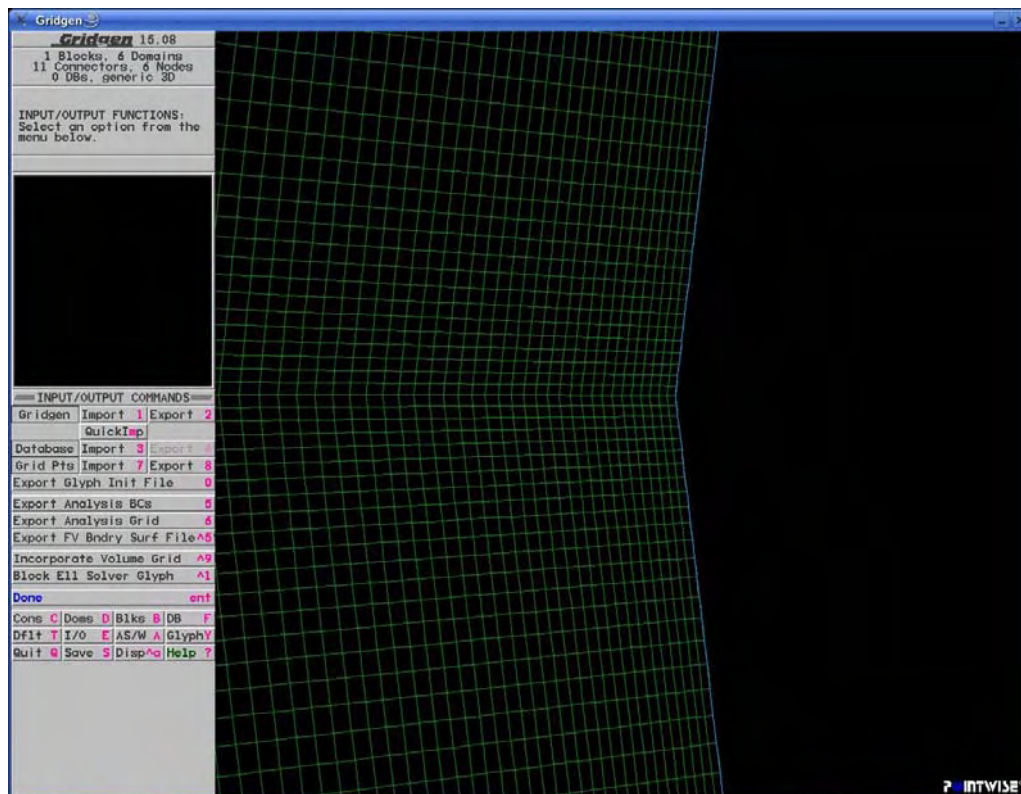


**Figure 2.5 Close-up on Structured Grid**

### 2.5.2 Viscous Grid and MultiGrid

In order to fully analyze an airfoil, viscous terms have to be included. Although CFD is no exact science, there is a general consensus given by experience, about how to create a grid that will be able to capture the effects of viscosity, turbulence, and vorticity. Grids designed to take into account the effect of viscosity and turbulent flows are called Viscous Grids. For viscous grids, CFL3D recommends the outer boundary of the domain to be thirty body lengths away from the body and it also recommend an initial spacing from the surface,  $y^+$ , to be approximately equal to one. An estimation of the initial dimensionless vertical

distance,  $y^+$ , from the surface is necessary when creating a grid for turbulent flow calculations. The  $y^+$  is defined by

$$y^+ = \frac{y}{\nu} \sqrt{\frac{\tau_w}{\rho}}, \quad \tau_w = \mu \frac{\partial u}{\partial y}, \quad \vartheta = \frac{\mu}{\rho}$$

One method of estimating  $y^+$  and subsequently the dimensional  $y$  is to assume that  $\rho_w = \rho_\infty$ ,  $\mu_w = \mu_\infty$ , where  $\rho_w$  is the density at the wall, and then use the coefficient of friction in equation

$$y^+ = \text{Re} \sqrt{\frac{c_f}{2}} y \quad 2.52$$

where using the flat plate skin friction coefficient correlation,

$$c_f \approx \frac{0.455}{\ln^2(0.06 \text{Re}_x)} \quad 2.53$$

$\text{Re}_x$  is the Reynolds number based on a specified downstream distance of  $x = 0.1$ , or 10% of the reference length and therefore,  $\text{Re}_x = x \cdot \text{Re}$ . The Reynolds number (Re), is defined as

$\text{Re} = \frac{\rho_\infty U_\infty D}{\mu_\infty}$ , where  $U_\infty$  is the freestream speed and  $D$  is a predefined distance which for

all the wings is the chord distance which is one meter.

A  $y^+$  of one was use for all the cases when first estimating the skin friction coefficient.

All grids were specifically designed in such a way that they could be multigrided and in doing so accelerate the convergence process. CFL3D offers a multigrid capability that allows the possibility to create one grid that could be multigrid into different grid sizes. For

all airfoil shapes, a fine two dimensional grid is created with a size of 1025 x 513. Using the multigrid algorithm, two other grids can be calculated with dimensions 513 x 257, and 257 x 129. Using the multigrid algorithm, the program starts to calculate the variables at the coarser 257 x 129 grid and proceeds to the finer grids after the program has completed the set amount of iterations for that grid size. Caution is needed when setting the number of iterations per grid size since it is necessary that a reasonable level of convergence is achieved at each grid before starting on the next finer grid size.

### 3 FLOW CHARACTERISTICS

For this thesis the viscous flow characteristics at subsonic and supersonic speeds were analyzed. Theoretically, the perfect gas viscous flow characteristics can be expressed from the relations used for the Fanno line. Using the continuity and energy equations it is possible to determine a relation between enthalpy and entropy describe as:

$$\frac{dh}{ds} = \frac{\gamma TM^2}{M^2 - 1} \quad 3.1$$

This equation can be used to get the Fanno curve (Appendix F). This equation helps to show the effects caused by friction in the subsonic and supersonic regimes. From equation 3.1, if the Mach number is less than one, the right hand of the equation is negative while if the Mach number is more than one, the right hand of the equation is positive. As shown in the Fanno line, the upper curve have a less than zero  $\frac{dh}{ds}$  which belongs a Mach number less than one, in other words at the subsonic regime, while the lower curve has a greater than zero  $\frac{dh}{ds}$  which belongs to a Mach number of more than one which belongs to the supersonic regime. In terms of the enthalpy, when the flow of a gas is accelerating, the enthalpy decreases while when the flow is decelerating, the enthalpy increases. Given that in a frictional adiabatic flow the entropy always increases due to the irreversibilities cause by friction, the only way that the change in enthalpy is negative at the subsonic regime is for the flow to be accelerating. Also, at the supersonic regime, the only way that the change in

enthalpy equals the positive right hand side of the equation is for the flow to be decelerating. Theoretically this explains the reason why at the subsonic regime the flow of a gas tends to accelerate while at the supersonic regime the flow of a gas tends to decelerate.

In order to characterize the flow, a computational fluid dynamics approach was used. The first step before obtaining results for the flow characteristics and entropy generation of different airfoils, is to compare simple cases with known answers. Given that the authors of CFL3D provided comparative results for the case of a viscous flat plate, it was necessary to provide results for an inviscid supersonic wedge. After these comparative results, the next step was to run all the airfoil cases. The results obtained from CFL3D were then processed by a Fortran program that was created. This program uses a central difference Taylor expansion to obtain the gradients defined by the entropy generation equations and determine the entropy generation rate close to the body around each airfoil at different at speeds and conditions.

### **3.1 Test Cases**

In order to determine the level of accuracy at supersonic speeds, a test case was run. In compressible inviscid supersonic flow theory, the Rankine-Hugoniot equations allow for the calculation of Mach number, pressure ratio, temperature ratio and other parameters before or after a compression shock wave. For this case, an inviscid flat plate with a 30 degrees flow deflection wedge angle was created in Fig 3.1. Although this test case considers inviscid supersonic flow, drag will be present in the form of wave drag cause by the irreversible

compression shock wave. The grid of the wedge had a fine mesh of 1025 points along the x-axis and 513 points along the y-axis, and was subsequently multigrided to two coarser mesh levels.

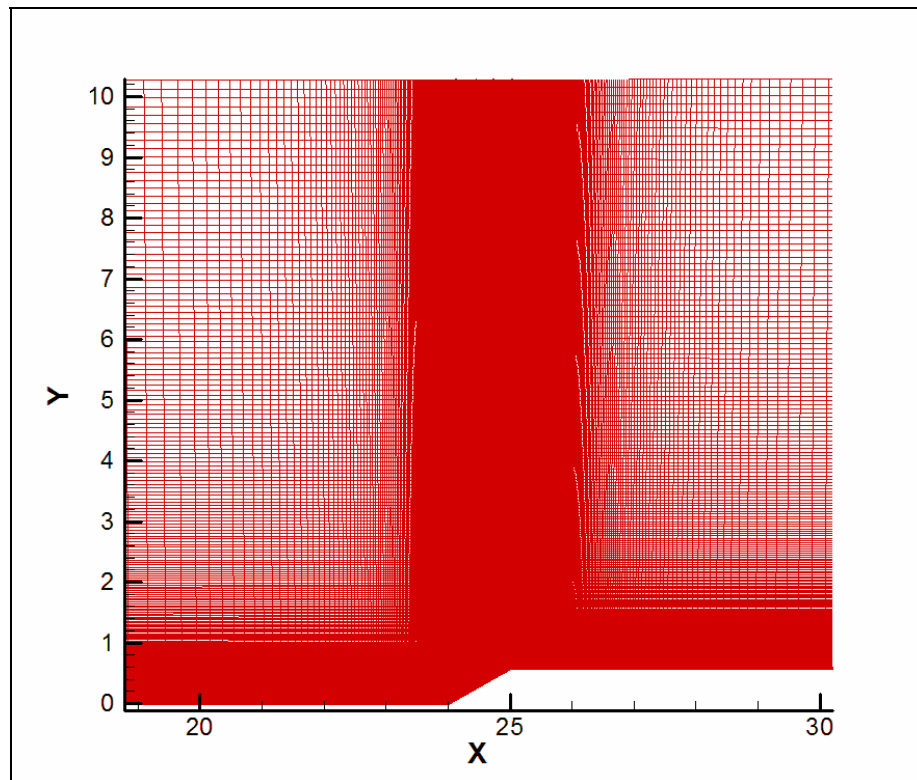


**Figure 3.1 Wedge Grid with 30-degree step**

Based on the Rankine-Hugonot relations (Appendix B), the program was run with air as a perfect gas flow at Standard Atmospheric Conditions with a temperature of  $288.15\text{ K}$ , a pressure of  $1013.25\text{ kPa}$ , and a density of  $1.23\frac{\text{kg}}{\text{m}^3}$ . This case was run with a Mach number

of 2.6, a Reynolds number of  $6.9 \times 10^7$  based on the wedge horizontal length, and a speed of  $884.683 \frac{m}{s}$ .

First, it is critical to analyze the convergence reached by the program, before using any results. The logarithmic of the residual is what is used to determine the reliability of the data as shown in Fig. 3.2. A good residual in this case is considered around  $1 \times 10^{-5}$  or less. It is also important to make sure that the convergence for the variables that are been observed like the coefficient of drag are relatively flat at the end of the iterations set in the program. In other words, the graphs of these variables should not be changing more than 10% at the end of the iterations and should have a zero gradient trend at the end. In Fig.3.2 the logarithmic of the residual stabilizes and stays with an almost zero gradient trend. The logarithmic residual at the last iteration is of 0.2486E-07.

Also, the degree of convergence of the program was compared with the drag results at consecutive iterations as it is shown in Fig. 3.4. The coefficient of drag stayed at an almost zero gradient trend or almost constant throughout the program although it was going from a coarser to a finer grid. It went 257 by 159 grid size to a finer 513 by 257 grid size after 10,000 iterations, and then to the finest grid size of 1025 by 513 grid size after the 20,000 iteration.

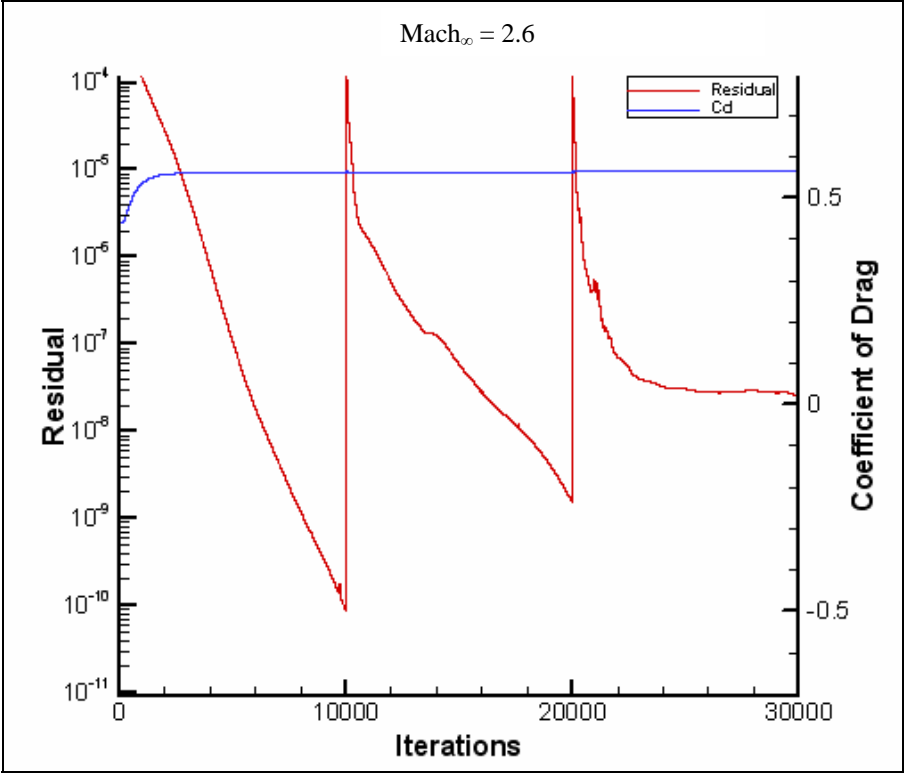
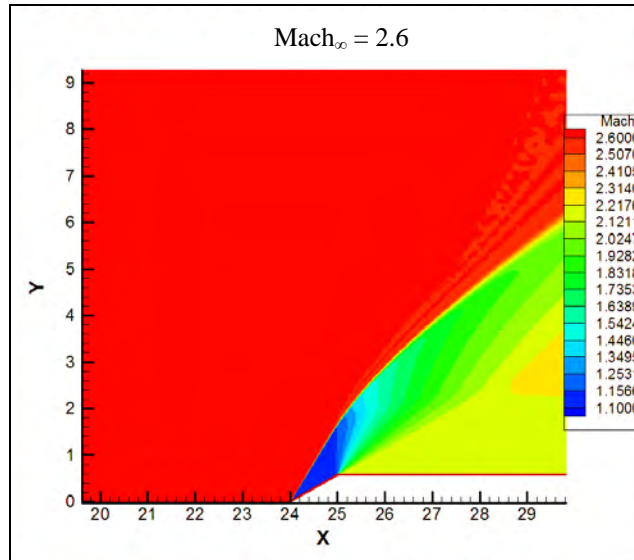


Figure 3.2 Residual and Coefficient of Drag for Wedge



**Figure 3.3 Mach 2.6 Contour for Wedge**

At this Mach number, the flow will create an attached weak shock at the bottom of the wedge and then an expansion fan as soon as the wedge turns horizontal as seen in Fig. 3.3.

Zooming into the wedge bottom corner (Fig. 3.4).

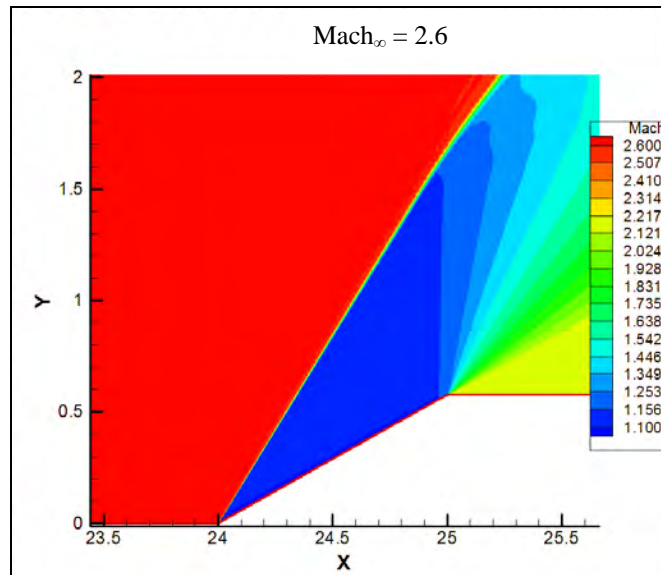


**Figure 3.4 Mach 2.6 Contour Closeup**

Once the program achieves a reliable convergence, it is important to analyze the result and behavior of the other variables. Figures 3.5 and 3.6 shows the Pressure Ratio Contour and the Temperature Ratio Contour respectively along the wedge. Using the normal shock wave flow theory, the Rankine-Hugoniot relations, and an oblique shock wave table, the theoretical Mach number, pressure ratio and temperature can be determined. Given that the flow deflection angle is  $\theta = 30^\circ$ , the upstream Mach number is 2.6, this gives a theoretical downstream Mach number of 1.10619. Compared to the Mach 1.10895 output in Fig. 3.7 by the program, this gives an error of 0.249%. In the case of the pressure ratio and temperature ratio, theoretically the results are 5.67064 and 1.88957 respectively. When the output pressure and temperature ratios between downstream and upstream values in Fig. 3.8 are compared with the theoretical results, there error is of 0.2% and 0.085% respectively. These results and their respective errors provide sufficient assurance that when viscosity is neglected from the analysis, the basic theoretical results can be achieved.

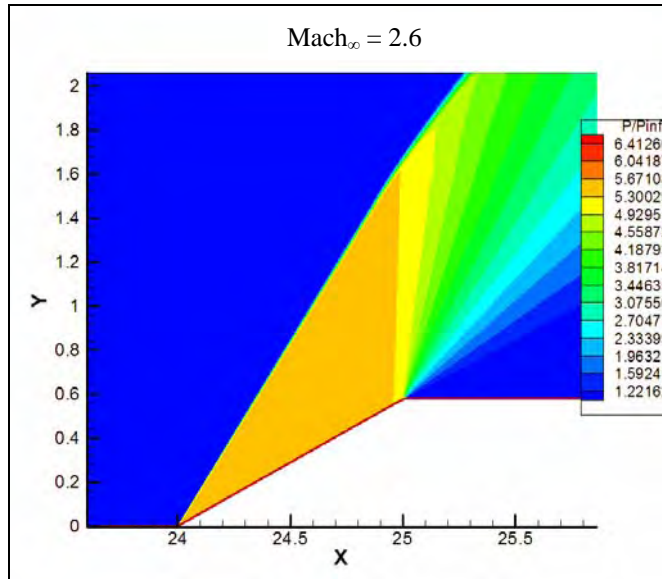


**Figure 3.5 Pressure Ratio Contour for Wedge**

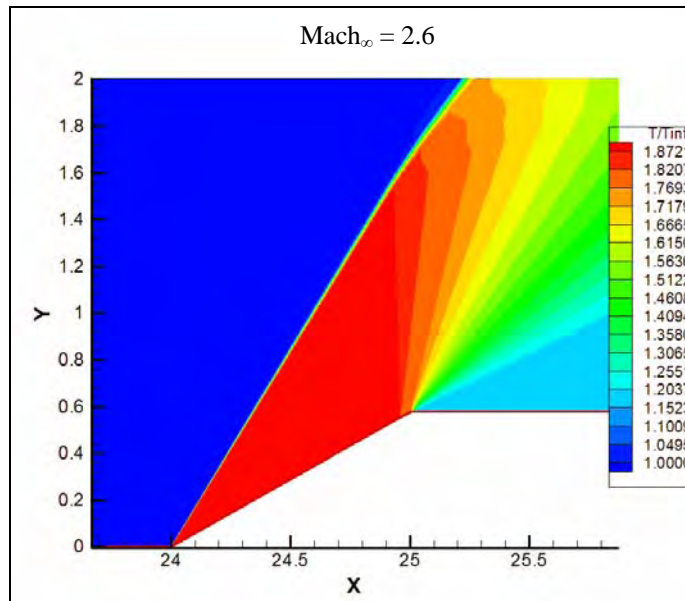


**Figure 3.6 Temperature Ratio for Wedge**

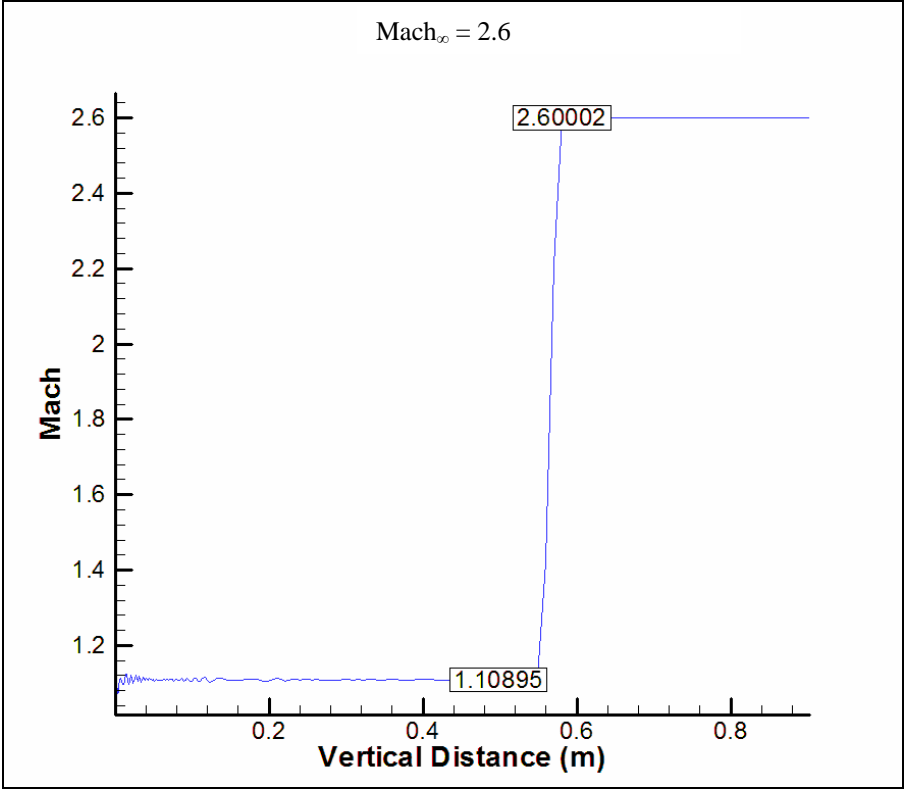
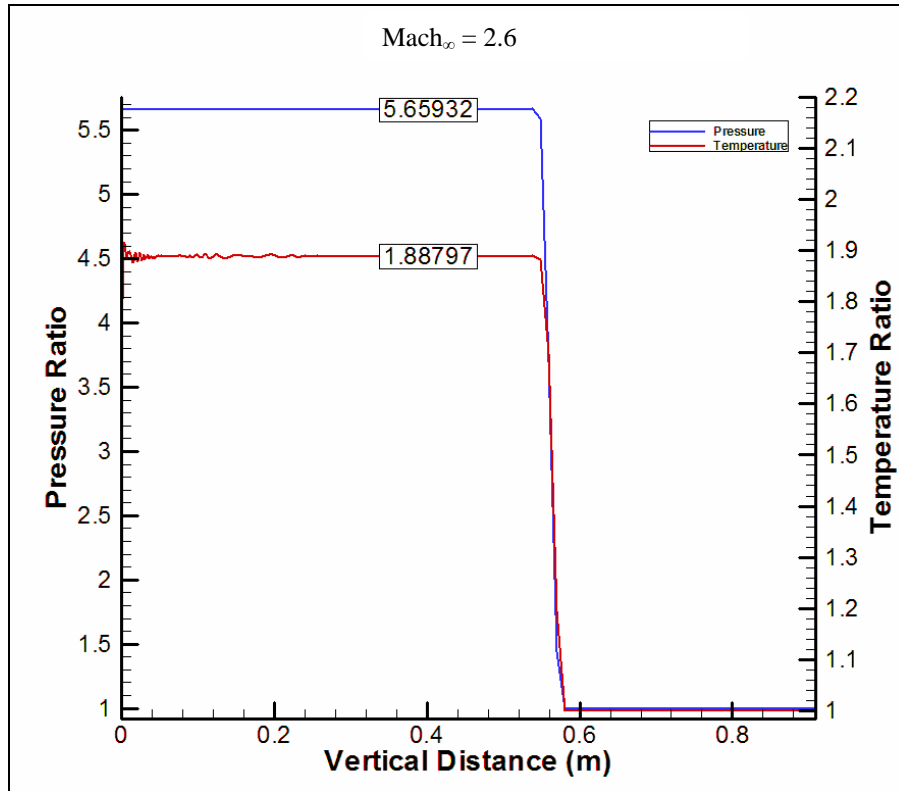
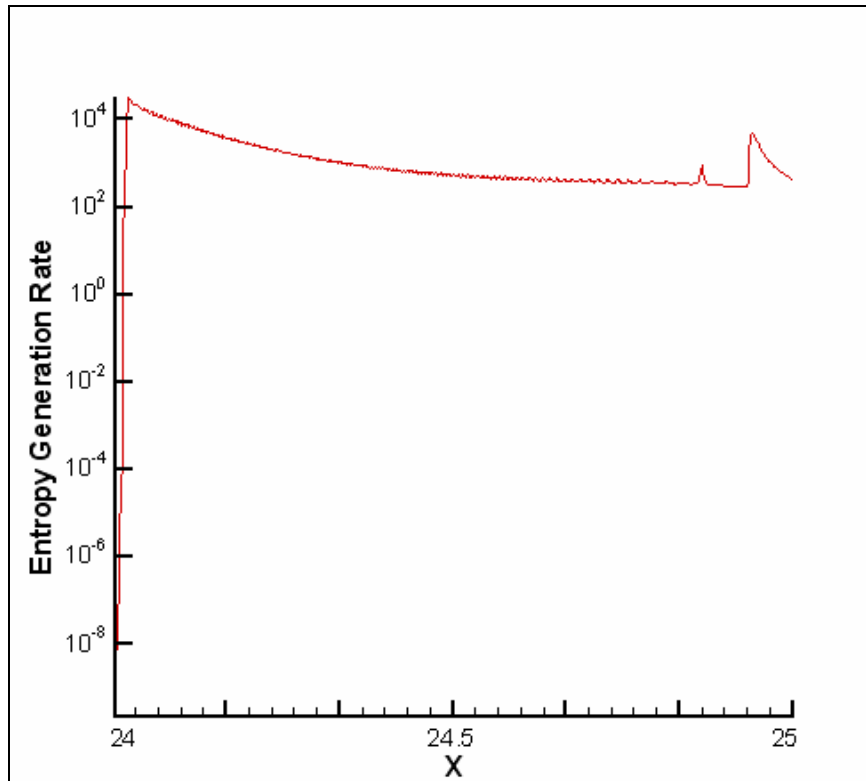


Figure 3.7 Mach Number change along a vertical distance at  $x = 24.5$  on the wedge



**Figure 3.8 Pressure and Temperature Ratio along a vertical distance at  $x = 24.5$**

As a fundamental case of supersonic flow over an inviscid wedge, this test case also provides the base for determining the volumetric entropy generation rate and will also shed light on what to expect for the viscous cases. Given that the entropy generation rate formula used in this thesis is based on generation due to viscosity and generation due to heat, it is expected to find the highest entropy generation rate at locations where high viscosity and heat dissipation rates are concentrated. Since the surface of the wedge is inviscid, the other locations where high entropy generation rates can be found are around the irreversible weak compression shock wave at the bottom of the wedge and around the expansion fan on top of the wedge.



**Figure 3.9 Entropy Generation Rate ( $\frac{W}{m^3 K}$ ) around Wedge Step**

As it is expected, the highest entropy generation rate per unit span is caused around the area at the bottom of the wedge by a weak shock wave. At that point, a highly irreversible weak attached compression shock wave is formed with high viscous and heat generation terms.

In order to analyze the entropy generation rate of the wedge, data is taken from inside an imaginary rectangle that is 1 meter in length and 45 meters in high. By having this configuration, the entire shock wave is captured. On the right side of Fig. 3.9, there are two peaks in entropy generation rate, which are caused by expansion fans. A weak expansion fan around the x position of 24.9 causes the smallest peak, which is the result of inaccuracies in

the grid when creating a straight line. A true physical expansion fan in the corner of the wedge at an x position of 25.0 causes the highest entropy generation rate peak on the right of the graph.

## **3.2 NACA 64215 Airfoil**

The first case that was tested was the NACA 64215 supercritical airfoil. This airfoil was tested numerically at a Mach number of 0.65, 0.3, 0.6, 2.0, and 3.0. The first Mach number of 0.65 was used to compare the CFL3D results with experimental results. Although the experimental results do not provide the air temperature at the day of testing, a temperature of 288.15K was used for the CFL3D analysis. The other four Mach numbers were used to compare all the three airfoils under the same air free stream speeds and temperatures. The grid that was created was used for all the cases. The grid consisted of three levels of refinement with a coarse grid level of 257 by 159 points, then a finer 513 by 257 grid points and lastly a 1025 by 513 grid points. In total, there were 1.38 million grid points.

### 3.2.1 Mach 0.3

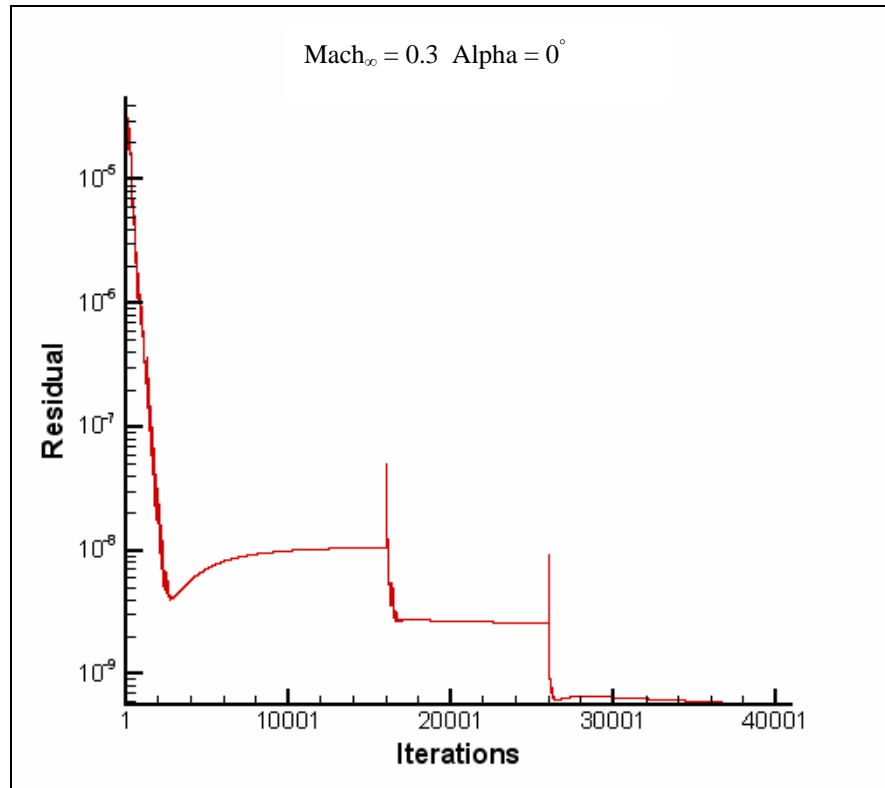


**Figure 3.10 Residual for NACA 64<sub>2</sub>A215 airfoil from CFL3D**

The first step to do before analyzing all the flow characteristics and properties is to determine the level of convergence in the results. For this case the 257 by 159 grid level was allowed to converge for 16000 iterations. Then the program passed to the finer 513 by 257 level for 10000 iterations and at the end it went to the finest 1025 by 513 grid level with 14000 iterations. As shown in Figure 3.10, the results converged to a level of accuracy of 9 decimal places.

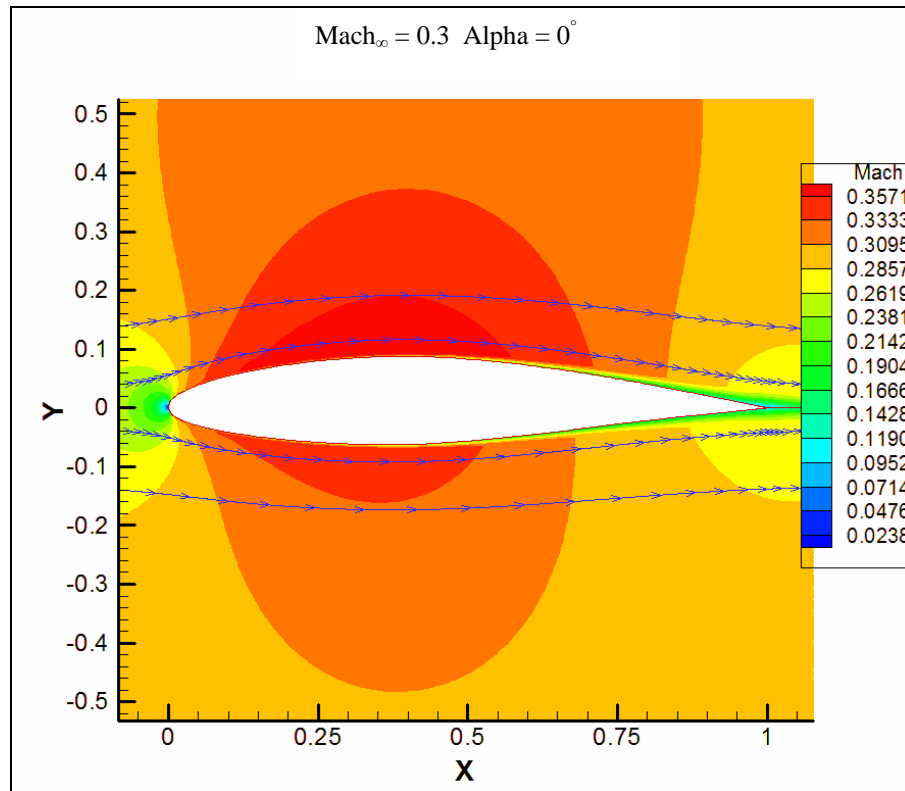


**Figure 3.11 Mach 0.3 Contour around NACA 64<sub>2</sub>A215 airfoil**

Figure 3.11 shows the mach contours around the NACA 64<sub>2</sub>A215 airfoil with a free stream speed of Mach 0.3 and a Reynolds number of 6.9 million.

As in the last case, the flow goes over, under or it reaches the stagnation point at the leading edge of the airfoil. It can be seen how the flow reaches a higher speed at the upper surface and for a longer distance than in the lower surface. As the flow passes over and under the airfoil, it starts to accelerate, reaches a maximum around half chord and then decelerates to the free stream speed.

This acceleration in speed is due to a decrease in pressure caused by the curvature of the airfoil. Figure 3.12 shows the pressure ratio between the local pressure and the free stream pressure. It shows how the pressure decreases as the flow goes over and under the airfoil.

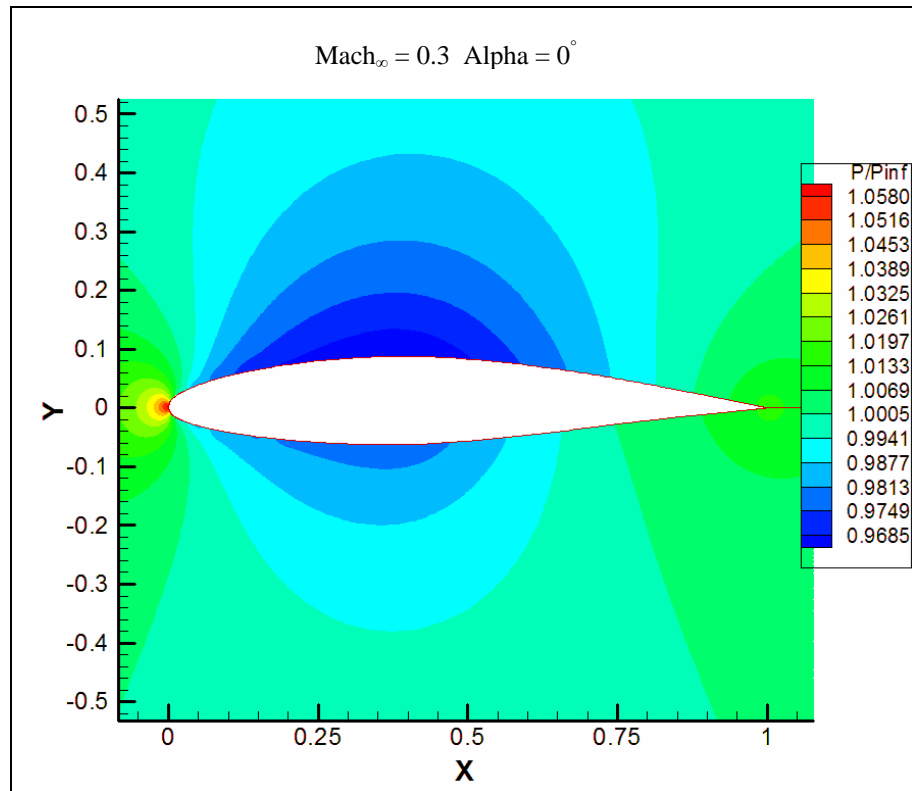


**Figure 3.12 Pressure Ratio Contour around NACA 64<sub>2</sub>A215 airfoil**

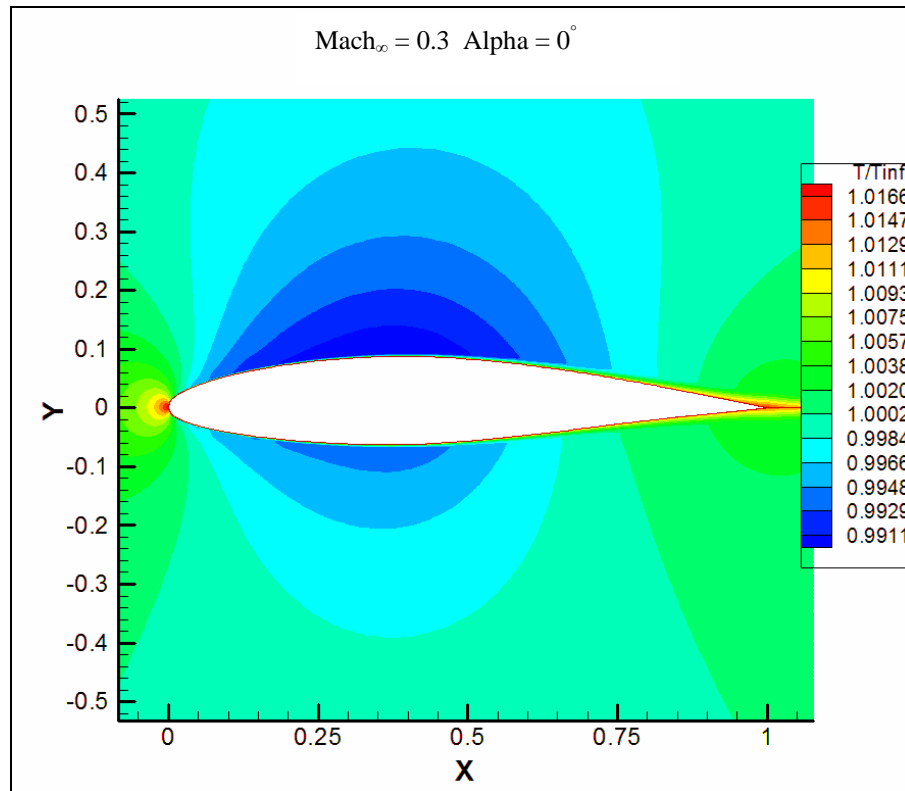


**Figure 3.13 Temperature Ratio Contour around NACA 64<sub>2</sub>A215 airfoil**

Also, there is a temperature ratio decrease as shown in Figure 3.13, which is associated with the pressure decrease as the flow goes over and under the airfoil. This decrease in temperature is expected from the perfect gas law.

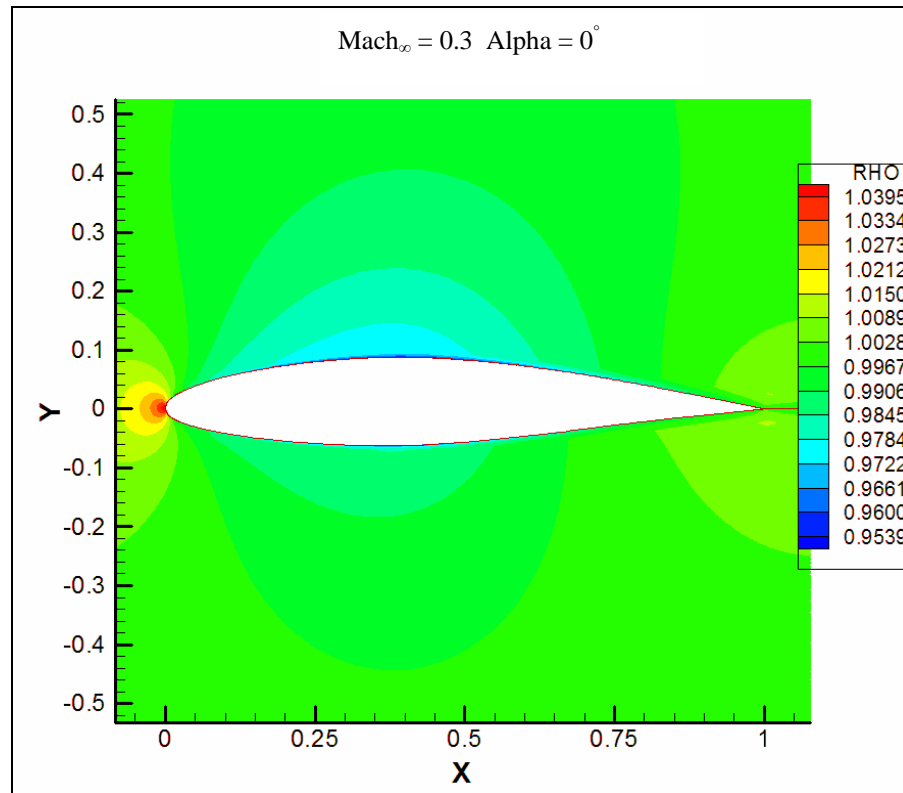


**Figure 3.14 Density Ratio Contour around NACA 64<sub>2</sub>A215 airfoil**

The density ratio for the Mach number of 0.3 can be seen in Figure 3.14. The Mach number 0.3 is considered the lower limit when dealing between incompressible and compressible flow. As shown in Figure 3.14, although there is a change in density around the airfoil, the change is subtle with only a 4% change in density.

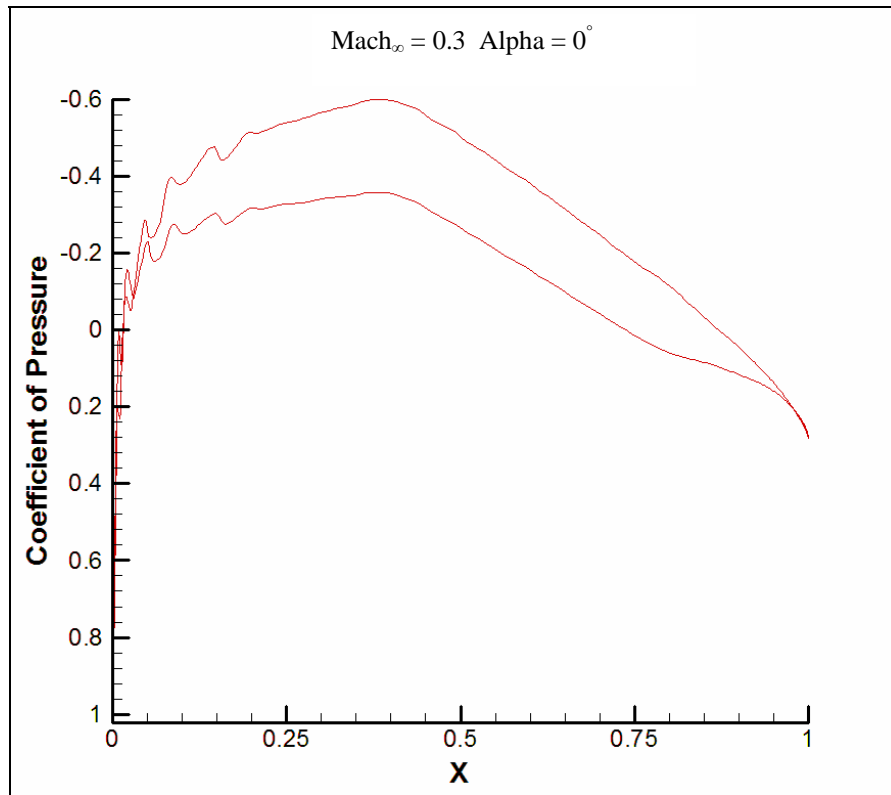


**Figure 3.15 Coefficient of Pressure around NACA 64<sub>2</sub>A215 airfoil**

Figure 3.15 shows the coefficient of pressure at the Mach number of 0.3. It shows a lower change in pressure than the change at the Mach number of 0.65

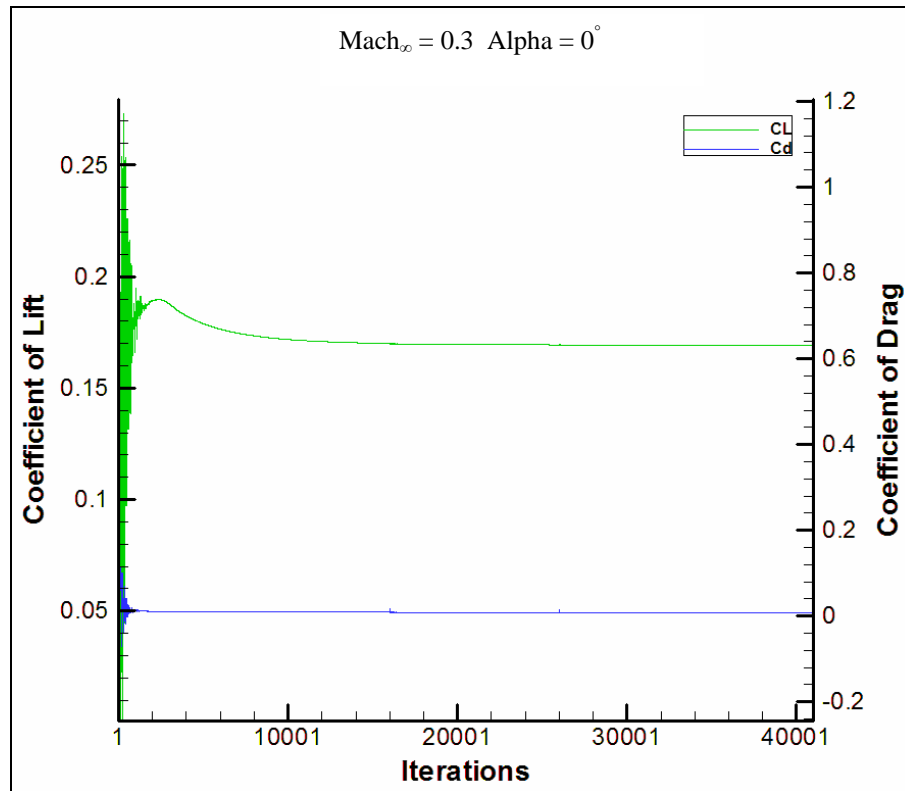


**Figure 3.16 Coefficient of Lift and Drag Convergence for NACA 64<sub>2</sub>A215 airfoil**

Figure 3.16 shows the coefficient of lift and the coefficient of drag attained by the program after 40000 iterations. The coefficient of lift converged to 0.1692 and the coefficient of drag converged to 0.008533.

### 3.2.2 Mach 0.6

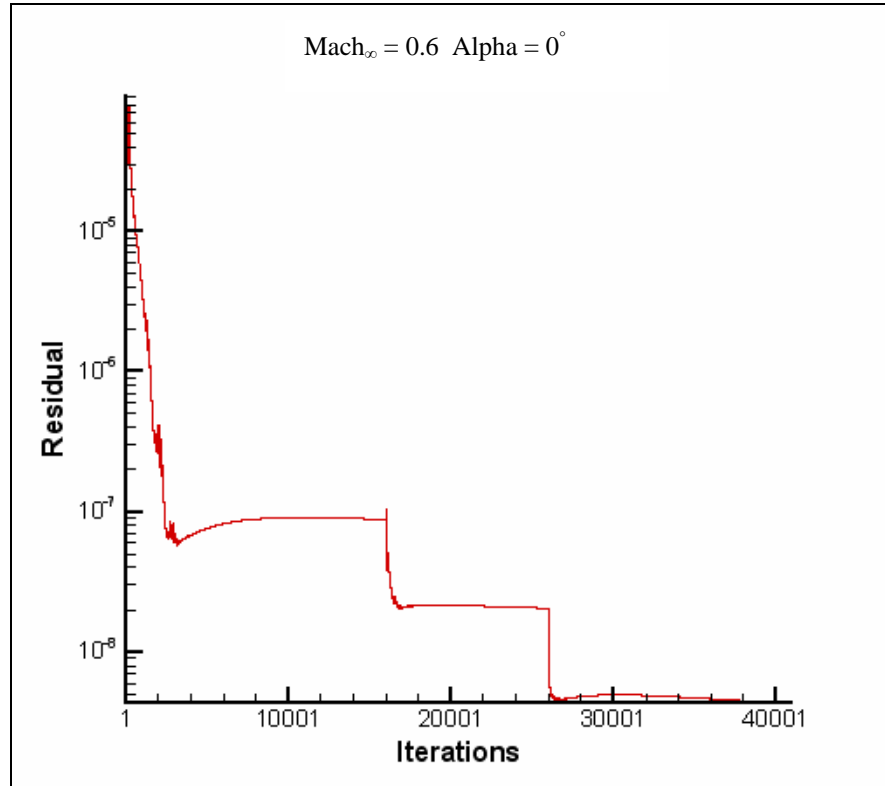


**Figure 3.17 Residual for NACA 64<sub>2</sub>A215 airfoil from CFL3D**

As before, the 257 by 159 grid level was allowed to converge for 16000 iterations. Then the program passed to the finer 513 by 257 grid level for 10000 iterations and at the end it went to the finest 1025 by 513 grid level with 14000 iterations. As shown in Figure 3.17, the results converged to a level of accuracy of around 8 decimal places.

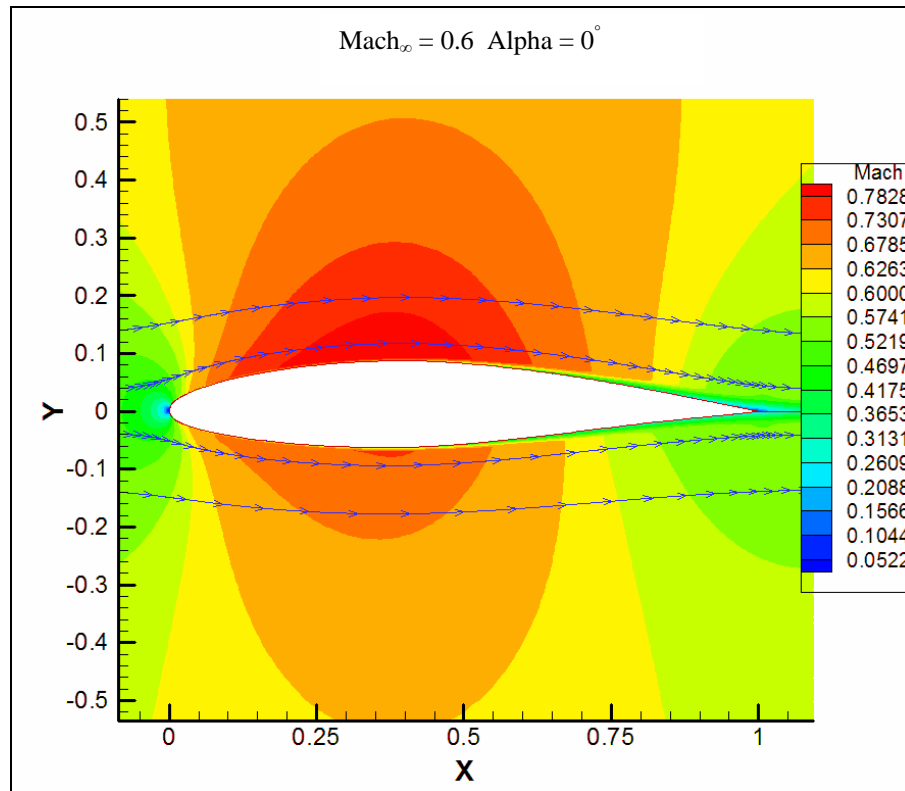


**Figure 3.18 Mach 0.6 Contour around NACA 64<sub>2</sub>A215 airfoil**

Figure 3.18 shows the mach contours around the NACA 64<sub>2</sub>A215 airfoil with a free stream speed of Mach 0.3 and a Reynolds number of 13.8 million.

As in the last case, the flow goes over, under or it reaches the stagnation point at the leading edge of the airfoil. It can be seen how the flow reaches a higher speed at the upper surface and for a longer distance than in the lower surface. This is mainly due to a higher pressure in the lower surface than in the upper surface. Again, this acceleration in speed is due to a decrease in pressure caused by the curvature of the airfoil. Figure 3.19 shows the pressure ratio between the local pressure and the free stream pressure. As in the last cases, there is a higher pressure ratio at the leading edge cause by the compression that is occurring at that

point. This compression will also cause an increase in temperature as shown in Figure 3.20. As the flow passes the leading edge, it starts to cool down to a minimum that occurs around center of the airfoil.

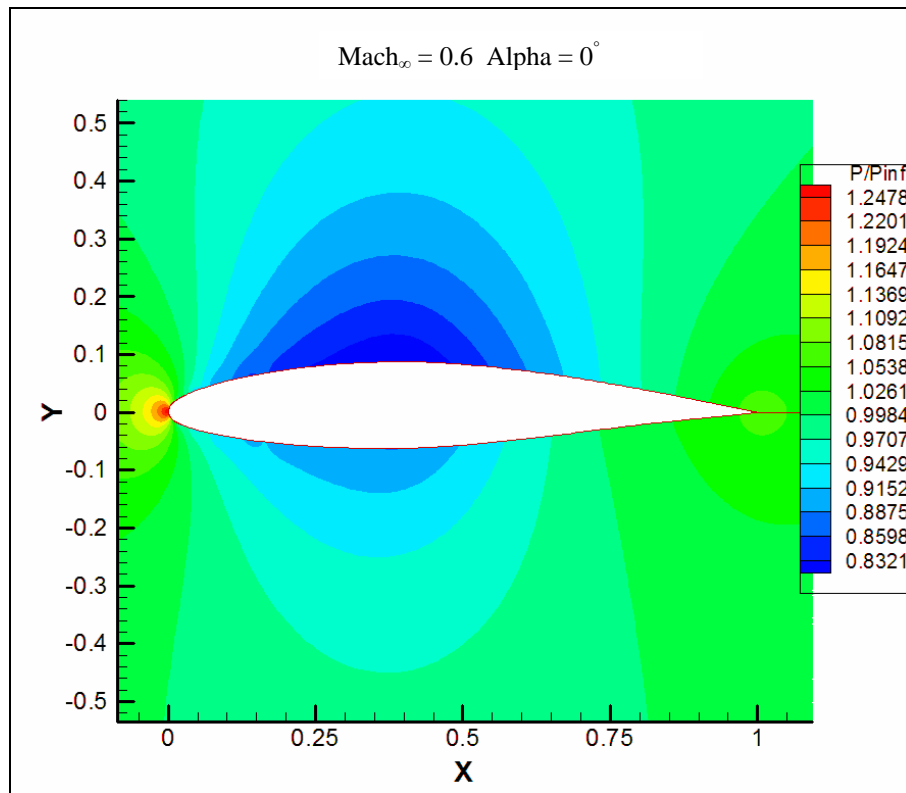
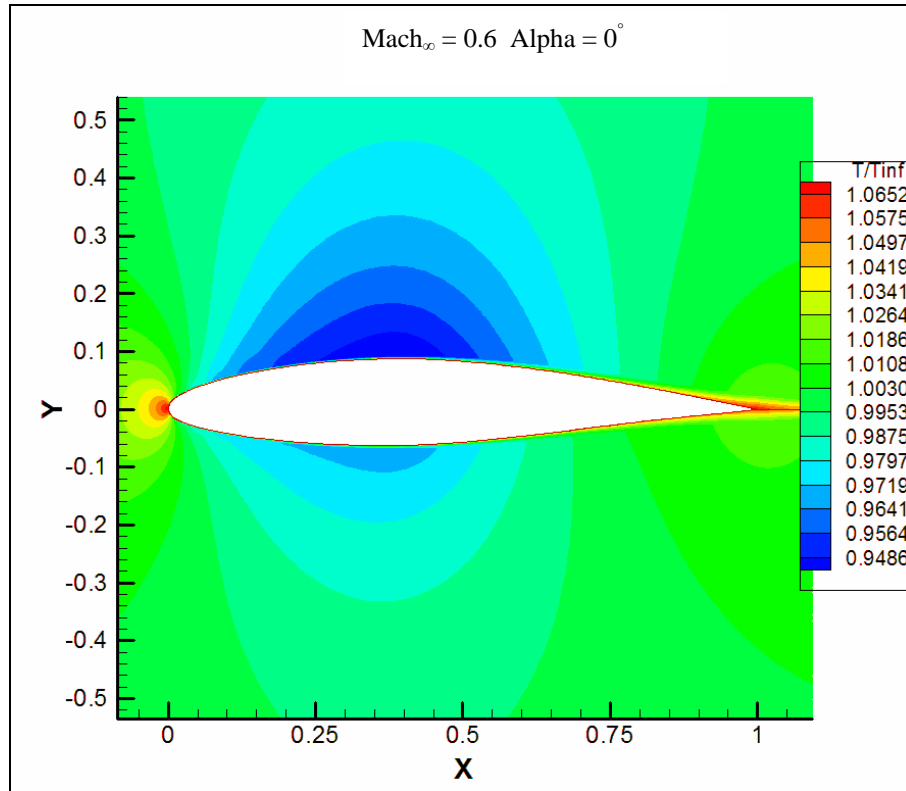
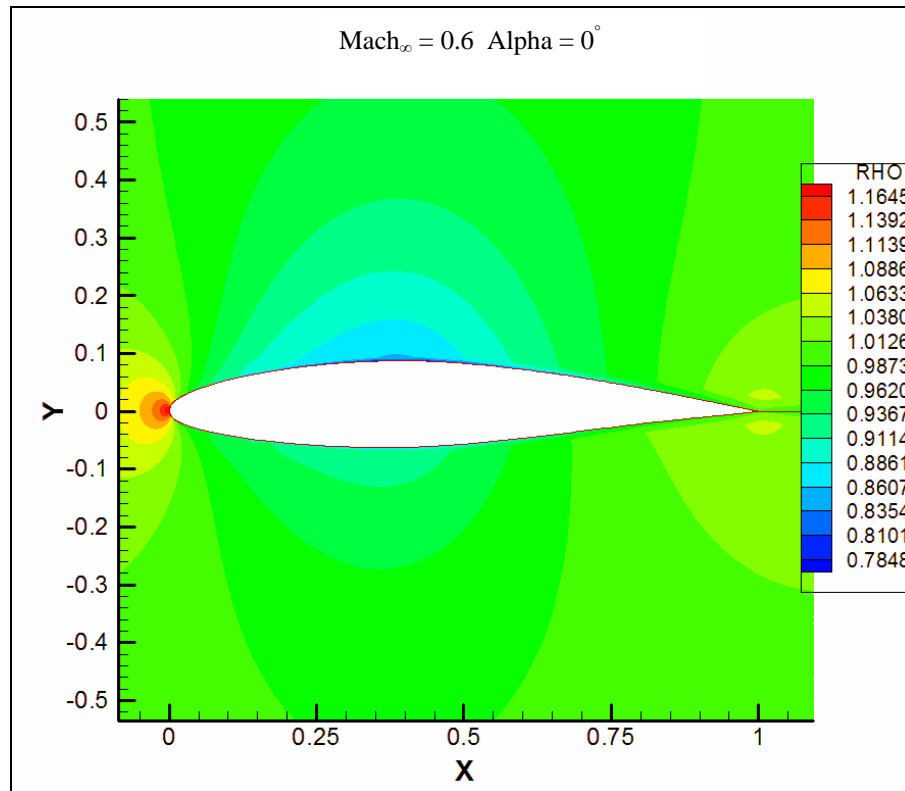


Figure 3.19 Pressure Ratio Contour around NACA 64<sub>2</sub>A215 airfoil



**Figure 3.20 Temperature Ratio Contour around NACA 64<sub>2</sub>A215 airfoil**



**Figure 3.21 Density Ratio Contour around NACA 64<sub>2</sub>A215 airfoil**

Given the proportional relation between density and pressure by the perfect gas law, Figure 3.21 shows how the density ratio also increases at the leading edge and then returns to an unity density ratio. Around the center of the airfoil, the density gets lower which is also associated with a lower temperature and a lower pressure.

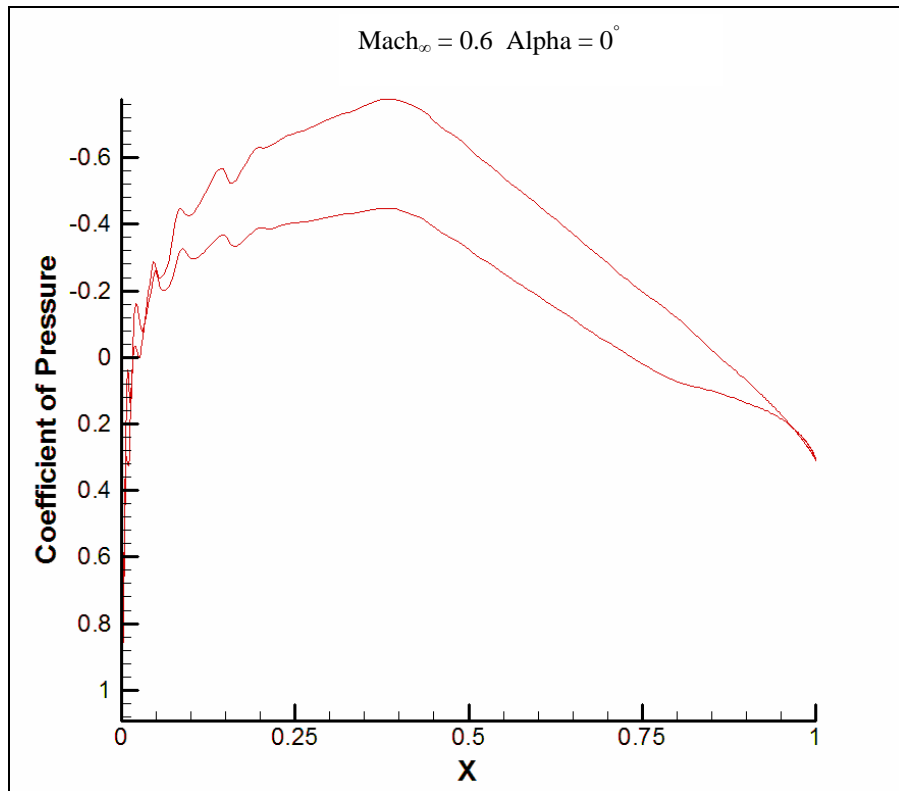


**Figure 3.22 Coefficient of Pressure around NACA 64<sub>2</sub>A215 airfoil**

Figure 3.22 shows the coefficient of pressure for a Mach number of 0.6. Just as in the other cases, the ups and downs in the results obtained are believed to be caused by peaks and valleys that can be formed when creating a grid given its resolution. For this Mach number, both surfaces have negative coefficient of pressure, which indicates acceleration in the airflow and a subsonic case.

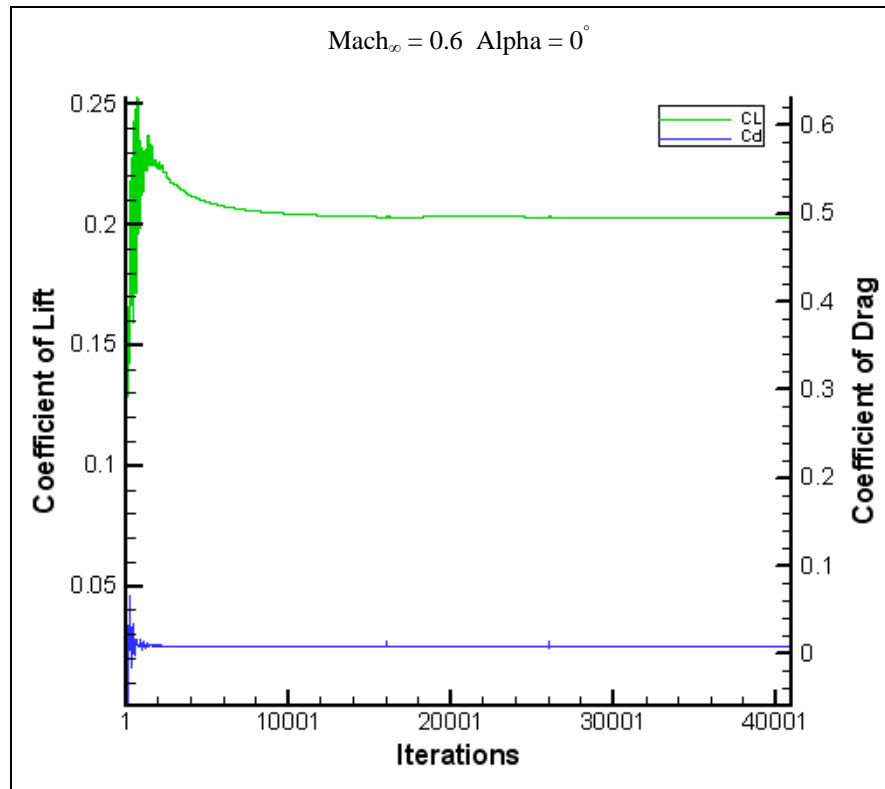


**Figure 3.23 Coefficient of Lift and Drag Convergence on NACA 64<sub>2</sub>A215 airfoil**

Figure 3.23 shows the convergence for the coefficient of lift and the coefficient of drag through 40000 iterations. After the 40000 iterations, it converged to a coefficient of lift of 0.203 and a coefficient of drag of 0.008042.

### 3.2.3 Mach 0.65

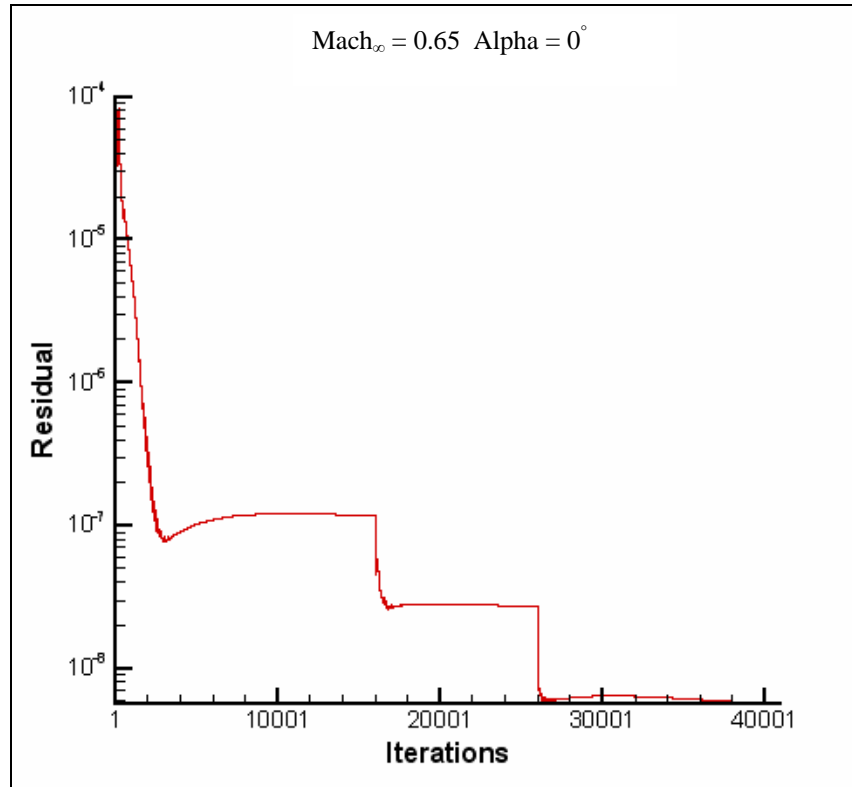


**Figure 3.24 Residual for NACA 64<sub>2</sub>A215 airfoil from CFL3D**

The first step to do before analyzing all the flow characteristics and properties is to determine the level of convergence in the results. This case as well as all the other cases analyzed in this thesis started with a coarse 257 by 159 grid level then it went to a finer 513 by 257 grid level and ended at the finest 1025 by 513 grid level. The 257 by 159 grid level was allowed to converge for 16000 iterations. Then the program passed to the finer 513 by 257 level for 10000 iterations and at the end it went to the finest 1025 by 513 level with 14000 iterations.

As shown in Figure 3.24, the results converged to a level of accuracy of 8 decimal places.

Taking all the grid levels, there were 1.38 million grid points in total.

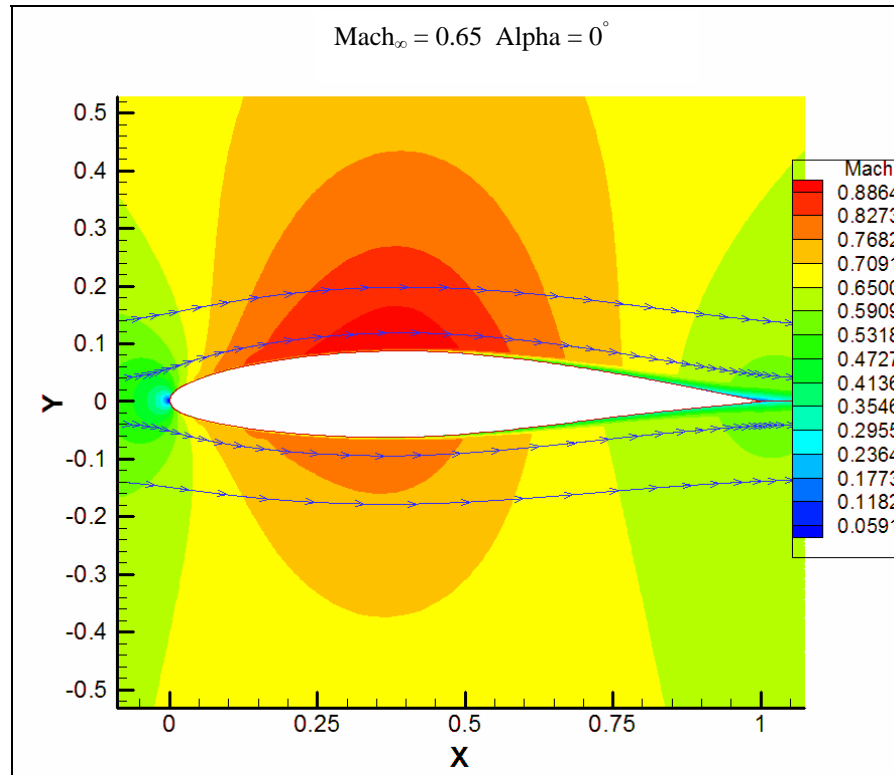


**Figure 3.25 Mach 0.65 Contour around NACA 64<sub>2</sub>A215 airfoil**

Figure 3.25 shows the mach contours around the NACA 64<sub>2</sub>A215 airfoil with a free stream speed of Mach 0.65 and a Reynolds number of 14.95 million.

As the flow first encounters the airfoil, it goes over, under or it reaches the stagnation point at the leading edge. Given that the flow is subsonic, as the flow passes over and under the airfoil, it starts to accelerate, reaches a maximum around half chord and then decelerates to the free stream speed.

This acceleration in speed is due to a decrease in pressure caused by the curvature of the airfoil. Figure 3.26 shows the pressure ratio between the local pressure and the free stream pressure. It shows how the pressure decreases as the flow goes over and under the airfoil which helps explain the acceleration in speed and therefore the increase in Mach number.

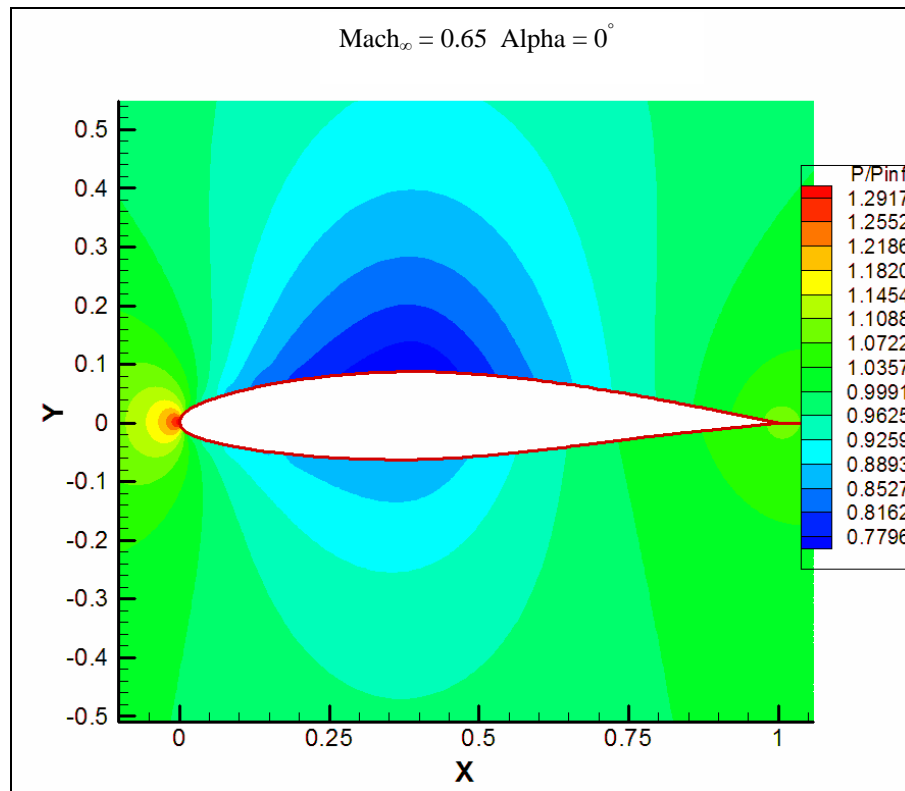
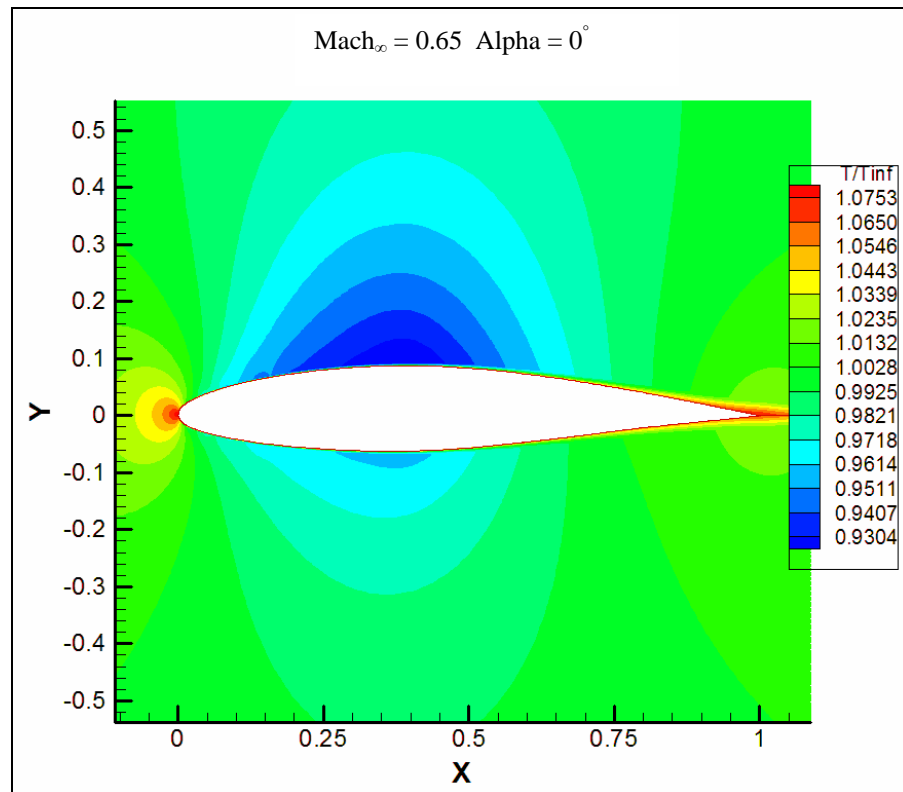


**Figure 3.26 Pressure Ratio Contour around NACA 64<sub>2</sub>A215 airfoil**

This differential in pressure between the upper and lower surface causes the creation of lift since the lower surface has a higher pressure than the upper surface due to its curvature. This decrease in pressure causes a suction effect, which increases the speed.

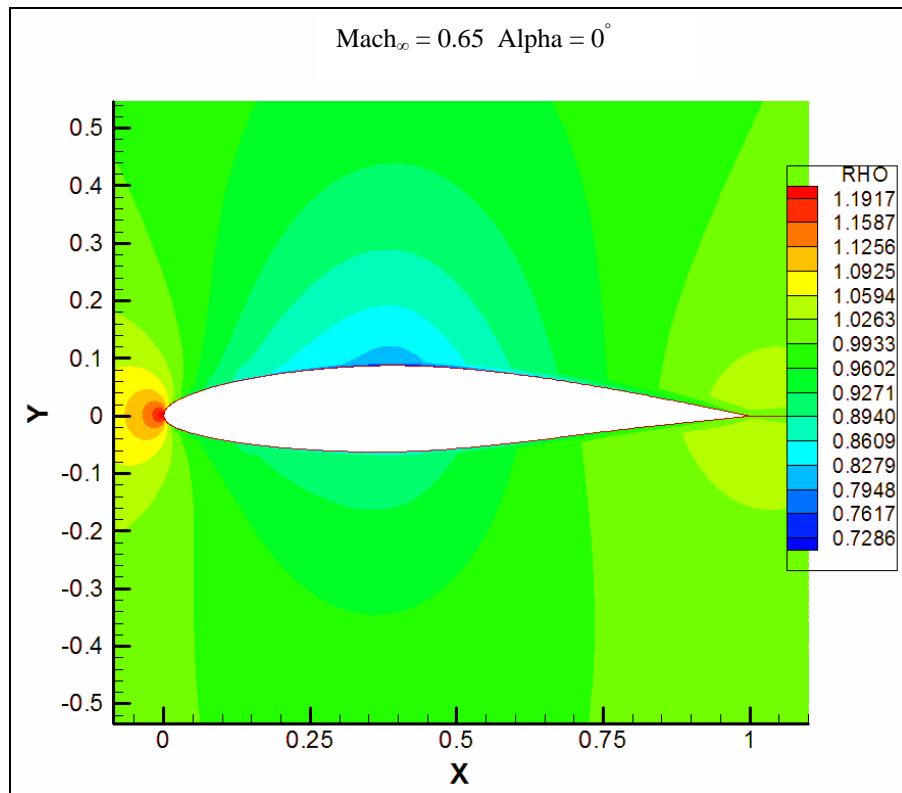
As the flow reaches the leading edge of the airfoil, it compresses, which causes an increase in temperature as shown in Figure 3.27. Then as the air flow accelerates due to a decrease in

pressure, the temperature and the density also decreases as shown in Figure 3.27 and in Figure 3.28.

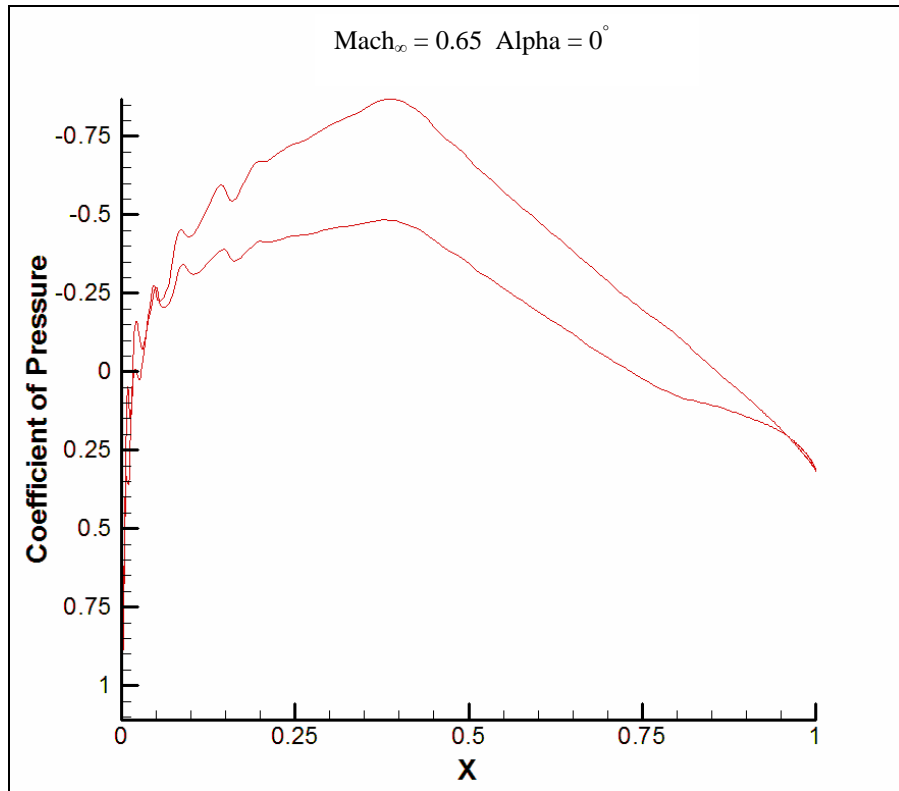


**Figure 3.27 Temperature Ratio Contour around NACA 64<sub>2</sub>A215 airfoil**

Given that the surface of the airfoil is viscous, a thin flow boundary layer will start to form. This boundary layer will also aid in the decrease of pressure. In Figure 3.27, the thin boundary layer can be seen just above the upper surface due to an increase in temperature caused by the viscosity and turbulence. This viscosity will cause a small turbulent flow to small forming and will increase the temperature as the flow passes the trailing edge of the airfoil.

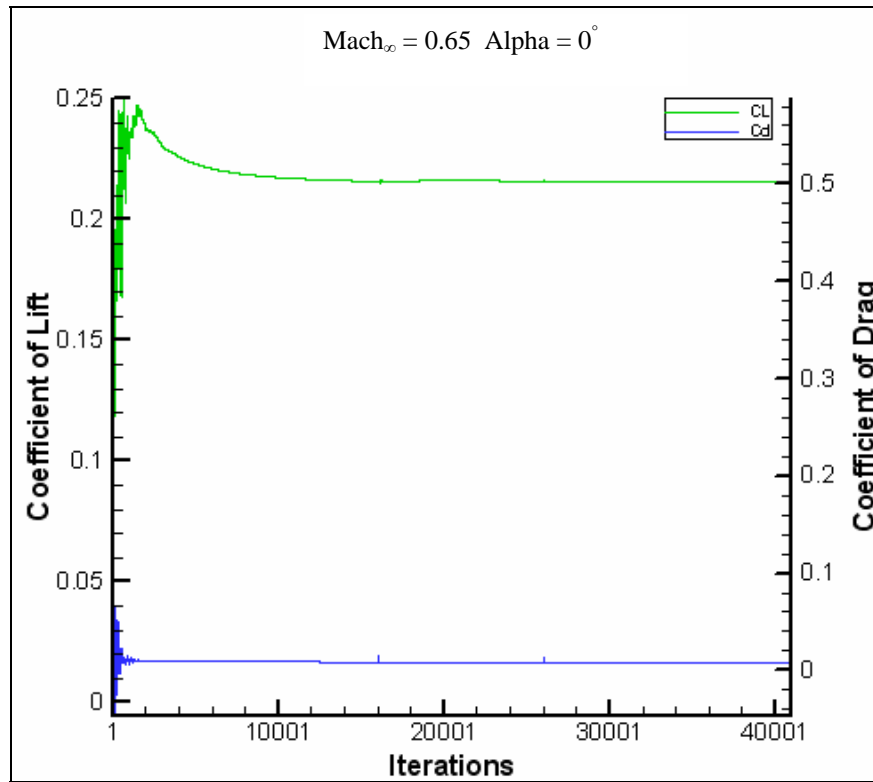


**Figure 3.28 Density Ratio Contour around NACA 64<sub>2</sub>A215 airfoil**



**Figure 3.29 Coefficient of Pressure around NACA 64<sub>2</sub>A215 airfoil**

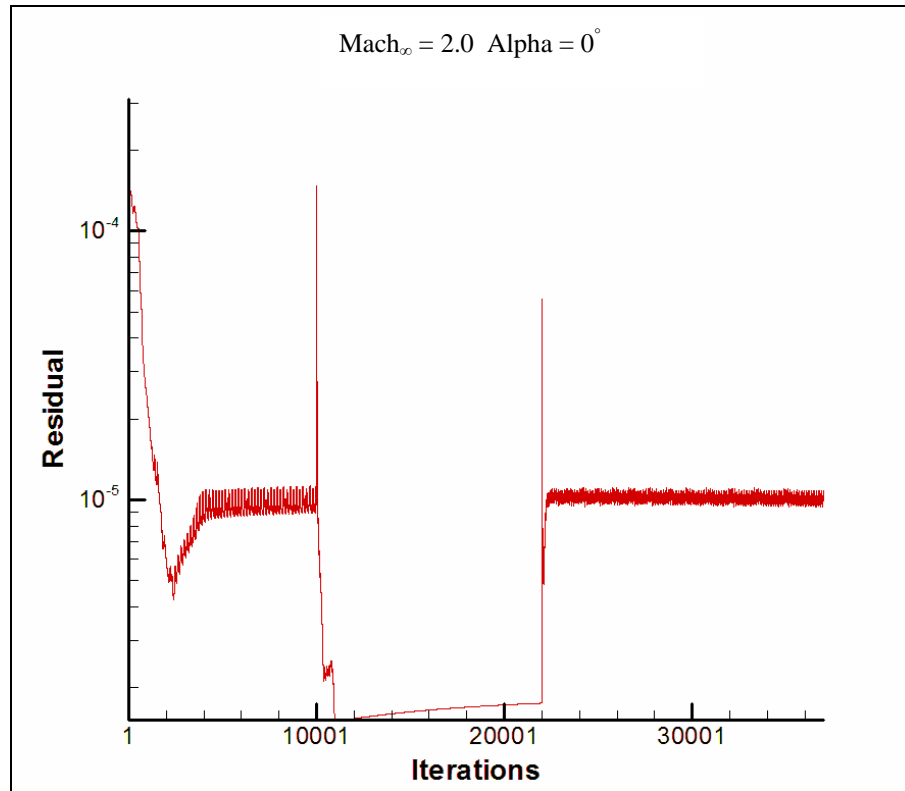
Figure 3.29 shows the coefficient of pressure around the upper and lower surface. The higher curve belongs to the coefficient of pressure on the upper surface while the lower curve belongs to the coefficient of pressure at the lower surface. The more negative upper surface will create a lower pressure at the top that will increase the speed while the lower surface will also increase the speed but to a lesser degree. The ups and downs in the coefficient of pressure close to the leading edge (at an X-position of zero), are believed to be caused by irregularities in the grid and not by physical causes.



**Figure 3.30 Coefficient of Lift and Drag Convergence for NACA 64<sub>2</sub>A215 airfoil**

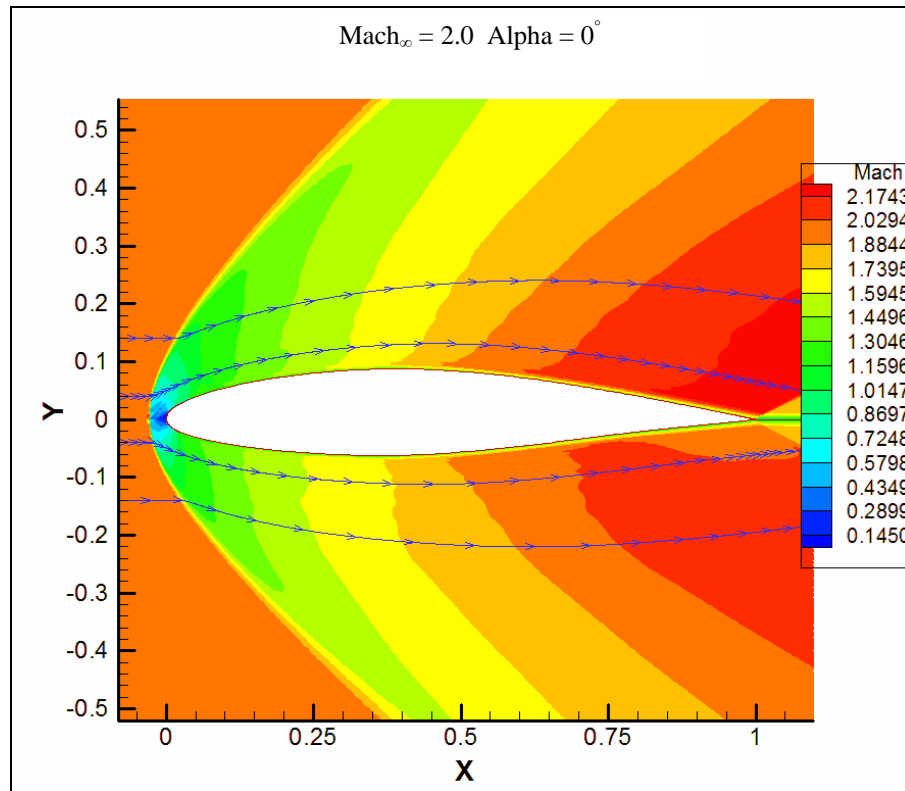
Figure 3.30 shows the coefficient of lift and the coefficient of drag after the 40000 iterations. It reached a coefficient of lift of 0.2159 and a coefficient of drag of 0.008119. These results were compared to the experimental results from Ref. 29 which reported a coefficient of lift of around 0.252 and a coefficient of drag of around 0.0095. This shows an estimated error of about 14% in the coefficient of lift and about 14.5% in the coefficient of drag. This level of accuracy is expected in the next runs given that the only variable that will be changing is the Mach number. It is worth mentioning that the difference in the results can be due to the discrepancies between the grid and the actual surface tested experimentally, and also to a difference between the assumed temperature used in the program and the actual temperature at the experimental facility.

### 3.2.4 Mach 2.0



**Figure 3.31 Residual for NACA 64<sub>2</sub>A215 airfoil from CFL3D**

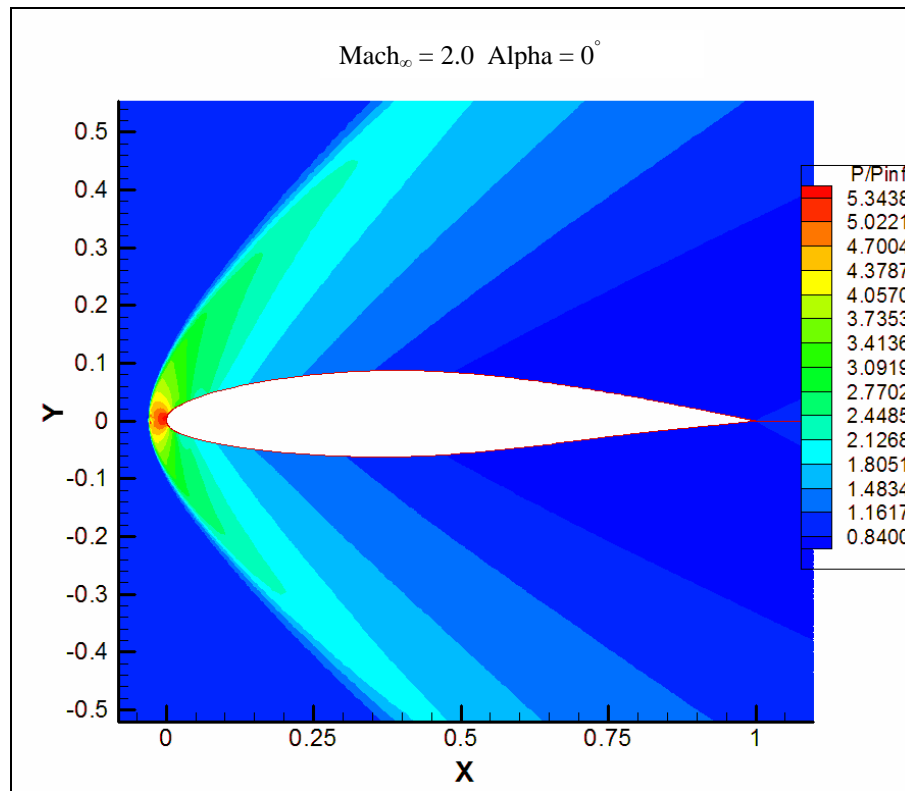
The first step before analyzing all the flow characteristics and properties is to determine the level of convergence in the results. For this case the 257 by 159 grid level was allowed to converge for 10000 iterations. Then the program passed to the finer 513 by 257 level for 12000 iterations and at the end it went to the finest 1025 by 513 grid level with 15000 iterations. As shown in Figure 3.31, the results obtained represent an average around an accuracy of 5 decimal places.



**Figure 3.32 Mach 2.0 Contour around NACA 64<sub>2</sub>A215 airfoil**

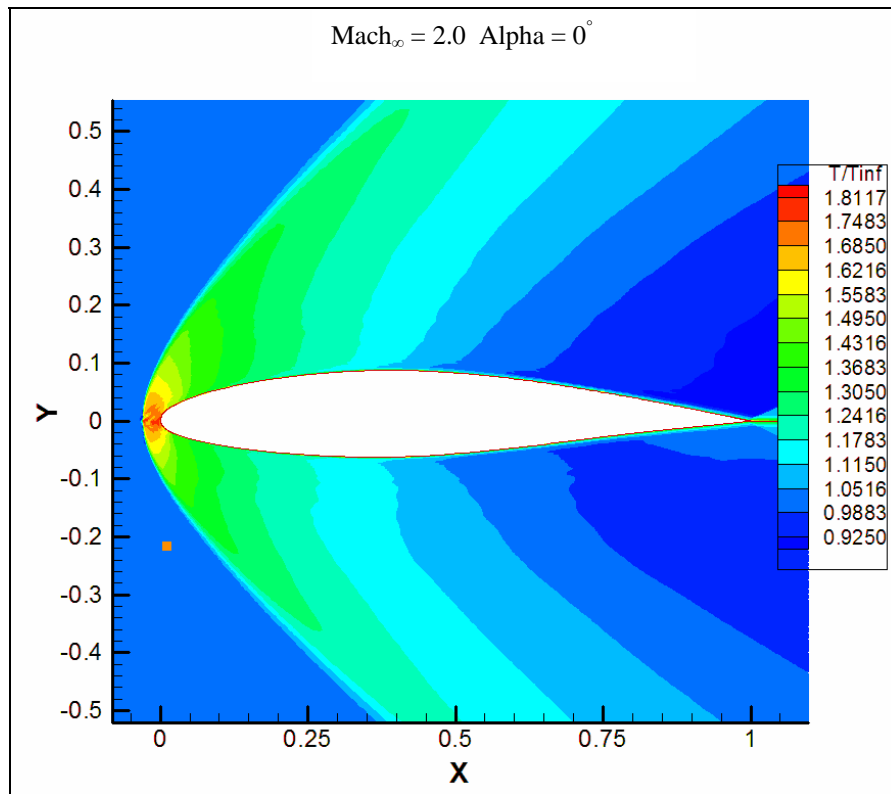
Figure 3.32 shows the mach contours for a free stream Mach number of 2.0 and a Reynolds number of 46 million. As the flow gets closer to the airfoil, it does not have an opportunity to expand and go over the airfoil. In other words, no compression or temperature information is passed to the front of the flow. This causes a compression shock wave at the leading edge of the airfoil that is also detached from the surface. As it was determined for the fanno line case, a supersonic flow will decelerate the flow and move it towards the sonic speed. The shock wave will cause a drop in Mach number from 2.0 to around 1.1.

It is believe that the reason for only achieving an average residual is either because of having a detached compression wave that could be pulsating in an unsteady way or because having such a fine grid where the shock is slightly moving and causing this frequency in the results.



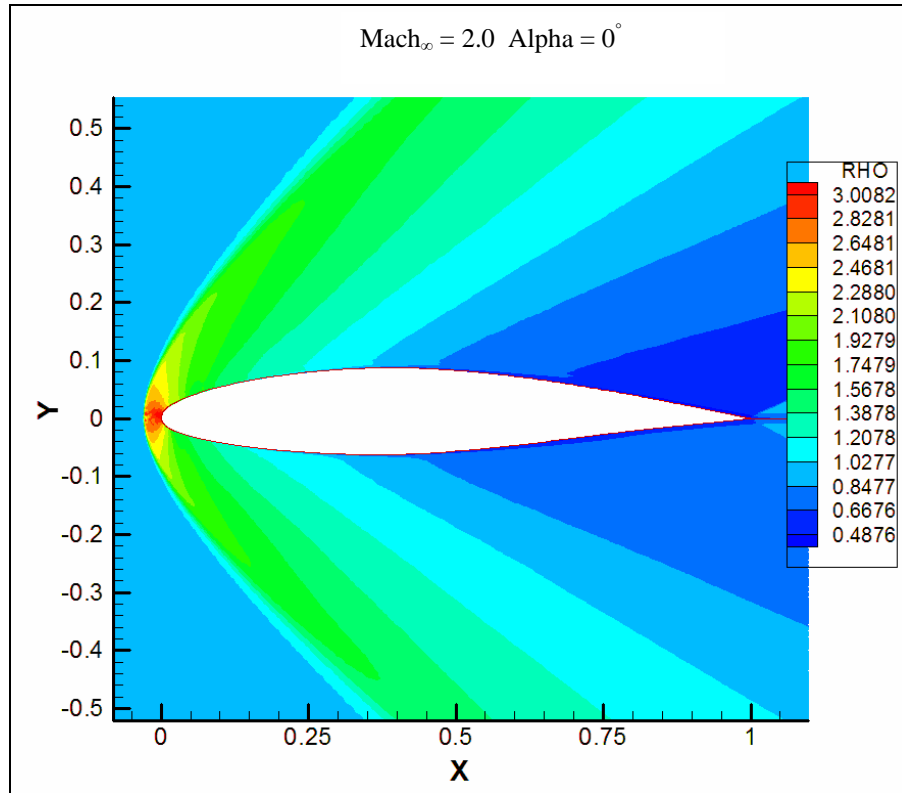
**Figure 3.33 Pressure Ratio Contour around NACA 64<sub>2</sub>A215 airfoil**

Figure 3.33 shows the pressure ratio contour lines for a Mach number of 2.0. For this supersonic case, there is a large increase in pressure at the leading edge of the airfoil and then changes to have a lower pressure ratio as it gets closer to the trailing edge. As the flow gets to the trailing edge it will experience another compression wave at the trailing edge which can be seen in Figure 3.32.



**Figure 3.34 Temperature Ratio Contour around NACA 64<sub>2</sub>A215 airfoil**

Figure 3.34 shows the temperature ratio around the airfoil at this supersonic speed. There is an increase in temperature at the leading edge because of this part of the airfoil supporting the shock wave that hits the leading edge. This collision of air particles at supersonic speeds will increase the temperature and also the density by having the flow compressed to that zone as shown in Figure 3.35.



**Figure 3.35 Density Ratio Contour around NACA 64<sub>2</sub>A215 airfoil**

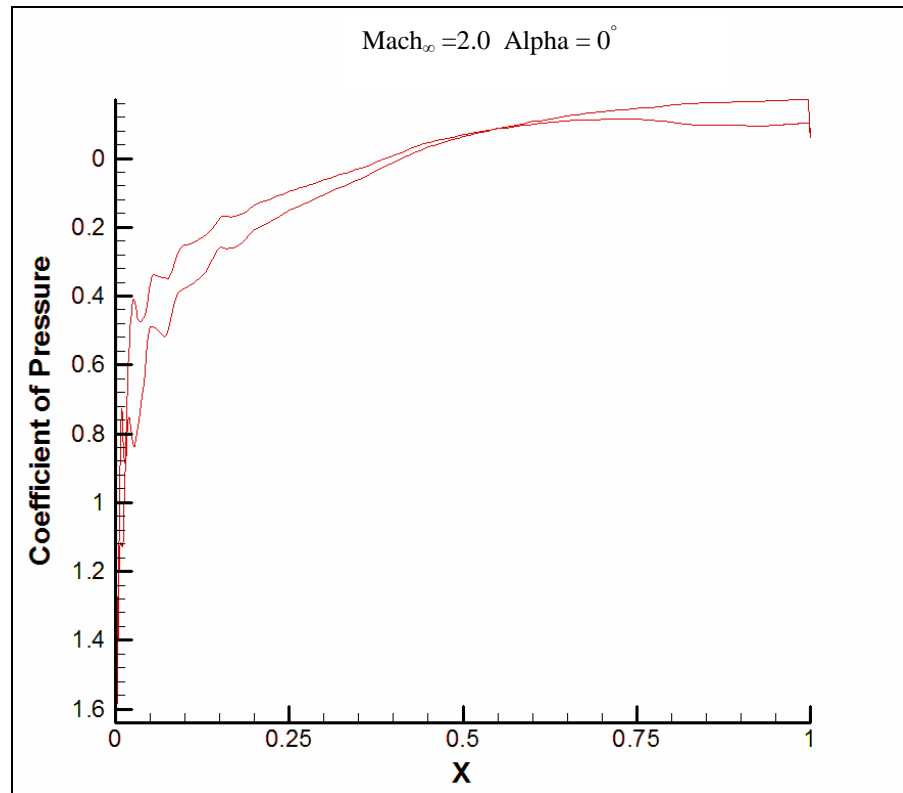


**Figure 3.36 Coefficient of Pressure around NACA 64<sub>2</sub>A215 airfoil**

On the other hand, the coefficient of pressure at supersonic speeds will be positive as shown in Figure 3.36. This positive coefficient of pressure shows a tendency toward decelerating the flow from its supersonic speeds given that the pressure downstream is higher than the pressure upstream. The coefficient of pressure goes from being positive to being slightly zero after the center of the airfoil.

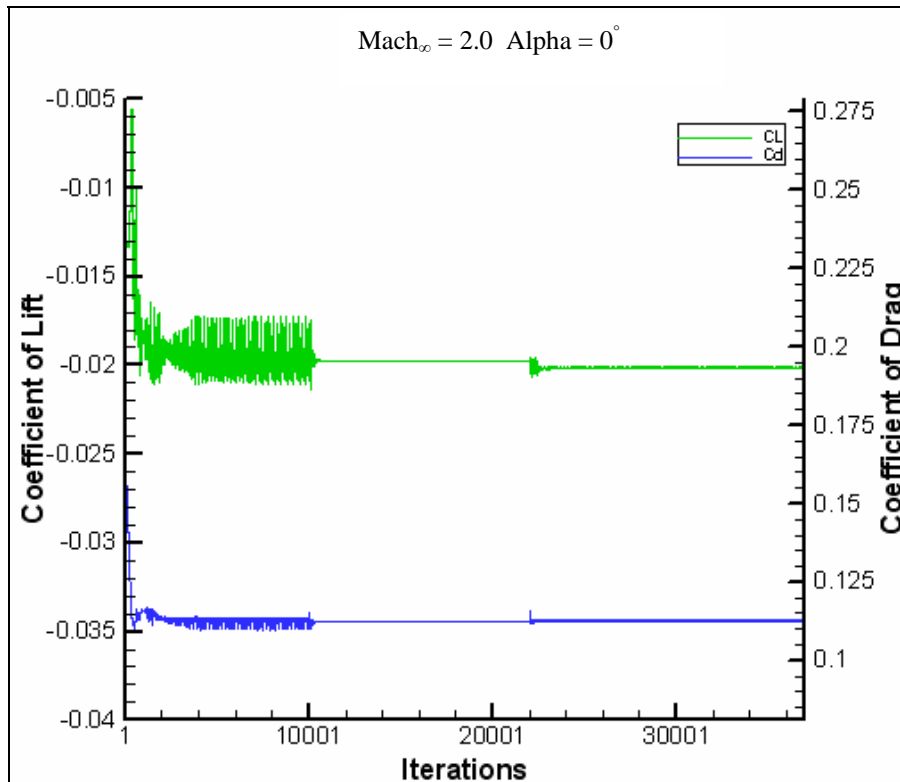


**Figure 3.37 Coefficient of Lift and Drag Convergence on NACA 64<sub>2</sub>A215 airfoil**

Figure 3.37 shows the coefficient of lift and the coefficient of drag convergence after 37000 iterations. For this case, both the coefficient of lift and the coefficient of drag converged. The coefficient of lift converged to  $-0.0201$  and the coefficient of drag converged to  $0.1127$ .

### 3.2.5 Mach 3.0

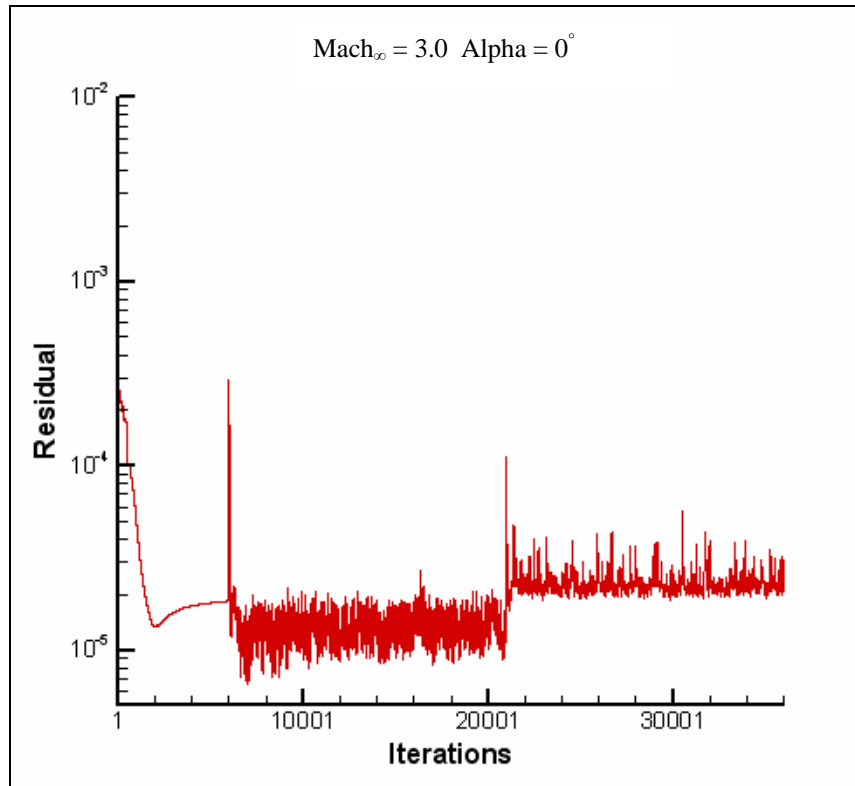


**Figure 3.38 Residual for NACA 64<sub>2</sub>A215 airfoil from CFL3D**

As before, the first step is to determine the level of convergence and accuracy of the results. For this case the 257 by 159 grid level was allowed to converge for 6000 iterations. Then the program passed to the finer 513 by 257 level for 16000 iterations and at the end it went to the finest 1025 by 513 grid level with 14000 iterations. As shown in Figure 3.38, the results obtained represent an average that are around an accuracy of 4 decimal places.

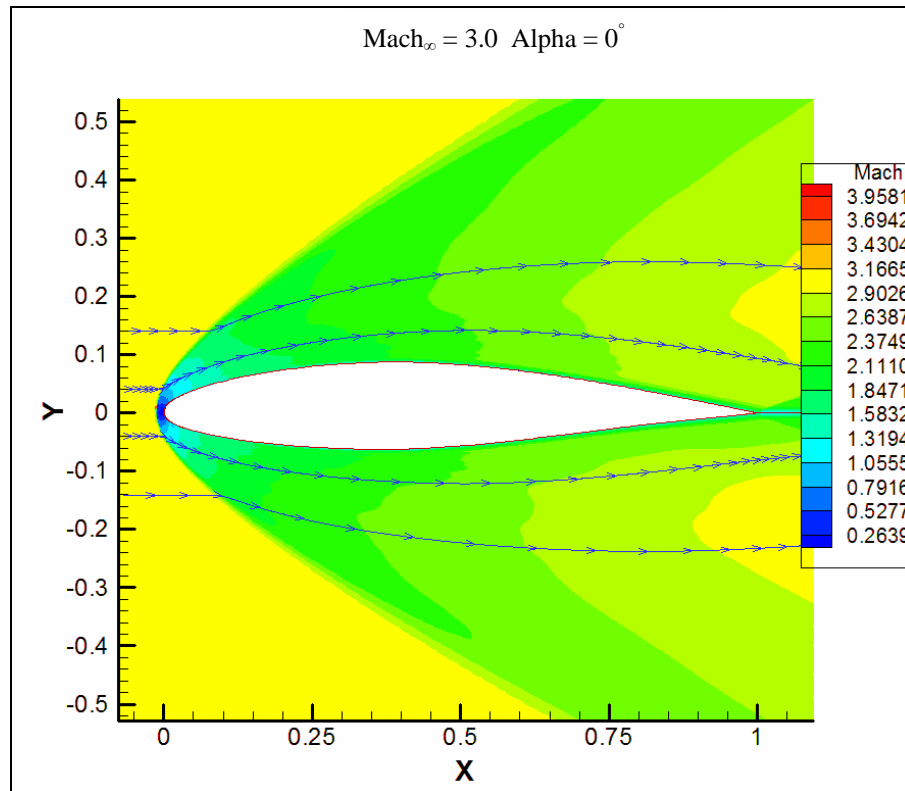


**Figure 3.39 Mach 3.0 Contour around NACA 64<sub>2</sub>A215 airfoil**

Figure 3.39 shows the mach contours for a free stream Mach number of 3.0 and a Reynolds number of 69 million. As in the case for a Mach number of 2.0, the flow does not have an opportunity to expand and go over the airfoil. In other words, no compression or temperature information is passed to the front of the flow. This causes a compression shock wave at the leading edge of the airfoil that is also detached from the surface. It can be seen at the leading edge a subsonic area followed by a supersonic area.

It is also believe that the reason for only achieving an average residual is either because of having a detached compression wave that could be pulsating in an unsteady way or because

having such a fine grid where the shock is slightly moving and causing this frequency in the results.

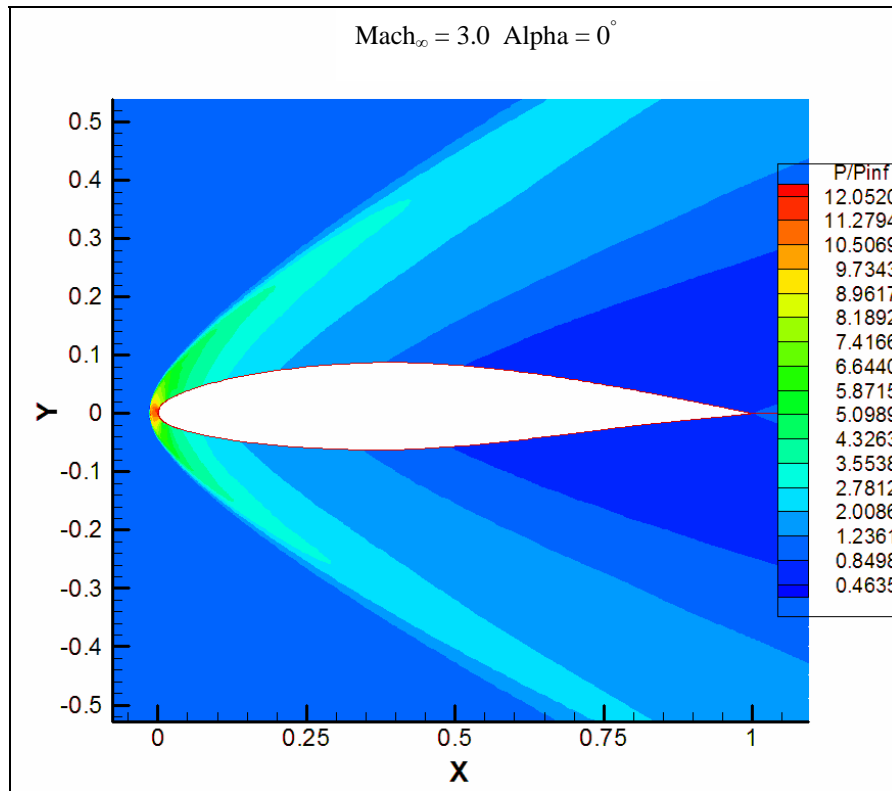


**Figure 3.40 Pressure Ratio Contour around NACA 64<sub>2</sub>A215 airfoil**

In Figure 3.40, the pressure ratio for Mach 3.0 airflow is shown. An area of even higher compression ratio is shown at the leading edge when compared to the Mach 2.0 case. This elevated pressure ratio will also cause a higher temperature ratio as shown in Figure 3.41. In Figure 3.40 and Figure 3.41 also shows almost identical pressure and temperature ratio around the upper surface and lower surface which will cause a zero lift coefficient.

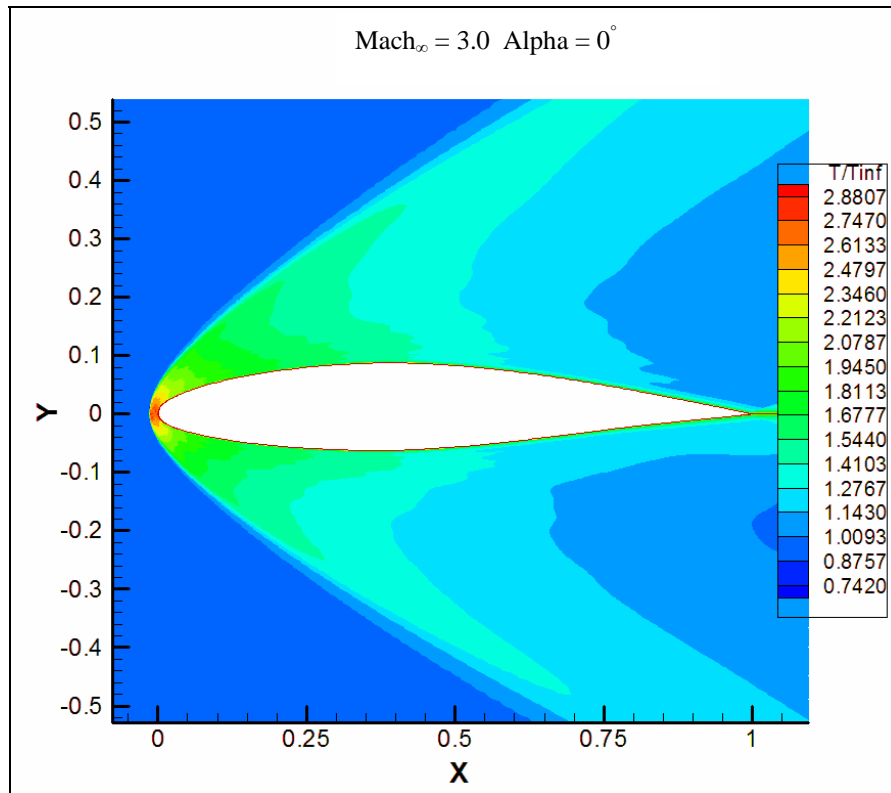


**Figure 3.41 Temperature Ratio Contour around NACA 64<sub>2</sub>A215 airfoil**

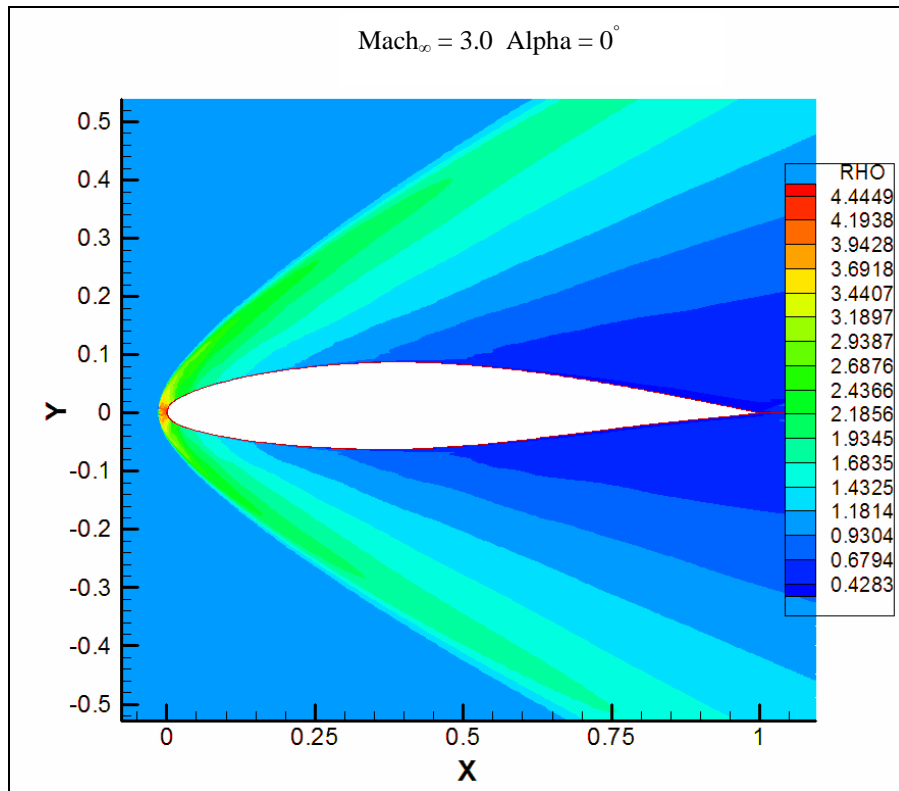


**Figure 3.42 Density Ratio Contour around NACA 64<sub>2</sub>A215 airfoil**

Figure 3.42 shows the density ratio that indicates similar flow patterns above and under the airfoil. These identical flows above and under the airfoil will cause a decrease to zero for the coefficient of lift and the possibility of having a lift coefficient only if the airfoil is at an angle of attack with respect to the free stream flow. This same pattern is observed in Figure 3.43 with an almost zero coefficient of pressure.

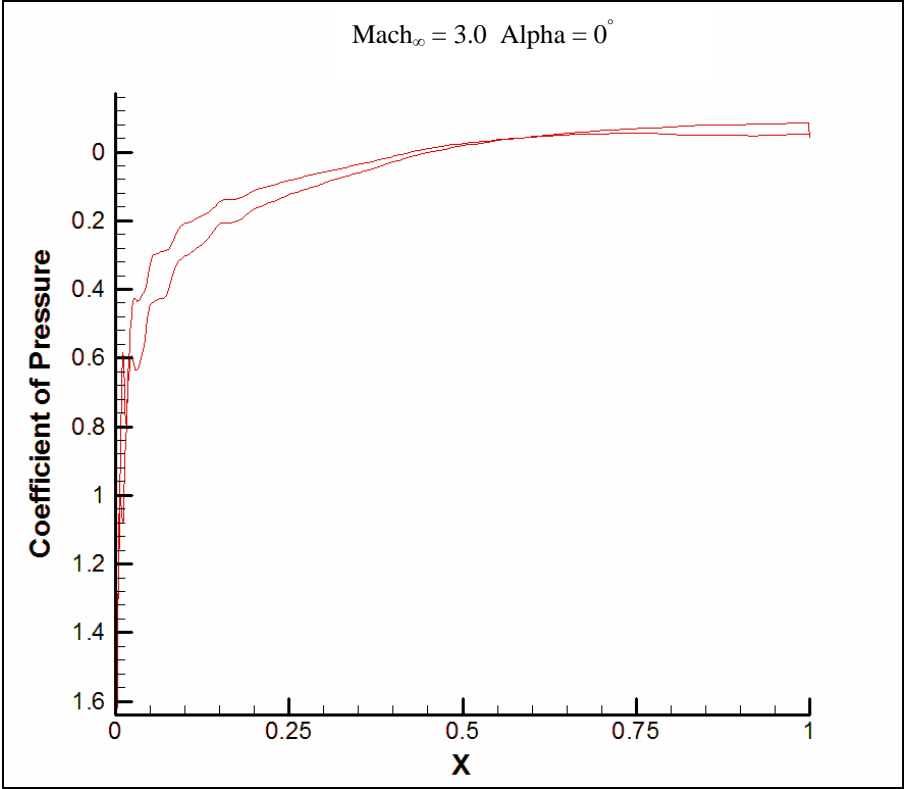


**Figure 3.43 Coefficient of Pressure around NACA 64<sub>2</sub>A215 airfoil**

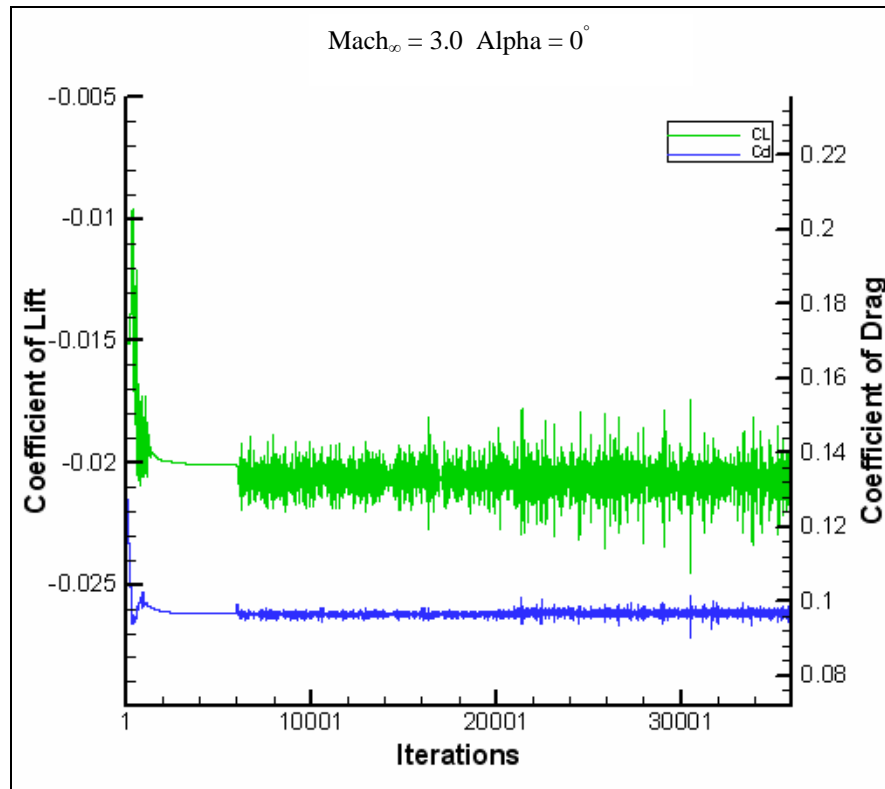


**Figure 3.44 Coefficient of Lift and Drag Convergence for NACA 64<sub>2</sub>A215 airfoil**

Figure 3.44 shows the average coefficient of lift and the coefficient of drag convergence at a supersonic speed of Mach 3.0. The coefficient of lift had an average of  $-0.0201$  and the coefficient of drag had an average of  $0.1127$ .

### 3.2.6 Entropy Generation Rate Comparison

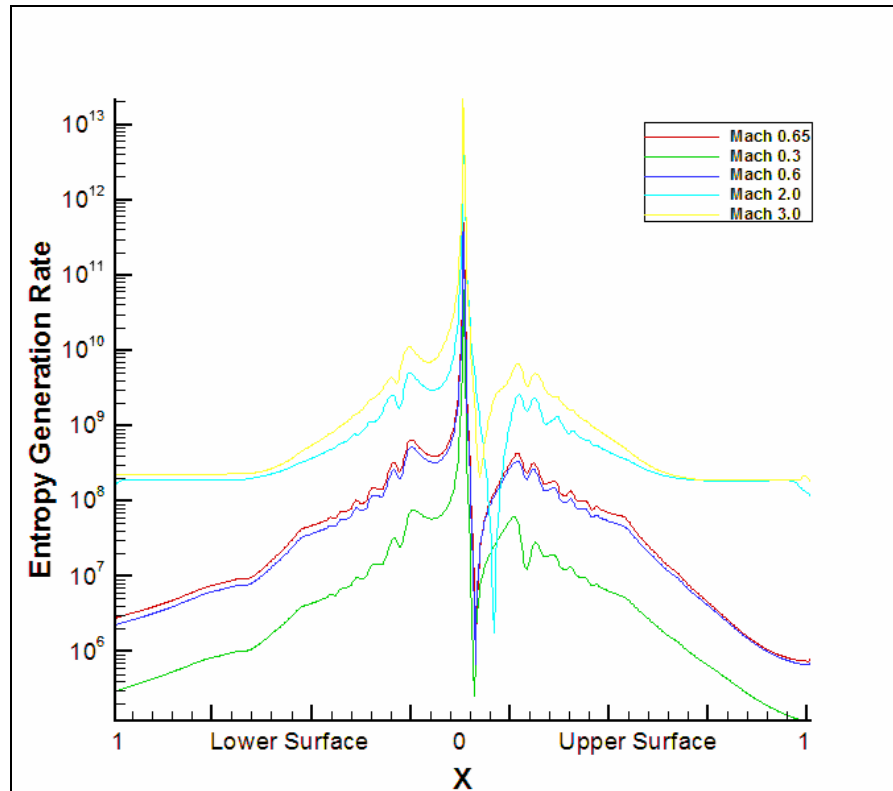


**Figure 3.45 Entropy Generation Rate ( $\frac{W}{m^3 K}$ ) around NACA 64<sub>2</sub>A215 airfoil**

Figure 3.45 shows the entropy generation rate per unit span caused one meter around the leading edge, the upper surface and the lower surface only. It does not show the entropy generated after the trailing edge.

Figure 3.45 shows the entropy generation rate per unit volume caused by the NACA 64<sub>2</sub>A215 airfoil at different Mach numbers from subsonic to supersonic speeds. The X-position of one is located at the trailing edge and the X-position of zero is the leading edge of the airfoil. As it is expected for the space that is analyzed, the maximum entropy generation

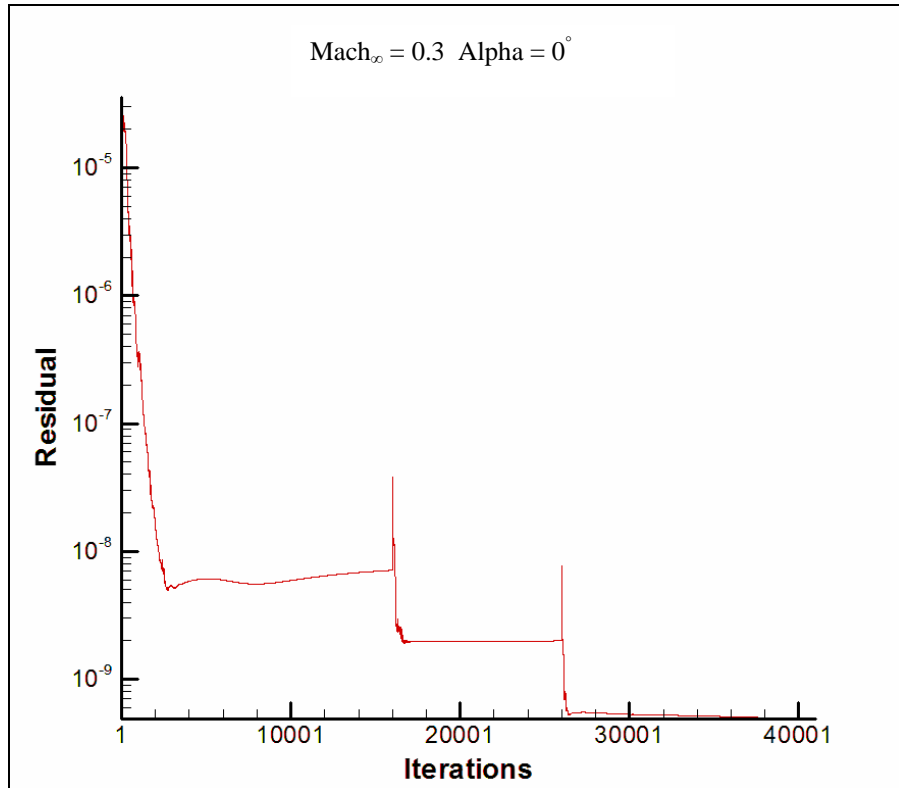
is caused at the leading edge where there are large changes in the velocity and temperature of the flow. The flow goes from the free stream Mach number to a stagnant point at the leading edge which will cause the entropy generation drop due to the zero velocity terms but with a generation due to the rise in temperature and density. As it is expected the least amount of entropy generation rate is caused by the slowest Mach number of 0.3.

Although the upper and lower surface meet in at the trailing edge, the pressure differential and the temperature difference is enough to cause a higher entropy generation rate at the lower trailing edge than at the higher trailing edge. It is interesting to notice that the entropy generation at the trailing edge for the subsonic Mach numbers is decreasing while the entropy generation for the supersonic Mach numbers appear to be level.

The two highest entropy generation are caused by the highest Mach numbers of 2.0 and 3.0. As it was expected, more entropy is generated due to the compression shock that form at the leading edge of the airfoil. The compression shock wave causes an almost instantaneous change in velocity gradients and an increase in temperature which will drive the increase in entropy generated.

## 3.3 K2 Airfoil

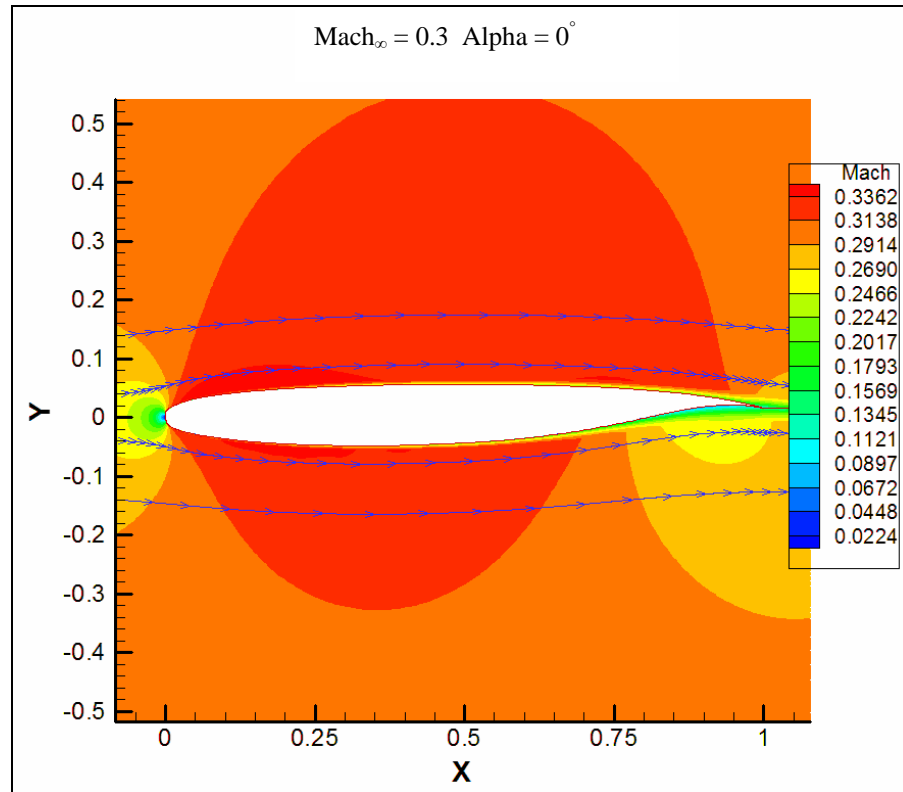
### 3.3.1 Mach 0.3



**Figure 3.46 Residual for K2 airfoil from CFL3D**

Figure 3.46 shows the level of convergence that is expected in the results. This case as well as all the other cases analyzed in this thesis started with a coarse 257 by 159 grid level then it went to a finer 513 by 257 grid level and ended at the finest 1025 by 513 grid level. The 257 by 159 grid level was allowed to converge for 16000 iterations. Then the program passed to the finer 513 by 257 level for 10000 iterations and at the end it went to the finest 1025 by 513

level with 14000 iterations. An accuracy of 9 decimal places is expected in the results given this residual.



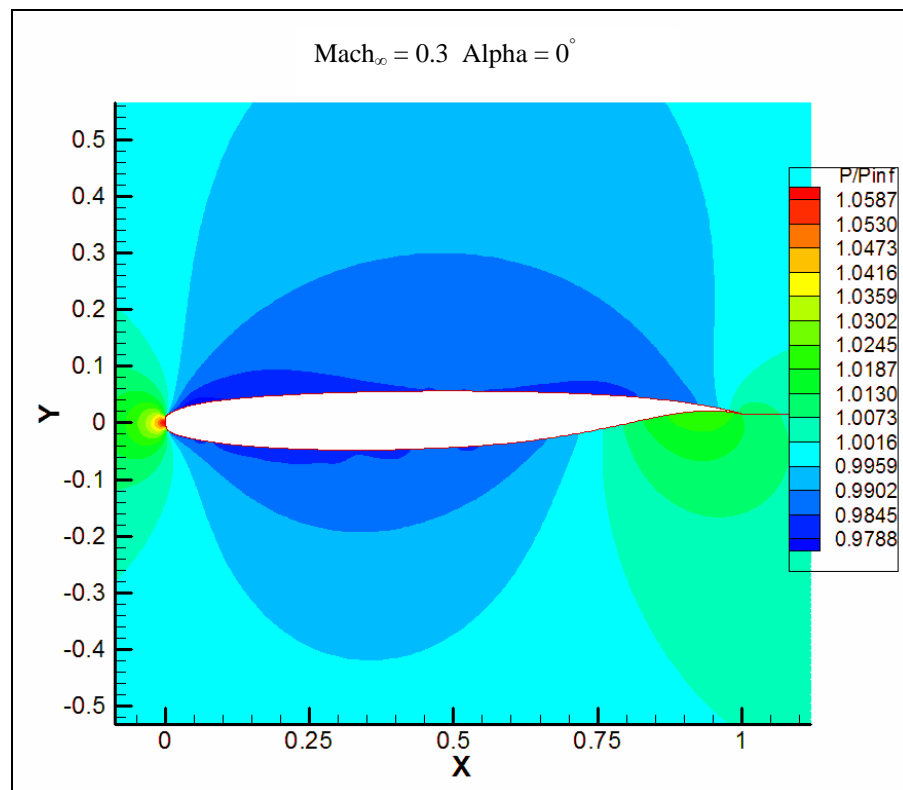
**Figure 3.47 Mach 0.3 Contour around K2 airfoil**

Figure 3.47 shows the mach contours around the K2 airfoil with a free stream speed of Mach 0.3 and a Reynolds number of 6.9 million.

As in the last case, the flow goes over, under or it reaches the stagnation point at the leading edge of the airfoil. It can be seen how the flow reaches a higher speed at the upper surface and for a longer distance than in the lower surface. As the flow passes over and under the airfoil, it starts to accelerate, reaches a maximum around half chord and then decelerates to the free stream speed. One important characteristic to notice is the lower maximum Mach

number that is achieved at the lower surface and also the Mach number bubble that is created close to the trailing edge of the lower surface which is caused by a higher pressure in that area as can be seen in Figure 3.48

This acceleration in speed is due to a decrease in pressure caused by the curvature of the airfoil. Figure 3.48 shows the pressure ratio between the local pressure and the free stream pressure. It shows how the pressure decreases on both the upper and lower surface but remains constant for a longer length along the upper surface, limiting the increases in speed towards sonic speed.



**Figure 3.48 Pressure Ratio Contour around K2 airfoil**

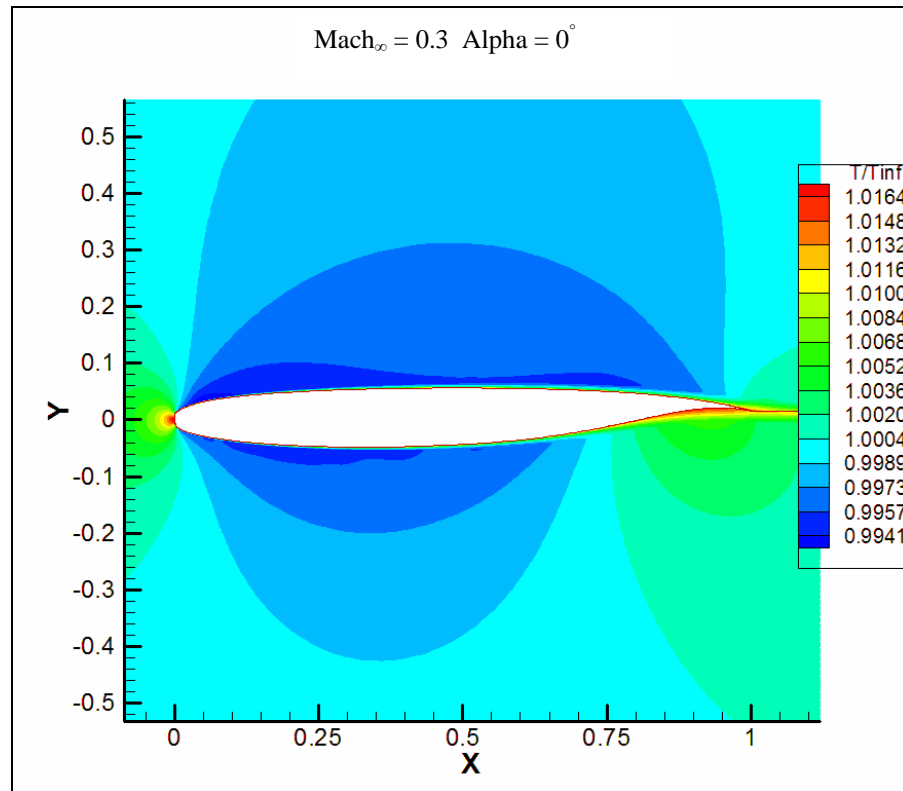


**Figure 3.49 Temperature Ratio Contour around K2 airfoil**

Figure 3.49 shows the temperature ratio contours around the K2 airfoil at a Mach number of 0.3. Given that this Mach number is the lower limit when considering compressible flow, the temperature increase at the nose is close to one which will coincide with a slight 4% increase in density as shown in Figure 3.50. As shown in Figure 3.49, there is a higher temperature at the trailing edge of the lower surface when compared to the trailing edge at the upper surface. This is in agreement with the higher pressure at that zone and with also the higher density.

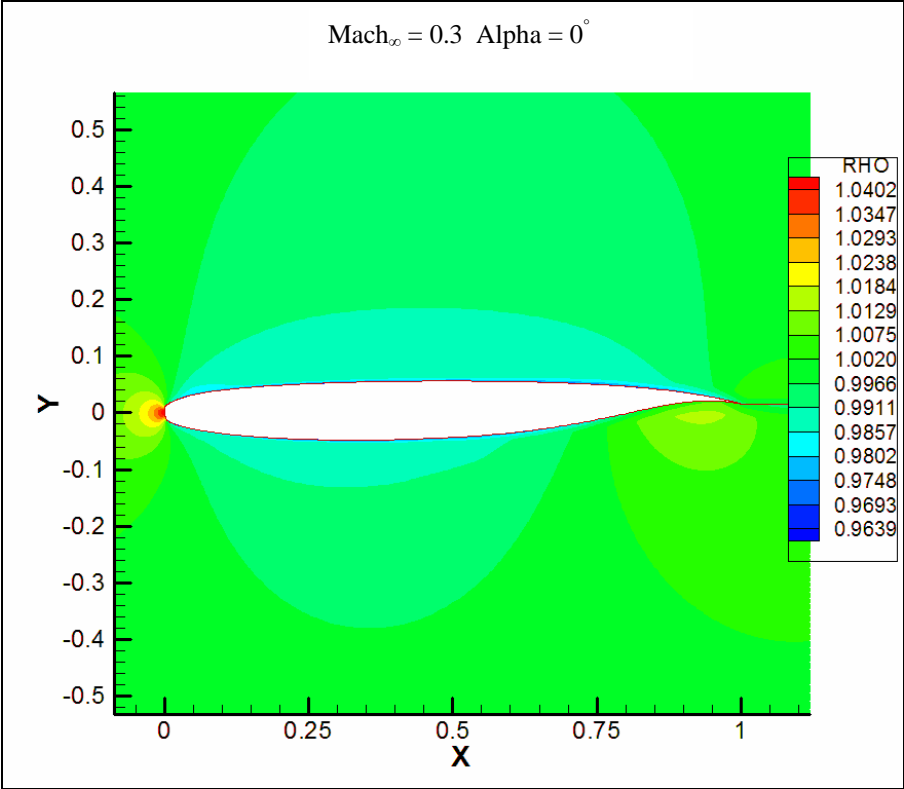


**Figure 3.50 Density Ratio Contour around K2 airfoil**

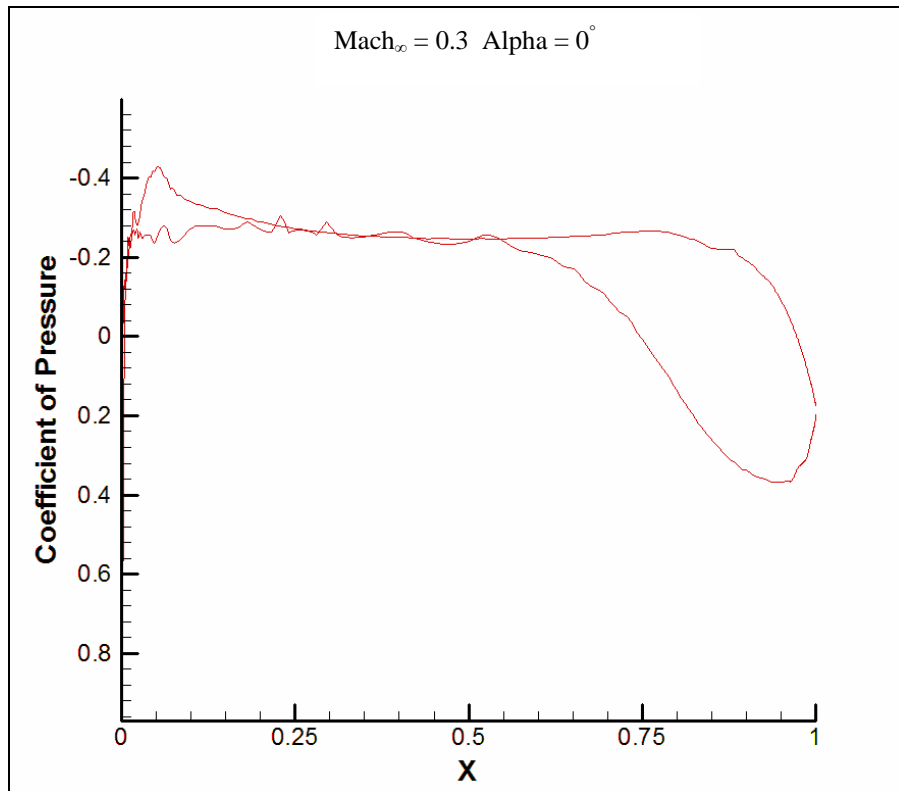


**Figure 3.51 Coefficient of Pressure around K2 airfoil**

Figure 3.51 shows the coefficient of pressure around the K2 airfoil. The open area at the right side of the coefficient of pressure is caused by numerical inaccuracies when assigning two different values at the same point at the trailing edge. One thing to notice is the extended negative constant pressure along the upper surface which changes positive the closer it gets to the trailing edge.

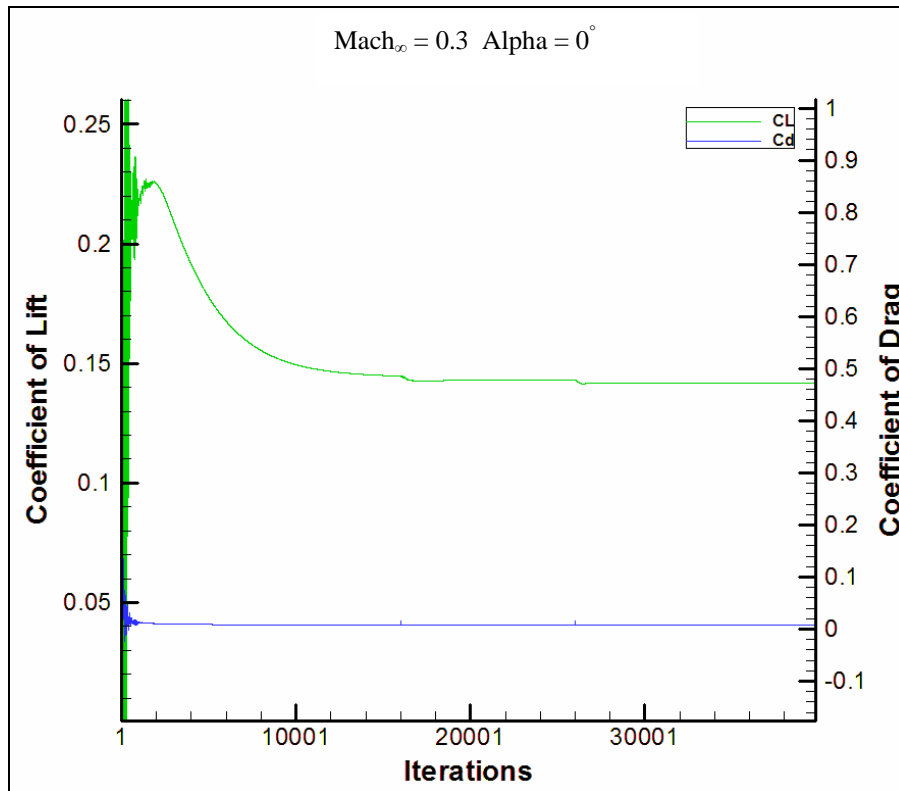


**Figure 3.52 Coefficient of Lift and Drag Convergence for K2 airfoil**

Figure 3.52 shows the coefficient of lift and the coefficient of drag convergence after 40000. First, it is important to know that these two variables stay constant along the iterations which indicate that the program has converged to the results. The program output a coefficient of lift of 0.1418 and a coefficient of drag of 0.007978.

### 3.3.2 Mach 0.6

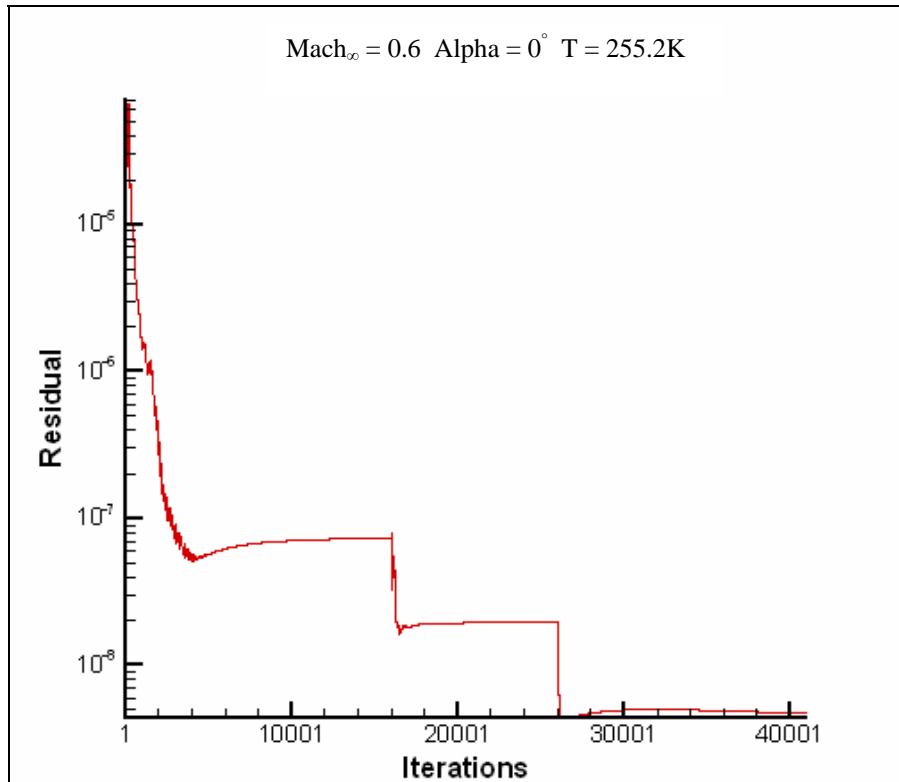


**Figure 3.53 Residual for K2 airfoil from CFL3D**

The first step to do before analyzing all the flow characteristics and properties is to determine the level of convergence in the results. This case as well as all the other cases analyzed in this thesis started with a coarse 257 by 159 grid level then it went to a finer 513 by 257 grid level and ended at the finest 1025 by 513 grid level. The 257 by 159 grid level was allowed to converge for 16000 iterations. Then the program passed to the finer 513 by 257 level for 10000 iterations and at the end it went to the finest 1025 by 513 level with 14000 iterations.

As shown in Figure 3.53, the results converged to a level of accuracy of 8 decimal places.

Taking all the grid levels, there were 1.38 million grid points in total.

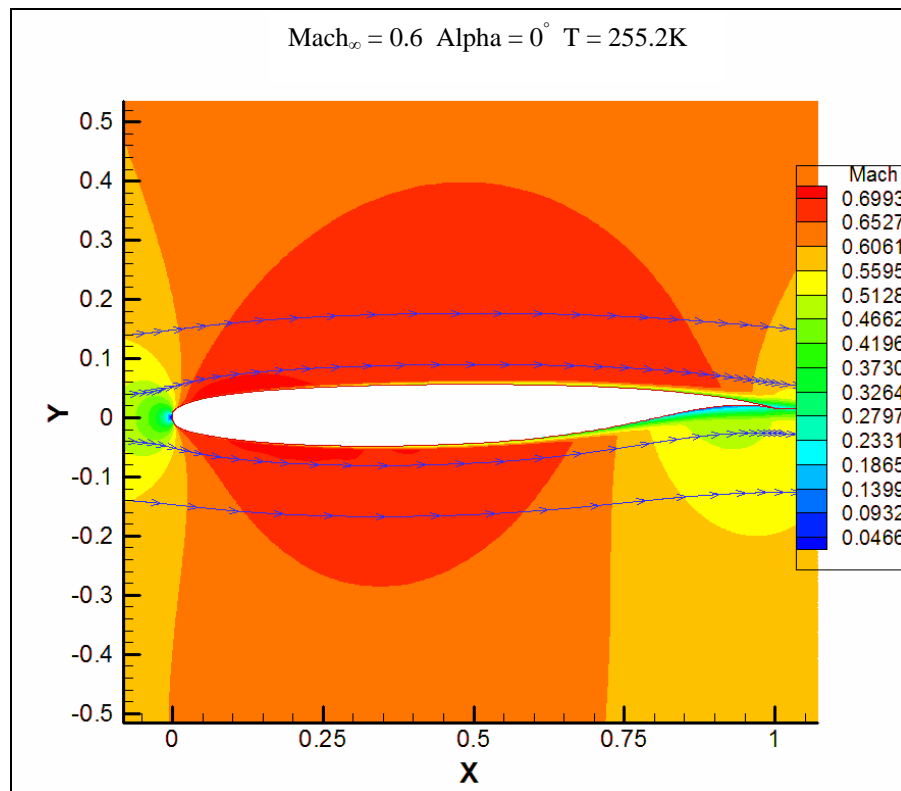


**Figure 3.54 Mach 0.6 Contour around K2 airfoil**

Figure 3.54 shows the mach contours around the K2 airfoil. The purpose of this first test is to compare the CFL3D results with experimental data. The experimental data had a free stream Mach number of 0.6, a Reynolds number of 6.0 million, and a free stream temperature of 255.2K which were matched in the CFL3D test run. For the other runs, the temperature was set to 288.15K.

As the flow first encounters the airfoil, it goes over, under or it reaches the stagnation point at the leading edge. Compression information is passed upstream of the flow, slowing down the flow in front of the leading edge since it is a subsonic flow. Given that the flow is subsonic, as the flow passes over and under the airfoil, it starts to accelerate, reaches a maximum around half chord and then decelerates to the free stream speed.

This acceleration in speed is due to a decrease in pressure caused by the curvature of the airfoil. Figure 3.55 shows the pressure ratio between the local pressure and the free stream pressure. It shows how the pressure decreases as the flow goes over and under the airfoil which helps explain the acceleration in speed and therefore the increase in Mach number. One of design specifications that is characteristic of supercritical airfoils is trying to maintain an almost constant pressure ratio above the upper surface. This almost constant pressure ratio will hold the flow from reaching close to sonic conditions and thus eliminating the compression shock and drag rise at the upper surface. As it is shown in Figure 3.55, the pressure ratios across the upper surface have an extended constant pressure bubble.

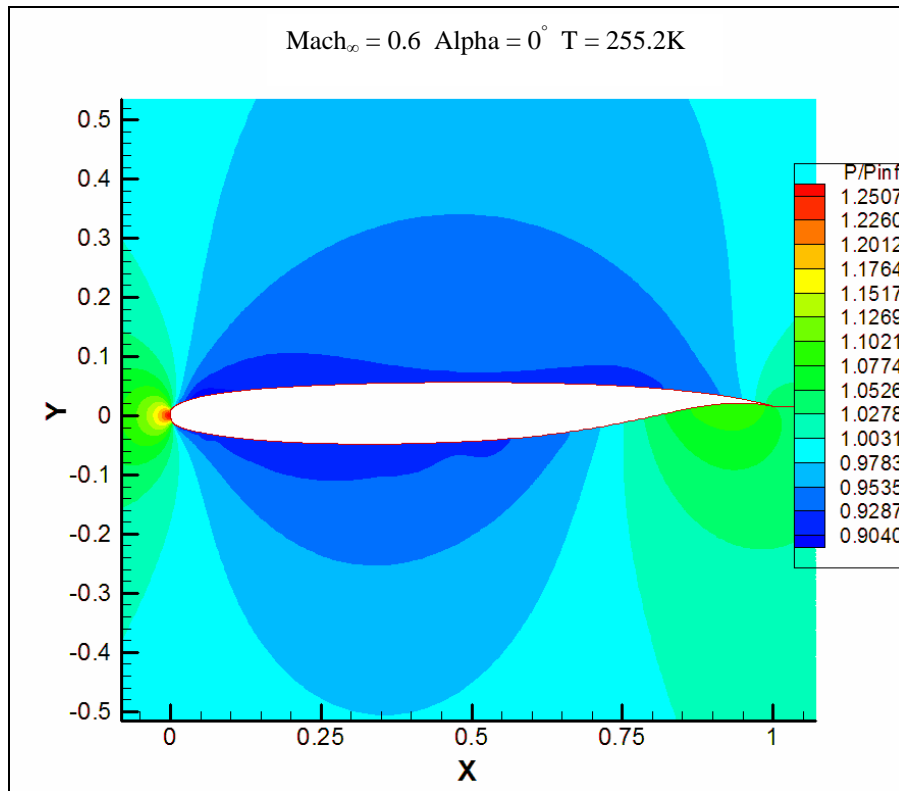


**Figure 3.55 Pressure Ratio Contour around K2 airfoil**

In Figure 3.56, the temperature ratio contours around the K2 airfoil are shown. As it expected the temperature decreases over and under the airfoil due to a decrease in pressure causing an increase in air flow speed. This decrease in temperature will also cause a decrease in density around the airfoil shown in Figure 3.57 which is theoretically explained by the perfect gas law.

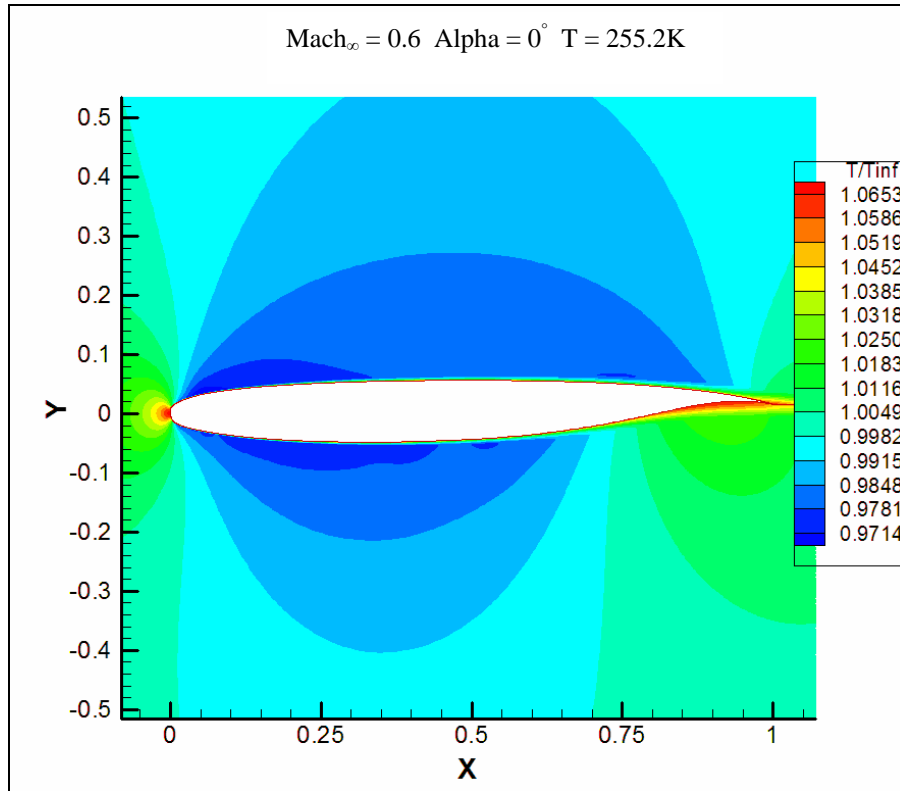


**Figure 3.56 Temperature Ratio Contour around K2 airfoil**

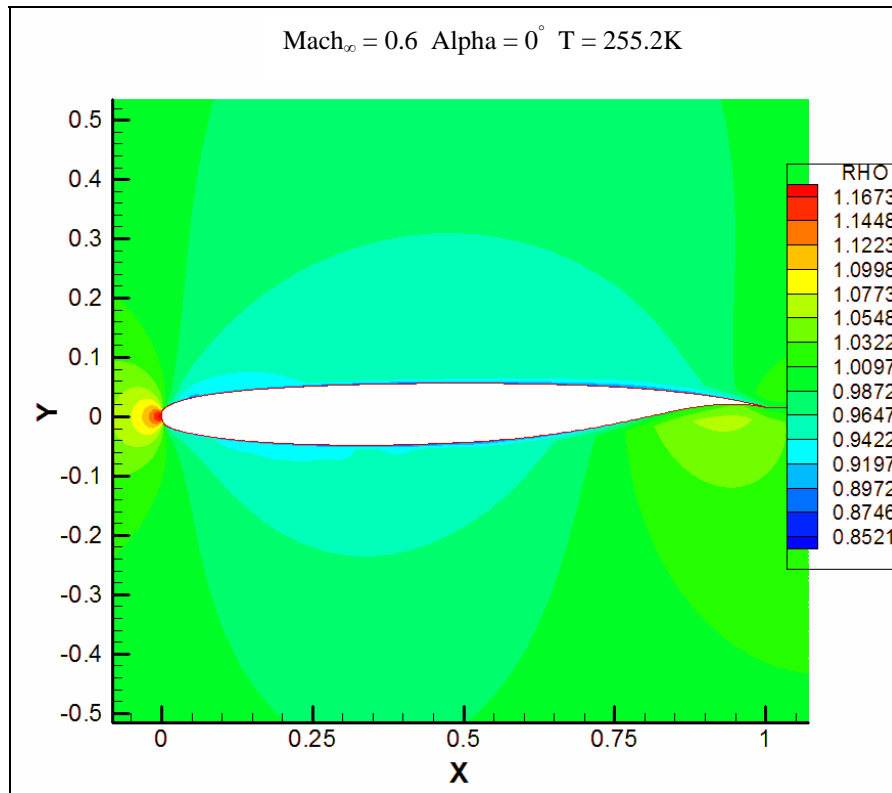


**Figure 3.57 Density Ratio Contour around K2 airfoil**

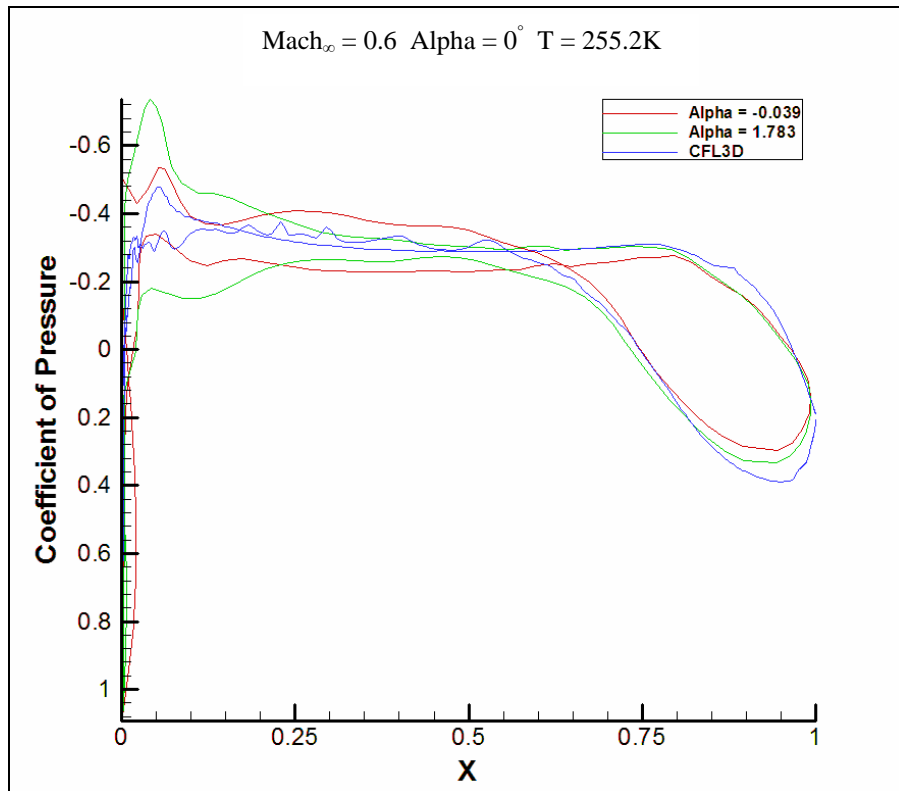


**Figure 3.58 Coefficient of Pressure around K2 airfoil**

Figure 3.58 shows two experimental results for coefficient of pressure and the numerical coefficient of pressure obtained from CFL3D. Given that the angle of attacks( $\alpha$ ) that were experimentally analyzed are not exactly zero as the one examined numerically, the results for two angles of attack are shown. This figure shows that initially the results obtained numerically are an underestimate close to the leading edge of the airfoil and then the results are an overestimate close to the trailing edge. The reason for these discrepancies can be caused by numerical inaccuracies in the grid creation, a change in temperature than the constant temperature reported in the experimental results, and/or numerical inaccuracies in CFL3D. The experimental data can be seen in Appendix C.1.

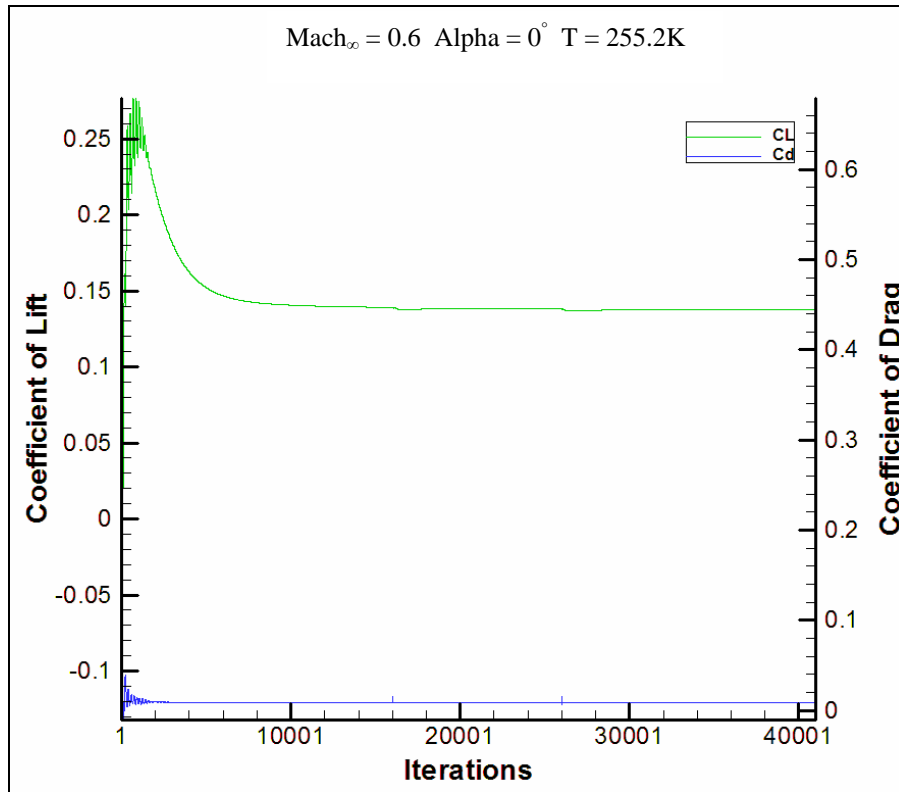


**Figure 3.59 Coefficient of Lift and Drag Convergence for K2 airfoil**

Figure 3.59 shows the coefficient of lift and the coefficient of drag convergence after 40000 iterations. Numerically the coefficient of lift converged to 0.1376 and the coefficient of drag converged to 0.008332. Experimentally the coefficient of drag can be obtained from Appendix C.1. Given that it does not vary between the two angle of attacks, the coefficient of drag is obtained as 0.0092 which is a difference of 9.43% between the numerical and experimental results.

### 3.3.3 Mach 0.6

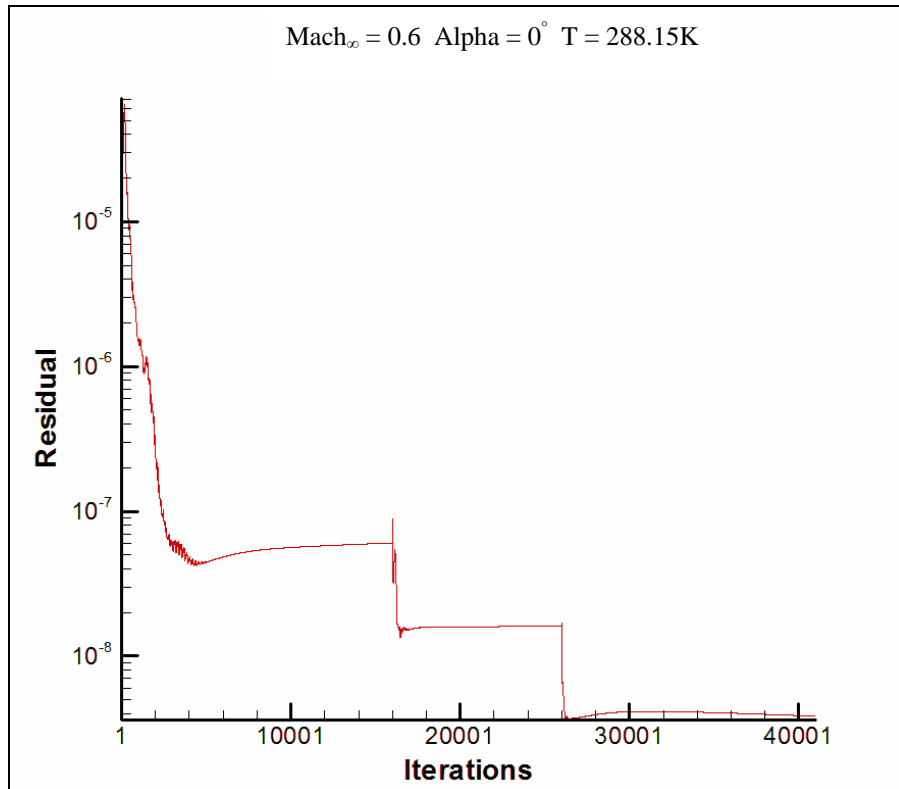


**Figure 3.60 Residual for K2 airfoil from CFL3D**

As before, the 257 by 159 grid level was allowed to converge for 16000 iterations. Then the program passed to the finer 513 by 257 grid level for 10000 iterations and at the end it went to the finest 1025 by 513 grid level with 14000 iterations. As shown in Figure 3.60, the results converged to a level of accuracy of around 8 decimal places.

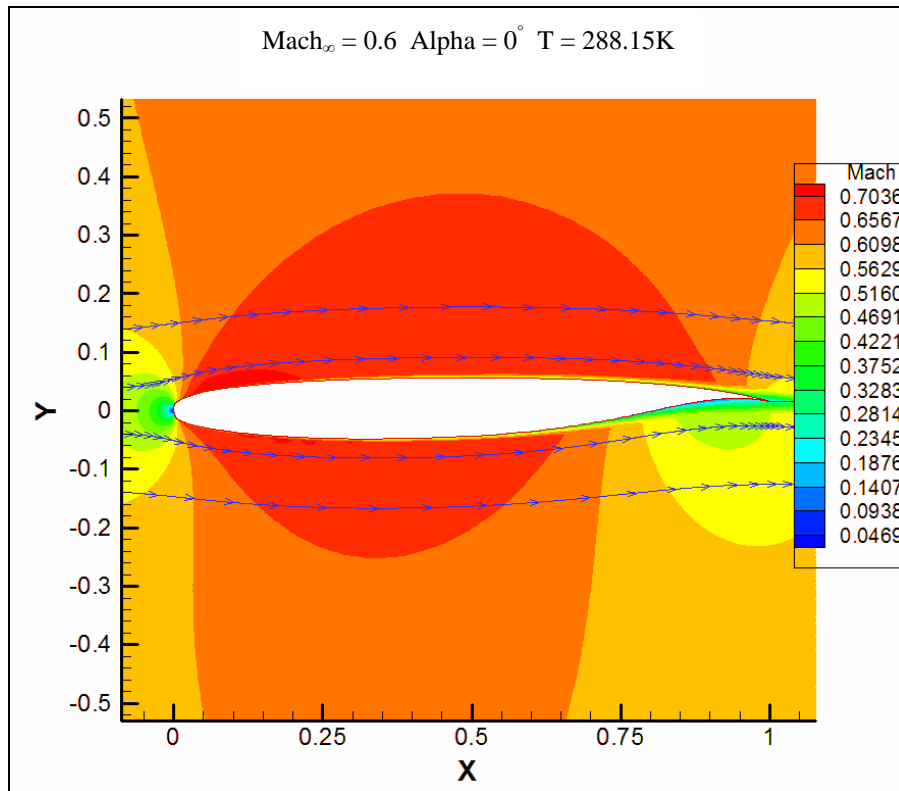


**Figure 3.61 Mach 0.6 Contour around K2 airfoil**

Figure 3.61 shows the mach contours around the K-2 airfoil with a free stream speed of Mach 0.3 and a Reynolds number of 13.8 million. Although the Mach number is the same as the first case for the K2 airfoil, the temperature is 288.15K instead of 255.56K.

As in the last case, the flow goes over, under or it reaches the stagnation point at the leading edge of the airfoil. It can be seen how the flow reaches a higher speed at the upper surface and for a longer distance than in the lower surface. This is mainly due to a higher pressure in the lower surface than in the upper surface. Again, this acceleration in speed is due to a decrease in pressure caused by the curvature of the airfoil. Figure 3.62 shows the pressure ratio between the local pressure and the free stream pressure. As in the last cases, there is a

higher pressure ratio at the leading edge cause by the compression that is occurring at that point. This compression will also cause an increase in temperature as shown in Figure 3.63. As the flow passes the leading edge, it starts to cool down to a minimum that occurs around center of the airfoil.

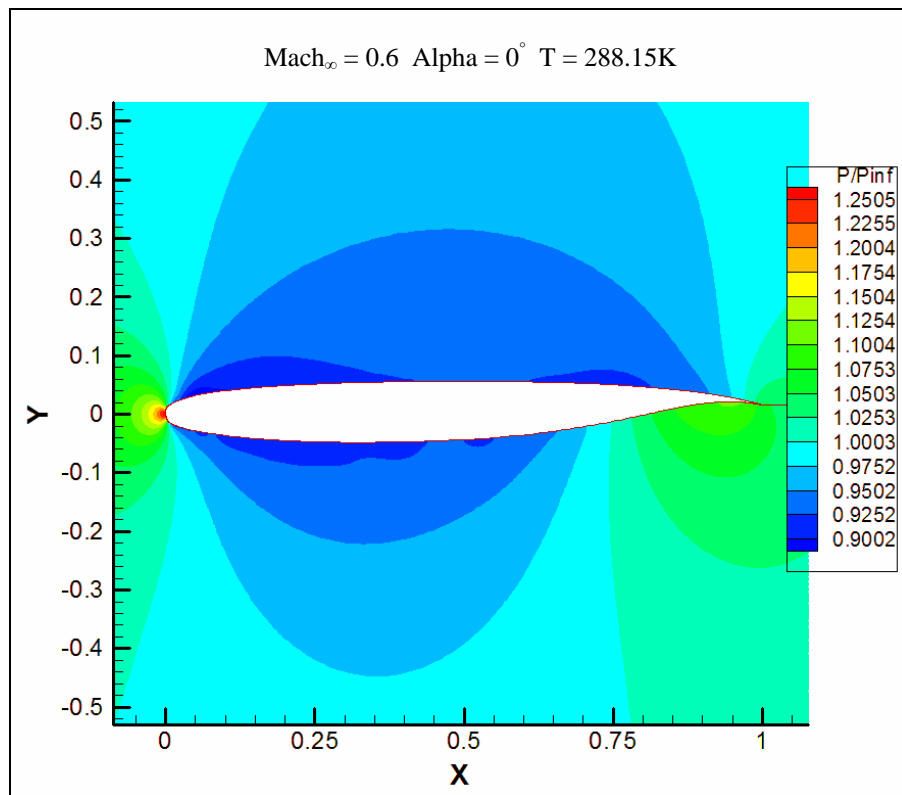


**Figure 3.62 Pressure Ratio Contour around K2 airfoil**

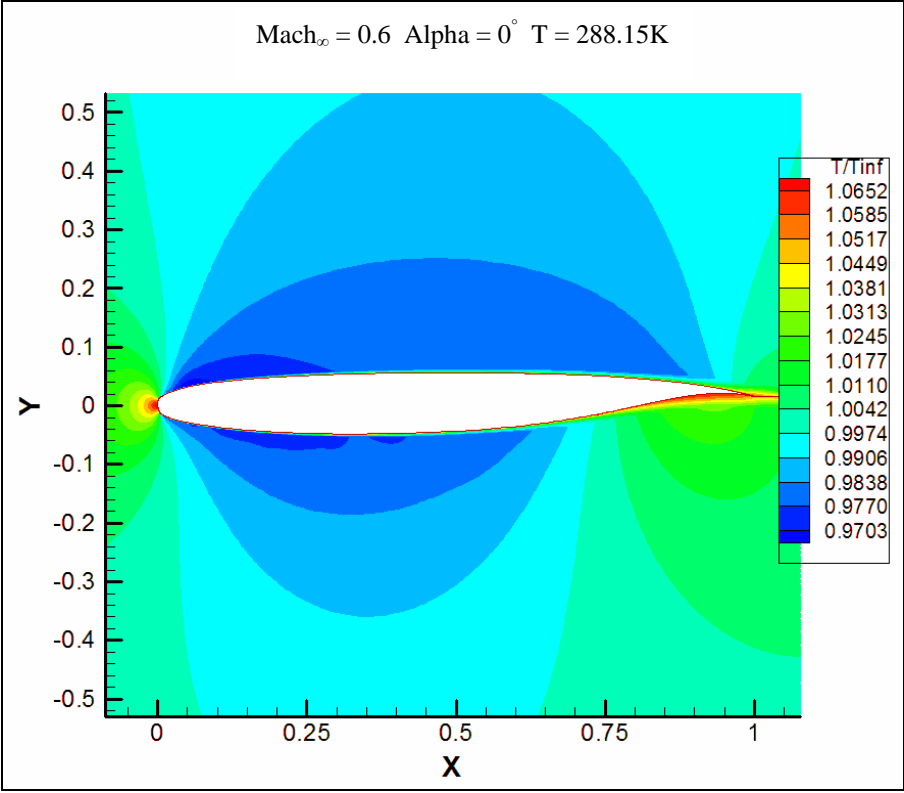


**Figure 3.63 Temperature Ratio Contour around K2 airfoil**

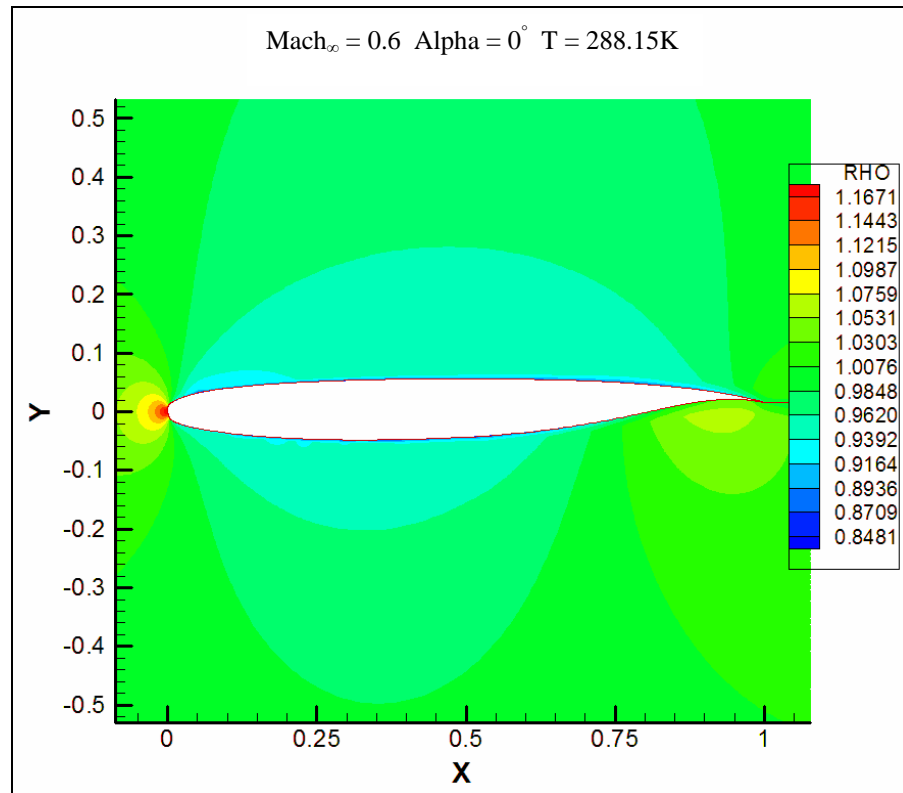


**Figure 3.64 Density Ratio Contour around K2 airfoil**

As in the last case, Figure 3.64 shows how the density ratio also increases at the leading edge and then returns to an unity density ratio but increases slightly close to the trailing edge at the lower surface. Around the center of the airfoil, the density gets lower which is also associated with a lower temperature and a lower pressure.

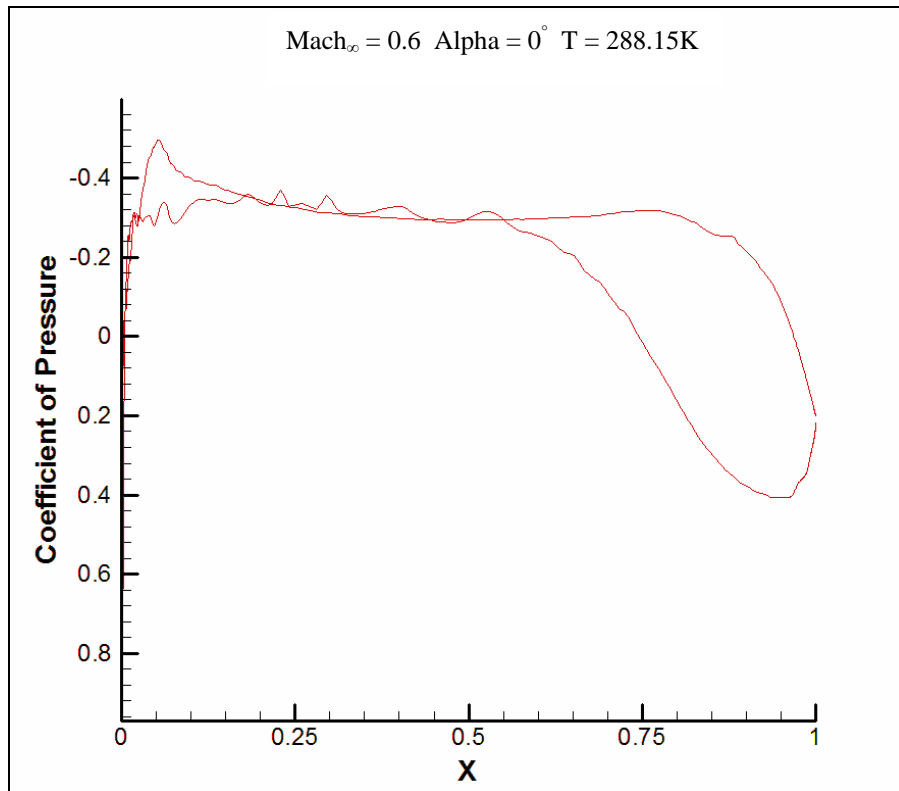


**Figure 3.65 Coefficient of Pressure around K2 airfoil**

The change in coefficient of pressure can be seen in Figure 3.65. As in the last case, the pressure stays with an almost constant negative coefficient of pressure of around -0.35. It stays with this value over a longer length along the upper surface than over the lower surface. It reaches a maximum positive pressure at the trailing edge which is the reason why the air flow start to decelerate around that zone.

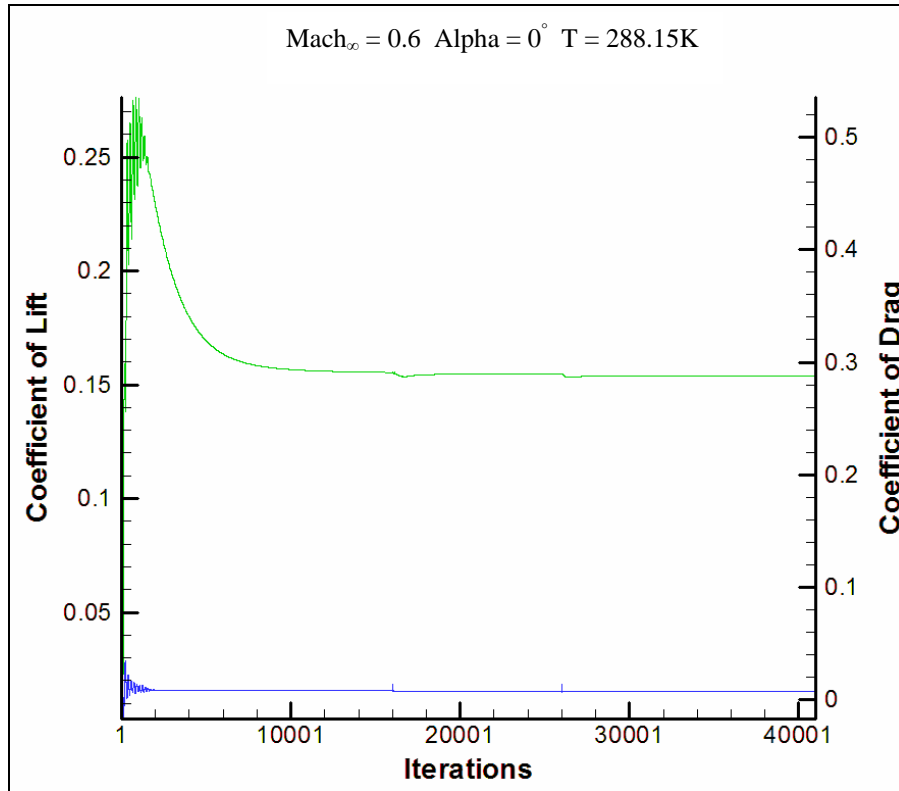


**Figure 3.66 Coefficient of Lift and Drag Convergence for K2 airfoil**

The coefficient of lift and the coefficient of drag convergence can be seen in Figure 3.66. Numerically, the run converged to a coefficient of lift of 0.1537 and a coefficient of drag of 0.007421. These results can be compared to the coefficient of lift and the coefficient of drag obtained at the same Mach number but lower temperature as in the first case. The first case achieved a coefficient of lift and the coefficient of drag of 0.1376 and 0.008332 respectively. As it is expected the higher temperature at the same Mach number causes an increase in lift and also a decrease in drag. The decrease in drag is caused because of a decrease in density which causes less air particles to be caused friction along the surface of the airfoil.

### 3.3.4 Mach 2.0

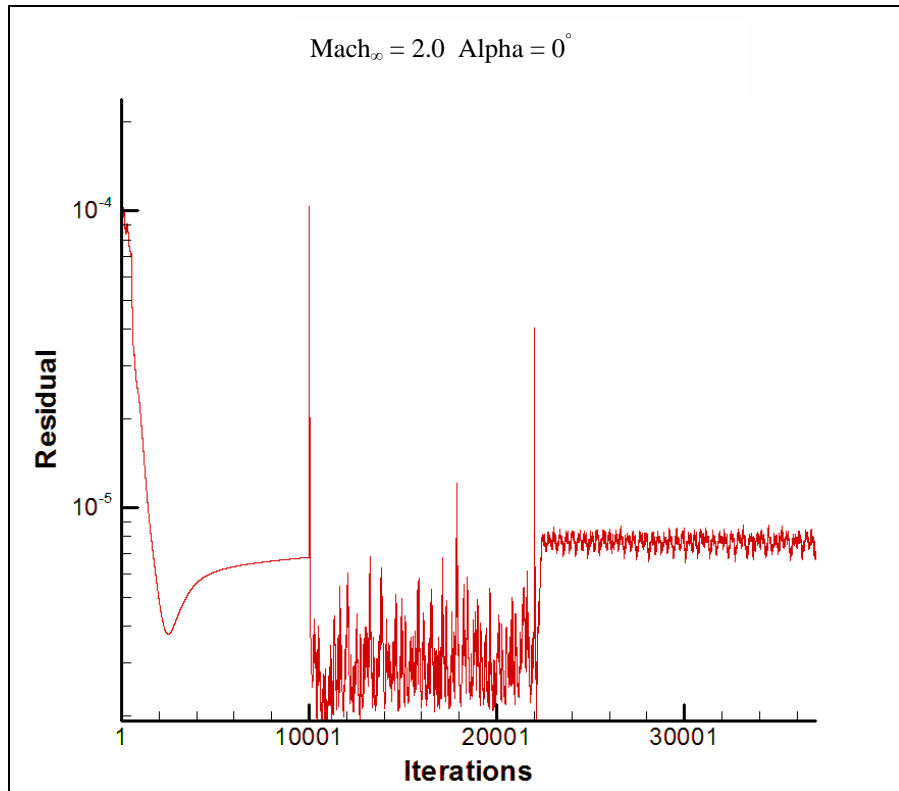


**Figure 3.67 Residual for K2 airfoil from CFL3D**

The first step before analyzing all the flow characteristics and properties is to determine the level of convergence in the results. For this case the 257 by 159 grid level was allowed to converge for 10000 iterations. Then the program passed to the finer 513 by 257 level for 12000 iterations and at the end it went to the finest 1025 by 513 grid level with 15000 iterations. As shown in Figure 3.31, the results obtained represent an average that are around an accuracy of 5 decimal places.

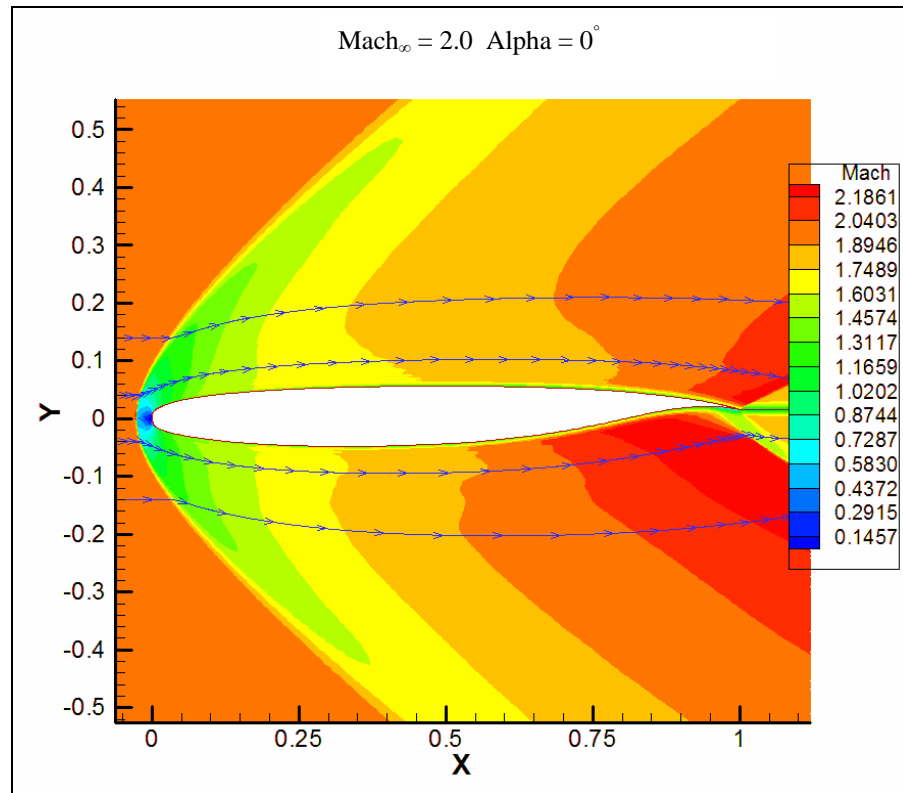


**Figure 3.68 Mach 2.0 Contour around K2 airfoil**

Figure 3.68 shows the mach contours for a free stream Mach number of 2.0 and a Reynolds number of 46 million. As the flow gets closer to the airfoil, it does not have an opportunity to expand and go over the airfoil. In other words, no compression or temperature information is passed to the front of the flow. This causes a compression shock wave at the leading edge of the airfoil that is also detached from the surface. As the flow passes over and under the leading edge of the airfoil, the changes in Mach number are similar on both sides. As the flow passes the center of the airfoil, it achieves a higher mach number at the lower surface than at the upper surface due to a favorable pressure gradient as it can be seen in Figure 3.69. As it gets close to the trailing edge the higher pressure at the lower surface

forces the airflow to decelerate and the lower pressure at the upper surface causes the airflow there to accelerate. Both airflows meet at the trailing edge causing an additional compression shock wave that will allow for the pressure to achieve a free stream pressure.

As before, it is believe that the reason for only achieving an average residual is either because of having a detached compression wave that could be pulsating in an unsteady way or because having such a fine grid where the shock is slightly moving and causing this frequency in the results.

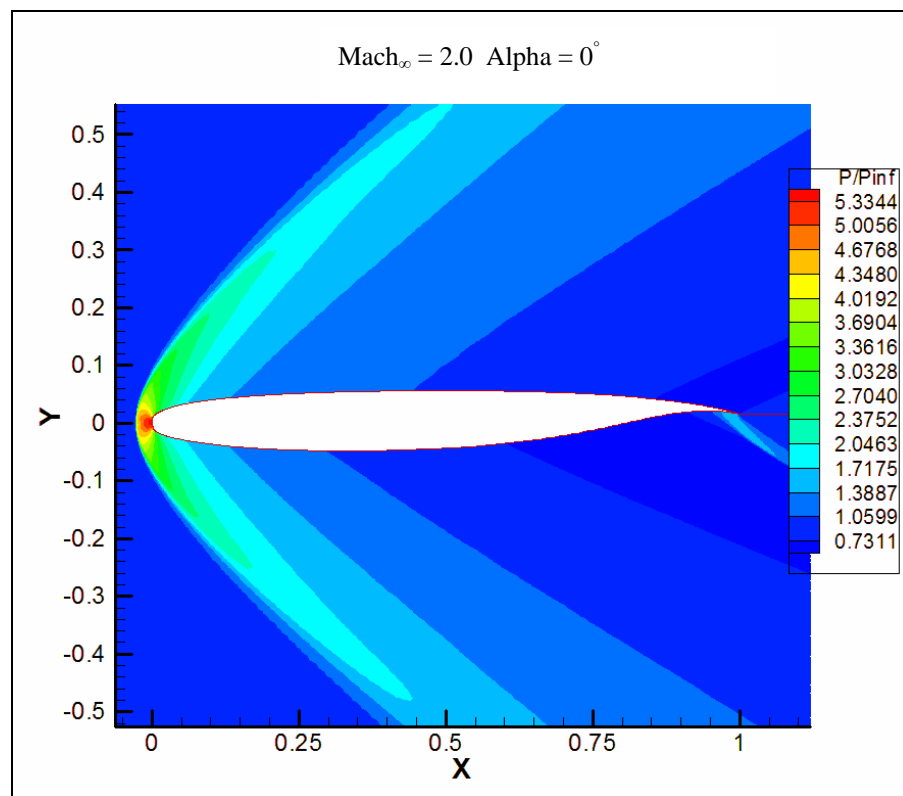


**Figure 3.69 Pressure Ratio Contour around K2 airfoil**

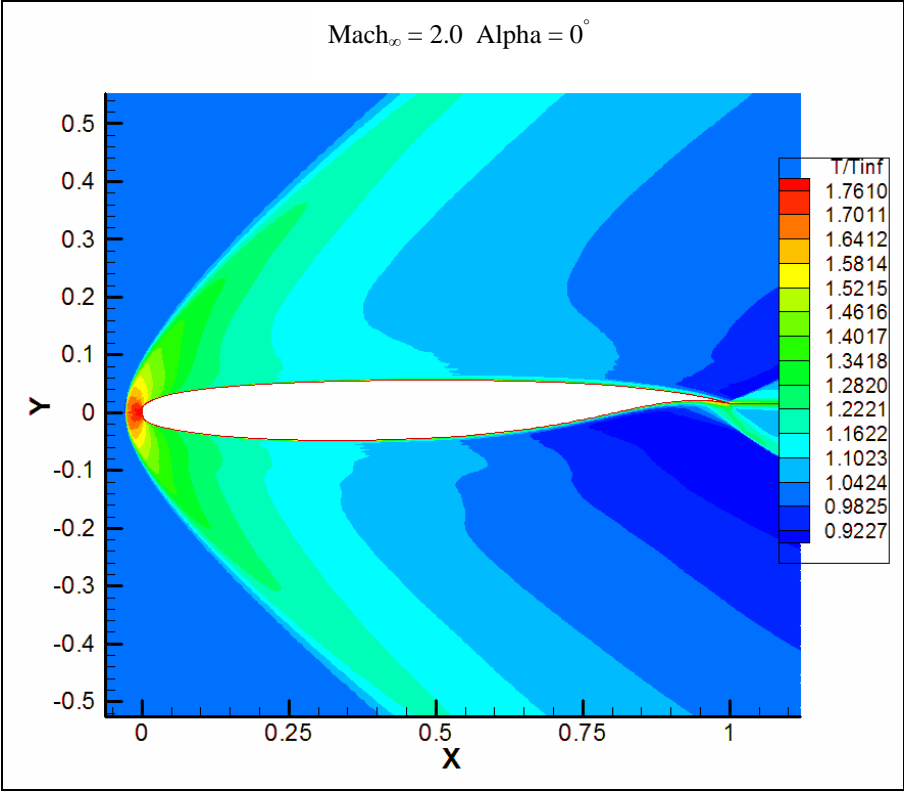


**Figure 3.70 Temperature Ratio Contour around K2 airfoil**

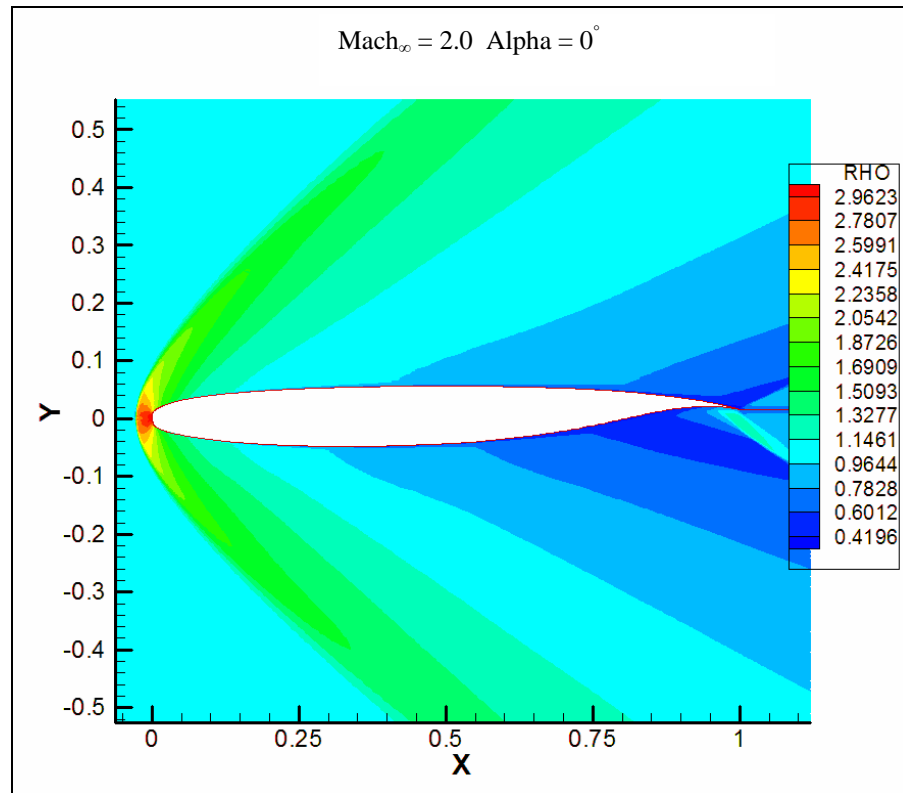


**Figure 3.71 Density Ratio Contour around K2 airfoil**

Follow the perfect gas law, both the density and temperature ratio contours in Figure 3.70 and 3.71 will increase or decrease accordingly. The increase in temperature and density in leading edge of the airfoil is a consequence of the compression shock wave. Also the increase in pressure along the trailing edge at the lower surface will cause an increase in both the temperature and the density.

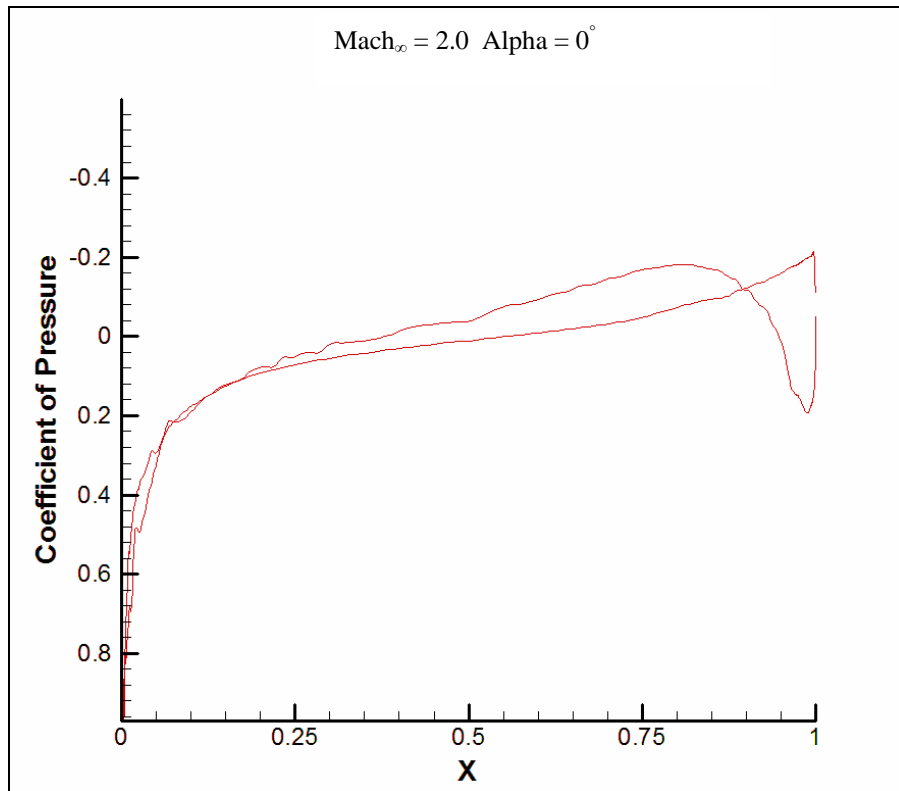


**Figure 3.72 Coefficient of Pressure around K2 airfoil**

Figure 3.72 shows the coefficient of pressure for the K2 airfoil at a Mach number of 2.0. At supersonic speeds, the coefficient of pressure will be positive due to an increase in pressure after the shock wave. Due to the design of this airfoil, a negative coefficient of pressure is observed after the center of the airfoil which indicates a favorable pressure gradient for an increase in Mach number and a decrease in temperature and density.

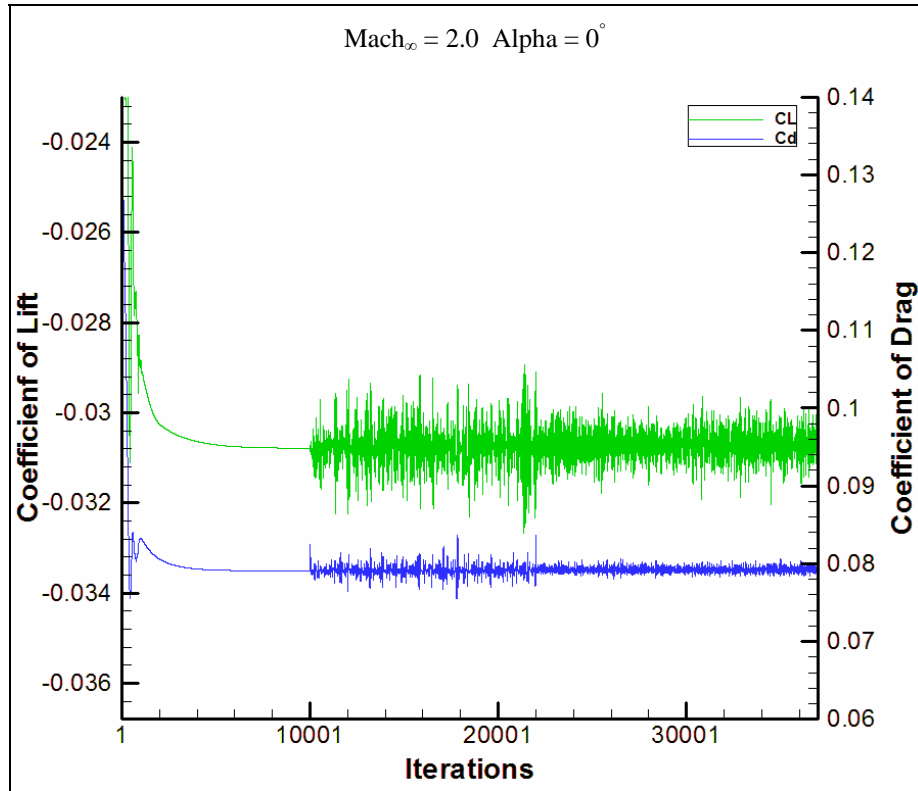


**Figure 3.73 Coefficient of Lift and Drag Convergence for K2 airfoil**

Figure 3.73 shows the average convergence for the coefficient of lift and coefficient of drag. For this run, the coefficient of lift is -0.03013 and the coefficient of drag of 0.07927. As explained before, the noise in the results is believed to be caused by the program, the grid that is analyzed, and/or because of trying to achieve a steady result for an unsteady case. A slightly negative lift is the result of a curved shock wave forming at the leading edge and creating a higher pressure area at the upper surface than at the lower surface as can be seen in Fig. 3.69.

### 3.3.5 Mach 3.0

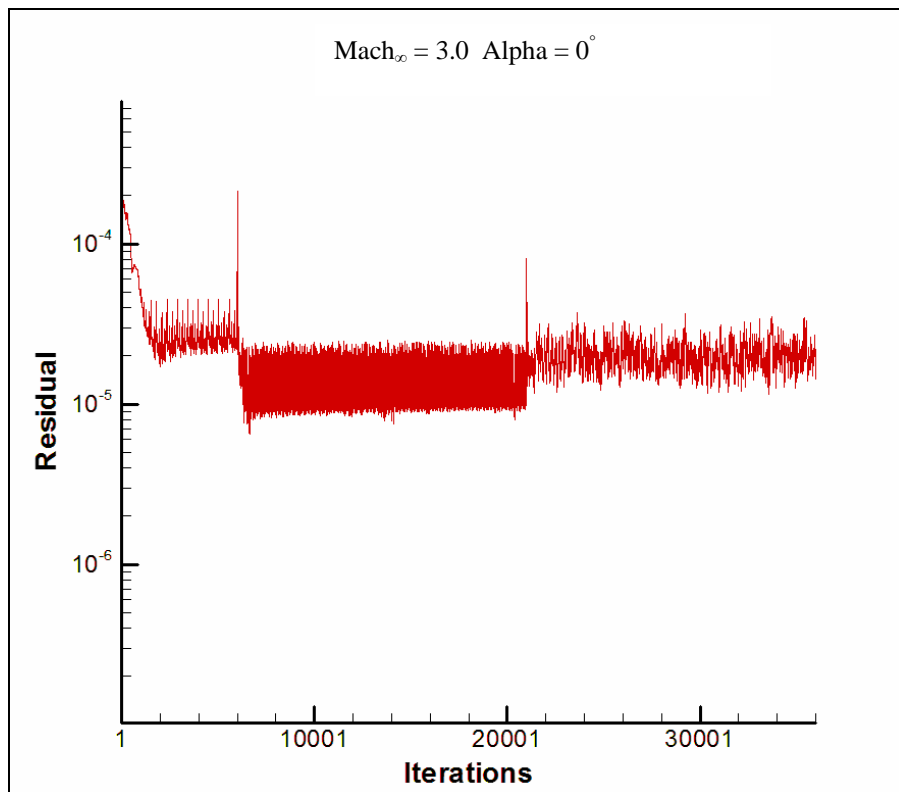


**Figure 3.74 Residual for K2 airfoil from CFL3D**

The first step before analyzing all the flow characteristics and properties is to determine the level of convergence in the results. For this case the 257 by 159 grid level was allowed to converge for 6000 iterations. Then the program passed to the finer 513 by 257 level for

15000 iterations and at the end it went to the finest 1025 by 513 grid level with 15000 iterations. As shown in Figure 3.74, the results obtained represent an average that is around an accuracy of 4 decimal places.

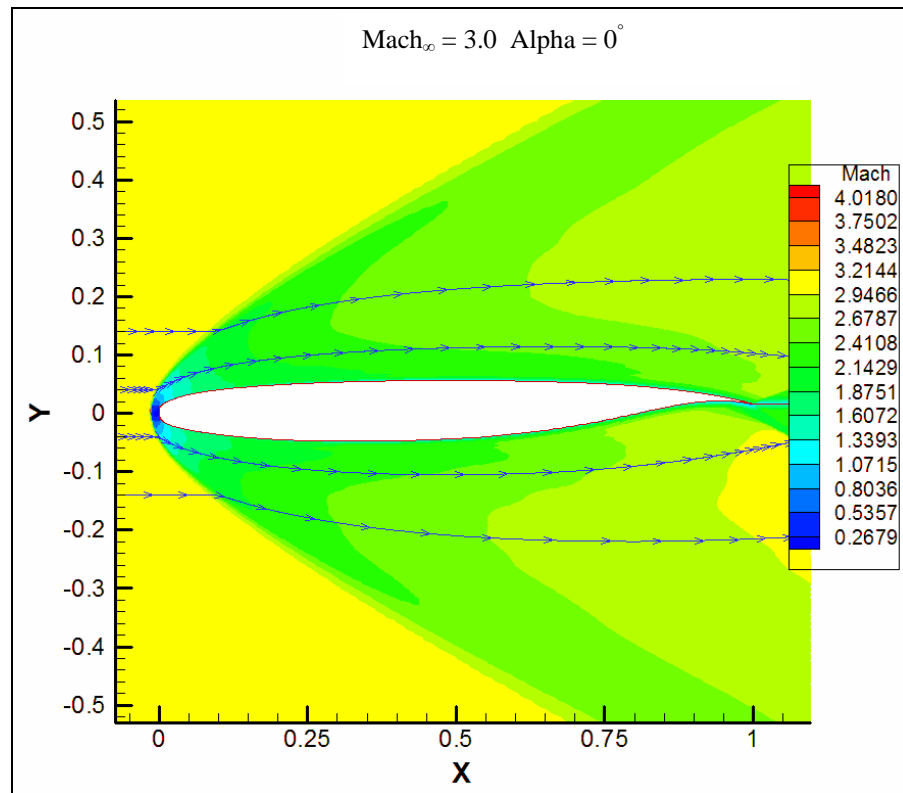


**Figure 3.75 Mach 3.0 Contour around K2 airfoil**

Figure 3.75 shows the mach contours for a free stream Mach number of 3.0 and a Reynolds number of 69 million. Given that the free stream speed is supersonic, a compression shock wave is formed at the leading edge of the airfoil that is also detached from the surface. As for a Mach number of 2.0, the flow achieves a higher mach number at the lower surface than

at the upper surface due to a favorable pressure gradient as it can be seen in Figure 3.76. As it gets close to the trailing edge the higher pressure at the lower surface forces the airflow to decelerate and the lower pressure at the upper surface causes the airflow there to accelerate. Both airflows meet at the trailing edge causing an additional compression shock wave that will allow for the pressure to achieve a free stream pressure.

As before, it is believe that the reason for only achieving an average residual is either because of having a detached compression wave that could be pulsating in an unsteady way or because having such a fine grid where the shock is slightly moving and causing this frequency in the results.

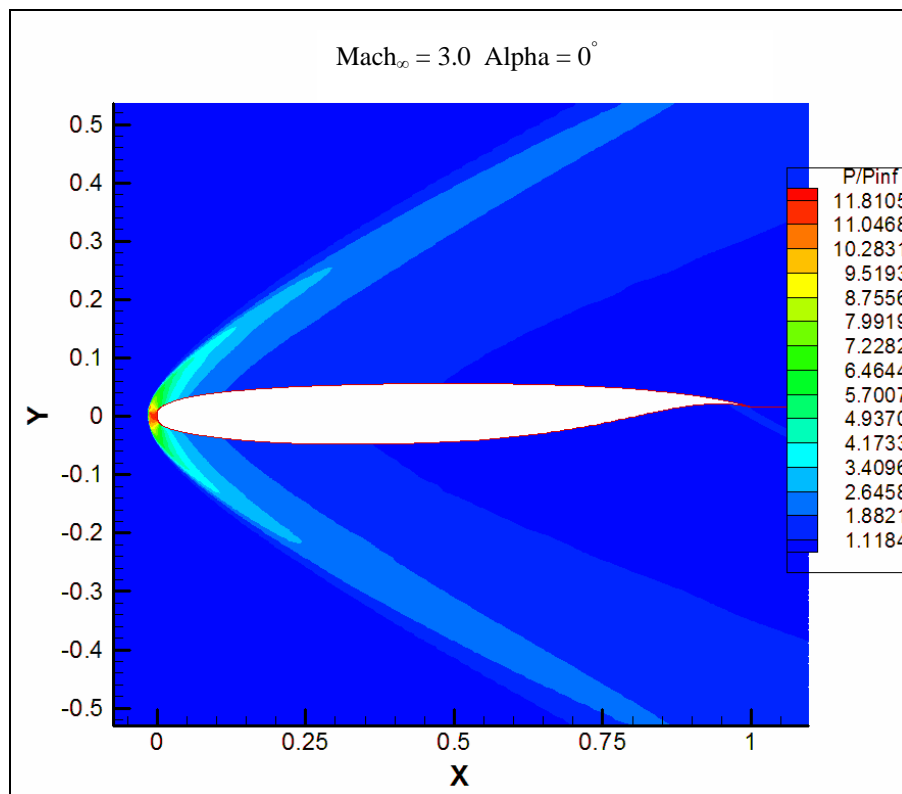


**Figure 3.76 Pressure Ratio Contour around K2 airfoil**

One important change to notice in Figure 3.76 is the high pressure ratio that is achieved at the leading edge of the airfoil. The high pressure ratio will also cause a high temperature ratio and density ratio which are important to take into account when designing an airfoil and selecting the material to use for making the airfoil.

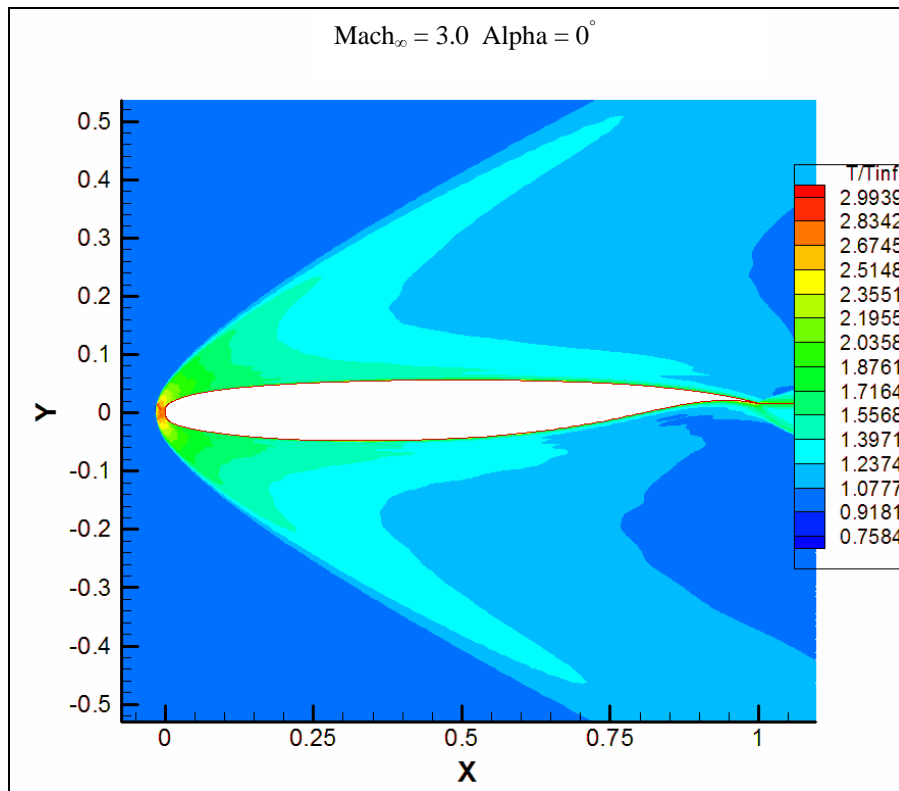


**Figure 3.77 Temperature Ratio Contour around K2 airfoil**

Figures 3.77 and Figure 3.78 shows temperature ratio and density ratio contours around the airfoil. It can be seen in Figure 3.78 that the air density at the leading edge is around four times higher than the free stream density with a temperature that is about three times higher.

Given that the free stream temperature is 288.15K, the leading edge will experience a temperature of 864.45K or 1096.34 Fahrenheit.

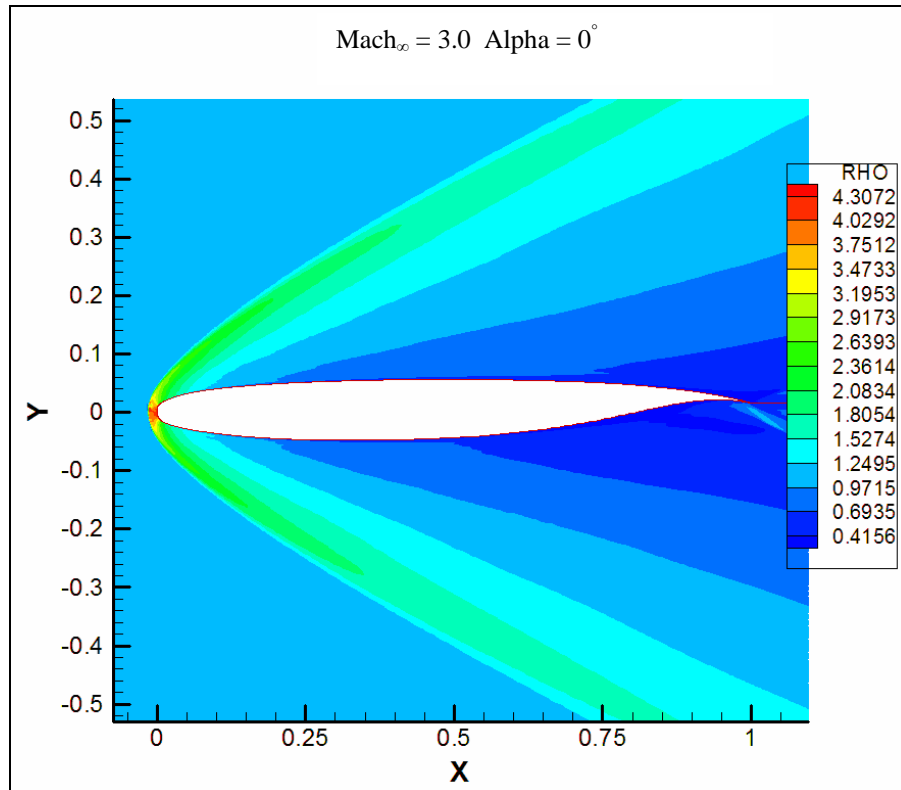


**Figure 3.78 Density Ratio Contour around K2 airfoil**

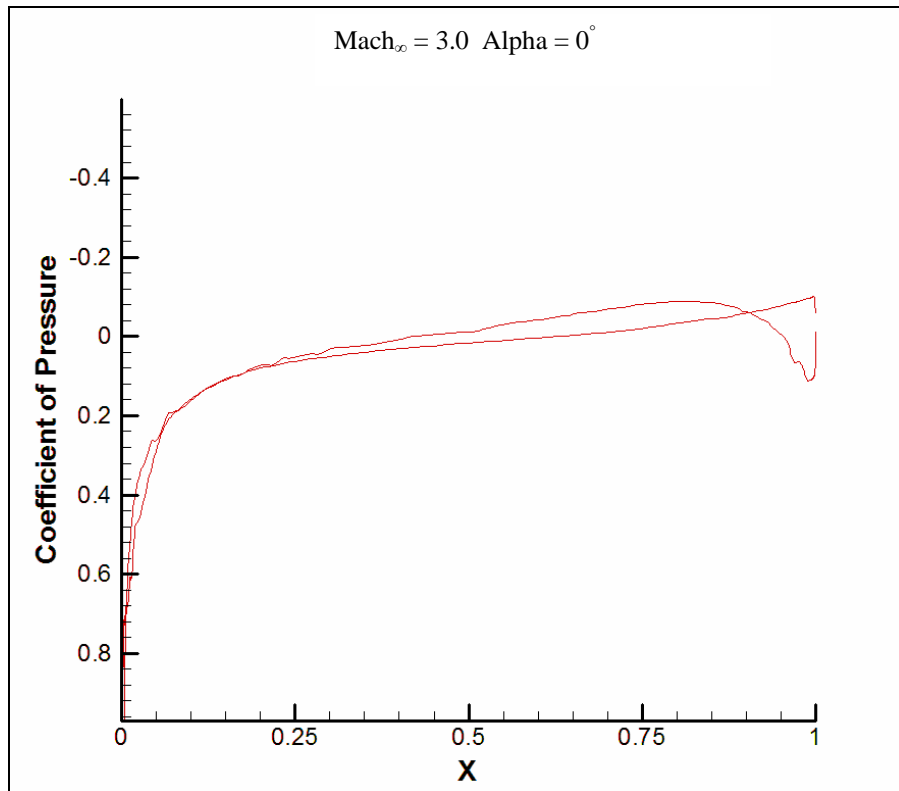


**Figure 3.79 Coefficient of Pressure around K2 airfoil**

Figure 3.79 shows the coefficient of pressure for the K2 airfoil at a Mach number of 3.0. As before, at supersonic speeds, the coefficient of pressure will be positive due to an increase in pressure after the shock wave. At this Mach number, the coefficient of pressure stays close to zero after 0.25 of the chord down from the leading edge. The change in coefficient of pressure close trailing edge is due to a high pressure at the lower surface compared to the upper surface.

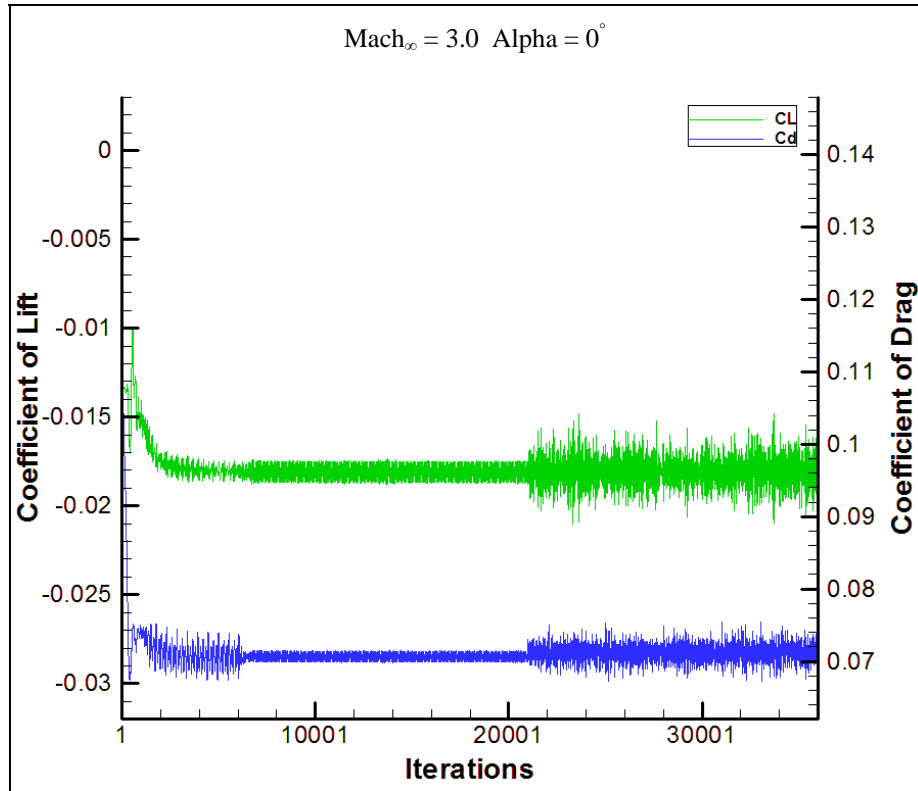


**Figure 3.80 Coefficient of Lift and Drag Convergence for K2 airfoil**

Figure 3.80 shows the coefficient of lift and the coefficient of drag convergence at a Mach number of 3.0. Although both coefficients are changing along the iterations, there is an average of -0.01745 for the coefficient of lift and 0.07123 for the coefficient of drag.

### 3.3.6 Entropy Generation Rate Comparison

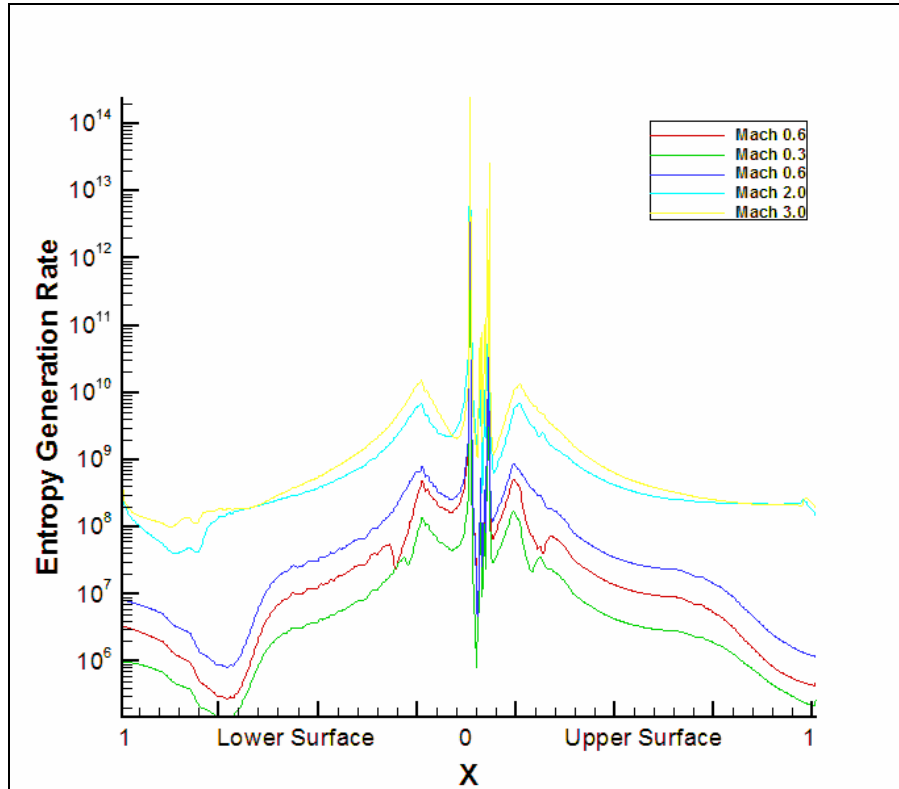


Figure 3.81 Entropy Generation Rate ( $\frac{W}{m^3 K}$ ) around K2 airfoil

Figure 3.81 shows the entropy generation rate per unit span caused one meter around the leading edge, the upper surface and the lower surface only. It does not show the entropy generated after the trailing edge.

Figure 3.81 shows the entropy generation rate per unit volume caused by the K2 airfoil at different Mach numbers from subsonic to supersonic speeds. The X-position of one is located at the trailing edge and the X-position of zero is the leading edge of the airfoil. As it

is expected for the space that is analyzed, the maximum entropy generation is caused at the leading edge where there are large changes in the velocity and temperature of the flow. The flow goes from the free stream Mach number to a stagnant point at the leading edge which will cause the entropy generation drop due to the zero velocity terms but with a generation due to the rise in temperature and density. As it is expected the least amount of entropy generation rate is caused by the slowest Mach number of 0.3.

One important point to notice is the difference in entropy generation rate produce for the two cases that have similar Mach numbers. The first case, which has a lower temperature, has a lower entropy generation rate than the third case that has the same Mach number but with a higher temperature.

Another peculiar characteristic is the decrease in entropy generation rate close to the trailing edge at the lower surface. This decrease in entropy generation is caused by having a favorable pressure gradient at that zone which increase the speed and lowered both the temperature and the density. Although there is a decrease in entropy generation rate, as the flow gets to the trailing edge, the entropy generation rate increases due to the compression shock that occurs at the trailing edge because of an increase in pressure and temperature.

The two highest entropy generation rates are caused by the highest Mach numbers of 2.0 and 3.0. As it was expected, more entropy is generated due to the compression shock that form at the leading edge of the airfoil. The compression shock wave causes an almost instantaneous change in velocity gradients and an increase in temperature which will drive the increase in entropy generated.

### 3.4 Whitcomb Integral Supercritical Airfoil

Four cases were run for the Whitcomb Integral Supercritical Airfoil. The four cases consisted of a Mach number of 0.3, 0.6, 2.0, and 3.0. Numerical results for the case of a Mach number of 0.6 is compared with experimental data. Although the report does not specify the temperature at the facilities used to take the data, CFL3D is run assuming a standard atmospheric temperature of 288.15K.

#### 3.4.1 Mach 0.3

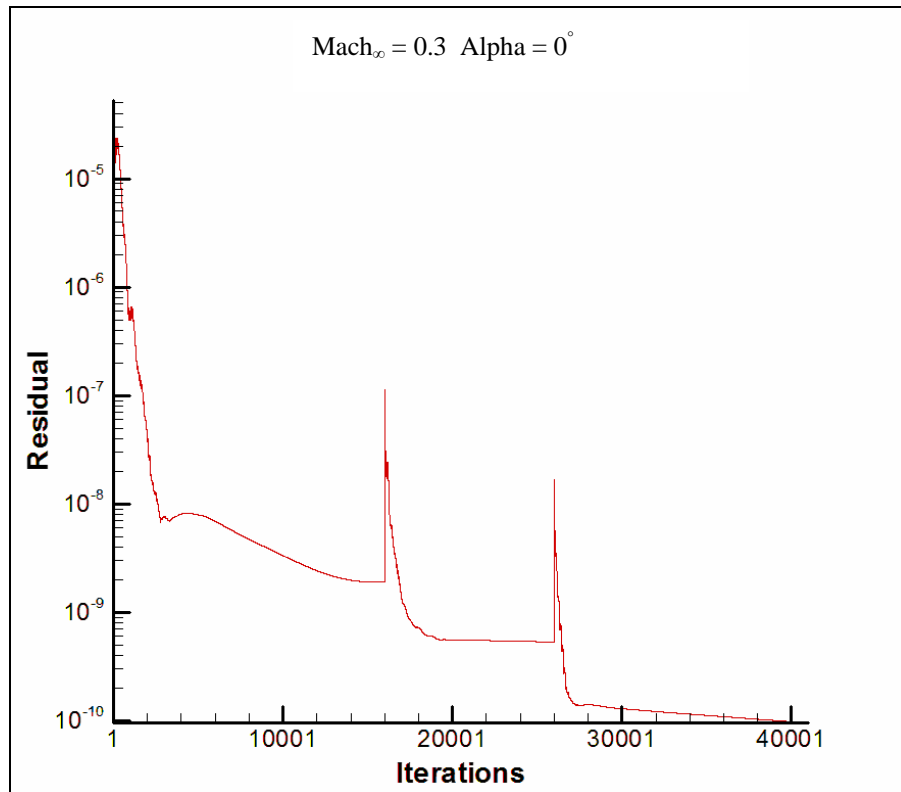
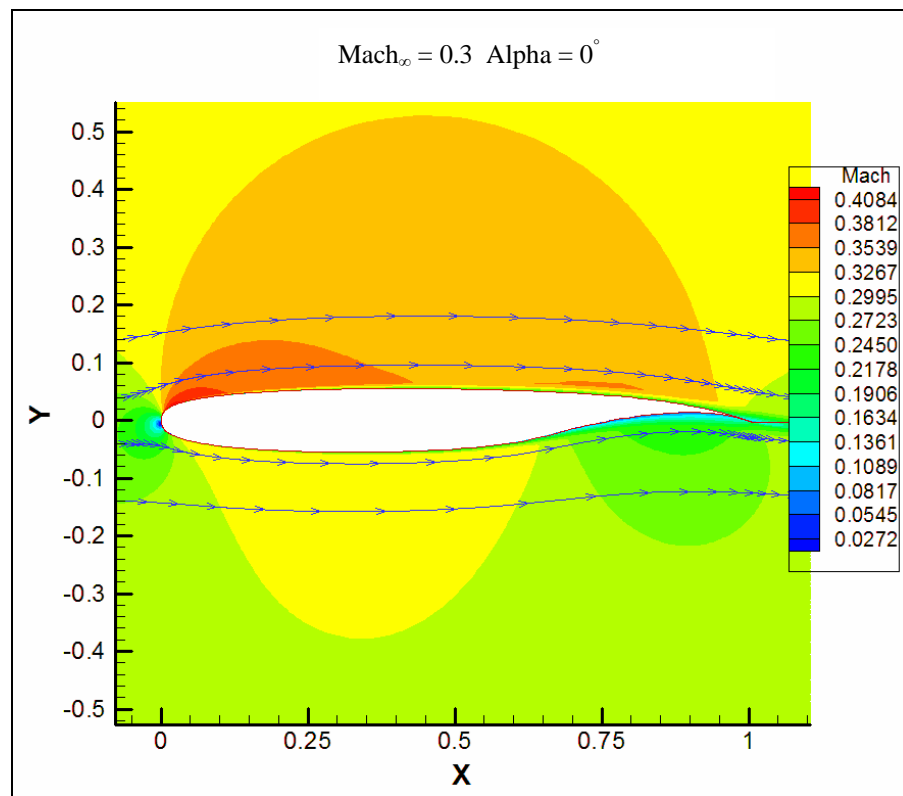


Figure 3.82 Residual for Whitcomb airfoil from CFL3D

Figure 3.82 shows the level of convergence which correspond to the accuracy that is expected in the results. This case as well as all the other cases analyzed in this thesis started with a coarse 257 by 159 grid level then it went to a finer 513 by 257 grid level and ended at the finest 1025 by 513 grid level. The 257 by 159 grid level was allowed to converge for 16000 iterations. Then the program passed to the finer 513 by 257 level for 10000 iterations and at the end it went to the finest 1025 by 513 level with 15000 iterations. An accuracy of 10 decimal places is expected in the results given this residual.



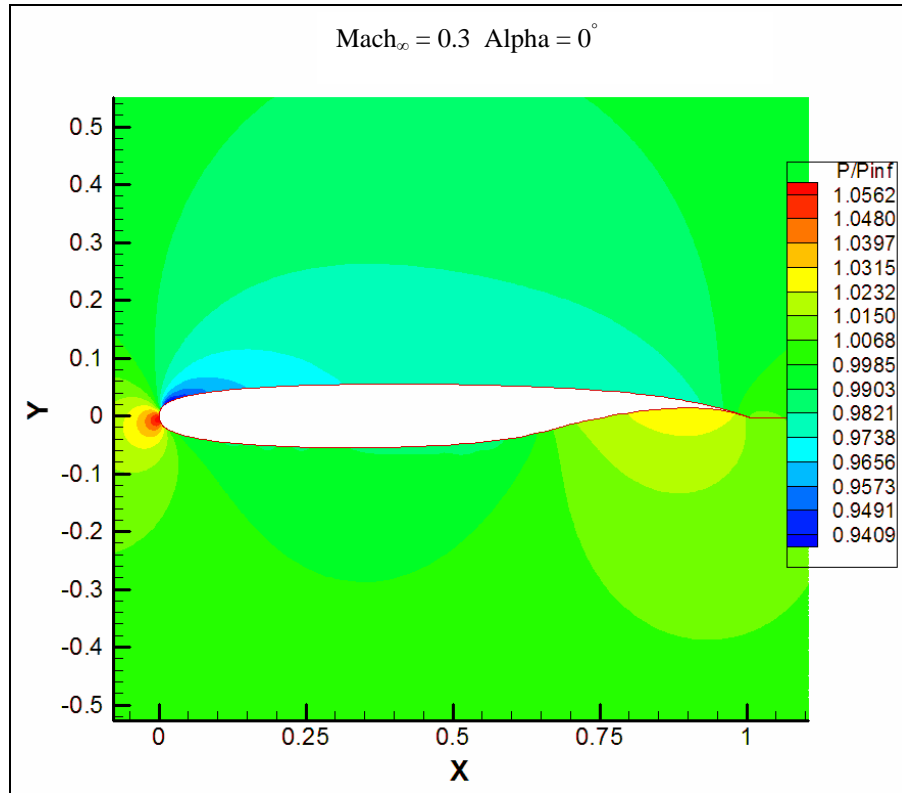
**Figure 3.83 Mach 0.3 Contour around Whitcomb airfoil**

Figure 3.83 shows the mach contours around the Whitcomb airfoil with a free stream speed of Mach 0.3 and a Reynolds number of 6.9 million.

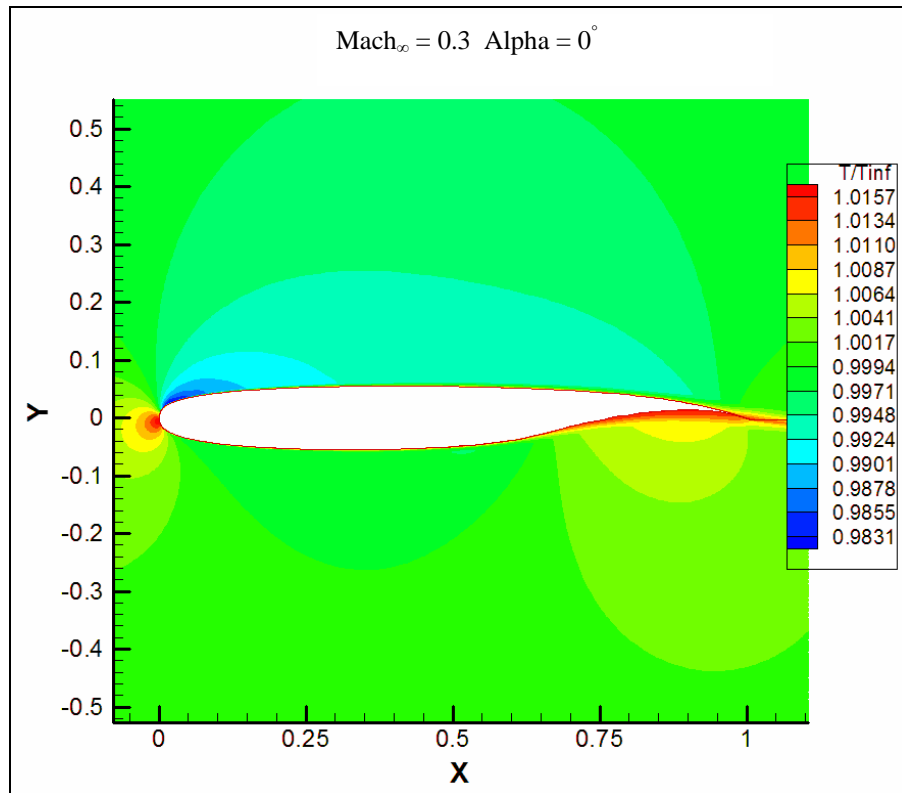
The flow goes over, under or it reaches the stagnation point at the leading edge of the airfoil. It can be seen how the flow reaches a higher speed at the upper surface and for a longer distance than in the lower surface. The maximum airflow is found around the first quarter of the after the leading edge on the upper surface. One important characteristic to notice is the deceleration that occurs on the last quarter along the lower surface which is caused by an increase in pressure in that area as can be seen in Figure 3.84

This acceleration in speed is due to a decrease in pressure caused by the curvature of the airfoil. Figure 3.84 shows the pressure ratio between the local pressure and the free stream pressure. It shows how the pressure decreases on both the upper and lower surface but remains constant for a longer length along the upper surface, limiting the increases in speed towards sonic speed.

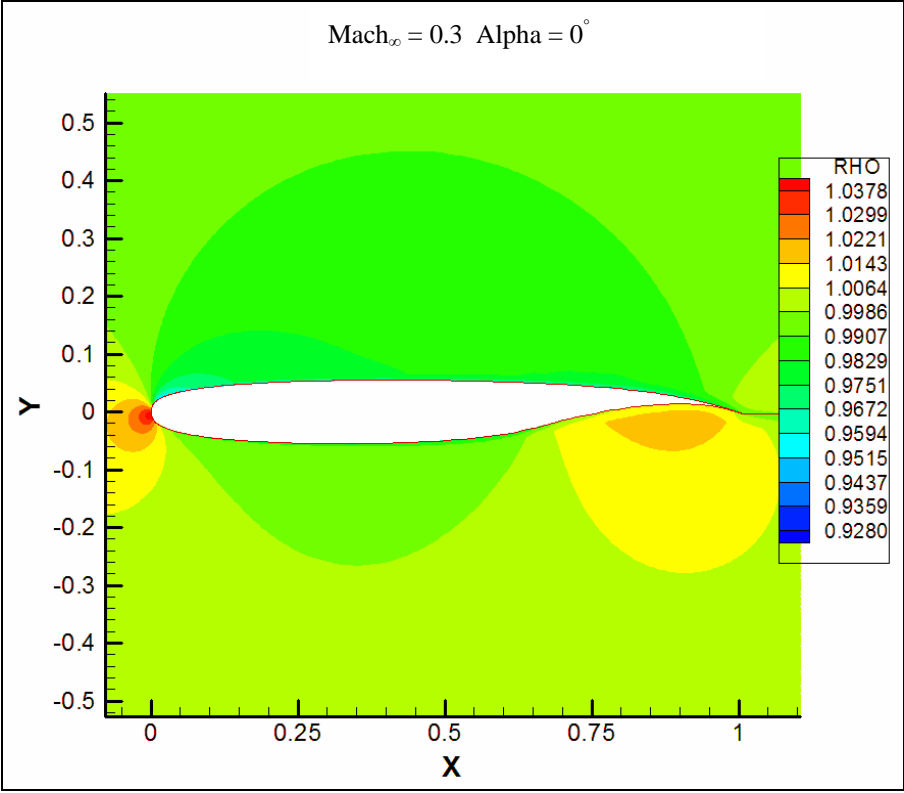
Figure 3.85 shows the temperature ratio contours around the Whitcomb airfoil at a Mach number of 0.3. Given that this Mach number is the lower limit when considering compressible flow, the temperature increase at the nose is close to one which will coincide with a slight 3.78% increase in density as shown in Figure 3.86. As shown in Figure 3.85, there is a higher temperature at the trailing edge of the lower surface when compared to the trailing edge at the upper surface. This is in agreement with the higher pressure at that zone and with also the higher density.



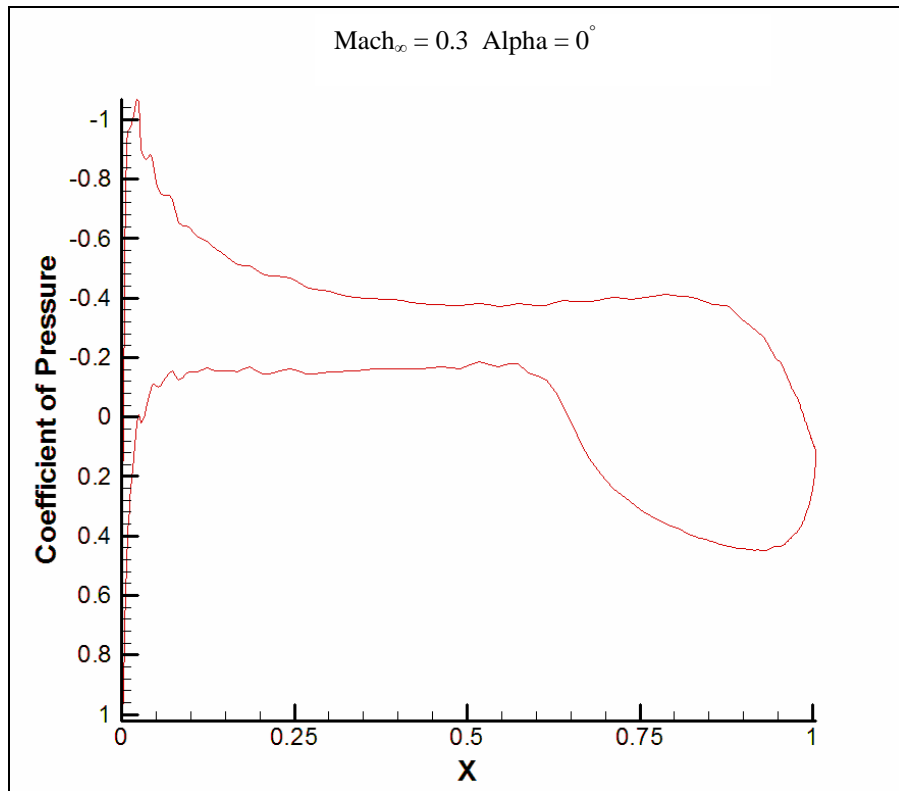
**Figure 3.84 Pressure Ratio Contour around Whitcomb airfoil**



**Figure 3.85 Temperature Ratio Contour around Whitcomb airfoil**

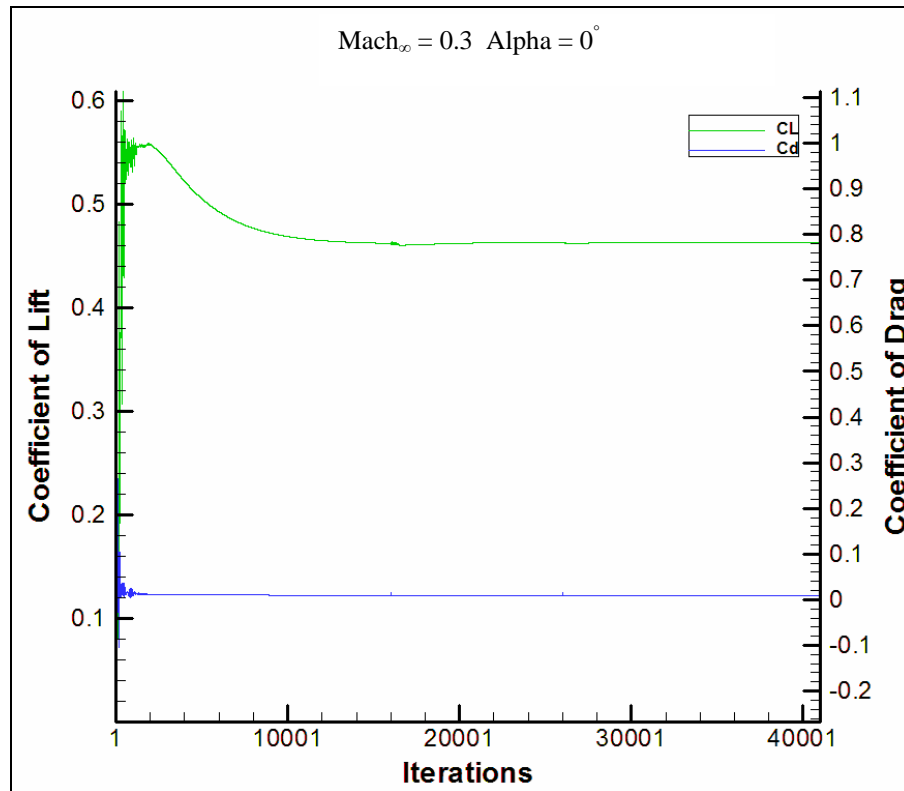


**Figure 3.86 Density Ratio Contour around Whitcomb airfoil**



**Figure 3.87 Coefficient of Pressure around Whitcomb airfoil**

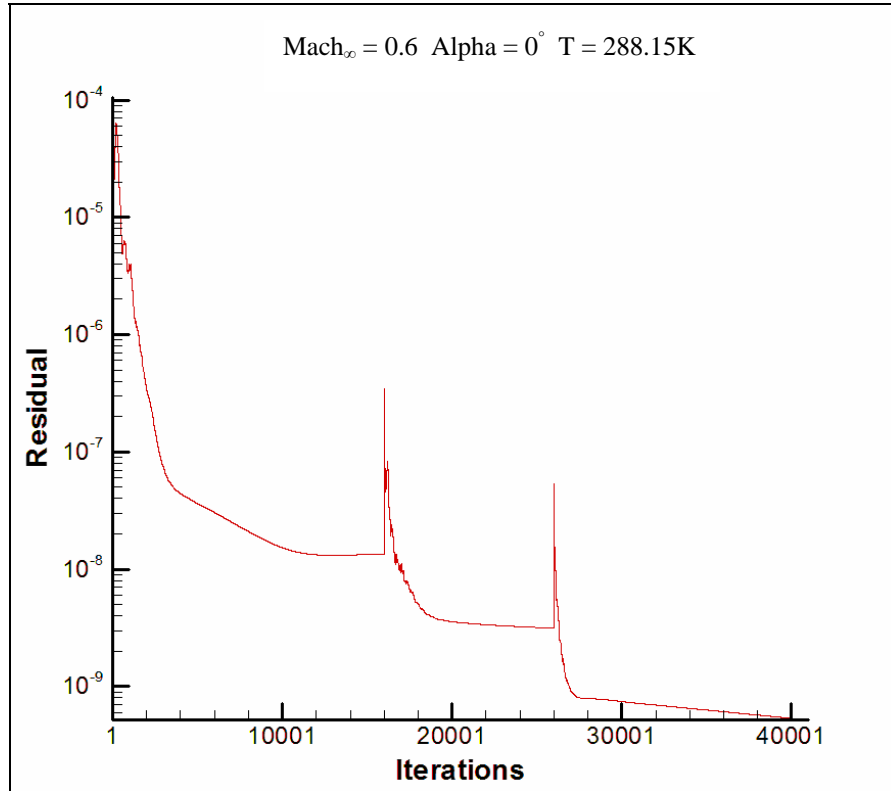
Figure 3.87 shows the coefficient of pressure around the Whitcomb airfoil with the higher curve corresponding to the upper surface and the lower curve corresponding to the lower surface. One important feature is the extension of an almost constant  $-0.4$  coefficient of pressure along the upper surface. This characteristic helps to control the speed changes as the flow goes around the airfoil. As the flow gets closer to the trailing edge, an increasingly larger pressure difference starts to build up between the upper surface and the lower surface which terminates in the creation of vortices when they unite after the trailing edge.



**Figure 3.88 Coefficient of Lift and Drag Convergence around Whitcomb airfoil**

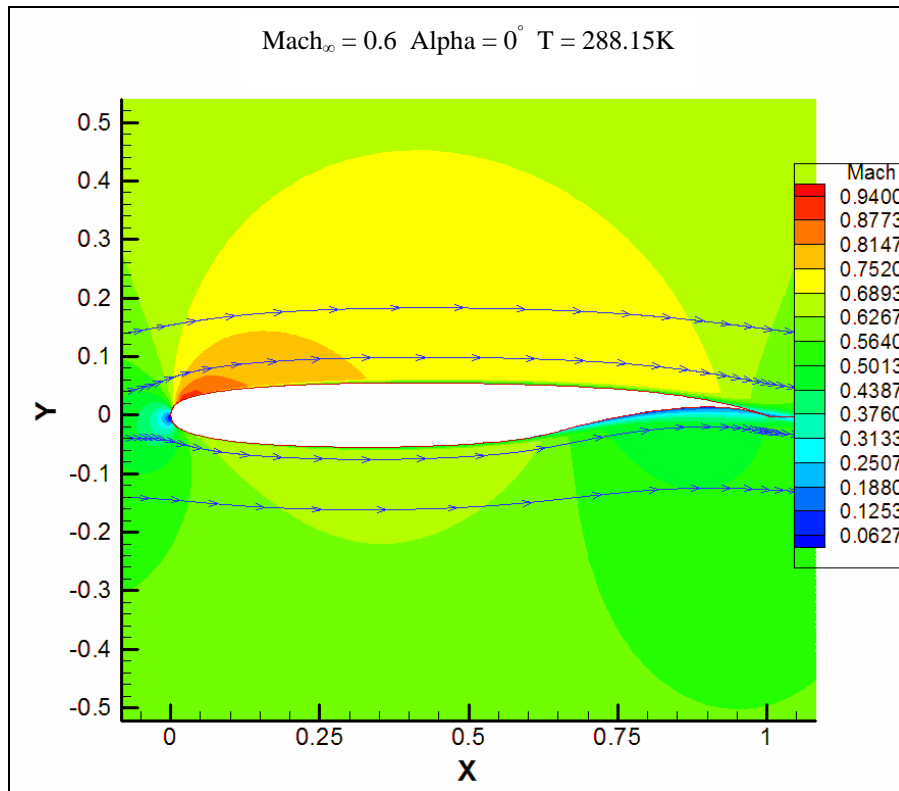
Figure 3.88 shows the convergence for the coefficient of lift and the coefficient of drag. It is important that both the lift and the drag achieves a final value and stays constant as the program goes from the coarser to the finest grid after 41000 iterations. The final converged value for the coefficient of lift is 0.4632 and for the coefficient of drag is 0.008688.

### 3.4.2 Mach 0.6



**Figure 3.89 Residual for Whitcomb airfoil from CFL3D**

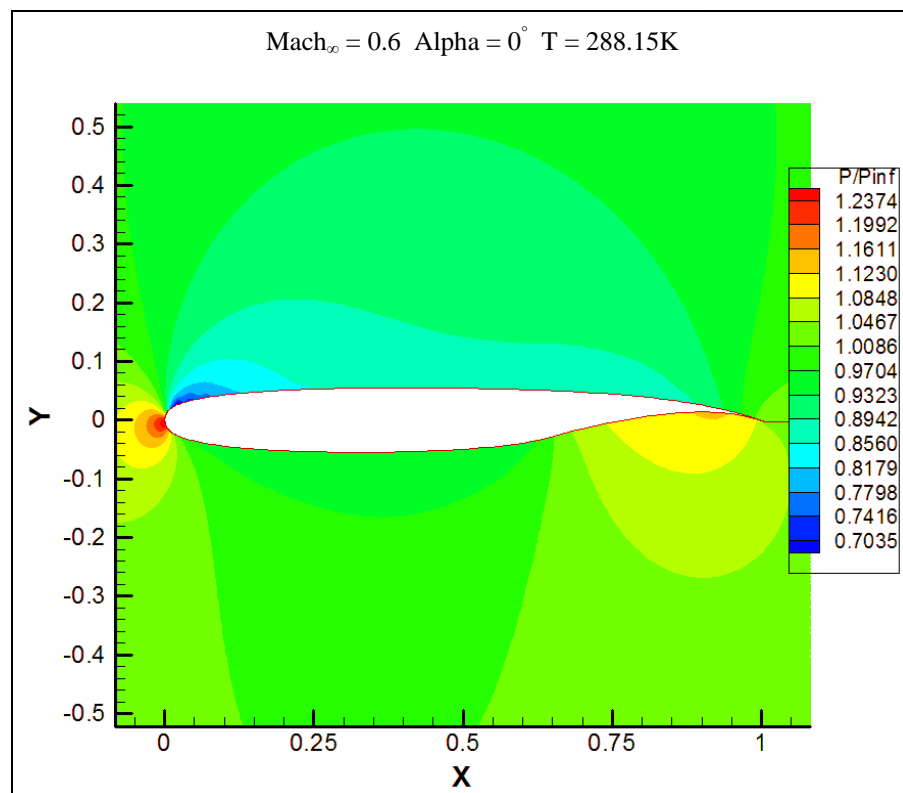
Figure 3.89 shows the residual achieved after 41000 iterations. The 257 by 159 grid level was allowed to converge for 16000 iterations. Then the program passed to the finer 513 by 257 level for 10000 iterations and at the end it went to the finest 1025 by 513 level with 15000 iterations. An accuracy of 9 decimal places is expected in the results given this residual.



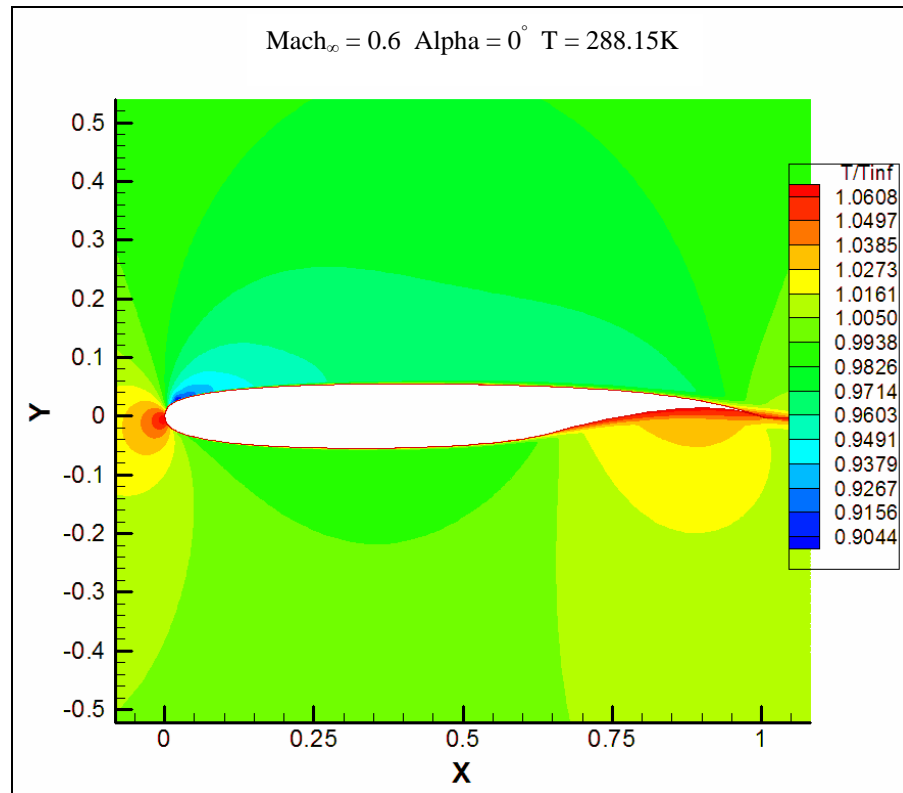
**Figure 3.90 Mach 0.6 Contour around Whitcomb airfoil**

Figure 3.90 shows the results for a free stream Mach number of 0.6 and a Reynolds number of 13.8 million. Just as it occurred in the last case, a maximum speed is achieved at the upper surface close to the leading edge, then it decelerates and stay with a relatively constant speed along the upper surface which is caused by when the pressure ratio stays the same as can be seen in Figure 3.91.

Figure 3.91 shows the decrease in pressure around the leading edge on the upper surface which will cause an increase in Mach number as shown and then an increase in pressure close to the trailing edge on the lower surface which will cause a deceleration in the airflow and a decrease in Mach number.

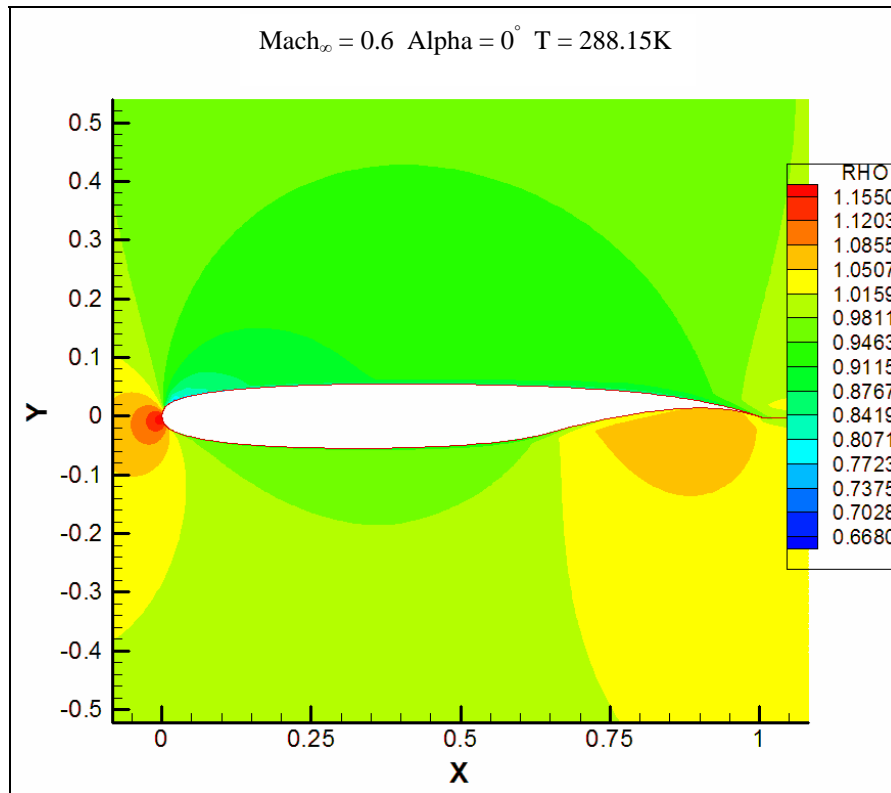


**Figure 3.91 Pressure Ratio Contour around Whitcomb airfoil**



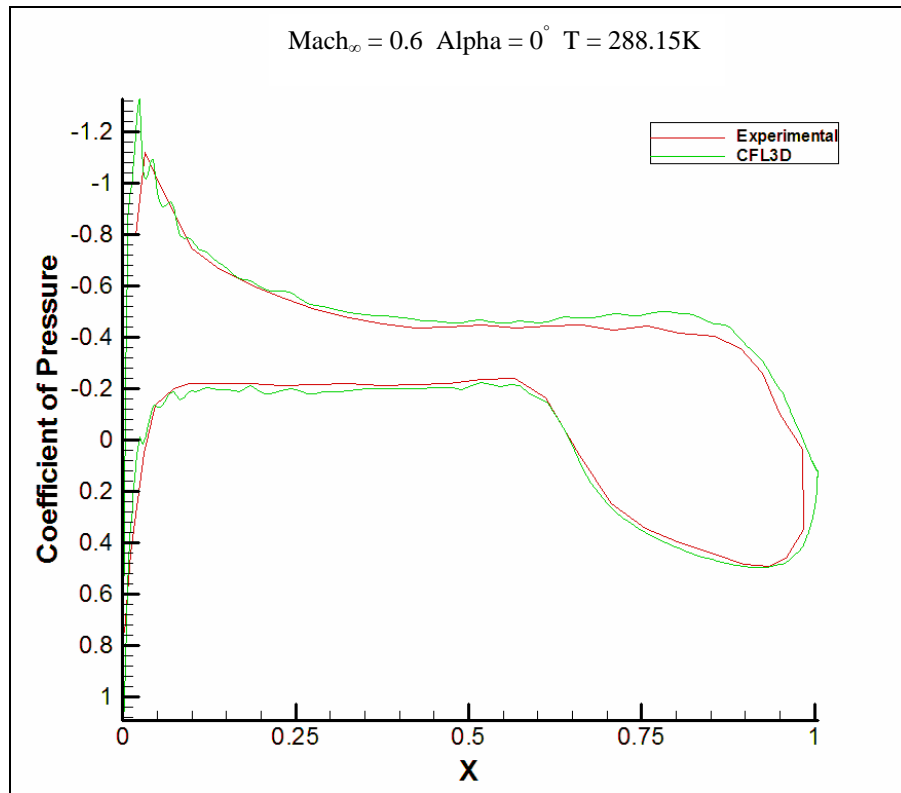
**Figure 3.92 Temperature Ratio Contour around Whitcomb airfoil**

Figure 3.92 and 3.93 shows the decrease in temperature and density on the upper surface close to the leading edge which correspond with a decrease in pressure. Back on the trailing edge along the lower surface, an increase in both temperature and density created by an increase in pressure will cause the flow to decelerate.



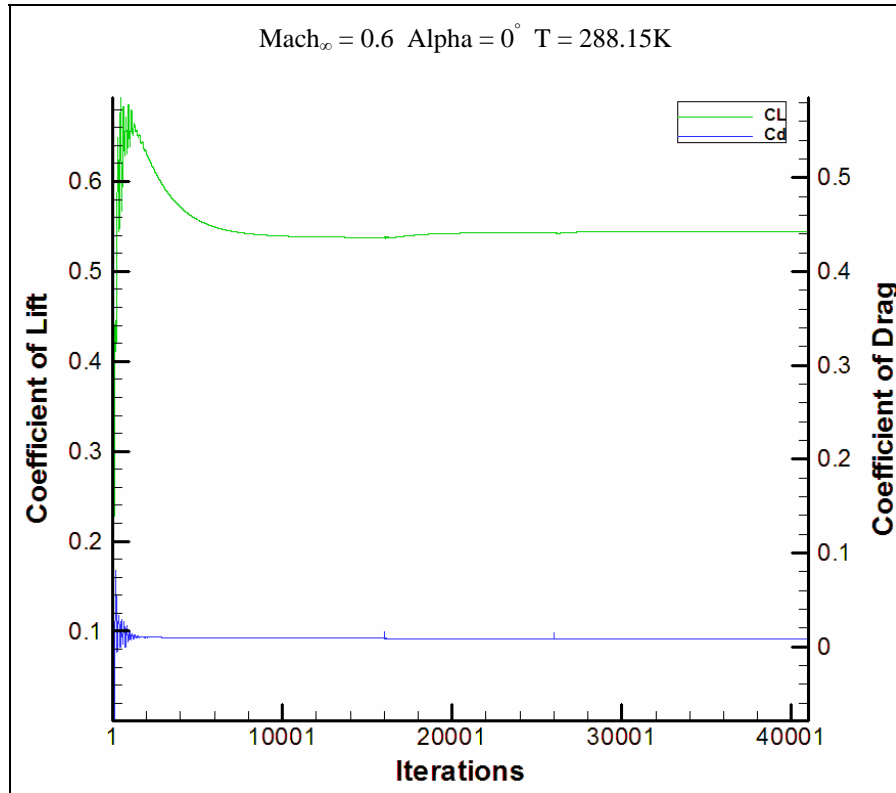
**Figure 3.93 Density Ratio Contour around Whitcomb airfoil**

Figure 3.94 shows the coefficient of pressure comparison between the numerical results output by CFL3D and the experimental data. It is worth noting that the temperature that was used to run the program was the standard atmospheric temperature of 288.15K and that the temperature on the day of the experimental runs could not be found. This comparison between the experimental and the numerical results aids in noticing the error or discrepancies that could be expected. Just as in the last case, the coefficient of pressure stays with an almost zero pressure gradient along both the upper and lower surface along the center of airfoil.



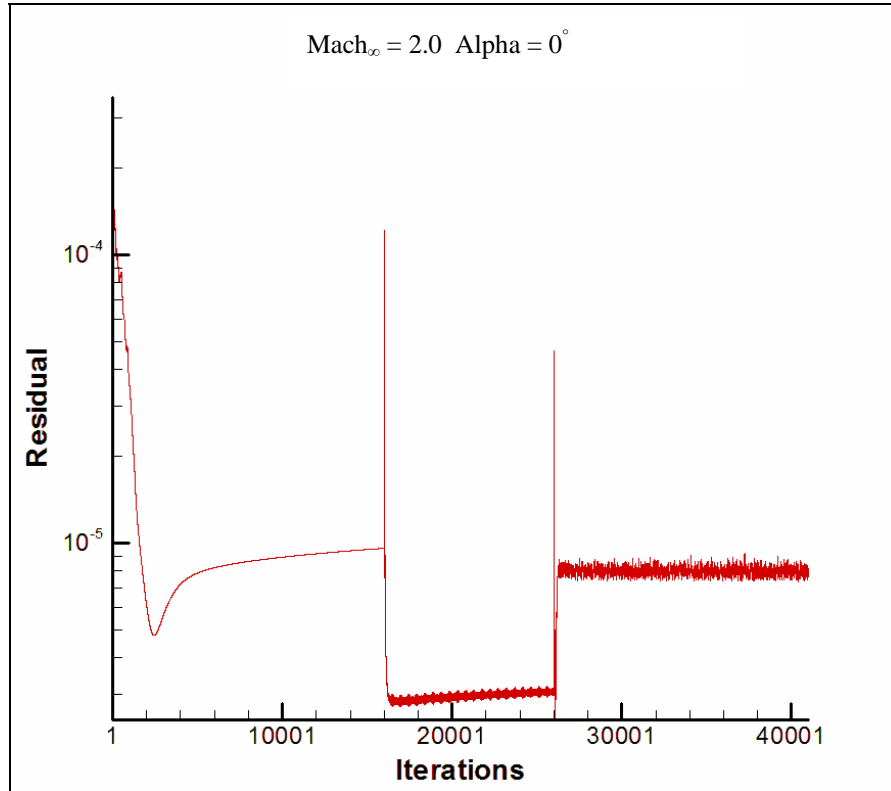
**Figure 3.94 Coefficient of Pressure around Whitcomb airfoil**

As shown in Figure 3.95, the results for both the lift and the drag coefficients converge after the 10000 iterations. The final result obtained for the coefficient of lift is 0.5442 and the final converged result for the coefficient of drag is of 0.008455. If the normal force coefficient in Appendix C.2 is taken as the coefficient of lift, then the results obtained by CFL3D have a difference of 9.94%.



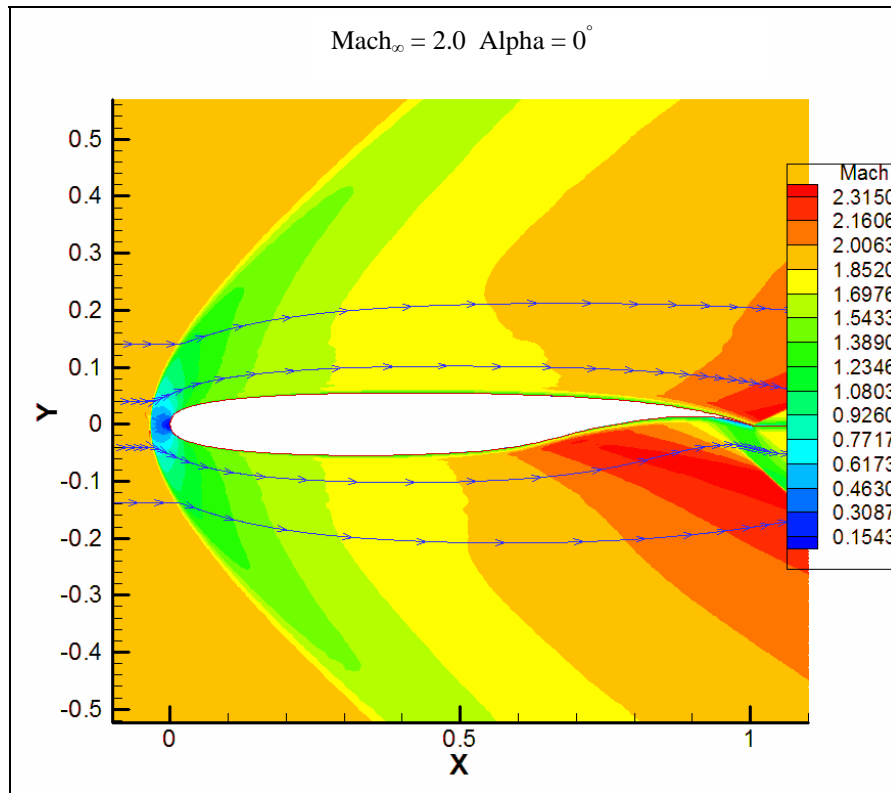
**Figure 3.95 Coefficient of Lift and Drag Convergence for Whitcomb airfoil**

### 3.4.3 Mach 2.0



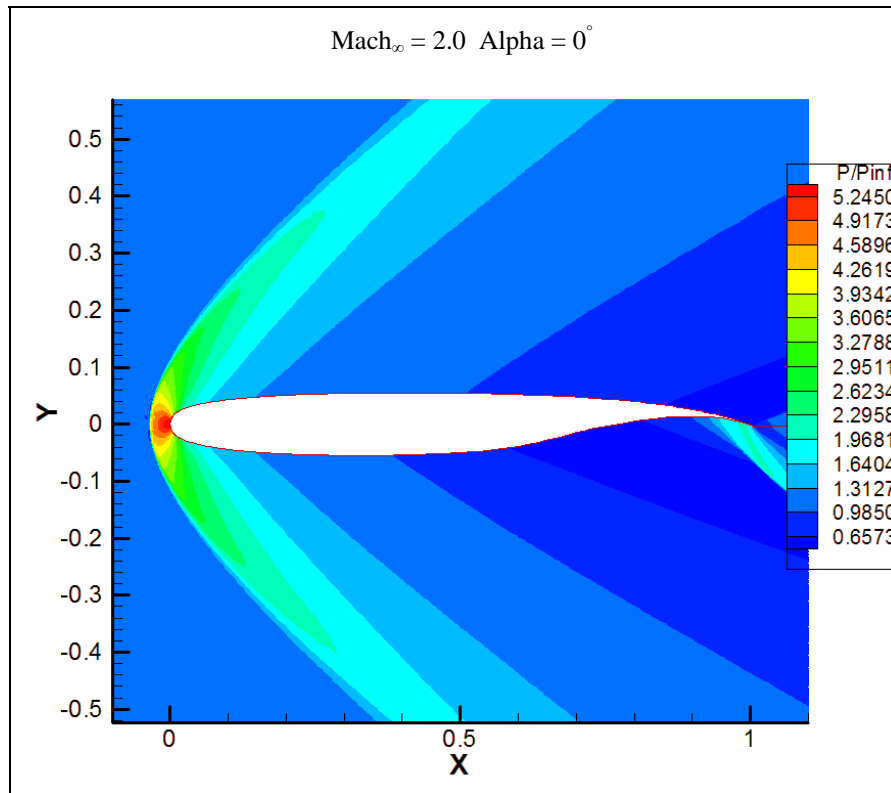
**Figure 3.96 Residual for Whitcomb airfoil from CFL3D**

Figure 3.96 shows the residual achieved after 41000 iterations. The 257 by 159 grid level was allowed to converge for 16000 iterations. Then the program passed to the finer 513 by 257 level for 10000 iterations and at the end it went to the finest 1025 by 513 level with 15000 iterations. An accuracy of 5 decimal places is expected in the results given this residual.



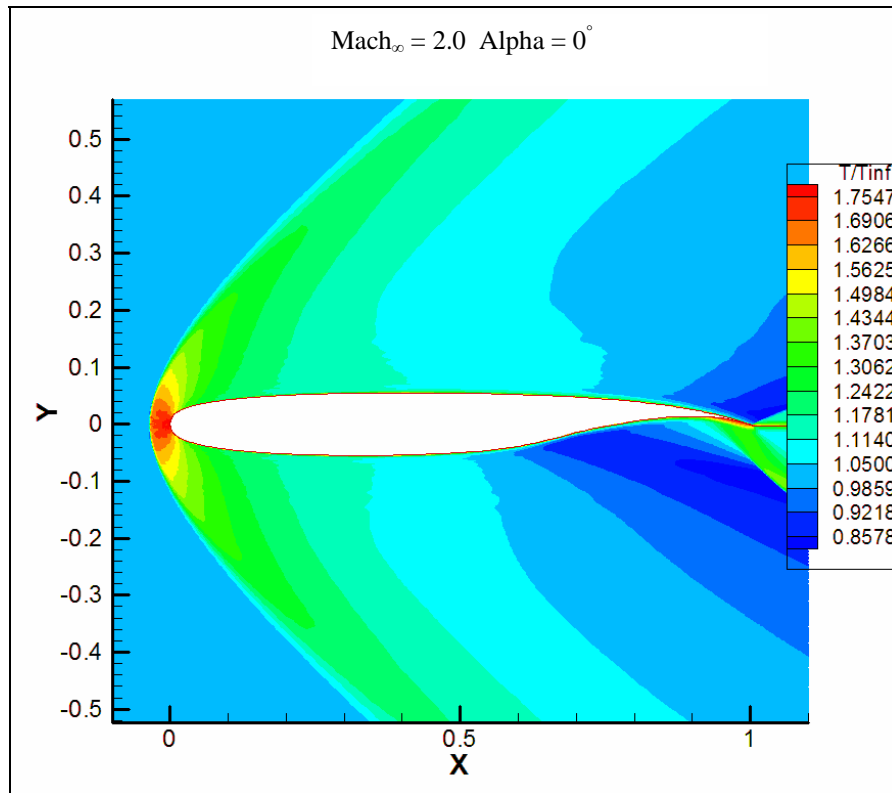
**Figure 3.97 Mach 2.0 Contour around Whitcomb airfoil**

Figure 3.97 shows a supersonic 2.0 Mach contour around the Whitcomb airfoil with a Reynolds number of 46 million. As it occurred in the K2 airfoil at supersonic speeds, the flow along the first half of the airfoil is relatively similar on both the upper and lower curve. Then, the on the lower surface accelerates due to a decrease in pressure as shown in Figure 3.98 and then a strong deceleration cause by an increase in pressure. This increase in pressure will also increase the temperature and density.

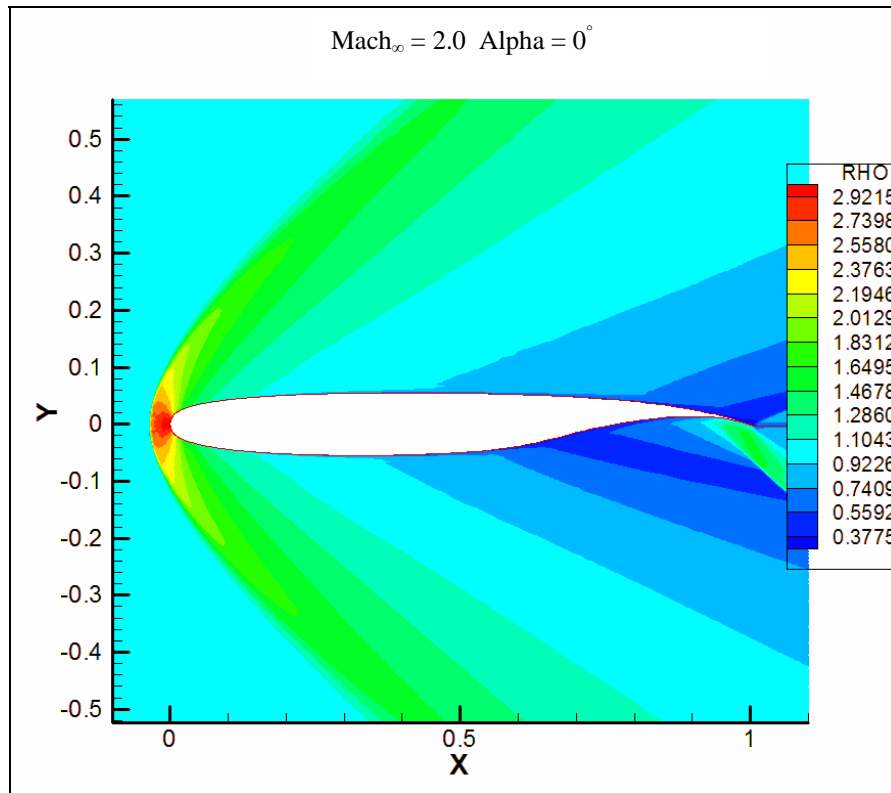


**Figure 3.98 Pressure Ratio Contour around Whitcomb airfoil**

Figures 3.99 and Figure 3.100 shows temperature ratio and density ratio contours around the airfoil. It can be seen in Figure 3.100 that the air density at the leading edge is around three times higher than the free stream density with a temperature that is about two times higher.



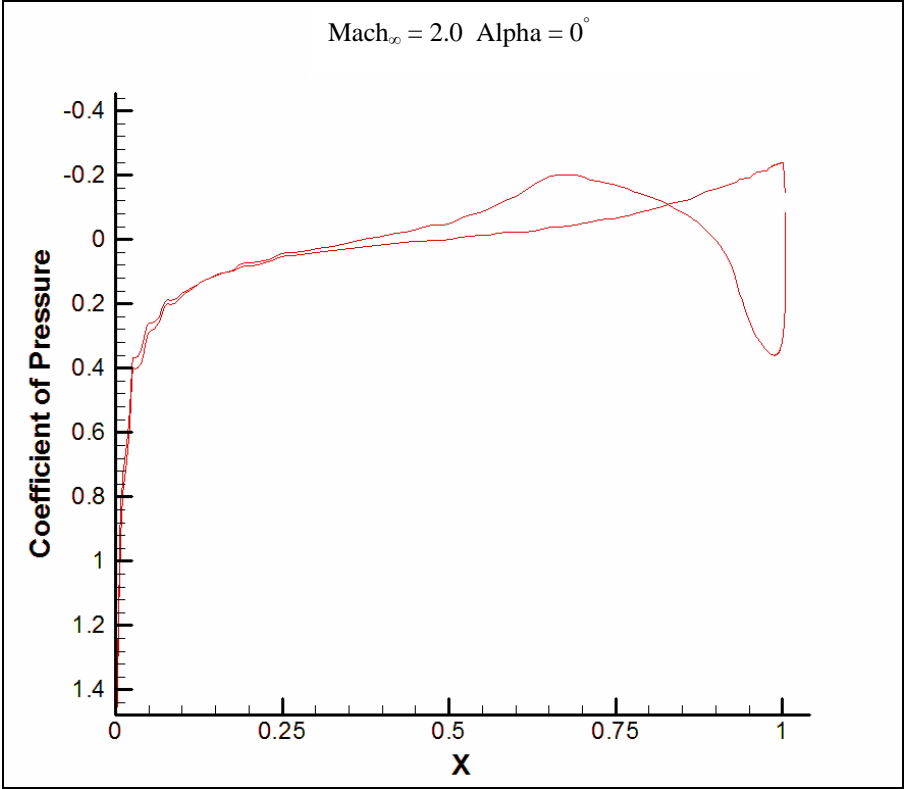
**Figure 3.99 Temperature Ratio Contour around Whitcomb airfoil**



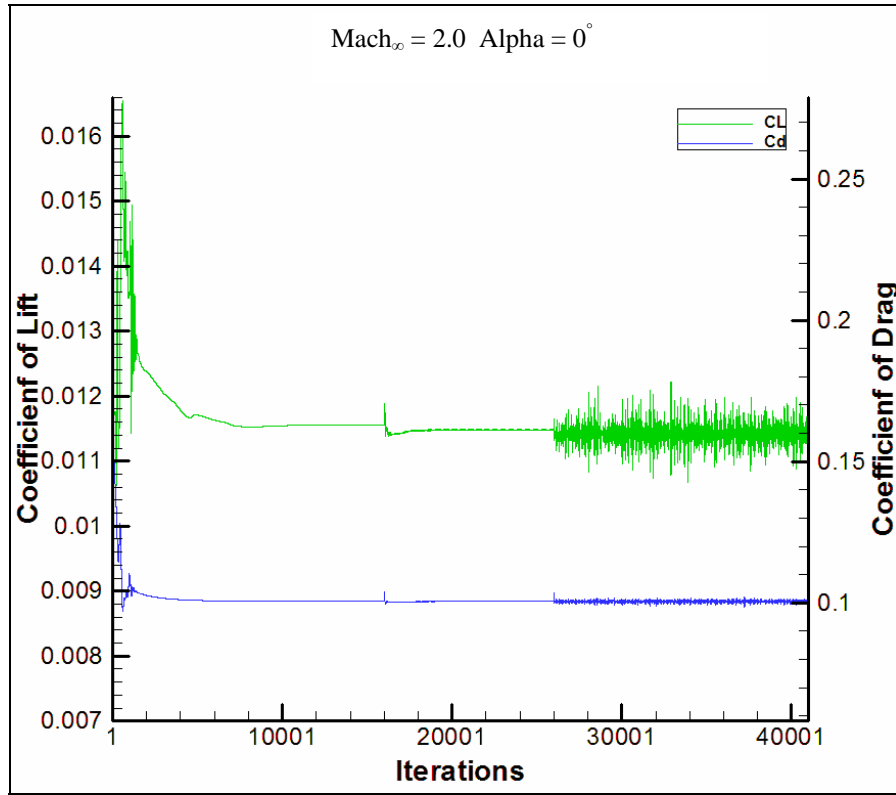
**Figure 3.100 Density Ratio Contour around Whitcomb airfoil**

Figure 3.101 shows the coefficient of pressure for a 2.0 Mach number. It shows the typical coefficient of pressure with a positive coefficient of pressure initially and then an almost zero coefficient of pressure.

Figure 3.102 shows the convergence for the coefficient of lift and the coefficient of drag. As seen before in supersonic flows, the results obtained from CFL3D are an average of the coefficient of lift oscillating as well as the coefficient of drag. The average coefficient of lift obtained is 0.01141 and a coefficient of drag of 0.1003.

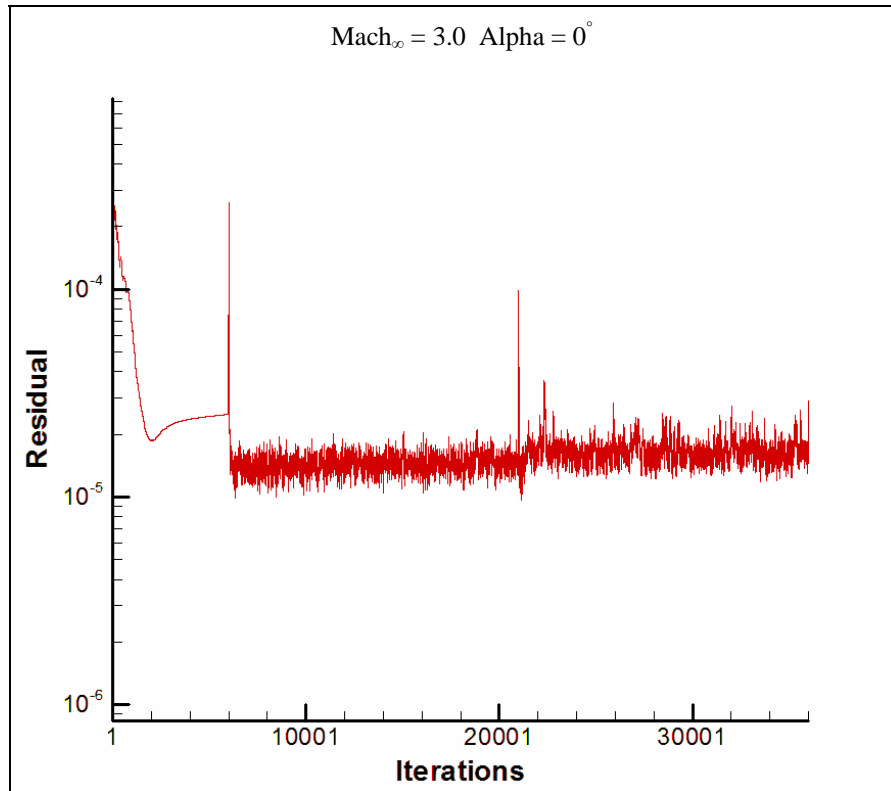


**Figure 3.101 Coefficient of Pressure around Whitcomb airfoil**



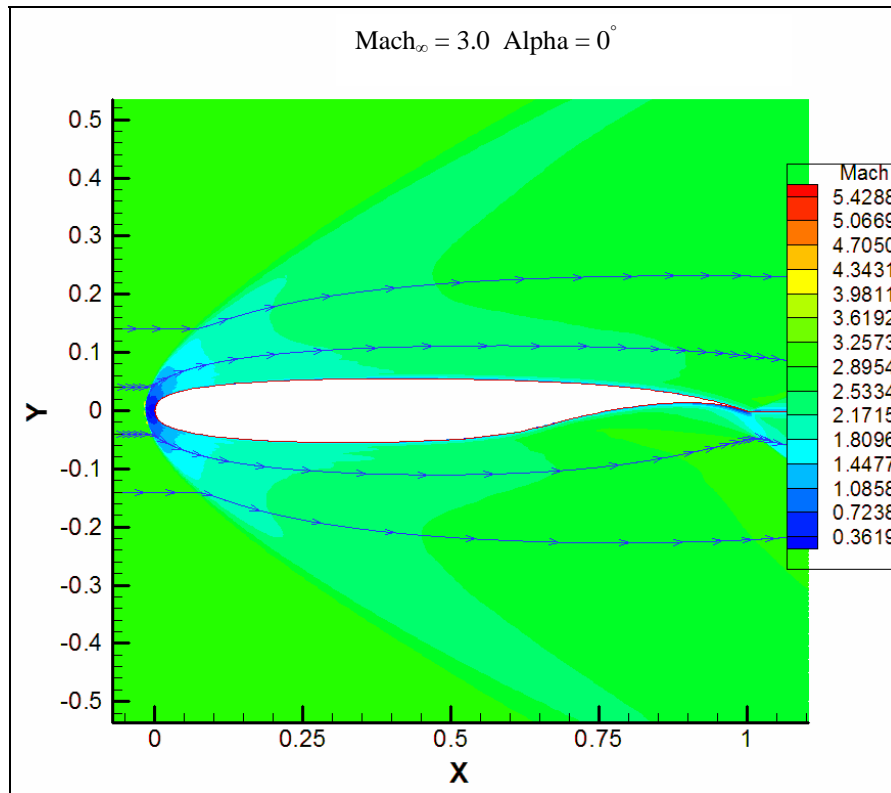
**Figure 3.102 Coefficient of Lift and Drag Convergence for Whitcomb airfoil**

### 3.4.4 Mach 3.0



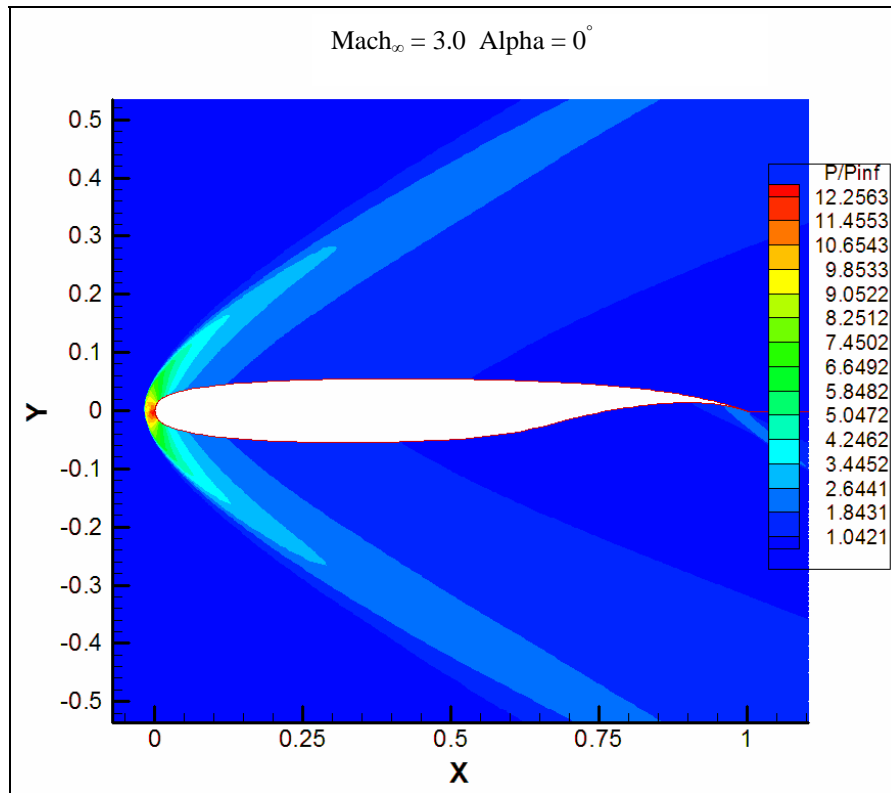
**Figure 3.103 Residual for Whitcomb airfoil from CFL3D**

Figure 3.103 shows the residual achieved after 36000 iterations. The 257 by 159 grid level was allowed to converge for 6000 iterations. Then the program passed to the finer 513 by 257 level for 15000 iterations and at the end it went to the finest 1025 by 513 level with 15000 iterations. An accuracy of 4 decimal places is expected in the results given this residual.



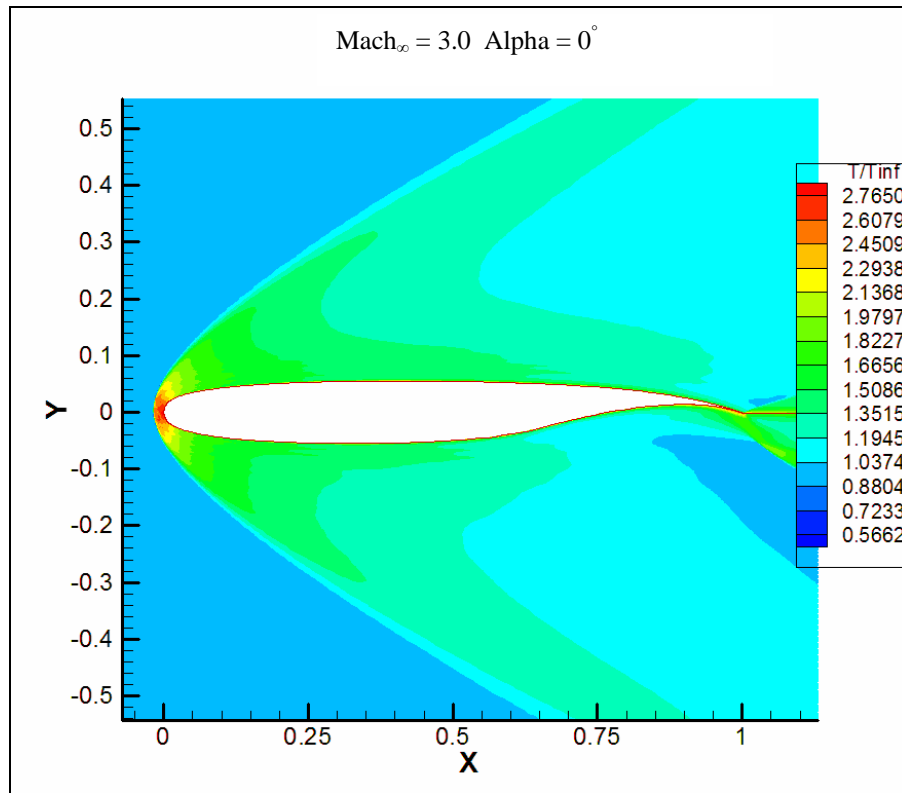
**Figure 3.104 Mach 3.0 Contour around Whitcomb airfoil**

Figure 3.104 shows the free stream Mach 3.0 air flow contour around the Whitcomb airfoil. As shown in Figure 3.105, the pressure ratios on both the upper and lower surface are almost identical which will cause and almost identical Mach contour as seen in Figure 3.104. As in the last case, a decrease in Mach number is shown at the lower surface close to the trailing which is caused by an increase in pressure ratio. As before, this increase in pressure ratio will also increase the temperature and density.

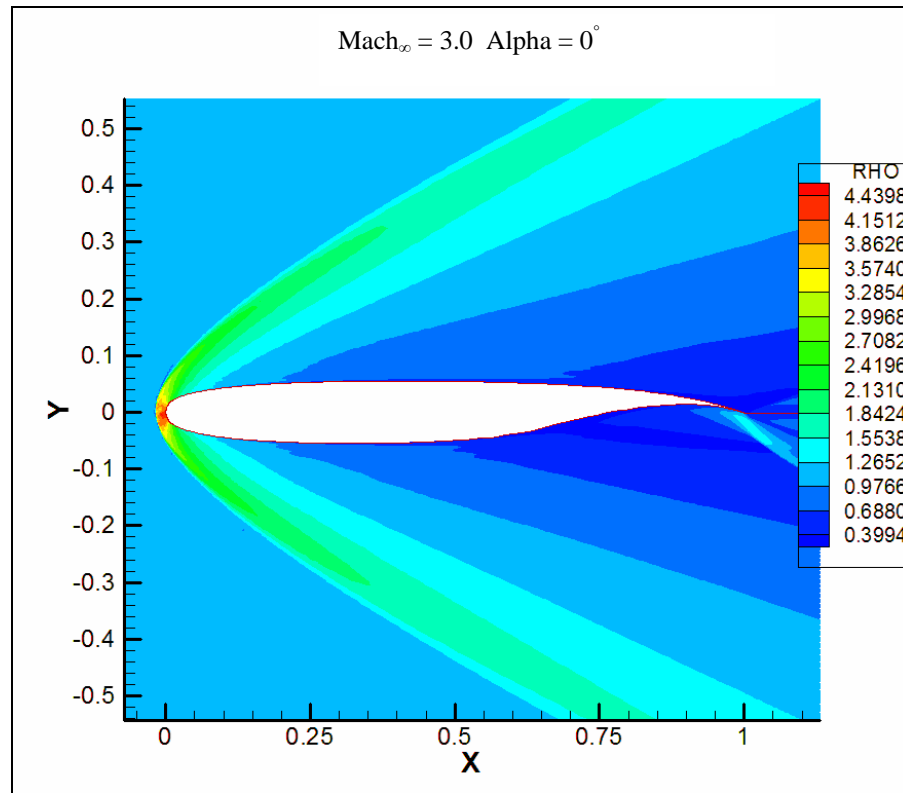


**Figure 3.105 Pressure Ratio Contour around Whitcomb airfoil**

Figure 3.106 shows the temperature ratio contour around the Whitcomb airfoil. It shows is higher temperature across the upper surface which is due to the higher pressure when compared to the lower surface. As it happened in the case of the expansion fan on the wedge, when the surface is moving away in a supersonic flow, the pressure and temperature decreases causing an increase in Mach number and speed. This effect can be seen on the upper surface close to the trailing edge. The opposite effect occurs when the surface moves towards the flow as it is the case of the lower surface close to the trailing edge. The effects of the shape of the surface for supersonic flow can be seen in Figures 3.106 and Figure 3.107.

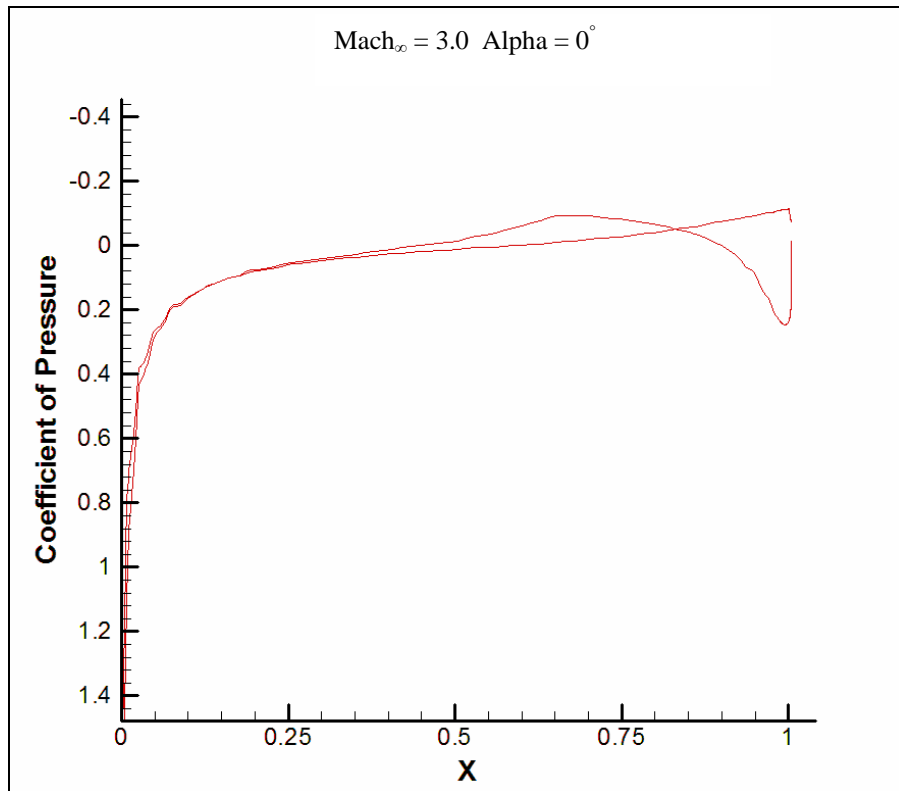


**Figure 3.106 Temperature Ratio Contour around Whitcomb airfoil**



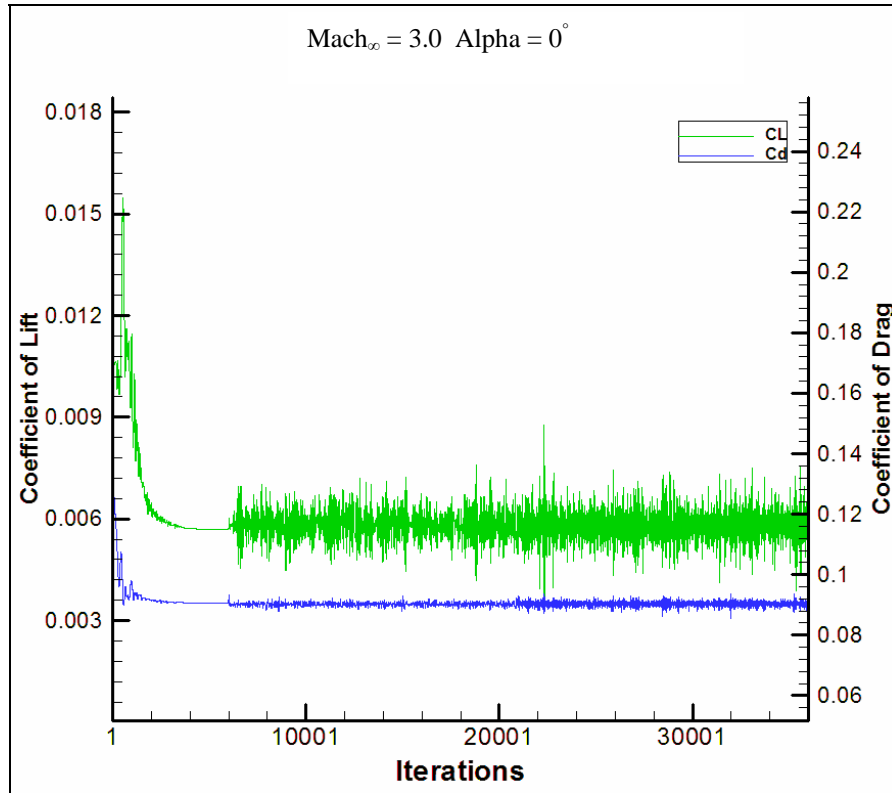
**Figure 3.107 Density Ratio Contour around Whitcomb airfoil**

Figure 3.108 shows the coefficient of pressure around the surface of the Whitcomb airfoil. As it is the case in supersonic flow, the coefficient of pressure is close to zero except at the leading edge where it is positive.



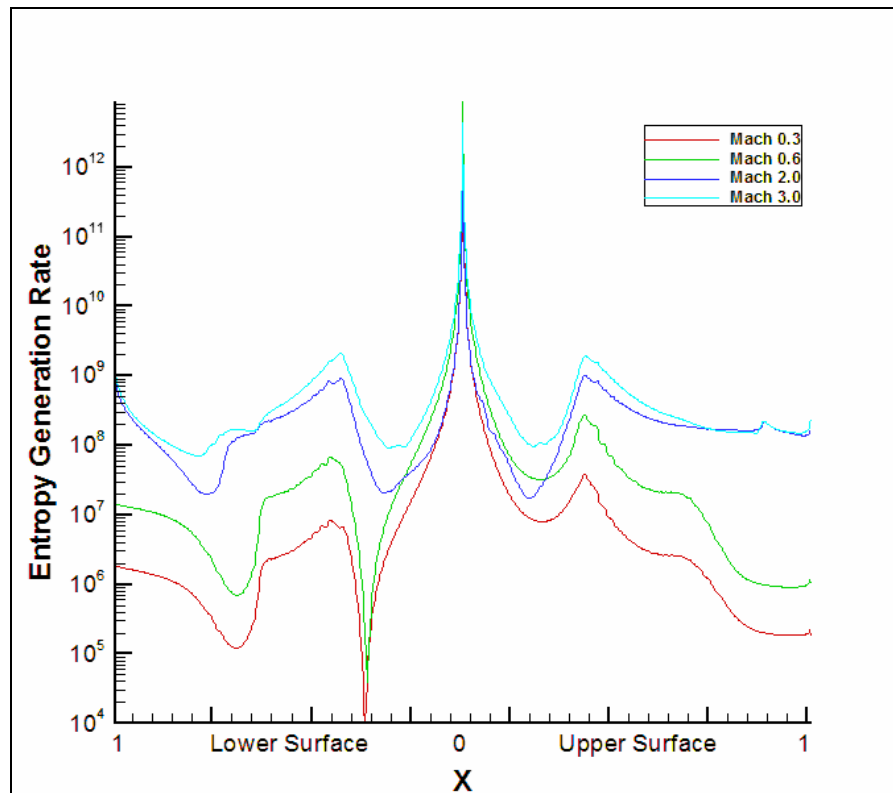
**Figure 3.108 Coefficient of Pressure around Whitcomb airfoil**

Figure 3.109 shows the convergence for the coefficient of lift and the coefficient of drag after 36000 iterations. As before, the resulted coefficient of lift and coefficient of drag is the average of the oscillations after all the iterations. It is important to notice that although both coefficients are oscillating, they stay within a constant range which indicates that the results can be used. The resulting average coefficient of lift is 0.00575 and the coefficient of drag is 0.0906.



**Figure 3.109 Coefficient of Lift and Drag Convergence for Whitcomb airfoil**

### 3.4.5 Entropy Generation Rate Comparison



**Figure 3.110 Entropy Generation Rate ( $\frac{W}{m^3 K}$ ) around Whitcomb airfoil**

Figure 3.110 shows the entropy generation rate per unit span caused one meter around the leading edge, the upper surface and the lower surface only. It does not show the entropy generated after the trailing edge.

Figure 3.110 shows the entropy generation rate per unit volume caused by the Whitcomb Integral Supercritical airfoil at different Mach numbers from subsonic to supersonic speeds.

The X-position of one is located at the trailing edge and the X-position of zero is the leading edge of the airfoil. One important aspect to notice is that at supersonic speeds, the decrease and increase in entropy generation close to the leading edge on both sides of the airfoil are almost identical.

At subsonic speeds, the decrease in entropy generation along the lower surface after the leading edge is caused by having an almost constant velocity terms which can be seen in the pressure ratio contours with an almost constant pressure ratio.

As it is expected for the space that is analyzed, the maximum entropy generation is caused at the leading edge where there are large changes in the velocity and temperature of the flow. The flow goes from the free stream Mach number to a stagnant point at the leading edge which will cause the entropy generation drop due to the zero velocity terms but with a generation due to the rise in temperature and density. One characteristic that was not expected from these results is that the entropy generation peak for a Mach 0.6 flow is higher than the entropy generation rate by a flow at Mach 3.0. Although the level of convergence achieved in the Mach 3.0 run is not as accurate as for the Mach 0.6 run, it might be the physical case that the pressure ratio bubble created at the upper surface close to the leading edge has enough gradients to increase the entropy generation rate. Due to the low convergence for the Mach 3.0 run, it is not possible to give a conclusion decision.

Another peculiar characteristic is the decrease in entropy generation rate close to the trailing edge at the lower surface. This decrease in entropy generation is caused by having a favorable pressure gradient at that zone which increase the speed and lowered both the

temperature and the density. Although there is a decrease in entropy generation rate, as the flow gets to the trailing edge, the entropy generation rate increases due to the compression shock that occurs at the trailing edge because of an increase in pressure and temperature.

### 3.5 Diamond Wedge

Two cases were run for the Diamond Wedge Airfoil. The two cases consisted of a Mach number of 0.6 and 3.0 at an angle of attack ( $\alpha$ ) of one degree. Given that the flow characteristics are going to be similar to the airfoils already shown, the images are going to be shown smaller.

#### 3.5.1 Mach 0.6

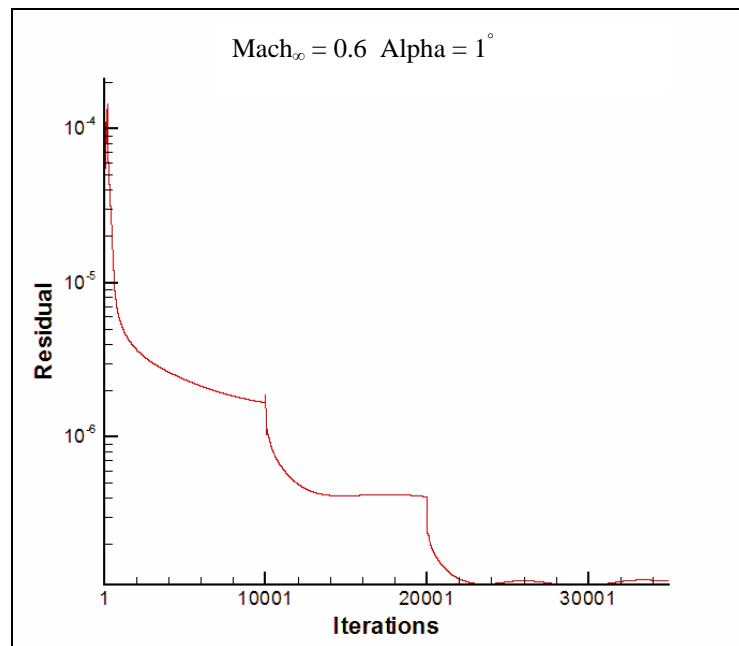


Figure 3.111 Residual for Diamond airfoil from CFL3D

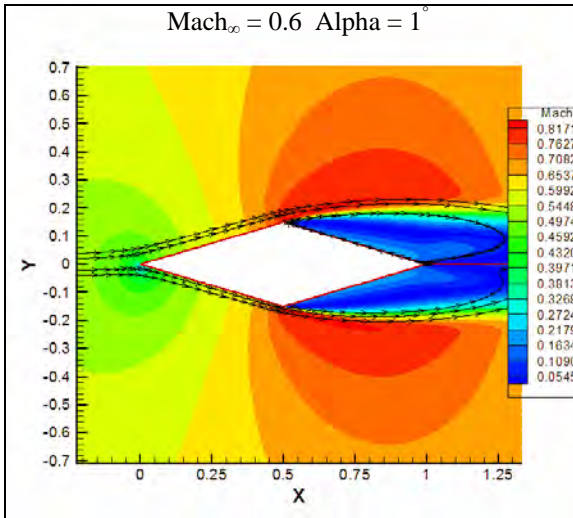


Figure 3.112 Mach 0.6 Contour around Diamond Airfoil

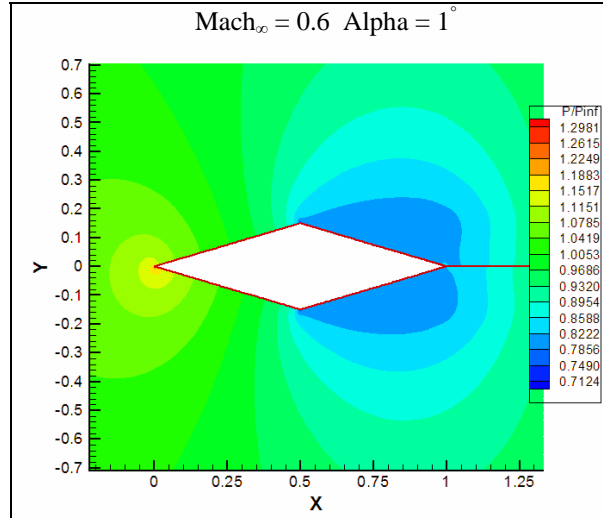


Figure 3.113 Pressure Contour around Diamond Airfoil

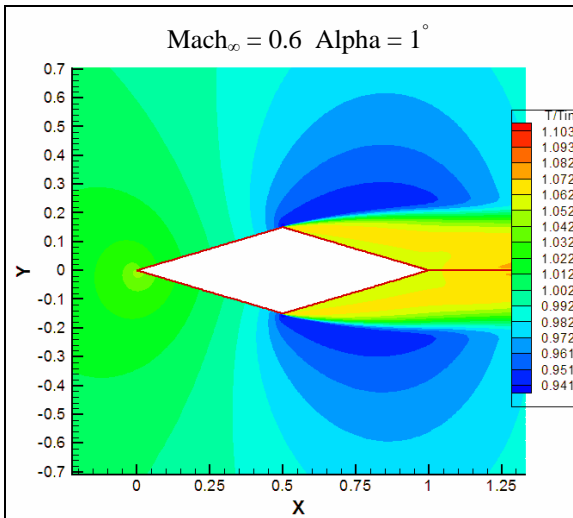


Figure 3.114 Temperature Contour around Diamond Airfoil

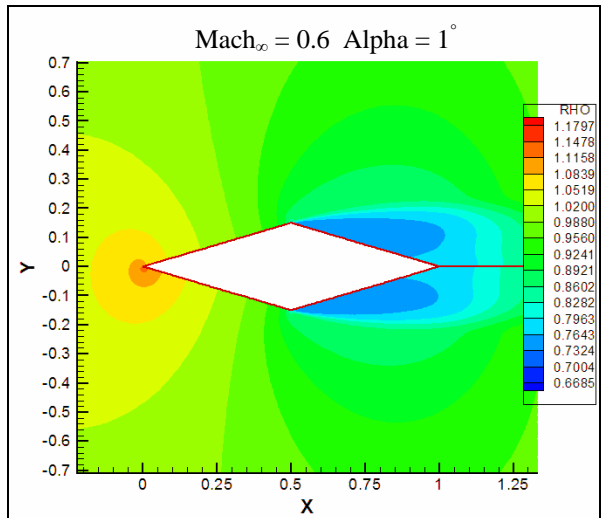
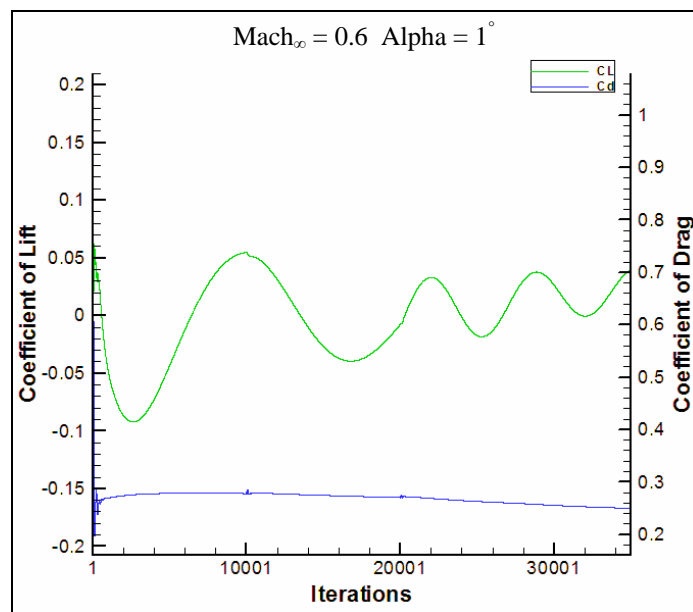


Figure 3.115 Density Contour around Diamond Airfoil

Figure 3.111 shows the residual at Mach 0.6 around a diamond shape airfoil as the program runs through three different size grids. The coarsest grid is a 273-by-87 grid points, which then changes to a finer 545-by-173 grid size, and then to the finest grid of 1089-by-345 grid

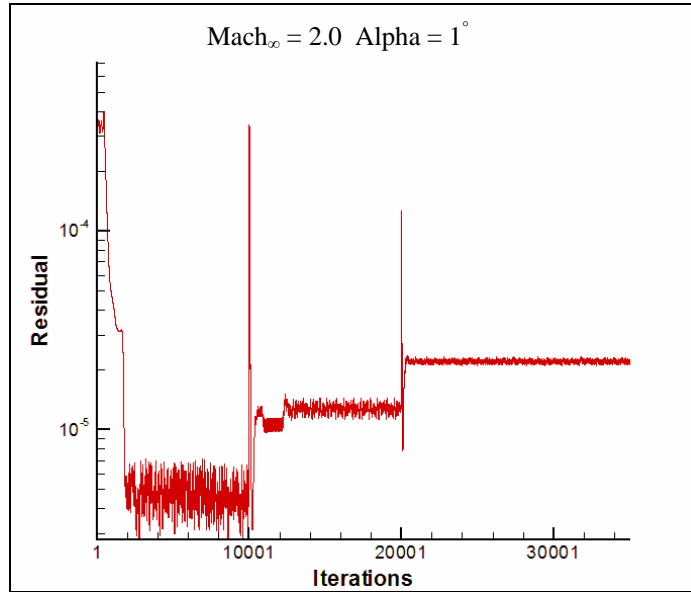
points. In total there are 987,482 grid points. From the residual figure, a convergence accuracy of about 7 decimal points is expected.

Figure 3.112, 3.113, 3.114, and 3.115 show the Mach, pressure, temperature, and density contours a diamond shape airfoil at a Mach number of 0.6 and at an angle of attack of one degree. Given that the flow is subsonic, information about the diamond leading edge is passed upstream and the flow bends accordingly. Due to the friction at the surface of the airfoil, once the flow passes the center it can not follow the airfoil shape so it separates and starts to rotate. This can be seen by the streamlines in Figure 3.112. The flow compresses approximately 18% at the nose which will also lead to an increase in temperature and pressure. From Fig. 3.116, the coefficient of lift was taken at 0.02 and the coefficient of drag as 0.25. It is important to notice that this type of configuration is not meant to be used at subsonic speeds given the symmetrical shape of the airfoil.



**Figure 3.116 Coefficient of Lift and Drag Convergence for Diamond Airfoil**

### 3.5.2 Mach 2.0



**Figure 3.117 Residual for Diamond airfoil from CFL3D**

In a similar manner Figure 3.117 shows the residual at Mach 2.0 around a diamond shape airfoil as the program runs through three different size grids. The coarsest grid is a 273-by-87 grid points, which then changes to a finer 545-by-173 grid size, and then to the finest grid of 1089-by-345 grid points. In total there are 987,482 grid points. From the residual figure, a convergence accuracy of about 4 decimal points is expected.

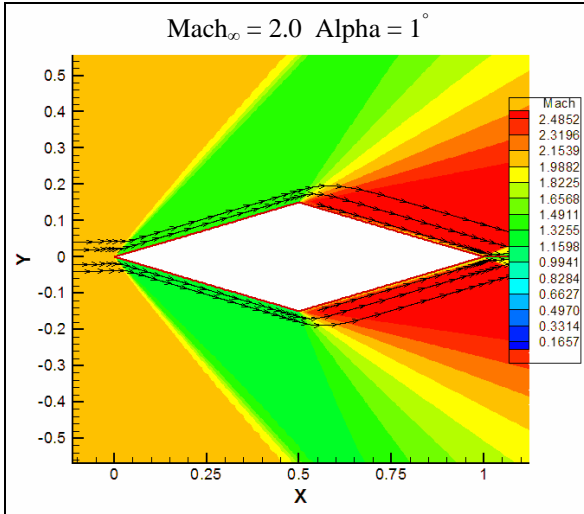


Figure 3.118 Mach 2.0 Contour around Diamond airfoil

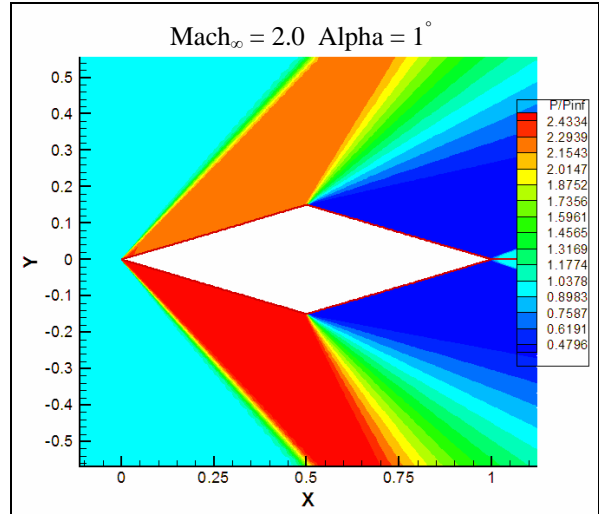


Figure 3.119 Pressure Ratio Contour around Diamond airfoil

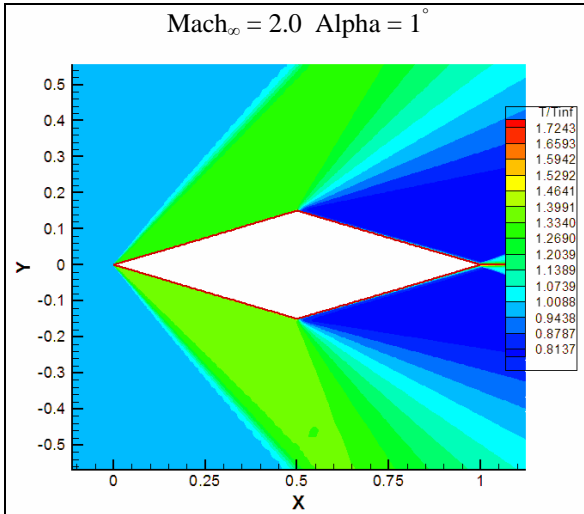


Figure 3.120 Temperature Ratio Contour around Diamond Airfoil

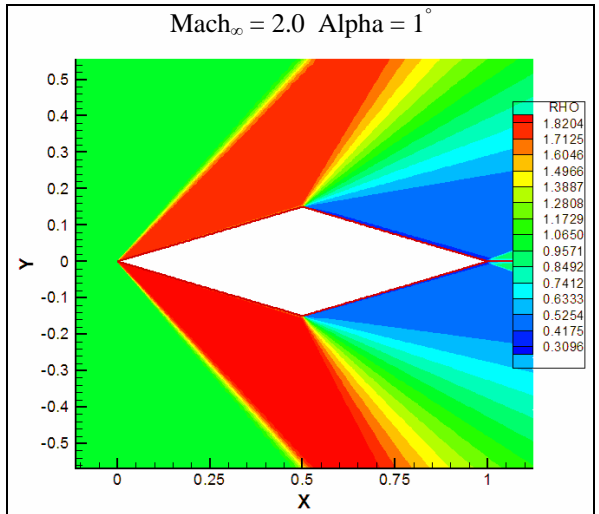
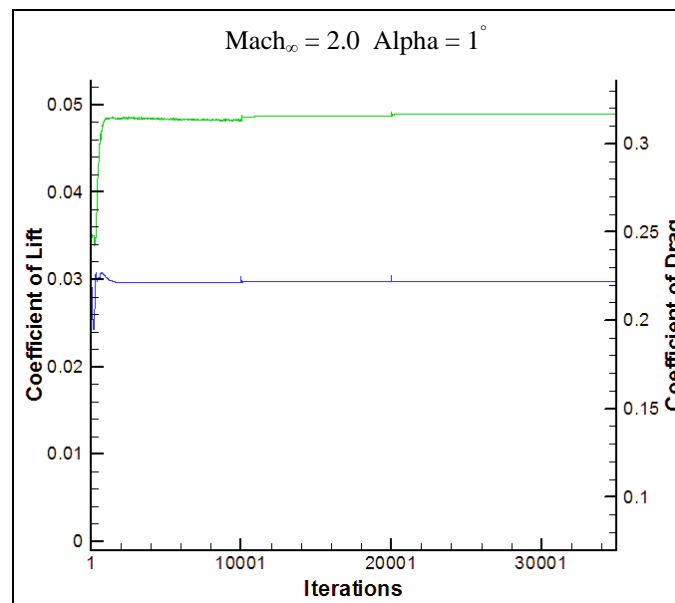


Figure 3.121 Density Ratio Contour around Diamond Airfoil

Figure 3.118, 3.119, 3.121, and 3.122 show the Mach, pressure, temperature, and density contours a diamond shape airfoil at a Mach number of 0.6 and at an angle of attack of one degree. In this case the flow is supersonic. By supersonic compressible flow theory, the boundary layer above the surface is expected to be only millimeters high at the leading edge,

so the downstream Mach number can be compared with inviscid flow theory. From inviscid compressible flow theory, the downstream upper Mach number is expected to be 1.41632 and the downstream lower Mach number at the leading edge is expected to be 1.32731. The numerical results obtained from CFL3D were 1.40774 and 1.33709 respectively for the upper and lower surface Mach number. This gives a difference of 0.606% and 0.737%, which is good for the analysis.

In this airfoil, an oblique shock wave forms instead of the curve shock wave that was formed for the other airfoils as can be seen by the streamlines in Figure 3.118. Figure 3.122 shows the coefficient of lift and the coefficient of drag convergence. The coefficient of lift finished with 0.049 and the coefficient of drag with 0.222.



**Figure 3.122 Coefficient of Lift and Drag Convergence for Diamond Airfoil**

### 3.5.3 Entropy Generation Rate Comparison

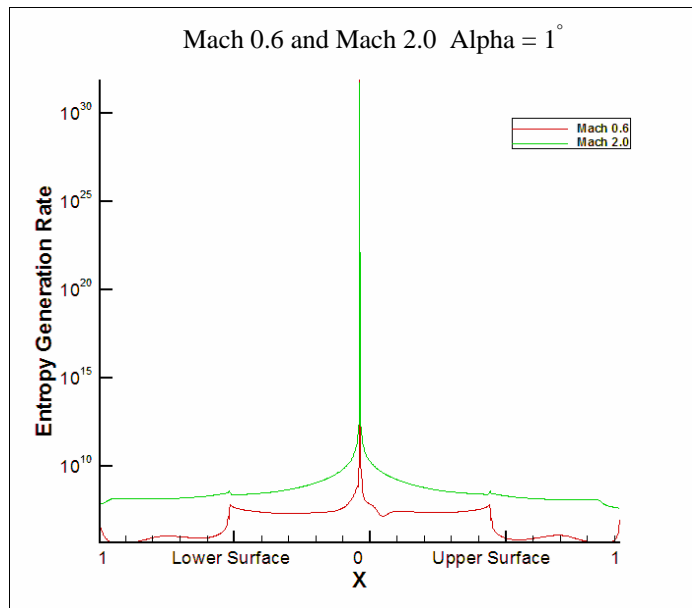


**Figure 3.123 Entropy Generation Rate ( $\frac{W}{m^3 K}$ ) around Diamond Airfoil**

Figure. 3.123 shows the volumetric entropy generation rate per unit span for the Diamond Wedge Airfoil at a Mach 0.6 and Mach 2.0. At Mach 0.6, most of the entropy generation is caused from the leading edge to the center of the airfoil due to the changes in velocity caused by viscous dissipation. Then, after the center of the airfoil, there is a slight rise in entropy generation caused by the turbulent rotation after the center of the airfoil. For the supersonic case, the highest entropy generation is caused at the leading edge of the airfoil and followed by an almost constant entropy generation after the leading edge. There is still a slight increase in entropy generation at the center similar to the increase in generation at the subsonic speed.

## 4 CONCLUSIONS AND FUTURE WORK

The first part of this thesis illustrates the subsonic and supersonic compressible regimes. It illustrates how friction helps accelerate the flow in subsonic flow but decelerates the flow in supersonic flows. Also, several graphs were shown to illustrate the change in pressure, temperature, and density as the airfoils goes from two subsonic Mach numbers to two supersonic Mach numbers.

The second part of this thesis opens the shows the usage of the entropy generation rate to show which airfoils are more efficient at the Mach numbers and atmospheric conditions that were studied numerically. A relation between the entropy generation rate and the changes velocity, pressure, temperature, and density was shown through the different graphs. This approach could be used as a mean to design before hand a better suited and more efficient wing for a given flight characteristics. Table 4.1 shows an integrated entropy generation rate per unit span at two different Mach numbers for all the airfoils. Given that the purpose of an airfoil is to generate lift, it is important that the entropy generation rate is analyzed together with the Lift-to-Drag (L/D) ratio.

The L/D or the coefficient of lift-to-coefficient of drag ratio is one of the most important characteristics to take into account as it is shown by Breguet's Formula for the range(R) of a

propeller driven airplane: 
$$R = \frac{\eta}{c} \frac{CL}{Cd} \ln \frac{W_0}{W_1}$$

As this formulas shows, the higher the lift-to-drag ratio, the longer the range of the airplane. A similar equation exists for jet propelled airplanes. Also, there is a similar conclusion for the endurance of an airplane.

**Table 4.1. Flow and Entropy Characteristics**

<b>Airfoil</b>	<b>Mach</b>	$\dot{S}'''$	<b>CL</b>	<b>Cd</b>	<b>CL/Cd</b>
<b>NACA 64215</b>	0.6	9.8049x10 <sup>11</sup>	0.2030	0.008042	25.24
<b>Whitcomb</b>	0.6	1.0356x10 <sup>13</sup>	0.5442	0.008455	64.36
<b>Grumman K2</b>	0.6	2.9043x10 <sup>13</sup>	0.1537	0.007421	20.71
<b>Diamond Wedge</b>	0.6	8.4102x10 <sup>31</sup>	0.02	0.25	0.08
<b>NACA 64215</b>	2.0	2.7440x10 <sup>13</sup>	-0.0201	0.1127	-0.1783
<b>Whitcomb</b>	2.0	2.1229x10 <sup>12</sup>	0.01141	0.1003	0.1137
<b>Grumman K2</b>	2.0	2.4934x10 <sup>14</sup>	0.1537	0.007421	-0.3801
<b>Diamond Wedge</b>	2.0	5.7594x10 <sup>31</sup>	0.049	0.222	0.2207

For a Mach 0.6, the Whitcomb Integral Airfoil has a higher entropy generation than the NACA 64215 airfoil but a lower entropy generation than the Grumman K2. On the other hand, the Whitcomb Integral has the highest L/D ratio at that speed. Therefore at that speed, the Whitcomb airfoil is a better airfoil than the other two. Of course, the Diamond Wedge

airfoil has the lowest L/D at this Mach number since that type of wing is use for supersonic flows.

At supersonic speeds the results are inconclusive given that the entropy generation per unit span for the Whitcomb airfoil was lower at supersonic than at subsonic. Similar results were obtained for the Diamond Wedge airfoil. One reason for this effect might be the creation of the grid.

Another result is that at subsonic the entropy generation rate was about 99% caused by viscous dissipation while at supersonic speeds, heat transfer dissipation needs to be taken into account. Heat transfer dissipation will become even more relevant, the faster the flow around the airfoil.

More research is needed in this area. Lack of experimental data at the studied subsonic and supersonic regimes limited the comparison between experimental and numerical data. This data could greatly reduce the cost in the future when designing airfoils due to the use of a proven CFD approach for the design.

## REFERENCES

- [1] Kostic, M. "Irreversibility and Reversible Heat Transfer: The Quest and Nature of Energy and Entropy", Proceedings of IMECE2004, ASME Int. Mech. Eng. Congress and R&D Expo, Anaheim, CA, IMECE2004-59282, November 2004
- [2] Bejan, Adrian, Entropy Generation Optimization, CRC Press, Florida, 1996
- [3] Bejan, Adrian, "Entropy generation minimization: The new thermodynamics of finite-size devices and finite time processes", J. Appl. Phys. Vol. 79, no. 3, pp. 1191-1218, 1996
- [4] Denton, J.D., "Loss Mechanisms in Turbomachines", ASME Paper No. 93-GT-435, 1993
- [5] Li, H. and Ben-Dor, G. 1996 "Application of the principle of minimum entropy production to shock wave reflections I Steady flows," American Institute of Physics Journal of Applied Physics, vol. 80 no. 4, pp 2027-2037
- [6] Li, H. and Ben-Dor, G. 1996 "Application of the principle of minimum entropy production to shock wave reflections II. Pseudosteady flows" American Institute of Physics Journal of Applied Physics, vol. 80 no. 4, pp 2038-2048
- [7] Walsh, Ed., Davies, Mark, and Myose, Roy 2002 "An Entropic Minimization Technique For Turbine Blade Profiles" Proceedings of ASME Turbo Expo, Amsterdam, The Netherlands, GT-2002-30346, June 2002
- [8] Walsh, Ed., Davies, Mark, and McEligot, Donald M. 2004, "On the use of Entropy to Predict Boundary Layer Stability," Entropy Vol. 6, no. 4, pp. 375-387
- [9] Walsh, Ed., Davies, Mark, Griffin, Philip C., and O'Donnell, Francis K. 2002 "The Effect of Reynolds Number, Compressibility and Free Stream Turbulence on Profile Entropy Generation Rate" Proceedings of ASME Turbo Expo, Amsterdam, The Netherlands, GT-2002-30330, June 2002
- [10] Thompson, Philip A., Strock, Thomas W., and Lim, David S., "Estimate of shock thickness based on entropy production" Physics Fluids Vol. 26, no. 1, pp. 48-49, 1983
- [11] Salas, Manuel D., "Shock Wave Interaction With an Abrupt Area Change", NASA TP-3113, 1991
- [12] Moretti, Gino, and Pandolfi, Maurizio, "Entropy Layers", Polytechnic Institute of Brooklyn Preston R. Bassett Research Laboratory, PIBAL Report 71-33, 1971

- [13] Abu-Hileh, Bassam A.K., and Heilen, Waleed N., "Entropy generation due to laminar natural convection over a heated rotating cylinder" *Int. J. Heat Mass Transfer* Vol. 42 pp. 4225-4233, 1999
- [14] Creager, Marcus O., "Effect of Leading Edge Thickness on the Flow Over a Flat Plate at a Mach Number of 5.7", NASA-TN-D-313, 1960
- [15] Camberos, José A. and Chen, Po-Heng, "Continuum Breakdown Parameter Based on Entropy Generation Rates", AIAA Technical Paper No. 2003-157, Reno, NV, American Institute of Aeronautics and Astronautics, January 2003
- [16] Naterer, G. F., and Camberos, J. A., "Entropy and the Second Law Fluid Flow and Heat Transfer Simulation", *Journal of Thermophysics and Heat Transfer*, Vol. 17, no. 3, pp. 360-371, 2003
- [17] Salas, Manuel D., and Iollo, Angelo, "Entropy Jump Across an Inviscid Shock Wave", NASA CR-195046 ICASE Report No. 95-12, 1995
- [18] Walsh, Ed., Myose, Roy, and Davies, Mark, "A Prediction Method for the Local Entropy Generation Rate in a Transitional Boundary Layer with a Free Stream Pressure Gradient", *Proceedings of ASME Turbo Expo*, GT-2002-30231, Amsterdam, The Netherlands, June 2002
- [19] Stack, John, "Tests of Airfoils Designed to Delay the Compressibility Bubble" NACA Report No. 763, 1939
- [20] Oswatitsch, Klaus, "Recent Advances, Special Problems of Inviscid Steady Transonic Flows", *Int. J. Engng Sci.*, Vol. 20, no. 4, pp. 497-540, 1982
- [21] Stewart, Warner L., Whitney, Warren J., Wong, Robert Y., "A Study of Boundary-Layer Characteristics of Turbomachine Blade Rows and their Relation to Over-All Blade Loss", *ASME Journal of Basic Engineering*, pp.580-592, 1960
- [22] Johnson, Charles B., Boney, Lillian R., "A Simple Integral Method for the Calculation of Real-Gas Turbulent Boundary Layers with Variable Edge Entropy", NASA TN-D-6217, June 1971
- [23] Amick, James L., "A Method of Selecting the Thickness, Hollowness, and Size of a Supersonic Wing for Least Drag and Sufficient Bending Strength at Specified Flight Conditions", NACA TN 2754, 1952

- [24] Délerly, J. M., “Shock Phenomena in high speed aerodynamics: still a source of major concern”, The Aeronautical Journal, Paper No. 2434, pp. 19-34, 1999
- [25] Ratts, Eric B., and Raut, Atul G., “Entropy Generation Minimization of Fully Developed Internal Convective Flows with Constant Heat Flux”, Proceeding of HT2003, ASME Summer Heat Transfer Conference, Las Vegas, NV, HT2003-47389, July 2003
- [26] Li, Haipeng, and Figliola, Richard S., “Exergy Based Design Methodology for Airfoil Shape Optimization”, AIAA/ISSMO Multidisciplinary Analysis and Optimization Conference, Albany, NY, AIAA 2004-4632, September 2004
- [27] Kock, Fabian, and Herwig, Heinz, “Local entropy production in turbulent shear flows: a high-Reynolds number model with wall functions”, Int. J. Heat Mass Transfer Vol. 47 pp. 2205-2215, 2004
- [28] Morduchow, Morris, “Analysis and Calculation by Integral Methods of Laminar Compressible Boundary Layer with Heat Transfer and with and without Pressure Gradient”, NACA Report 1245, 1955
- [29] Whitcomb, Richard T., Clark, Larry R., “An Airfoil Shape For Efficient Flight At Supercritical Mach Numbers”. NASA TM X-1109, 1965
- [30] Harris, Charles D., “NASA Supercritical Airfoils A Matrix of Family-Related Airfoils”, NASA Technical Paper 2969, 1990
- [31] Evans, W., Mac Kenzie, D., Romanowski, R., “The Design, Test, and Evaluation of Shockless Transonic Airfoils”, NAVY AIR-5301, 1973
- [32] CFL3D Program Version 5.0 Manual, Appendix H “Turbulence Model Equations”

## APPENDIX A. RANKINE-HUGONIOT RELATIONS

Assuming an irreversibly adiabatic normal shock wave, it is possible to derive the Rankine-Hugoniot Relations. If both the continuity and the momentum equations are combined for a normal shock wave, then the pressures on both side of the shock wave are expressed so that,

$$p_2 - p_1 = \rho_1 V_1^2 - \rho_2 V_2^2$$

and rearranging,

$$V_2 = \left[ \frac{(p_2 - p_1)\rho_1}{(\rho_2 - \rho_1)\rho_2} \right]^{1/2}$$

where the subscripts 2 and 1 define the conditions downstream and upstream of the shock wave respectively.

Given that the enthalpy for a perfect gas can be expressed as

$$h = c_p T = \frac{\gamma}{\gamma - 1} \frac{p}{\rho}$$

where  $c_p$  is the specific heat at constant pressure and  $\gamma$  is the specific heat ratio which for air as a perfect gas has a value of 1.4. These expressions can be put into the energy equation to get,

$$\frac{\gamma}{\gamma - 1} \frac{p_1}{\rho_1} + \frac{p_2 - p_1}{2(\rho_2 - \rho_1)} \frac{\rho_2}{\rho_1} = \frac{\gamma}{\gamma - 1} \frac{p_2}{\rho_2} + \frac{p_2 - p_1}{2(\rho_2 - \rho_1)} \frac{\rho_1}{\rho_2}$$

and rearranging for the pressure and density ratios across a normal shock wave,

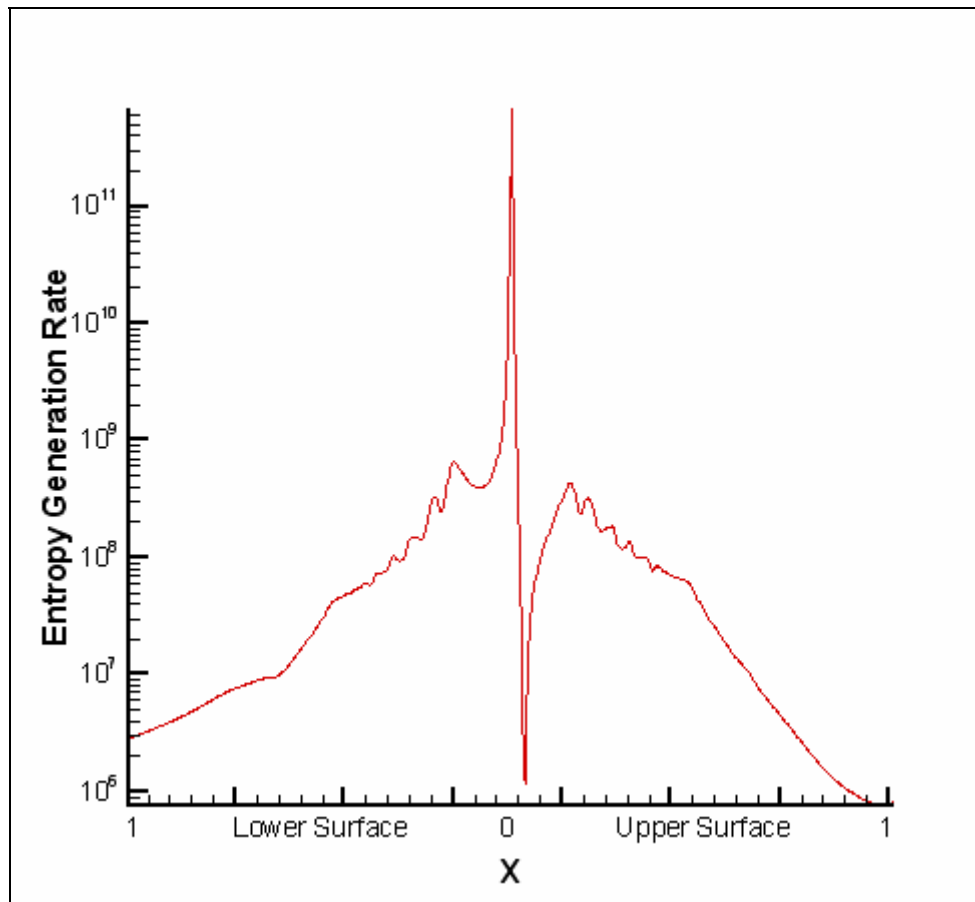
$$\frac{p_2}{p_1} = \frac{\frac{\gamma + 1}{\gamma - 1} \frac{\rho_2}{\rho_1} - 1}{\frac{\gamma + 1}{\gamma - 1} - \frac{\rho_2}{\rho_1}} \quad \text{and} \quad \frac{\rho_2}{\rho_1} = \frac{\frac{\gamma + 1}{\gamma - 1} \frac{p_2}{p_1} + 1}{\frac{\gamma + 1}{\gamma - 1} + \frac{p_2}{p_1}}$$

which are the Rankine-Hugoniot relations.

## APPENDIX B. ENTROPY GENERATION RATE

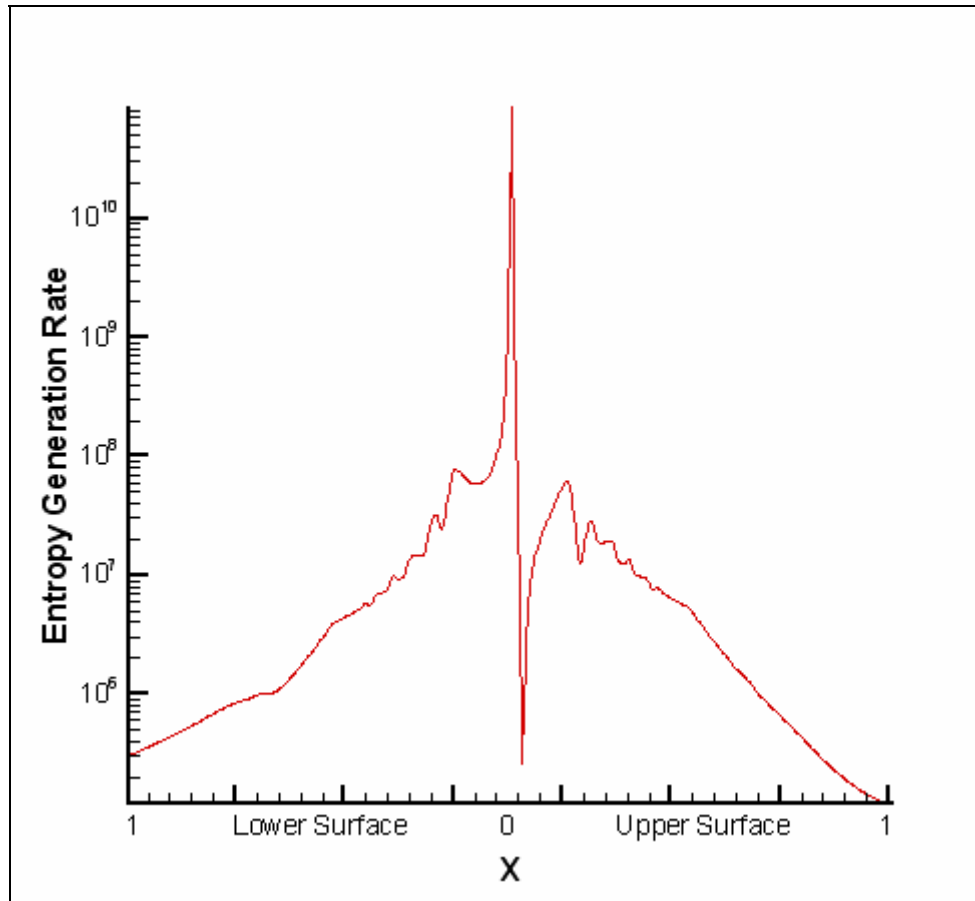
### APPENDIX B1 NACA 642A215 Airfoil

#### B.1.1 Mach 0.65



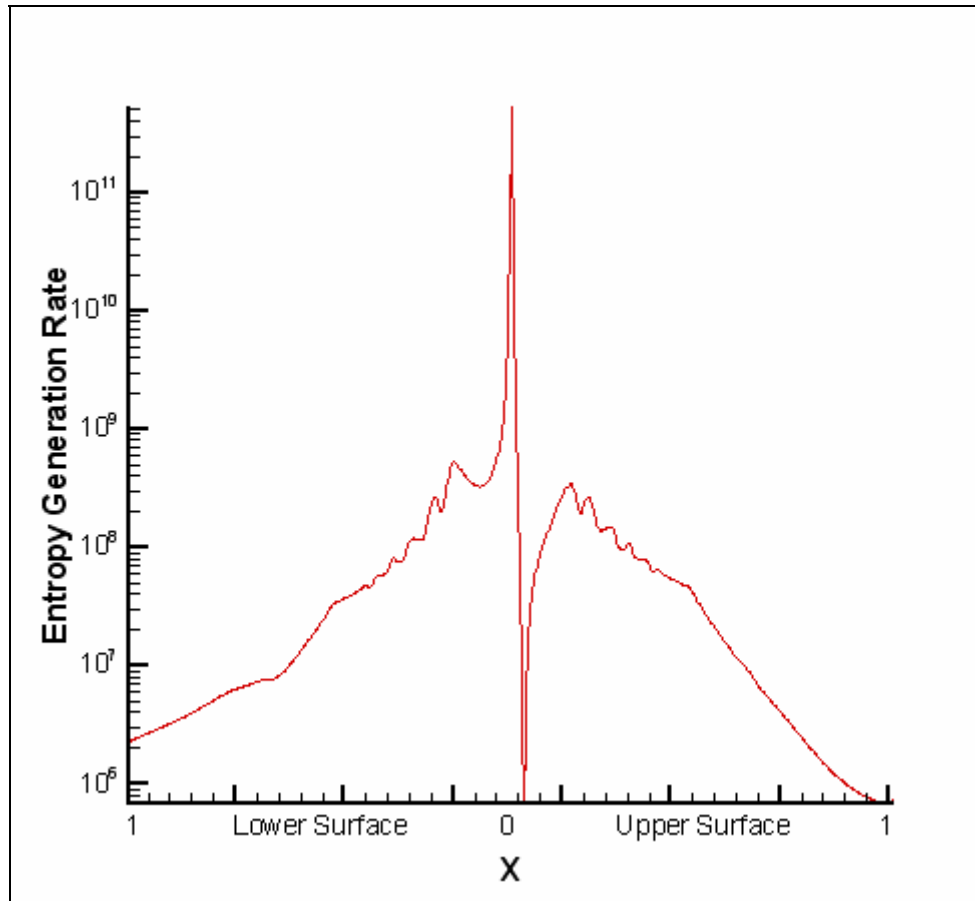
Entropy Generation Rate ( $\frac{W}{m^3 K}$ ) around NACA 64<sub>2</sub>A215 airfoil

**B.1.2 Mach 0.3**



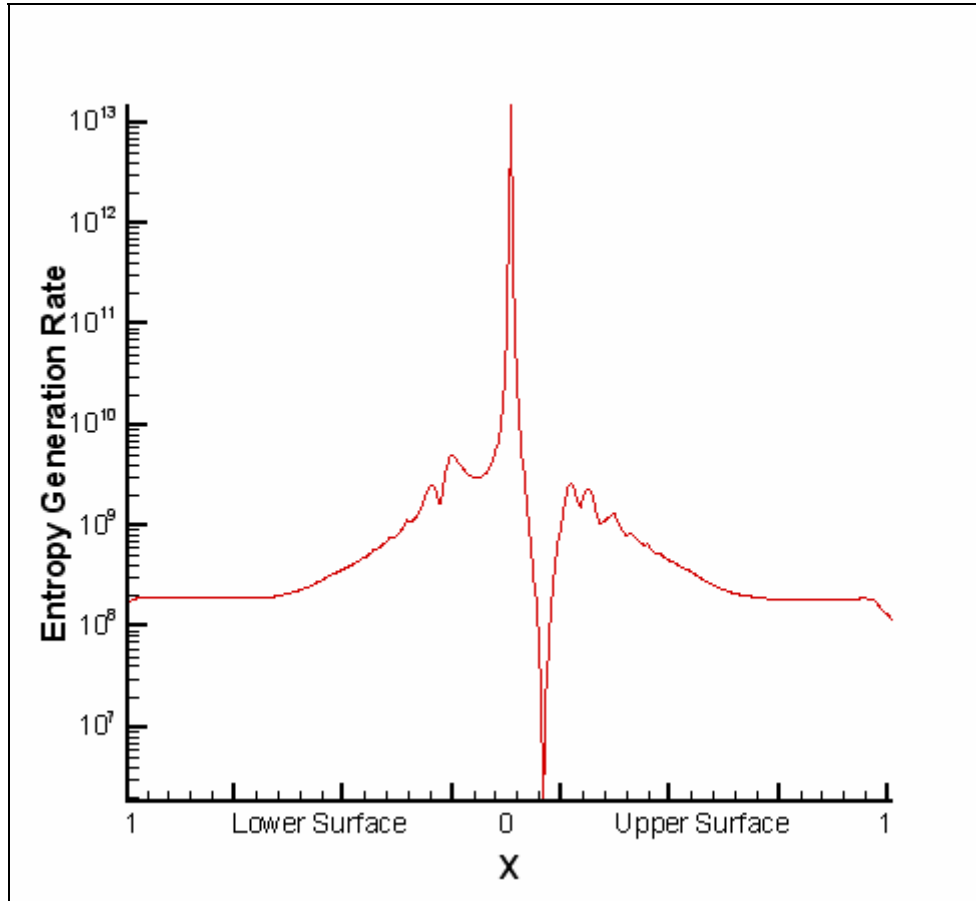
**Entropy Generation Rate ( $\frac{W}{m^3 K}$ ) around NACA 64<sub>2</sub>A215 airfoil**

**B.1.3 Mach 0.6**



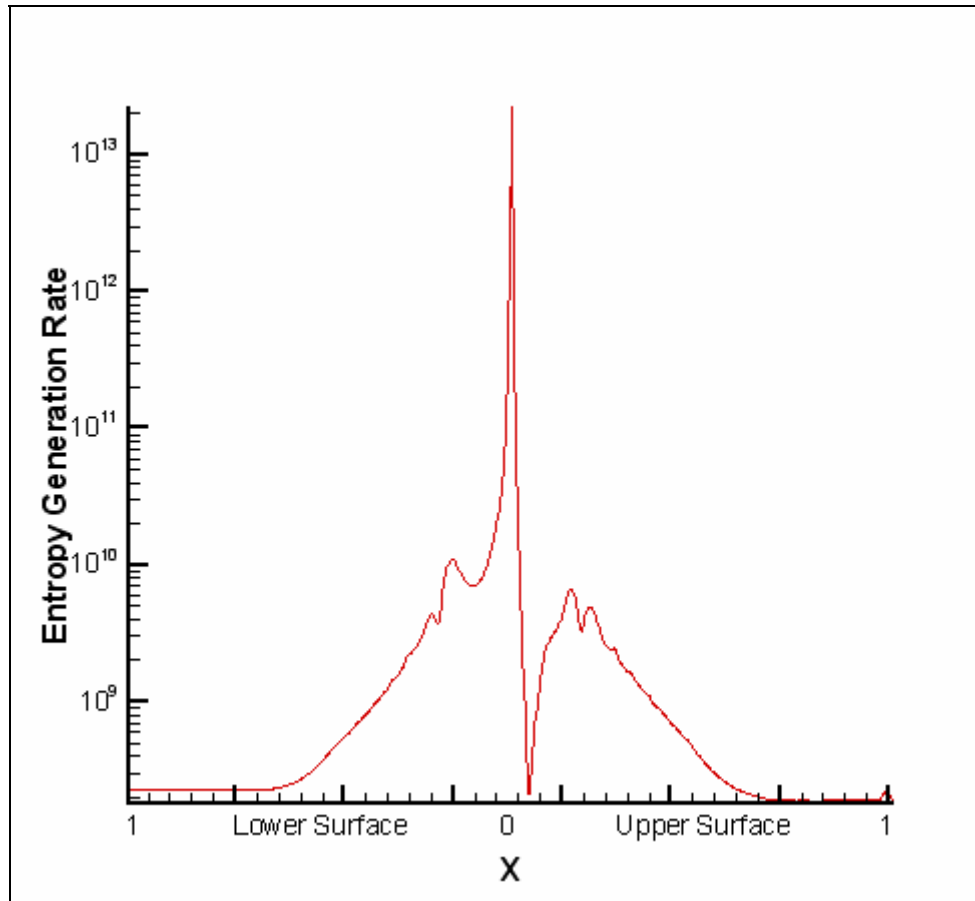
**Entropy Generation Rate ( $\frac{W}{m^3 K}$ ) around NACA 64<sub>2</sub>A215 airfoil**

***B.1.4 Mach 2.0***



**Entropy Generation Rate ( $\frac{W}{m^3 K}$ ) around NACA 64<sub>2</sub>A215 airfoil**

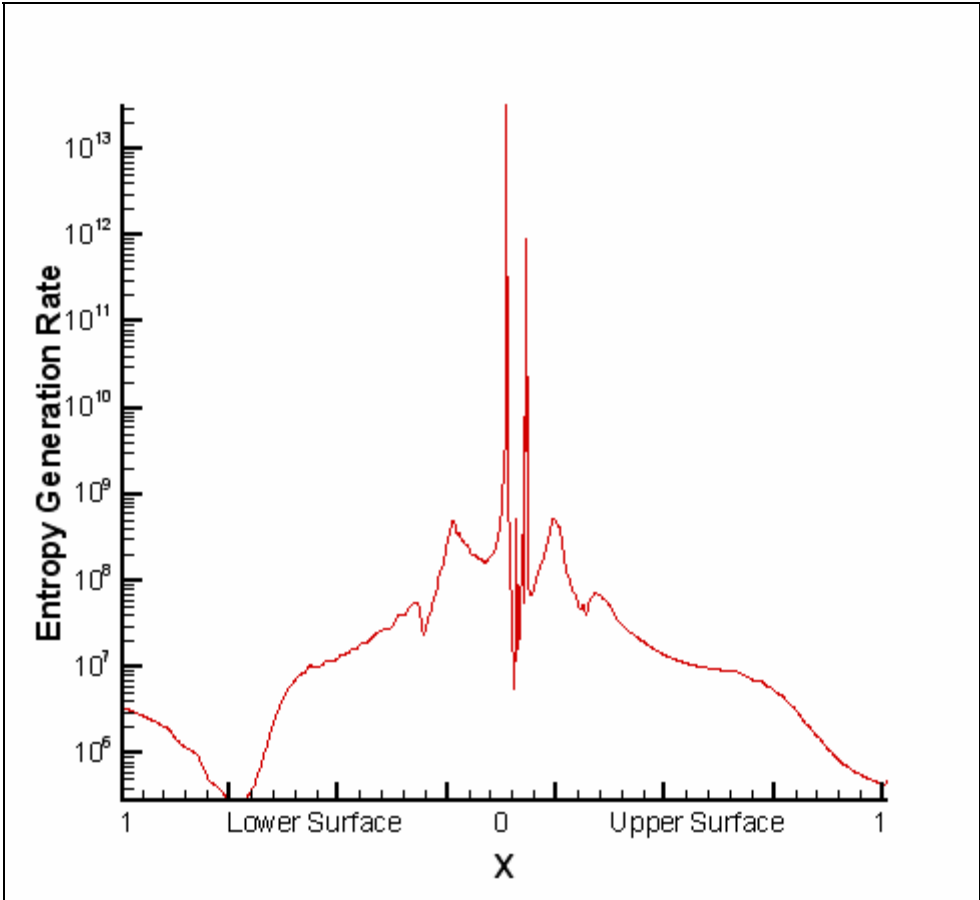
***B.1.5 Mach 3.0***



**Entropy Generation Rate ( $\frac{W}{m^3 K}$ ) around NACA 64<sub>2</sub>A215 airfoil**

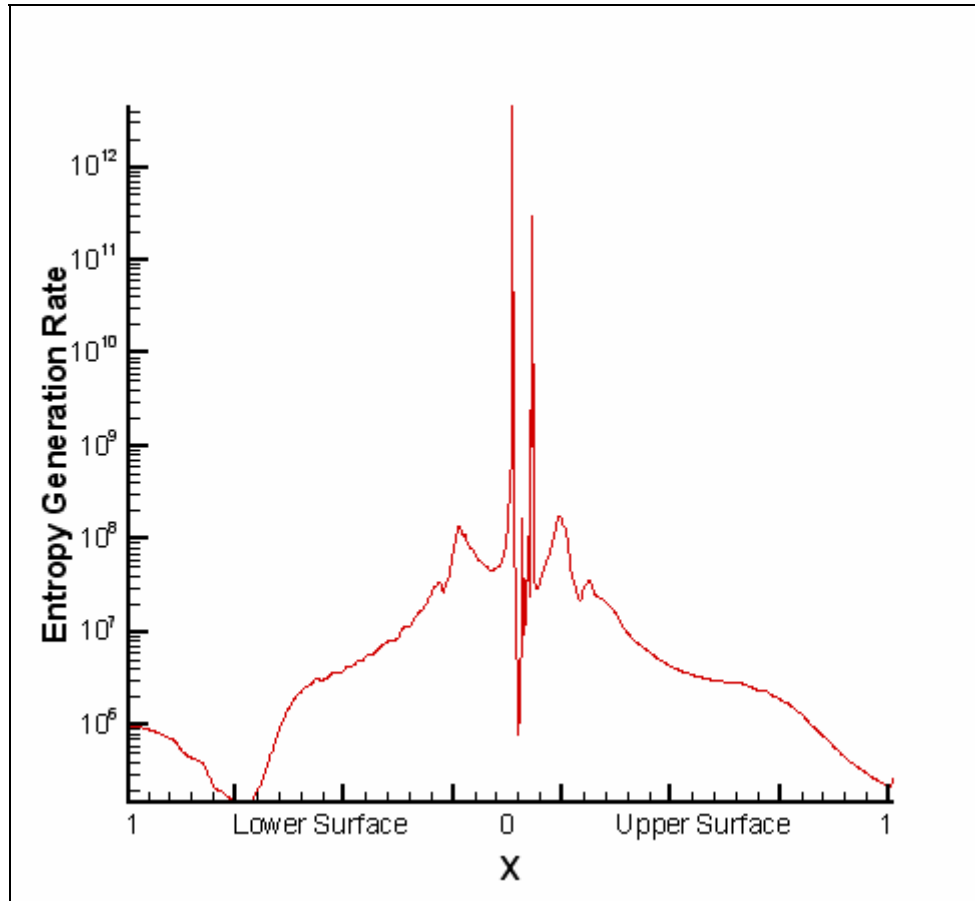
# APPENDIX B.2 K-2 Airfoil

## B.2.1 Mach 0.6



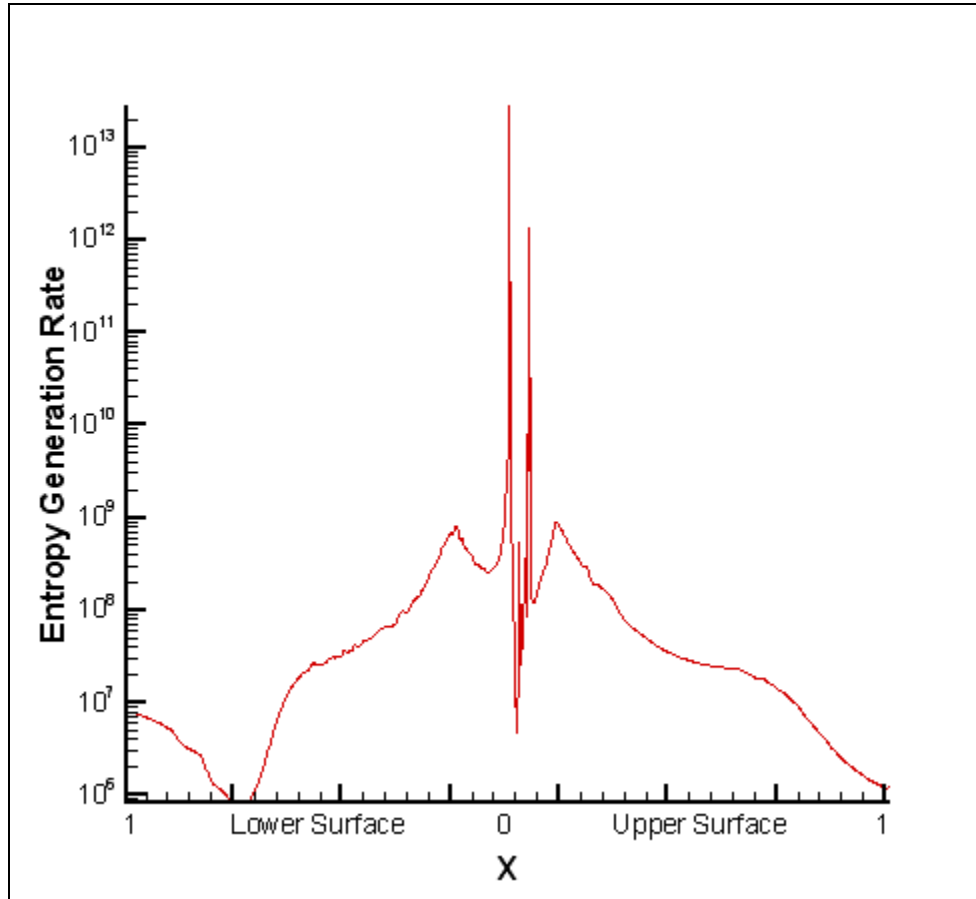
Entropy Generation Rate ( $\frac{W}{m^3 K}$ ) around K2 airfoil

**B.2.2 Mach 0.3**



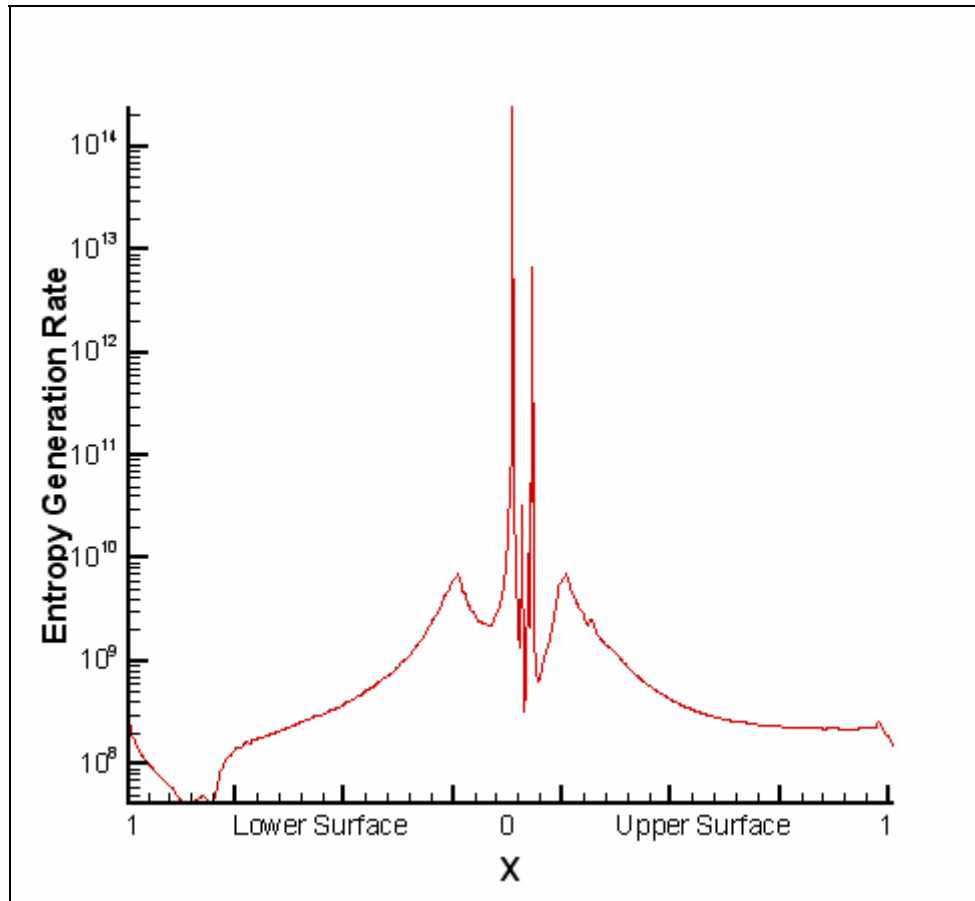
**Entropy Generation Rate ( $\frac{W}{m^3K}$ ) around K2 airfoil**

***B.2.3 Mach 0.6***



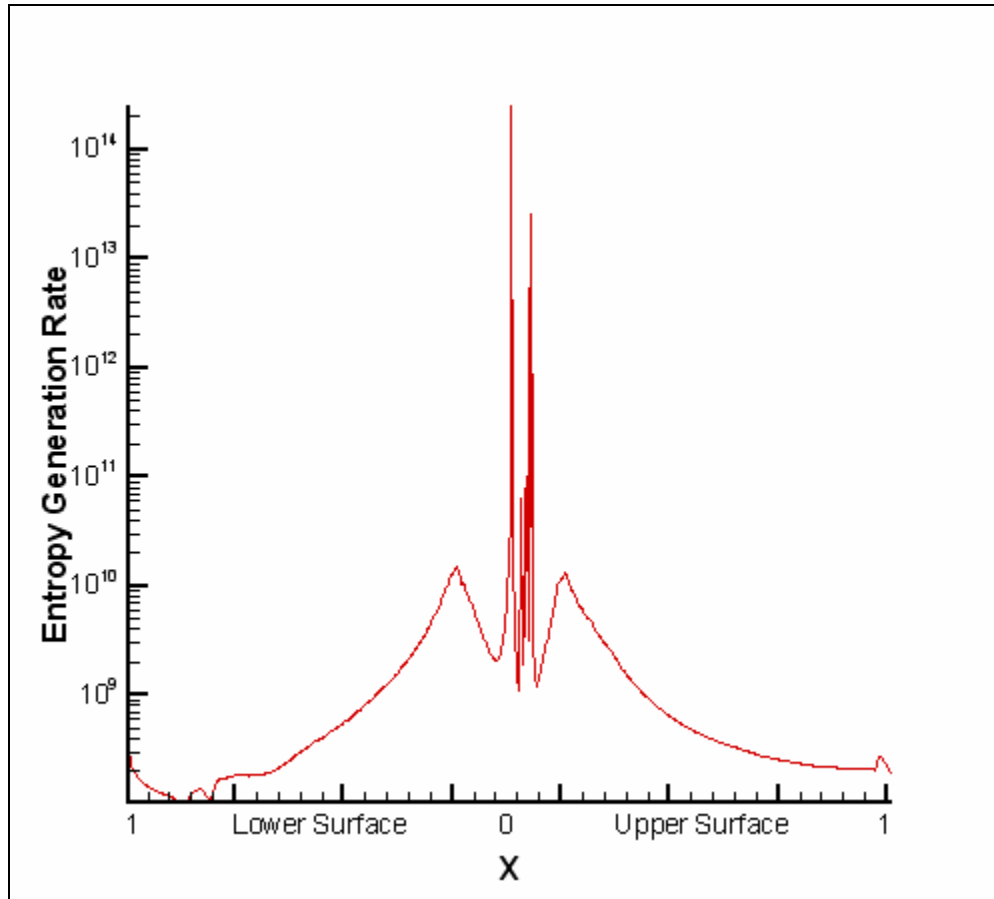
**Entropy Generation Rate ( $\frac{W}{m^3 K}$ ) around K2 airfoil**

**B.2.4 Mach 2.0**



**Entropy Generation Rate ( $\frac{W}{m^3 K}$ ) around K2 airfoil**

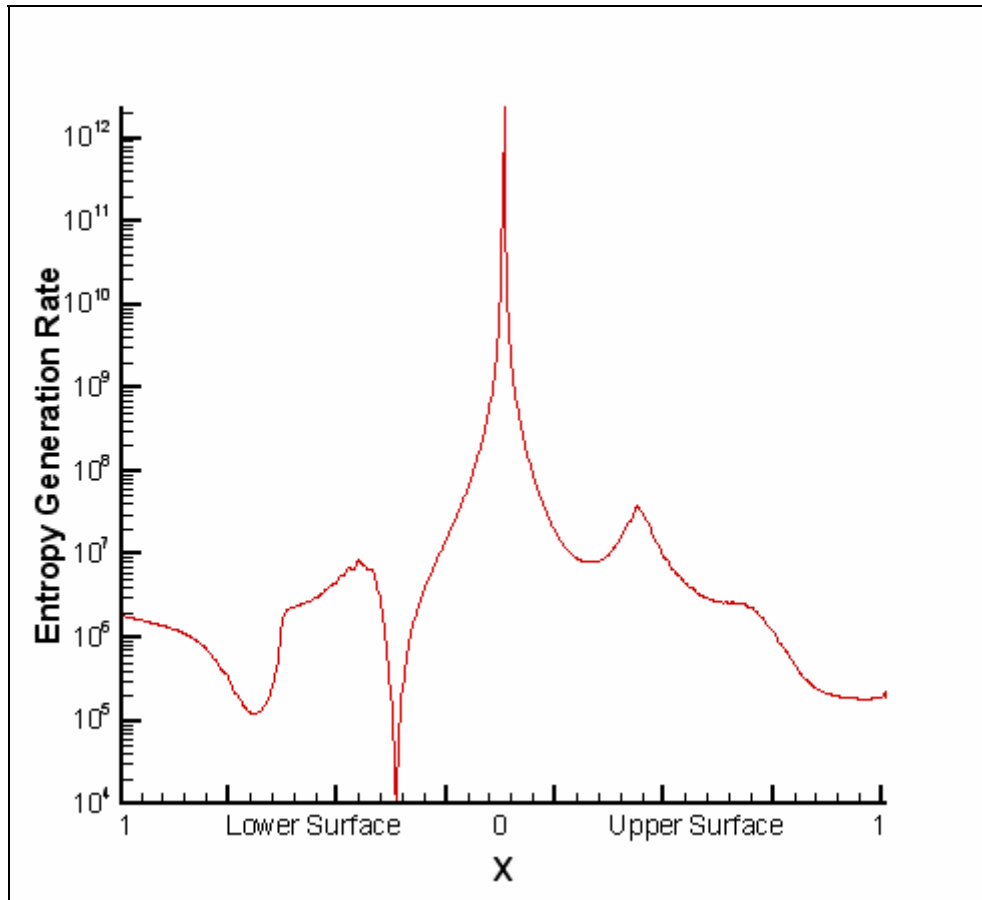
**B.2.5 Mach 3.0**



**Entropy Generation Rate ( $\frac{W}{m^3 K}$ ) around K2 airfoil**

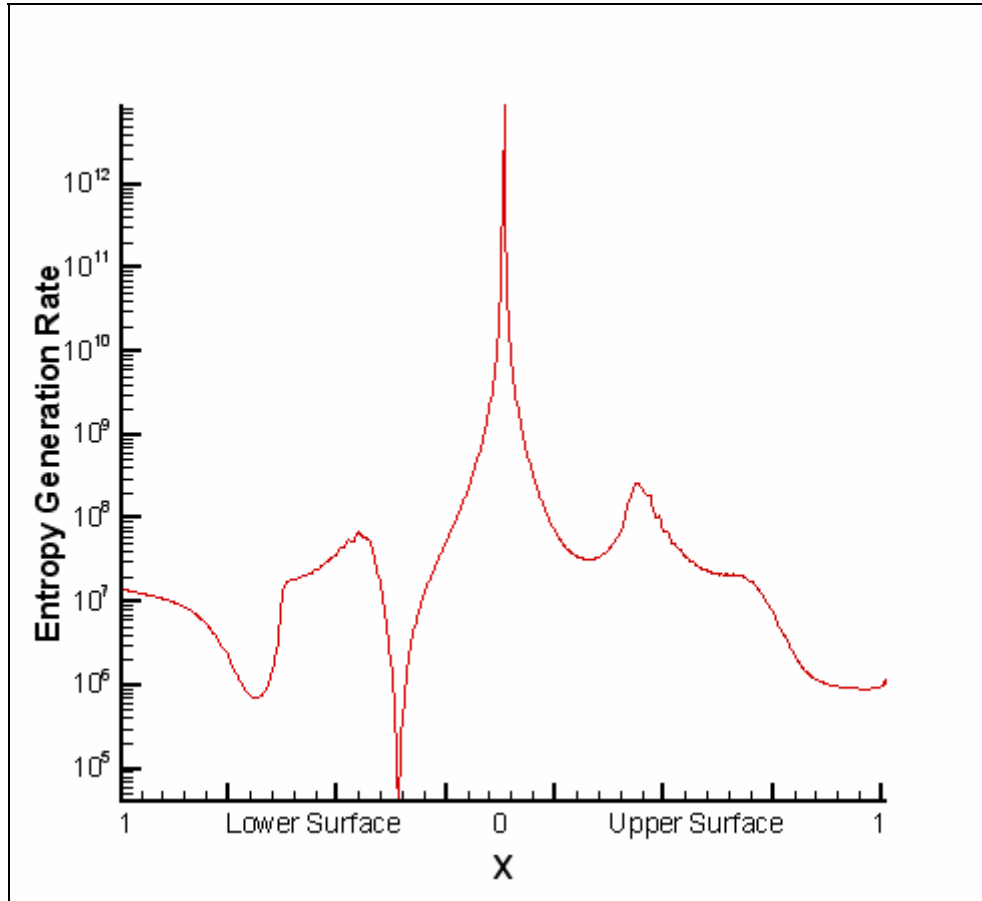
## APPENDIX B.3 Whitcomb Integral Supercritical Airfoil

### B.3.1 Mach 0.3



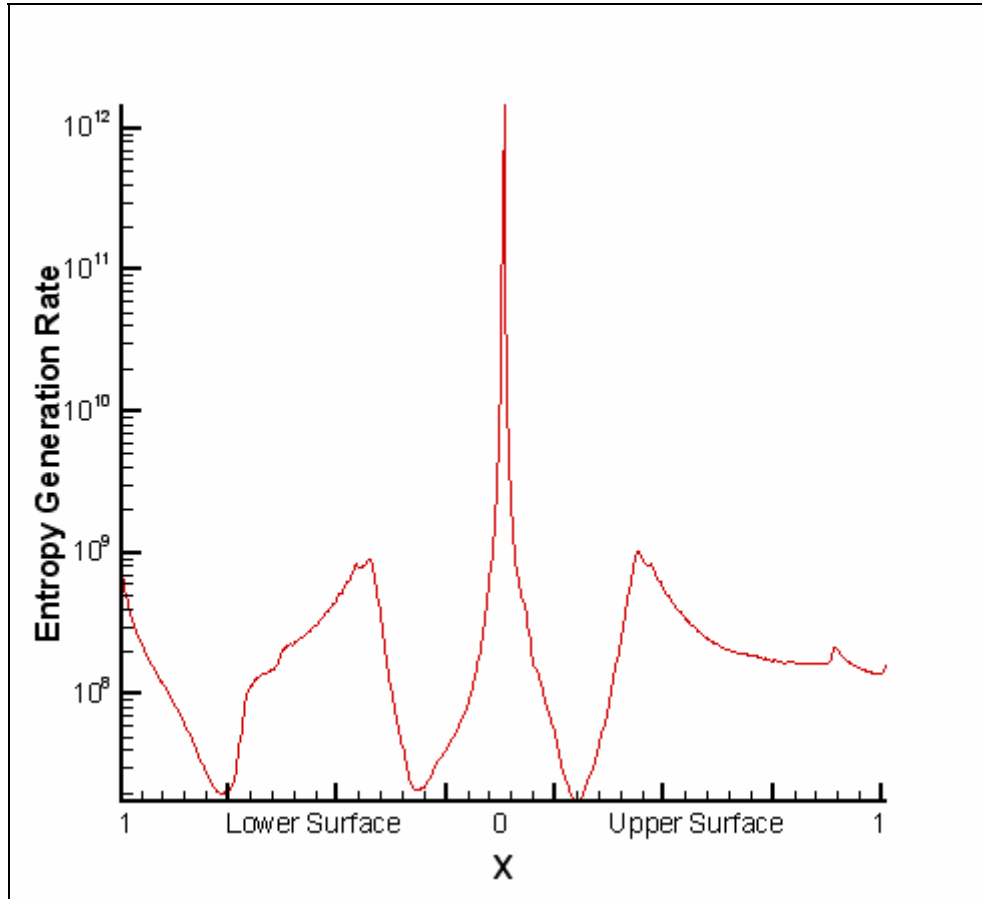
Entropy Generation Rate ( $\frac{W}{m^3K}$ ) around Whitcomb airfoil

***B.3.2 Mach 0.6***



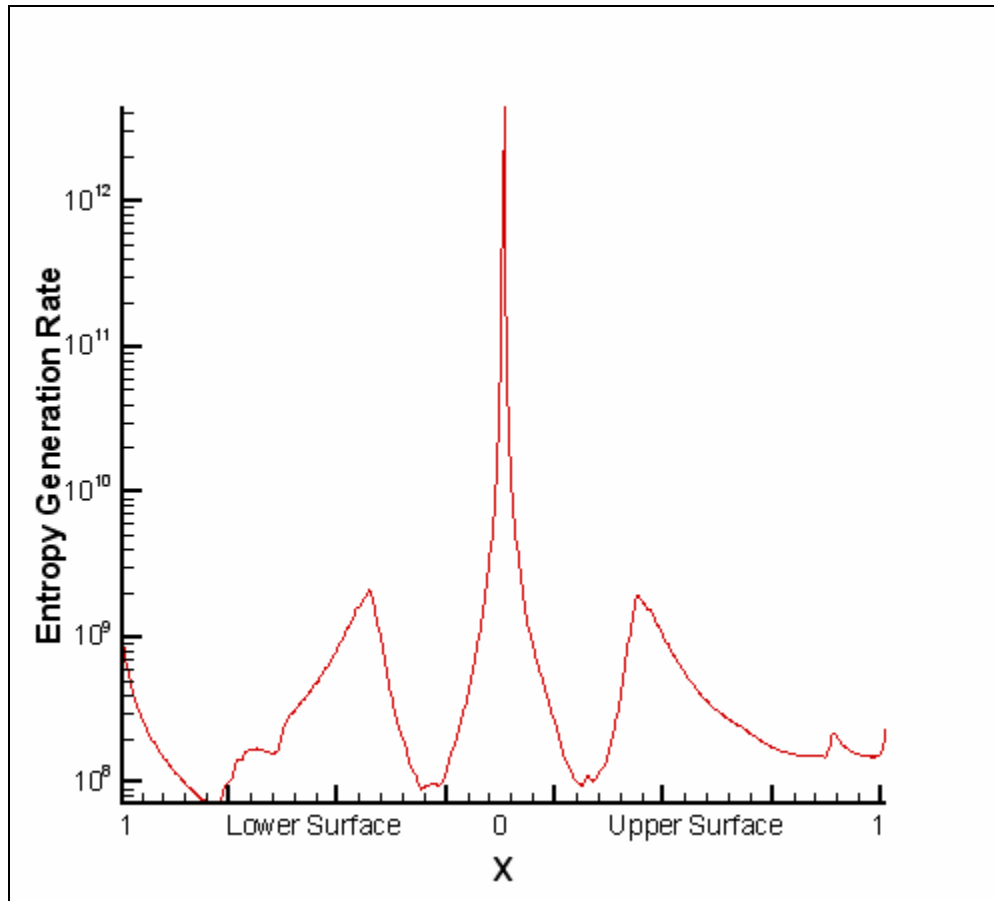
**Entropy Generation Rate ( $\frac{W}{m^3K}$ ) around Whitcomb airfoil**

### B.3.3 Mach 2.0



Entropy Generation Rate ( $\frac{W}{m^3K}$ ) around Whitcomb airfoil

**B.3.4 Mach 3.0**

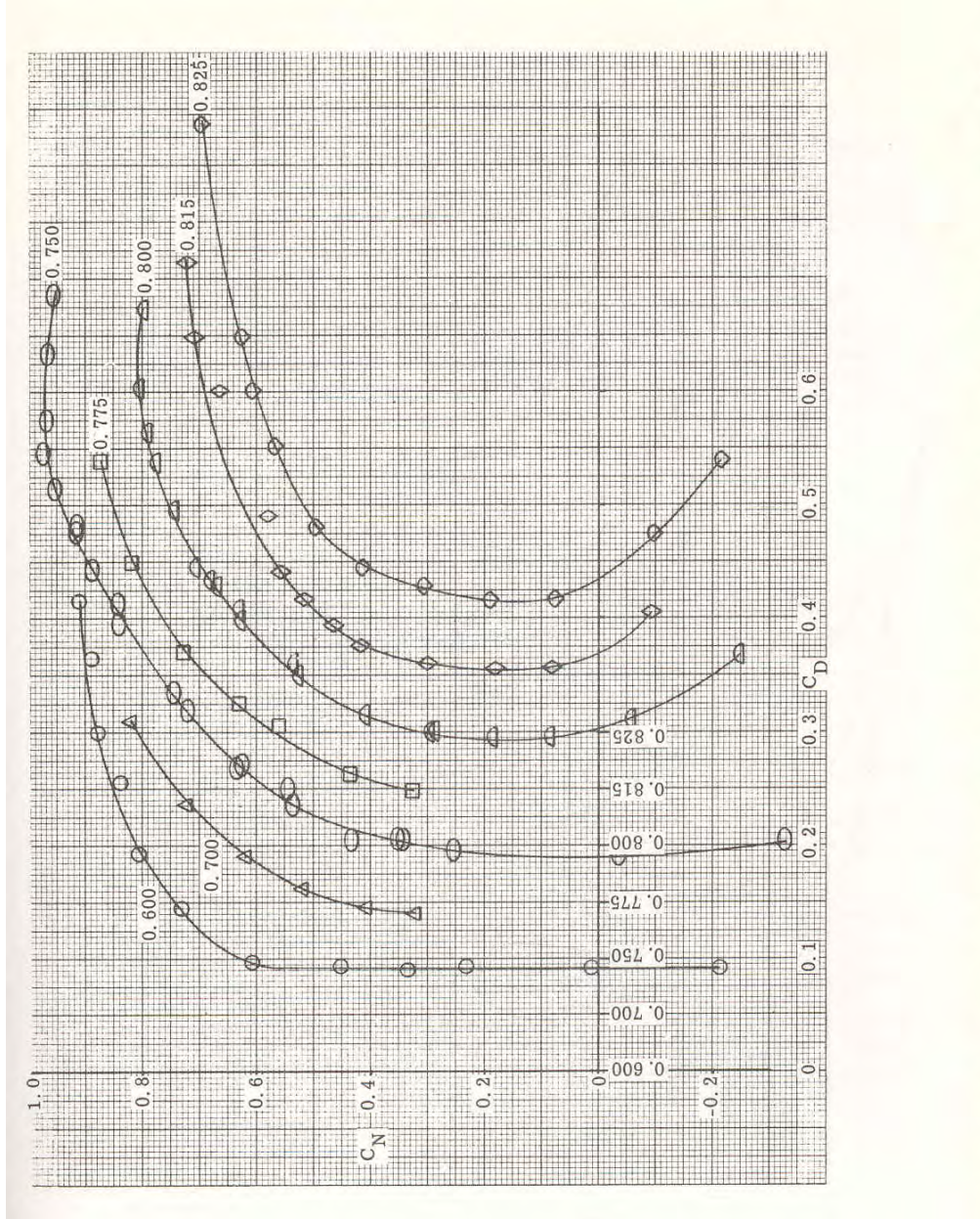


**Entropy Generation Rate ( $\frac{W}{m^3 K}$ ) around Whitcomb airfoil**

# APPENDIX C. EXPERIMENTAL DATA

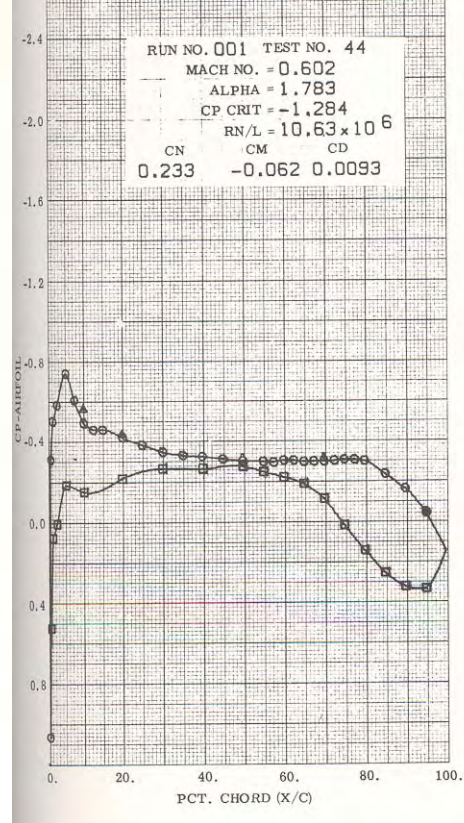
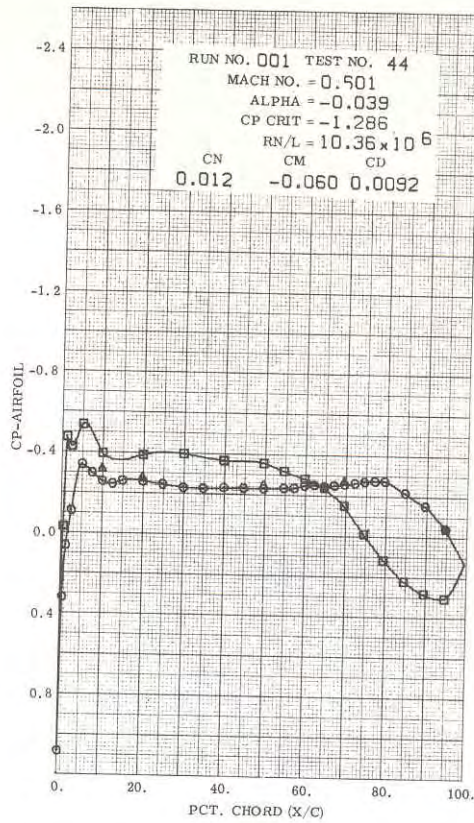
## APPENDIX C.1 K-2 Airfoil

### C.1.1 Drag Polar



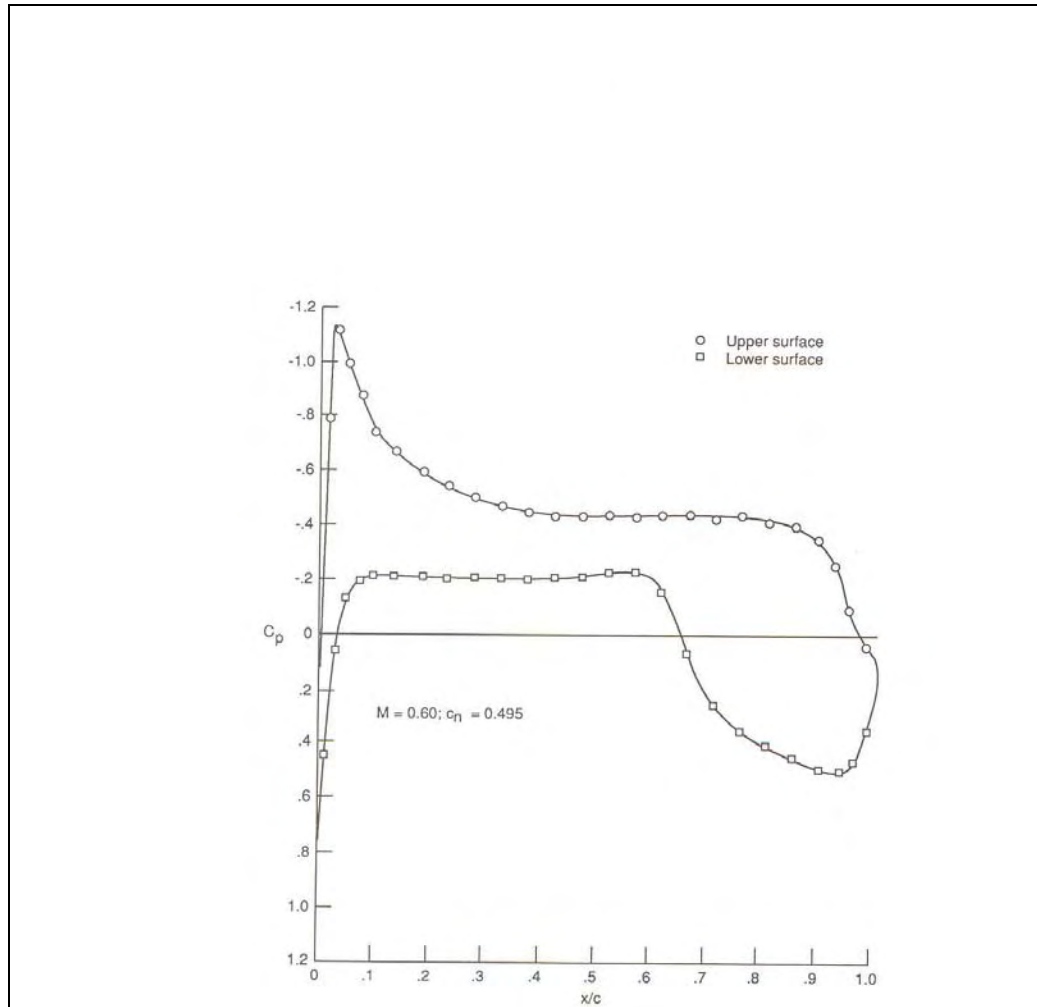
Drag Polar for a Reynolds Number of  $6.0 \times 10^6$  based on chord length.

### C.1.2 Normal Force



**Coefficient of Pressure around Airfoil at Different Angle of Attacks**

## APPENDIX C.2 Whitcomb Integral Supercritical Airfoil



Coefficient of Pressure around Whitcomb Supercritical Integral Airfoil

# APPENDIX D. ENTROPY GENERATION RATE PROGRAM

```
! Fortran Created by: Enrique G. Martínez Martí
!#####
PROGRAM ENRIFV
!#####
! This program opens a cfl3d.prout data file from CFL3D,
!obtains all the data and calculate the entropy generation
!rate.
!#####
IMPLICIT NONE

INTEGER, PARAMETER :: JMAX=705
INTEGER, PARAMETER :: KMAX=373
REAL, PARAMETER :: PI=3.141592653589793
REAL, PARAMETER :: CVIS=110.4 !CONSTANT FOR SUTHERLAND VISCOSITY
REAL, PARAMETER :: MVIS=0.0000178 !MOLECULAR VISCOSITY (KG/M*S)
REAL, PARAMETER :: TINF=288.15, Pr=0.72 !FREE STR. VELOCITY AND PRANDTL
REAL, PARAMETER :: Pt=0.9 !TURBULENT PRANDTL
REAL, PARAMETER :: HECND=0.003166059 !HEAT CONDUCTIVITY FOR AIR AT STD.
REAL, PARAMETER :: CPRE=1004.8 !SPECIFIC HEAT AT CONSTANT PRESSURE (J/KG*K)
REAL, PARAMETER :: HIL=5*10**18 !Check for really big number
INTEGER NC,JC,KC,JCO,KCO,OpenStatus

REAL I(JMAX,KMAX),J(JMAX,KMAX),K(JMAX,KMAX),X(JMAX,KMAX),
+ Y(JMAX,KMAX),Z(JMAX,KMAX),U(JMAX,KMAX),V(JMAX,KMAX),
+ W(JMAX,KMAX),P(JMAX,KMAX),T(JMAX,KMAX),MACH(JMAX,KMAX),
+ CP(JMAX,KMAX),TURB(JMAX,KMAX),DEVUX(JMAX,KMAX),
+ DEVUY(JMAX,KMAX),DEVVX(JMAX,KMAX),DEVVY(JMAX,KMAX),
+ TEMPX(JMAX,KMAX),TEMPY(JMAX,KMAX),SGEN(JMAX,KMAX),
+ VINFI,UDIM(JMAX,KMAX),VDIM(JMAX,KMAX),TDIM(JMAX,KMAX),
+ PDIM(JMAX,KMAX),WDIM(JMAX,KMAX),
+ SGENT(JMAX),SGENTC,VISEF(JMAX,KMAX),VISLA(JMAX,KMAX),
+ HEATCL(JMAX,KMAX),HEATCV(JMAX,KMAX),HEATEF(JMAX,KMAX),
+ SGENTH(JMAX,KMAX),SGENV(JMAX,KMAX),SGENTV(JMAX,KMAX),SGENVV

PRINT *, "What is the Free Stream Mach Number"
READ *, VINFI

PRINT *, "HIL: ", HIL

! READ FILE NAMES AND OPEN FILES (This program reads a
! cfl3d.prout input file
OPEN(UNIT=3,FILE="cfl3d.prout",STATUS="OLD",ACTION="READ",
& IOSTAT=OpenStatus)
REWIND 3
OPEN(UNIT=7,FILE="Output.DAT",STATUS="NEW")
REWIND 7

PRINT *, OpenStatus

READ(3,1)
1 FORMAT(/////////)

DO KC = 1, KMAX
DO JC = 1, JMAX

READ(3,*) I(JC,KC),J(JC,KC),K(JC,KC),X(JC,KC),Y(JC,KC),
```

```

+Z(JC,KC),UDIM(JC,KC),VDIM(JC,KC),WDIM(JC,KC),PDIM(JC,KC),
+TDIM(JC,KC),MACH(JC,KC),CP(JC,KC),TURB(JC,KC)

END DO
END DO

PRINT *, "VELOCITY, TEMP: ", VDIM(705,354), TDIM(705,354), MVIS
!Dimensionalize the u and v components of velocity

DO KC = 1, KMAX
DO JC = 1, JMAX

U(JC,KC)=UDIM(JC,KC)*VINFI*SQRT(1.4*287*TINF)
V(JC,KC)=VDIM(JC,KC)*VINFI*SQRT(1.4*287*TINF)
T(JC,KC)=TDIM(JC,KC)*TINF

!DEFINE THE LAMINAR VISCOSITY COEFFICIENT USING SUTHERLAND'S LAW
VISLA(JC,KC)=MVIS*(TDIM(JC,KC)**1.5)*((TINF+CVIS)/
&(T(JC,KC)+CVIS))

!DEFINE THE EFFECTIVE VISCOSITY WITH THE EDDY VISCOSITY
VISEF(JC,KC)=VISLA(JC,KC)+TURB(JC,KC)*MVIS

!DEFINE THE LAMINAR HEAT THERMAL CONDUCTIVITY
HEATCL(JC,KC)=(CPRE*VISLA(JC,KC))/Pr

!DEFINE THE TURBULENT HEAT THERMAL CONDUCTIVITY
HEATCV(JC,KC)=(CPRE*TURB(JC,KC)*MVIS)/Pr

!EFFECTIVE HEAT COEFFICIENT
HEATEF(JC,KC)=HEATCL(JC,KC)+HEATCV(JC,KC)

END DO

END DO

!
!This part calculates the entropy generation rate
!caused by viscous dissipation, eliminating the end points

!This part calculates the change in u-velocity and
!temperature versus y

KCO = 1

DO KC = 1, KMAX-1
JCO =1

DO JC= 1, JMAX-1

DEVUY(JCO,KCO) = (U(JC,KC+1)-U(JC,KC))/
& (ABS(Y(JC,KC+1)-Y(JC,KC)))
DEVVY(JCO,KCO) = (V(JC,KC+1)-V(JC,KC))/
& (ABS(Y(JC,KC+1)-Y(JC,KC)))
TEMPY(JCO,KCO) = (T(JC,KC+1)-T(JC,KC))/
& (ABS(Y(JC,KC+1)-Y(JC,KC)))

IF (DEVUY(JCO,KCO) > HIL .OR. DEVVY(JCO,KCO) > HIL .OR.
& TEMPY(JCO,KCO) > HIL) THEN
PRINT *, "INFINITY FOUND1: ", DEVUY(JCO,KCO),DEVVY(JCO,KCO),
& TEMPY(JCO,KCO), JCO,KCO
DEVUY(JCO,KCO) = 0
DEVVY(JCO,KCO) = 0
TEMPY(JCO,KCO) = 0
END IF

```

```

JCO = JCO +1

END DO

KCO = KCO +1

    END DO

!
!This part calculates the change in u-velocity and
!temperature versus x
KCO = 1
DO KC = 1, KMAX-1
JCO =1

DO JC= 1, JMAX-1

DEVUX(JCO,KCO) = (U(JC+1,KC)-U(JC,KC))/
& (ABS(X(JC+1,KC)-X(JC,KC)))
DEVVX(JCO,KCO) = (V(JC+1,KC)-V(JC,KC))/
& (ABS(X(JC+1,KC)-X(JC,KC)))
TEMPX(JCO,KCO) = (T(JC+1,KC)-T(JC,KC))/
& (ABS(X(JC+1,KC)-X(JC,KC)))

IF (DEVUX(JCO,KCO) > HIL .OR. DEVVX(JCO,KCO) > HIL .OR.
& TEMPX(JCO,KCO) > HIL) THEN
PRINT *, "INFINITY FOUND2: ", DEVUX(JCO,KCO),DEVVX(JCO,KCO),
& TEMPX(JCO,KCO), JC,KC
DEVUX(JCO,KCO) = 0
DEVVX(JCO,KCO) = 0
TEMPX(JCO,KCO) = 0
END IF

JCO = JCO +1

END DO

KCO = KCO +1

END DO

!This step is to calculate the entropy generation rate
!at each point

DO KCO = 2,KMAX-1
DO JCO = 2,JMAX-1

!VISCOUS ENTROPY GENERATION
SGENV(JCO,KCO) = (VISEF(JCO,KCO)/T(JCO,KCO)) *
& (2*(DEVUX(JCO,KCO)**2 + DEVVY(JCO,KCO)**2) +
& (DEVUY(JCO,KCO)+DEVVX(JCO,KCO))**2)

!THERMAL ENTROPY GENERATION
SGENTH(JCO,KCO)=(HEATEF(JCO,KCO)/(T(JCO,KCO)**2))*
& (TEMPX(JCO,KCO)**2 + TEMPY(JCO,KCO)**2)

SGEN(JCO,KCO)=SGENV(JCO,KCO)+SGENTH(JCO,KCO)

END DO
END DO

!Add up all the entropy generation at each point

```

```

DO JCO = 2,JMAX-1

SGENTC=0 !THIS INITIALIZES THE ENTROPY GENERATION COUNTER
SGENVC=0 !INITIALIZING THE COUNTER FOR VISCOUS ENTROPY GENERATION

DO KCO = 2,KMAX-1

SGENTC=SGENTC + SGENT(JCO,KCO)
SGENVC=SGENVC + SGENV(JCO,KCO)

END DO

SGENT(JCO) = SGENTC
SGENTV(JCO) = SGENVC

END DO

PRINT *, "ENTER SGENT: ", SGENT(200)

WRITE(7,*) '#      J X  TOTAL ENTROPY GENERATION
& VISCOUS ENTROPY GENERATION'

!WRITE ALL THE ENTROPY GENERATION RATES AT EACH POINT IN THE DATA FILE
DO JCO = 2,JMAX-1

WRITE(7,*) JCO, X(JCO,1), SGENT(JCO), SGENTV(JCO)

END DO

END

```

---

This is part of the cfl3d.prout output that was used for the Naca airfoil at Mach 0.65:

```

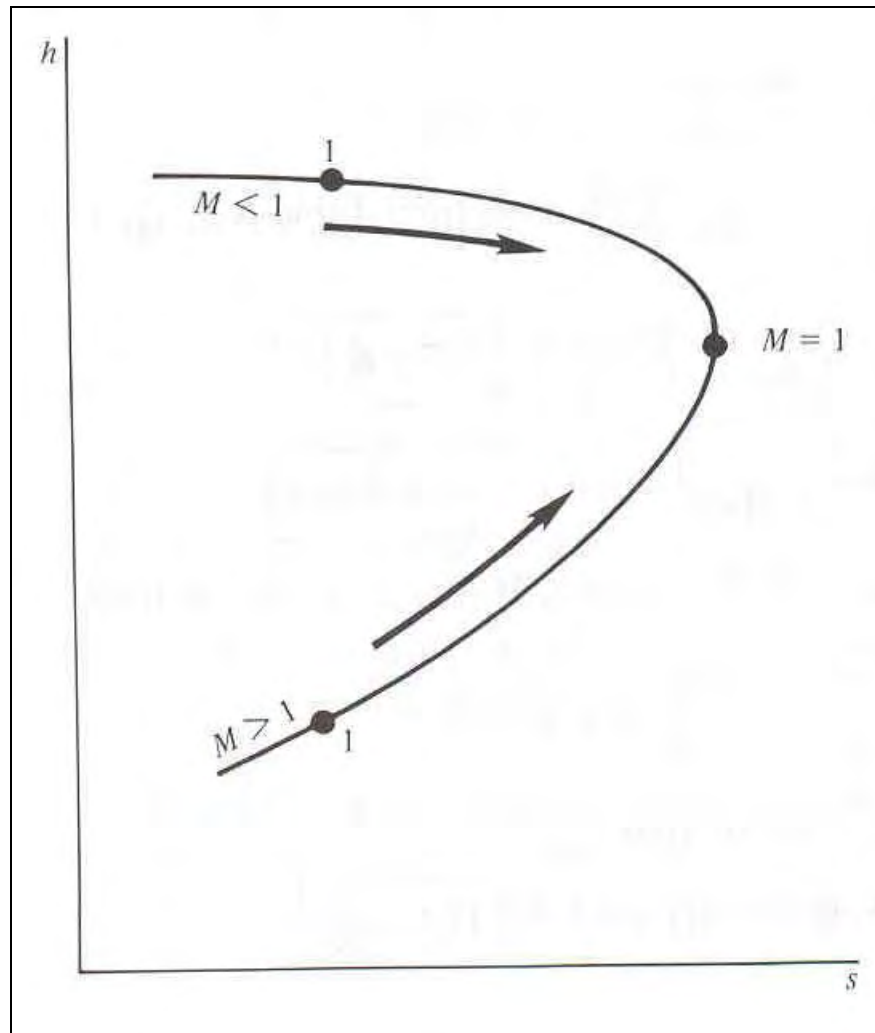
NACA64
Mach      alpha      beta      ReUe      Tinf,dR      time
0.65000   0.00000   0.00000  0.150E+08  518.67000   0.00000

BLOCK 1 (GRID 1)      IDIM,JDIM,KDIM=      2 1025  513
NOTE: endpts may not be reliable

I J K  X      Y      Z      U/Uinf  V/Vinf  W/Winf  P/Pinf  T/Tinf  MACH  cp  tur. vis.
1 161 1 0.100000E+01 0.0000E+00 0.000000E+00 0.2620366E-01 0.3260641E-02 0.0000000E+00 0.1093352E+01
    0.1080868E+01 0.1650918E-01 0.3156457E+00 0.7040774E+00
1 162 1 0.9999006E+00 -0.1114021E-04 0.0000000E+00 0.0000000E+00 0.0000000E+00 0.0000000E+00 0.1092089E+01
    0.1080454E+01 0.0000000E+00 0.3113736E+00 0.0000000E+00
1 163 1 0.9997979E+00 -0.2265300E-04 0.0000000E+00 0.0000000E+00 0.0000000E+00 0.0000000E+00 0.1092144E+01
    0.1080288E+01 0.0000000E+00 0.3115618E+00 0.0000000E+00
1 164 1 0.9996918E+00 -0.3455074E-04 0.0000000E+00 0.0000000E+00 0.0000000E+00 0.0000000E+00 0.1091833E+01
    0.1080205E+01 0.0000000E+00 0.3105094E+00 0.0000000E+00

```

## APPENDIX E. FANNO CURVE



**Enthalpy versus Entropy Relation for a gas with friction**